

Synthesis and in-depth characterization of mono- and bimetallic nanoparticles

Dissertation

Zur Erlangung des akademischen Grades eines

Doktors der Naturwissenschaften

Dr. rer. nat.

vorgelegt von

Kevin Pappert

Fakultät für Chemie

Institut für Anorganische Chemie

Universität Duisburg-Essen

2018

If you trust in yourself, and believe in your dreams, and follow your star... you'll still get beaten by people who spent their time working hard and learning things and weren't so lazy.

‡ The Wee Free Man ‡

Terry Pratchett

Die vorliegende Arbeit wurde im Zeitraum von Januar 2016 bis Dezember 2018 im Arbeitskreis von Prof. Dr. Matthias Epple am Institut der Anorganischen Chemie der Universität Duisburg-Essen angefertigt.

Gutachter: Prof. Dr. Matthias Epple
Prof. Dr. Malte Behrens

Vorsitzender: Prof. Dr. Alexander Probst

Tag der Disputation: 06.02.2019

Table of contents

Table of contents	V
1. Introduction and motivation	1
2. Theoretical background.....	4
2.1 Nanoparticles and colloids.....	4
2.2 Synthesis of nanomaterials	5
2.3 Crystallization of nanoparticles	6
2.4 Stabilization of nanoparticles.....	8
2.5 Shape control of metallic nanoparticles.....	10
2.6 Bimetallic systems and galvanic replacement	12
2.7 Surface plasmon resonance.....	14
3. Methods.....	15
3.1 Dynamic light scattering and ζ -potential	15
3.2 Differential centrifugal sedimentation	16
3.3 UV/Vis spectroscopy	17
3.4 Atomic absorption spectrometry.....	18
3.5 X-ray photoelectron spectroscopy	19
3.6 X-ray powder diffraction	20
3.6.1 Synchrotron radiation.....	22
3.7 Scanning electron microscopy and energy dispersive X-ray spectroscopy	23
3.8 Transmission electron microscopy	24
3.9 Differential scanning calorimetry	24
4. Experimental section	25
4.1 Software/databases used	25
4.2 Chemicals used	26
4.3 Devices used	27

4.4 Synthesis of silver nanoparticles with glucose.....	28
4.5 Metallic nanoparticles from reduction with sodium borohydride	29
4.5.1 Synthesis of silver nanoparticles	29
4.5.2 Synthesis of iridium nanoparticles	30
4.5.3 Synthesis of porous iridium/iridium dioxide nanostructures.....	30
4.5.4 Synthesis of silver-iridium core-shell systems	31
4.6 Metallic nanoparticles from the polyol process	32
4.6.1 Synthesis of silver nanocubes (oxidative etching)	32
4.6.2 Synthesis of silver nanowires (seed and growth)	33
4.6.4 Synthesis of iridium nanoparticles in a microwave.....	33
4.6.3 Synthesis of silver nanoparticles in a microwave.....	34
4.7 Synthesis of core-shell particle (seed and growth).....	35
4.8 Experimental setup of the dissolution experiments.....	36
5. Results and discussion.....	37
5.1 Synthesis of silver nanoparticles from glucose	37
5.1.1 Characterization of nanoparticles synthesized with glucose	37
5.1.2 Bimetallic nanoparticles based on the glucose synthesis	43
5.1.3 Core-Shell nanoparticles based on the glucose synthesis.....	61
5.2 Synthesis of silver nanoparticles with sodium borohydride.....	68
5.2.1 Characterization of silver nanoparticles from sodium borohydride	69
5.2.2 Reproducibility and long-term stability.....	86
5.2.3 Core-shell particles based on the synthesis with sodium borohydride.....	90
5.3 Synthesis of silver nanoparticles with the polyol process.....	103
5.3.1 Characterization of silver nanocubes generated by oxidative etching	104
5.3.2 Core-Shell particles based on silver nanocubes	110
5.3.3 Characterization of silver nanowires synthesized with hetero seeds.....	119
5.3.4 Core-shell particles based on silver nanowires.....	126
5.4 Dissolution of silver-based nanoparticle systems	132

5.4.1 Evaluation of the dissolution experiments	133
5.5 <i>In-situ</i> powder diffraction of silver nanoparticles.....	139
5.5.1 Characterization of silver nanoparticles from a polyol process in a microwave..	140
5.6 Synthesis of iridium nanoparticles with the polyol process	154
5.6.1 Characterization of iridium nanoparticles synthesized with the polyol process ..	155
5.7 Synthesis of iridium nanoparticles using sodium borohydride.....	159
5.7.1 Characterization of iridium nanoparticles using sodium borohydride.....	159
5.8 Synthesis of porous nanospheres of Ir/IrO ₂ with sodium borohydride.....	162
5.8.1 Characterization of porous Ir/IrO ₂ nanostructures	163
5.8.2 Temperature-dependent investigations of porous Ir/IrO ₂ nanostructures	173
5.8.3 Reproducibility and size control of porous Ir/IrO ₂ nanostructures	184
6. Conclusion.....	188
7. Zusammenfassung.....	192
8. References	196
9. Appendix	206
9.1 List of publications	206
9.2 Posters and presentations	207
9.3 Curriculum Vitae	208
9.4 Danksagung	209
9.5 Eidesstaatliche Erklärungen.....	210

1. Introduction and motivation

In modern science, nanomaterials have gained more and more interest based on their size dependent properties in comparison to the bulk material. In fact, they are a bridge between the bulk material and the atomic scale. Their properties often change regarding optical, thermal and electrical nature. Spherical silver nanoparticles in dispersion for example appear in a yellow to grey color, whereas spherical gold nanoparticles are known to show red to rose colors. These observations can be made because nanomaterials exhibit plasmonic resonances caused by quantum effects.^[1] Regarding thermal properties, metallic nanoparticles show a size and shape depending melting behavior resulting in significantly lowered melting points.^[2-3]

Especially silver, which is a ductile material normally crystallizing in the face-centered cubic structure, has already a lot of possible and practical applications regarding the bulk material. Silver possesses the highest thermal, as well as electrical conductivity of all known metals.^[4-5] Due to the properties in the nanoscale, it finds application in catalysis^[6-7], photonics^[8-9], surface enhanced Raman spectroscopy (SERS)^[10-11] as well as energy storage and conversion systems.^[12-13] Especially the antibacterial effects of silver, which are known for roughly 4000-5000 years^[14-15], again arouse great interest. Since conventional methods like antibiotics conquer pathogens like methicillin-resistant *staphylococcus aureus* (MRSA), which are resistant against nearly all known antibiotic classes^[16-17], silver becomes an alternative. Silvers antibacterial effects are attributable to the release of ions.^[15, 18-20]

Consequently, the ion release rate is the determining factor which decides over the efficiency of the applied silver in a possible medical application. Since nanomaterials have a high surface area to volume ratio, the active surface area is drastically increased compared to the same amount of bulk silver. Different studies have shown that the ion release is strongly dependent on the size as well as the shape of silver nanoparticles.^[21-23] Furthermore, the release rate can be influenced by the formation of an alloy, where different compositions leads to delayed or lowered ion release rates.^[24]

Another field of interest is the combination of pure-phased nanoscaled materials. Sputtered dots of silver showed an increased cytotoxicity when applied on nobler substrates. Especially a combination of silver and iridium showed a significant increase efficiency compared to gold or palladium surfaces. This increased cytotoxicity is attributed to a sacrificial anode effect.^[25-26] A combination of the size and shape depending dissolution as well as the synthesis of bimetallic systems with separated phases might therefore lead to an enhanced ion release which can be “designed” by combinations of several factors like shell shaping, thickness or the used material.

This combination was one aim of this work. Alloyed systems containing silver can be realized by simultaneous reduction of both metal precursors. Normally, this leads to alloyed particles if a co-crystallization of both systems is possible.^[27] Since in alloyed systems nobler atoms protect a certain amount of silver, which could be shown using cyclic voltammetry^[28], these kinds of two-phased systems are not promising to increase the silver ion release rate.

To mimic the system of sputtered silver dots of a nobler metal with nanoparticles a core-shell approach was chosen. To induce a sacrificial anode effect, the shell shall not be closed. That allows oxidizing species to interact with silver atoms. However, this approach brings some limitations regarding the preservation of certain morphologies. Since silver is less noble than gold, iridium or palladium, the silver particles are partially dissolved in a galvanic replacement reaction.^[29-33] This effect can on the one hand be used to generate hollow and porous structures or to investigate the crystallization and the replacement of certain facets of the used nanocrystals.^[34-36] On the other hand, multi-faceted crystals, which particle morphologies often consist of, show greater susceptibility and higher reactivity towards etching.^[37] For this particular problem, certain solutions are accessible in the literature where, for example the reducing agent ascorbic acid and its reduction potential is increased by higher pH values.^[38-39] Another possibility is the really slow addition of the shell-precursor. Due to the low concentrations of metal precursor ions the reduction is likelier by the reducing agent in a high concentration than by the metallic silver particles themselves.^[40] These methods mostly refer to a certain morphology and cannot be applied for other particle morphologies or sizes. Consequently, the development of a synthesis which could be applied to silver spheres in different sizes, silver nanowires and silver nanocubes was an aim of this work. These particles were then to be tested in dissolution experiments to possible synthesize particles with “designed” silver ion release rates by variation of the shell thickness as well as the shell material.

Another important field of nanoscience is the investigation of the nucleation and growth kinetics of particles. Since the catalytic activity^[41-43] or optical properties^[44-45] directly correlate to specific crystallographic facets, it is important to understand the mechanisms which lead to the formation of anisotropic shapes, branched structures or why nanoparticulate systems result in broad or narrow size distributions. *In-situ* X-ray scattering techniques are often used to conquer these questions. Methods like small angle X-ray scattering (SAXS) or X-ray powder diffraction (XRPD) can help to get deeper insight into the nanoparticle nucleation as well as the growth during the synthesis.^[46-48] Especially high flux X-ray sources can help to increase the

resolution dramatically. Investigations of a nanoparticle synthesis using a laboratory microwave reactor at a synchrotron source for example led to the findings that the formation of silver nanoparticles can be separated into four different stages.^[49] Comparable experiments were also performed in this work to answer the questions of the influence of a stronger reducing agent (diethylene glycol vs. ethylene glycol) and significantly higher concentrations of precursor on the crystallization of the particles. Additionally, the datasets were complemented with different colloidal and microscopic methods like dynamic light scattering, differential centrifugal sedimentation, scanning electron microscopy and transmission electron microscopy. Furthermore, the resolution of the experiments could be increased compared to the work by Sun et al.

The third important part of this work consist of the syntheses of iridium nanostructures. The heavy metal iridium with a melting point of 2466 °C, a density of 22.56 g cm⁻³ which crystallizes in the fcc-structure is one of the rarest non-radioactive metals on earth.^[50] The main application of iridium is in the formation of alloys to increase or tune their properties. In the last decades, iridium has also found applications as catalyst for the reaction of acetic acid. Iridium nanoparticles are of great interest in modern science since it was shown that iridium and iridium oxides have promising properties for water-splitting^[51-52], oxygen reduction in fuel cells^[53-54] or as catalytic sensor materials.^[55-56] Former studies of iridium nanoparticles have revealed that the formation of well faceted nanostructures of iridium is unlikely and hence not described by accessible literature. This phenomenon can be ascribed to the relatively low energy barrier for a homogenous nucleation compared with that for a heterogeneous nucleation. Newly formed iridium atoms will consequently self-nucleate which results in small branched particles rather than well-defined faceted structures.^[57] Consequently the aim of this work was to optimize reaction conditions to synthesize spherical homogenous iridium nanoparticles as reference material for biological experiments like cytotoxicity assays. The optimization of those syntheses led to nano-porous spherical materials containing iridium and iridium oxide. Due to their high surface area to volume ratio those materials were promising for further investigations

2. Theoretical background

2.1 Nanoparticles and colloids

Nanomaterials consist of small particles in the nanometer size range (10^{-9} m). The term nanos is descended from the Greek language and translates to dwarf.^[58] Particles in this size range often have different properties compared to their bulk materials such as different melting points^[59-60], optical^[8, 44, 61-62] or electrical properties.^[63-64] Since they are smaller than bacteria or cells nanoparticles can be used as carrier for molecules like proteins, amino acids or active pharmaceutical ingredients (API) and are consequently in the field of interest for therapy and diagnostic.^[65-68]

There are lots of different definitions of nanomaterials from various national and international bodies like BSI, FDA, Health Canada, ISO 2008, OECD 2008, and SCENIHR 2007.^[69-70] All definitions set different standards like crystallinity, size of lateral dimensions, size distribution, redox potential or surface modification to describe nanomaterials. However, a commonly accepted definition is formulated by the International Organization for Standardization (ISO) and shall be mentioned: “A nanoparticle is a particle which spans 1 nm – 100 nm in diameter.^[71]” An addition to this definition was added by the Committee on Consumer Products (SCCP) which said that at least one dimension of the particle has to be in the nanometer range (1 nm – 100 nm).^[71] This definition consequently includes nanowires, platelets or other particles with an anisotropic shape.

Nanoparticles are often stored in a second phase or medium. In these two-phase systems the particles are homogeneously distributed. Stabilized nanoparticles do not sediment if they are stored in a solution. Consequently, the resulting dispersion shows the properties of a solution. Those two-phased systems are called colloids and can be compiled as follows:

Table 1: Possible colloidal systems of different two-phased mixtures. Adapted from ref.^[72]

Disperse phase	Medium		
	Gas	Liquid	Solid
Gas	-	Foam	Solid foam
Liquid	Liquid aerosol	Liquid emulsion	Solid emulsion
Solid	Solid aerosol	Sol	Solid Sol

Colloids were further divided into sub groups by Staudinger.^[73] Those sub groups are the dispersion colloids, molecular colloids and association/micellar colloids. The synthesized and characterized nanoparticles in this work belong to the sub group of dispersion colloids. They are thermodynamically unstable and can contain polydisperse particles with different morphologies which are typically hydrophobic.

2.2 Synthesis of nanomaterials

The realization of nano-sized materials can be done by two different approaches. Those are bottom-up and top-down methods (Fig. 1).

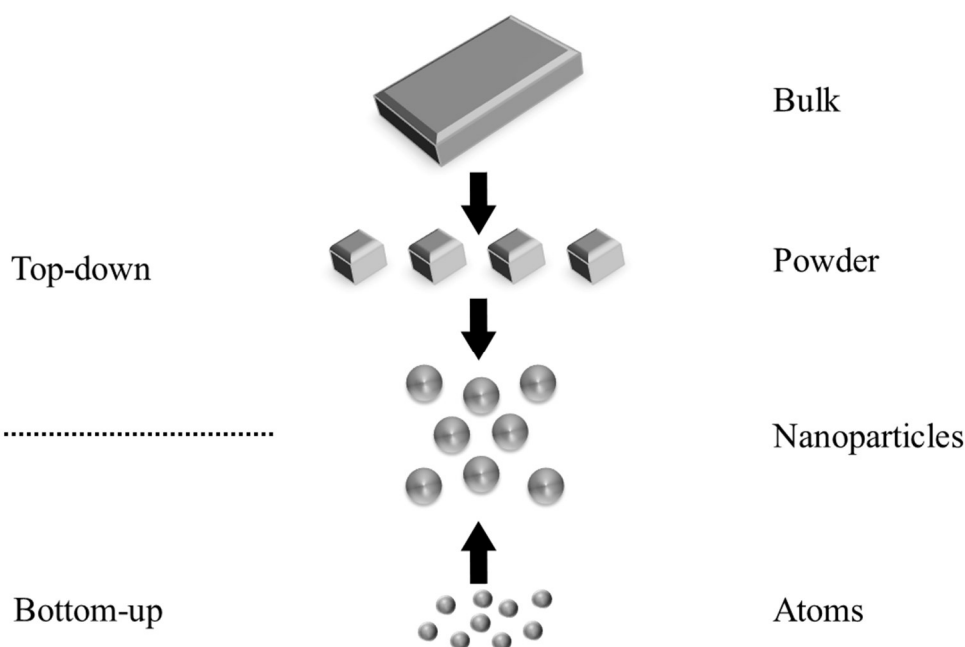


Fig. 1: Schematic drawings of the bottom-up and top-down approaches to generate nanomaterials.

To generate nanomaterials with the top-down approach, the bulk material is downscaled by appliance of a physical force. The most common method is the grinding of bulk material by ball mills.^[74] In contrast, the bottom-up approach is fulfilled by the reduction of a metallic precursor in solution. A third possibility is the laser ablation where the material is vaporized and starts to form clusters subsequent nanoparticles.^[75] Since bulk material is used to generate atoms, the laser ablation can be seen as a hybrid method. All approaches have certain limitations and advantages. The grinding of bulk materials can be used to produce large quantities of

material, but the morphology and the size of the particles cannot be controlled. Laser ablation also leads to high yields of particles in a short time, but the particle size distribution is rather broad. The particle sizes must be separated by sedimentation which is a time-consuming process with varying results. Furthermore, the particle morphology cannot be controlled. Consequently, only spherical particles are obtained from the method. The reduction of a metallic precursor to generate particles leads to well defined morphologies and narrow size distributions when the reaction parameters are well controlled. However, the yield of the syntheses is comparatively small.

2.3 Crystallization of nanoparticles

Since the bottom-up approach is a crystallization process, several parameters can be modified to take an influence on the resulting particle shape and size. Already in 1950, LaMer purposed a mechanism to describe the formation of monodisperse hydrosols.^[76] The model describes a three staged process (Fig. 2), where in the first step (I) the increase of forming atoms leads to a supersaturated state (II) which initiates the formation of nuclei (C_{min}). The consumption of atoms leads to a decrease in concentration until the supersaturated state is left. Consequently, the remaining atoms are only used to increase the particle size of the already formed nuclei (III).

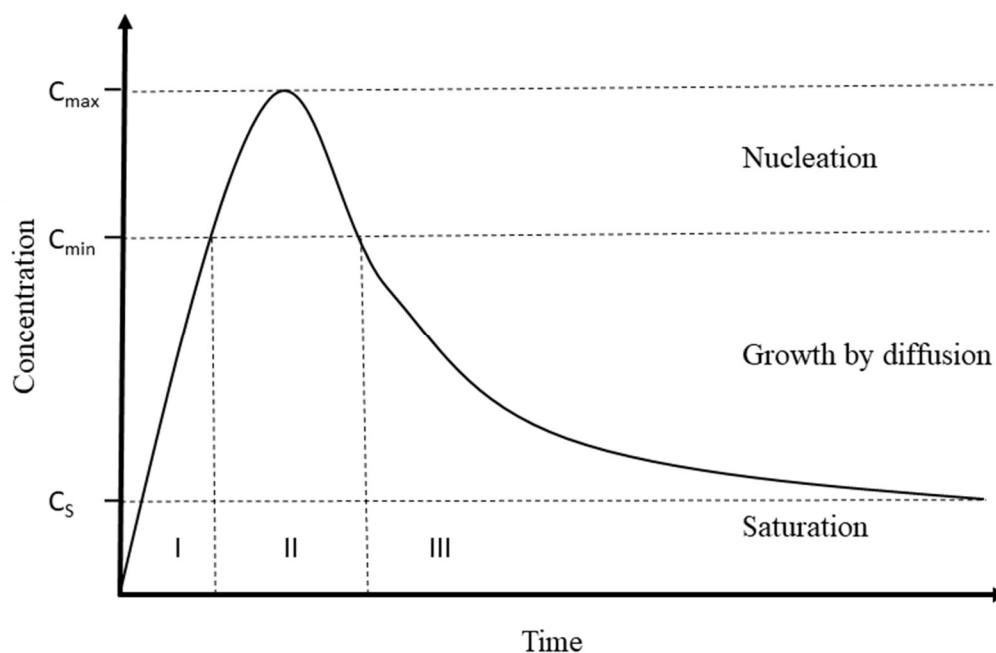
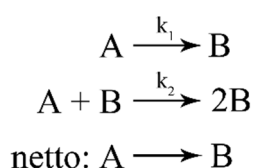


Fig. 2: LaMer model to describe the three steps leading to nucleation and growth of nanoparticles in dispersion. The concentration of atoms is plotted against the time.

The nanoparticles seed formation consequently depends on the strength of the reducing agent used. Weaker agents, like ascorbic acid, only deliver two electrons per molecule to the reaction. This results in a slow crystallization process leading to a lower number of seeds. In contrast, strong agents, like sodium borohydride can yield up to eight electrons per molecule which leads to a higher atom concentration resulting in more nuclei. The formation of more nuclei results in smaller particles at the end of the reaction. Since the model is from the 1950s, several additions and changes have been made by several groups and researchers.^[77] Today, the most commonly expansion of the model is the two-step mechanism proposed by Finke et al. which assumes two different reactions for the formation of nanoparticles.^[78-79]



Where k_1 is the rate constant which describes the formations of seeds from atoms and k_2 the rate constant for the autocatalytic particle surface growth. In a lot of reactions, k_1 is significantly smaller than k_2 after the state of supersaturation is left. This leads to only a few new seeds whereas the most silver ions are used to drive on the growth of the particles. This relationship changes under certain circumstances. This can be caused by high concentrations of precursor or by low amounts of weak reducing agents. This behavior has a huge influence on the dispersity of the system. The resulting nanoparticles have a high surface energy due to the huge surface area to volume ratio. Consequently, colloidal systems tend to agglomerate to minimize the free enthalpy (G).

$$dG = \gamma dA_G \quad (1)$$

Where the free enthalpy equals the surface tension γ times the particle surface A_G . A reduction of the particle surface therefore results in a decrease of free enthalpy. This mathematical relationship is also the cause for Ostwald ripening.^[72-73, 80] In this process, smaller particles dissolve to atoms which diffuse to bigger particles and crystallize on their surface. This mechanism minimizes the free enthalpy of the system. Therefore, a maximization of the particle surface will occur over time. To prevent these processes and preserve the size, nanoparticles need to be stabilized.

2.4 Stabilization of nanoparticles

To minimize the energy of the systems, nanoparticles tend to agglomerate and aggregate in solution. The agglomeration is driven by the attractive force of van der Waals interaction. To prevent this attraction, counter forces need to be applied. This can either be done by coating the nanoparticles with sterically demanding ligands or by electrostatical effects where the nanoparticles are loaded with charged molecules forming an electrochemical double layer (Fig. 3).

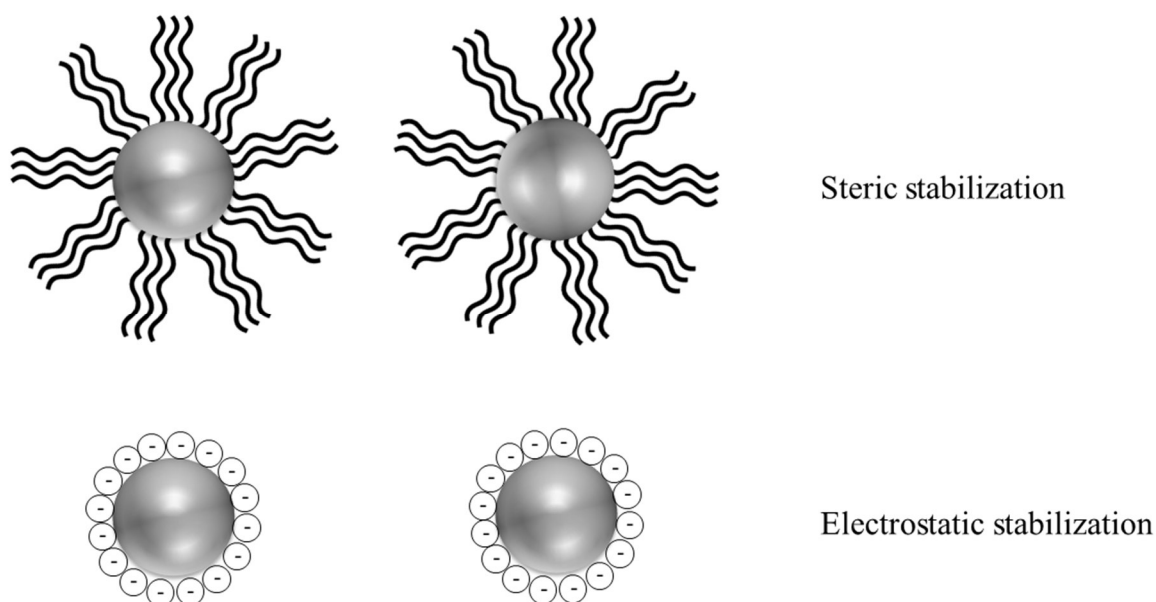


Fig. 3: Schematic drawings of steric and electrostatic stabilization of nanoparticles. The tortuous lines represent polymers (steric stabilization) and the spheres containing minus signs represent charged molecules on the particle surface (electrostatic stabilization).

A third possibility consists of the combination of both methods where charged sterically demanding ligands are applied to functionalize the particle surface. Common examples for the sterical functionalization of the particle surface are compounds like poly (N-vinylpyrrolidone) (PVP), polyvinyl alcohol (PVA) or sodium dodecyl sulfate (SDS).^[40] Electrostatic stabilization can be achieved by using strongly charged molecules like trisodium citrate or sodium ascorbate.^[62, 81] The combination can be realized by charged polymers like sodium polystyrene sulfonate (PSS). Examples of each class are shown in Figure 4.

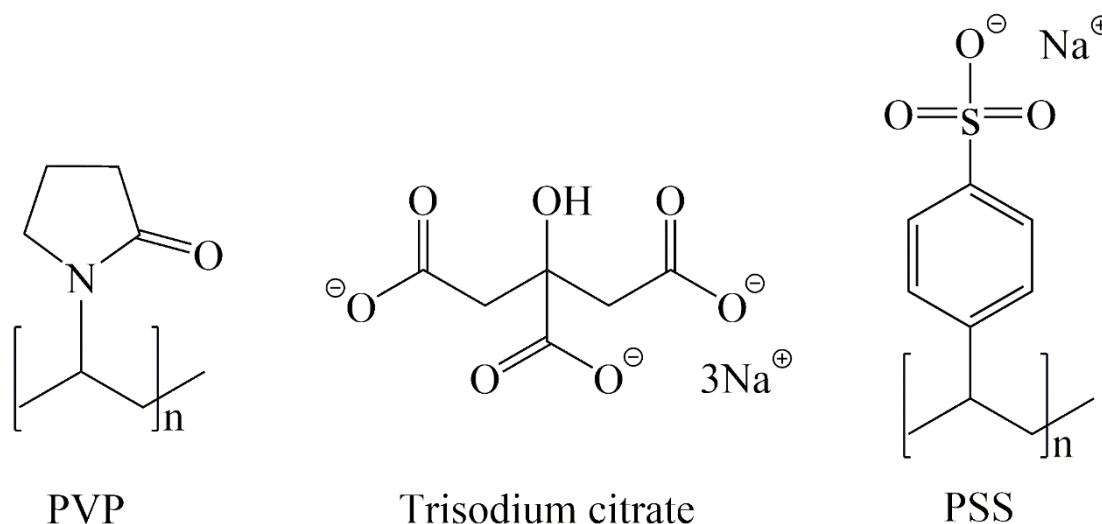


Fig. 4: Lewis-structures of different molecules used for nanoparticle stabilization. With examples for steric stabilization (PVP), electrostatic stabilization (trisodium citrate) and PSS which combines both stabilizing methods.

The attractive and repulsive interactions of disperse systems are described by the DLVO-theory which is based on the Lenard-Jones potential. The total interaction ($V_t / k_b T$) is plotted against the distance (nm). Where V_t is the sum of all repulsive and attractive forces in the system.

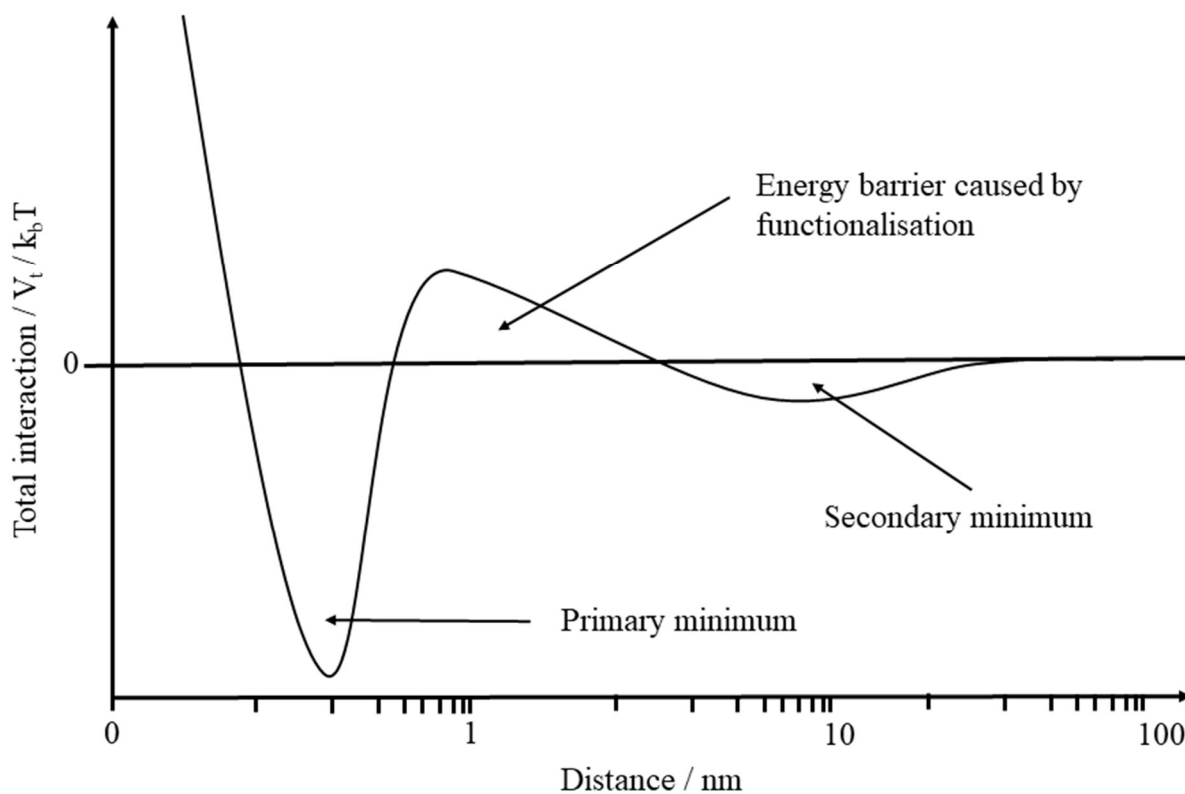


Fig. 5: Simplified graph of the sum of all contributing repulsive and attractive energies generating the total energy function of the DLVO-Theory.

The contribution to the total energy function are the repulsive forces in form of the functionalization (steric or electrostatic) and the Born-rejection complemented by the attractive force of van der Waals attraction.^[73] If the applied functionalization is sufficient, the energy barrier between the secondary minimum (reversible agglomeration) and the primary minimum (irreversible aggregation) is high enough to prevent the systems to pass into the primary minimum (Fig. 5). Consequently, the particles are stabilized.

2.5 Shape control of metallic nanoparticles

To ensure the stabilization of the nanoparticles, molecules like PVP or trisodium citrate are often present before the crystallization process is started. Under well controlled circumstances, these polymers have a huge influence on the crystallization process of metallic nanoparticles. Since the forming crystallographic surfaces of seeds and nanocrystals have different free energies, additives can be used to inhibit the growth of certain crystallographic facets. The energy difference of crystallographic facets for an fcc-lattice can be assumed by the density of surface atoms and the number of broken bonds. This results in the following gradation for the free surface energy (γ) of low indexed fcc-lattice planes:

$$\gamma_{\{111\}} < \gamma_{\{100\}} < \gamma_{\{110\}} \quad (2)$$

To minimize the free surface energy, the system is consequently anxious to maximize the number of $\{111\}$ -facets which often results in octahedra or tetrahedra.^[82] Is the reaction performed under kinetically controlled conditions, the used polymers have a huge influence on the growth of nanoparticles. Kinetic growth occurs when the active metal atom concentration is capped at a low level. The selective adsorption of single polymers like PVP or molecules like trisodium citrate inhibits the growth by complexation of the favored lattice planes. For example, PVP strongly adsorbs to the $\{100\}$ and trisodium citrate to the $\{111\}$ -lattice planes of fcc-structures. In the case of PVP as capping agent this can yield nanocubes^[37, 83-84] or wires^[85-90] under the right reaction conditions. The schematic kinetic controlled growth induced by additives of an imaginary 2D crystal is depicted in Figure 6.

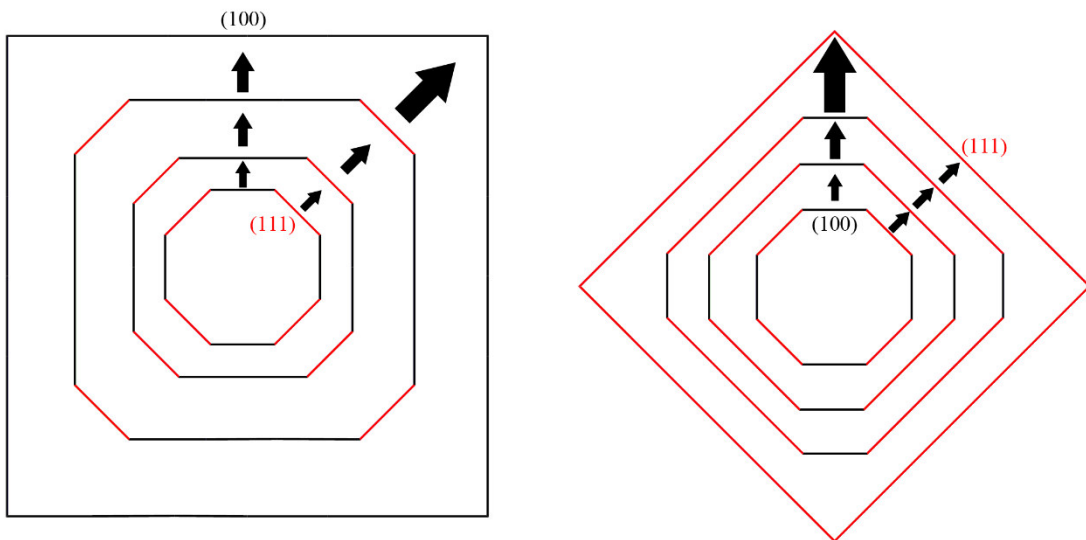


Fig. 6: Growth of an imaginary 2D-crystal with different capped crystallographic facets. Rapid addition of material on a specific surface leads to an elongation of the other facet. The arrows and their size indicate the growth velocity of the system. The picture is adapted from ref^[82].

Due to the fast growth of the $\{111\}$ -crystallographic facet the slow growing $\{100\}$ -plane starts to elongate (Fig. 6, left) and vice versa (Fig. 6, right). Twinned seeds and stacking faults can also influence the particle morphology. Due to certain geometrical considerations, twinned particles have already blocked facets where the twinned seed has grown. This leads to further particle shapes like dodecahedral structures (obtained from the glucose synthesis).^[82, 91] Furthermore, there are examples in the literature where an hcp-phase of silver is used to generate silver nanoprisms.^[92-93] Consequently, the combination of single crystalline and twinned seeds as well as the selection of suitable ligands results in different morphologies.

2.6 Bimetallic systems and galvanic replacement

The realization of different bimetallic systems can be aroused by the reaction conditions. In general, bimetallic systems are categorized in three different types. They can form core-shell particles, alloys with a homogenous distribution of both elements or Janus particles with a strict separation of both materials in the same particle. All three possibilities can be combined and yield mixed configurations. The three basic types are shown in Figure 7.

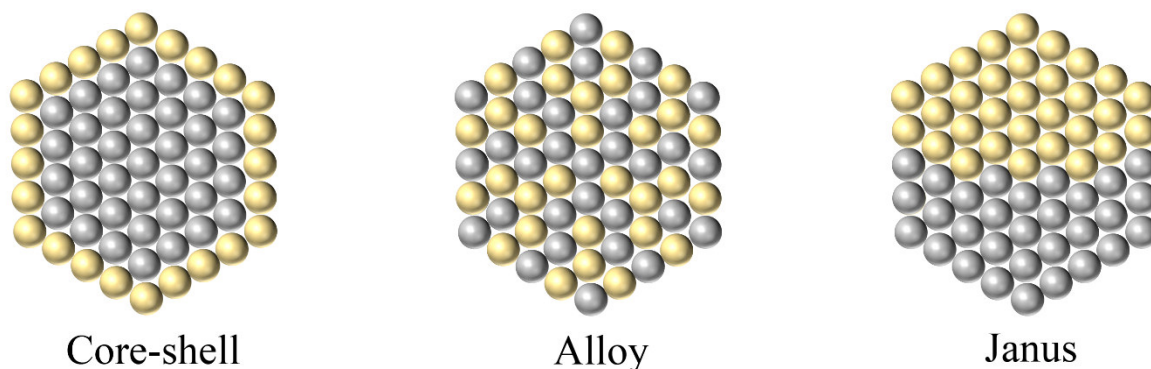


Fig. 7: Different types of bimetallic nanoparticles. The combination of the three types yields more possibilities which are not shown for reasons of simplification.

Core-shell particles are often synthesized in a seed and growth method where the core of the bimetallic particle is synthesized in the first step. The addition of a second precursor leads to the crystallizations of the second metal on the particle surface.^[38, 94-99] The addition rate of the second material is critical since a rapid addition can result in the formation of new seeds (compare chapter 2.3). Alloyed particles are often produced by co-reduction of both metal precursors.^[27, 33, 100] To generate Janus particles lots of different methods exist. Normally pre-synthesized nanoparticles are masked with a matrix and the second phase is subsequently applied by stamping, sputtering or a chemical reaction at the seed interface.^[61] Another possibility is a self-assembly of two different particles by attractive interactions.^[44]

To successfully generate bimetallic particles in a bottom-up approach, the to-be mated systems need to fulfill certain requirements. To co-crystallize two materials, the lattice parameters and the atom size must match each other. This means that only a maximal deviation of $\sim 5\%$ of both parameters is tolerated.^[59] If the crystal is obtained from solution, the solubility of the precursor as well as the standard potential of the compounds plays a key role to a successful synthesis. For example, in the case of a bimetallic nanoparticle redox reaction, the material with the higher

standard potential will be reduced easier. Therefore, the number of atoms of the nobler metal will be higher compared to the less noble material. This leads to an enrichment of the nobler material in the particle core during crystallization. Consequently, the particle will have a gradient structure and not a homogenous distribution of elements like an ideal alloy.^[24, 27]

For the generation of core-shell systems, different standard potentials of the metals and their precursors generate another problem. If the preformed core material is less noble than the to-be applied shell material, a galvanic replacement reaction will occur. In this reaction the less noble metal is dissolved by oxidation because of an electron transfer to the nobler metal. There are some examples of nanoparticles which show that this effect can be used to generate hollow structures with a high surface area while combining two materials.^[29-31, 34-35] Only few solutions to counter galvanic replacement can be found in the literature. It is either the adjustment of the pH value of the synthesis to increase the reduction potential of a specific reducing agent (ascorbic acid)^[39, 99] or by replacing ascorbic acid with hydroxylamine while applying the precursor over a time period of 12 hours.^[40] However, these methods are specific for a particle morphology and the shell material.

Especially nanomaterials of gold and silver show strongly different optical properties to the bulk materials. A combination of both systems can be used to enhance these properties. For example, alloyed nanoparticles of silver-gold in a 50:50 composition show an absorption maximum right between both maxima of the pure materials.^[27-28] In contrast, the optical properties of core-shell particles of the same materials strongly depend on the shell thickness. If the shell is thick enough, the core materials absorption is completely restrained. The phenomenon of the absorption of light by metallic nanoparticles is called surface plasmon resonance.

2.7 Surface plasmon resonance

Metallic nanoparticles show size, shape, composition, and dielectric constant dependent absorption of visible and ultra-violet light which can be detected with UV/Vis spectroscopy.^[62] This optical properties are caused by surface plasmon resonance (SPR). SPR describes the collective motion of the electron gas (conductive band electrons) relative to the core by excitation with a specific energy which corresponds to the absorbed wavelength. The electron gas starts to oscillate, caused by the electric field component of the light and Coulomb attractions between the electrons and the nucleus.^[44, 61] The oscillation frequency for the electron motion depends hereby on the electron density and the charge distribution.

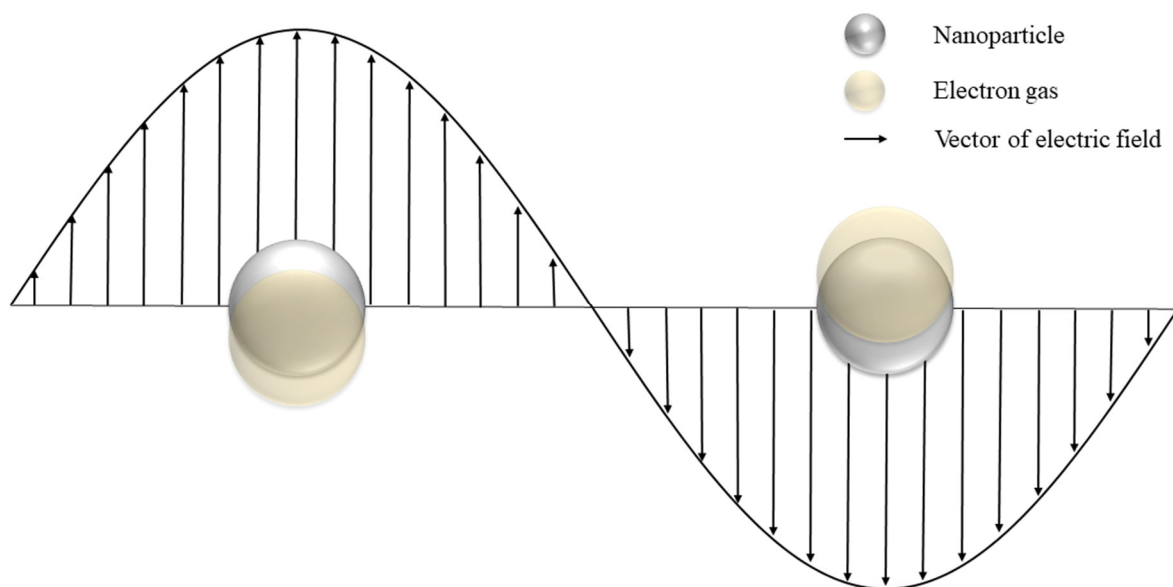


Fig. 8: Scheme of the induced dipole moment by the electric field of the incident light leading to surface plasmon resonance of metallic nanoparticles.

To induce SPR, the particles need to be smaller than the light wavelength. Anisotropic nanoparticles develop several absorption bands where the number is corresponding to the different geometrical surfaces and their size. Consequently, metallic nanorods and wires of silver and gold show two different absorption bands which represent the longitudinal and the transversal surfaces and the corresponding induced dipolar moments.^[61, 101-102]

3. Methods

3.1 Dynamic light scattering and ζ -potential

The size of colloidal systems can be determined by dynamic light scattering (DLS). Highly diluted particle dispersions are rayed by monochromatic laser light. The scattered light rays from the particles can be detected by a photodetector which is normally positioned in a 173° angle to the light source. The intensity recorded by the detector fluctuates due to the Brownian motion of the particles. The Doppler effect shifts the wavelengths of the scattered rays when particles move towards or away from the detector. Consequently, this leads to constructive or destructive interference. An autocorrelation function which evaluates the distribution of scatter intensity over time is used to calculate the diffusion coefficient D . With the aid of the Stokes-Einstein equation^[73], the hydrodynamic radius of the particles can be calculated:

$$r_{HD} = \frac{k_B \cdot T}{6\pi \cdot \eta \cdot D} \quad (3)$$

With r_{HD} for the hydrodynamic radius, k_B the Boltzmann constant, T the temperature, D the diffusion coefficient and η for the viscosity of the used solvent. The method however has certain limitations. Since the hydrodynamic radius is determined the particle size is overestimated. Furthermore, the DLS is “blind” for fractions of small particles. The scatter intensity of bigger particles is proportional to the radius ($I \sim r^6$). Consequently, bigger particles scatter one million times stronger compared to smaller particles. The Stokes-Einstein equation (3) contains the irrational constant π which shows that the formula only describes particles with a spherical morphology. These particles only possess one diffusion coefficient and are easily to evaluate by an auto correlation function. In contrast, anisotropic particles, like wires, prisms or platelets often have two or more different diffusion coefficients. Consequently, these particles often result in a bimodal size distribution if the technique is not modified.

The polydispersity index (PDI) of the system can be calculated from peak data obtained by DLS measurements. The software used calculates the PDI with formula (4).^[103]

$$PDI = \left(\frac{FWHM}{x_c} \right)^2 \quad (4)$$

With the polydispersity index (PDI), FWHM for the full width at half maximum and x_c with the peak center of the Gaussian peak fit. To calculate the PDI a Gaussian fit function is used to describe the obtained dataset. PDIs between 0 and 0.3 are referred to as monodisperse. PDIs above 0.3 indicate polydisperse systems. In this work, all PDI's were calculated with formula (4) to guarantee a comparability of all datasets (DCS, SEM or TEM) obtained. The ζ -potential is measured by applying an electric field. Nanoparticles form an electrical double layer (EDL) in solution. Due to the charge of the particles they move to the opposite charged electrode. If the particles possess a high ζ -potential (potential between the rigid double layer and the diffuse layer) the velocity in the applied electrical field directly correlates to it. Consequently, the zeta potential can be measured by determining the diffusion in an applied electrical field.

3.2 Differential centrifugal sedimentation

Another method to determine the particle size of colloidal systems is differential centrifugal sedimentation (DCS) where a gradient of sucrose is filled into a transparent rotating disc. At the edge of the disc, a monochromatic light beam is focused onto a detector. If a dispersion is injected, the particles migrate through the gradient with different velocities based on their particle size. When a particle fraction reaches the laser beam detector couple the beam intensity is weakened. Varying sizes of particles need different times to reach the detector. Consequently, a dataset is obtained where the absorption is plotted against the time. To correlate the time to the size, a calibration standard with a known particle size is measured before each measurement. With all known parameters, the Stokes equation (5) is used to determine the particle diameter:^[104]

$$D = \sqrt{\frac{18 \cdot \eta \cdot \ln\left(\frac{R_f}{R_0}\right)}{(\rho_p - \rho_f) \cdot \omega^2 \cdot t}} \quad (5)$$

With the particle diameter D , the viscosity η , the outer disc radius R_f , the inner disc radius R_0 , the particle density ρ_p , the fluid density ρ_f , the angular velocity ω and the sedimentation time t . The DSC has certain limitations. Since formula (5) needs the particle density, the nominal density of monometallic or a mixed density for bimetallic particles is used in the software. This given density differs to the real one because of the polymeric shell that surrounds the particles. Hence, the particle size is slightly underestimated. To measure a sample, 0.1 mL of concentrated particle solution is inserted.

3.3 UV/Vis spectroscopy

UV/Vis spectroscopy is performed to measure the needed energy and consequently the corresponding wavelength to bring electrons of a compound from the ground state into the excited state.^[105] This is done by generating an absorption spectrum of the compound by using light in a certain range of wavelengths. Most commonly the visible range between 380 nm up to 800 nm and the ultra violet range from 200 nm to 380 nm is detected. Since metallic nanoparticles exhibit surface plasmon resonance which absorbs light in the investigated region, they can be characterized by UV/Vis spectroscopy. The absorption maxima contain lots of information like particle morphology, polydispersity and the composition of the system (monometallic, core-shell or alloy). Furthermore, the absorption of the particles is proportional to the concentration and can therefore be described by the Lambert-Beer law (6):

$$E = \log\left(\frac{I_0}{I}\right) = \varepsilon \cdot c \cdot d \quad (6)$$

With the extinction E , the incident light intensity I_0 , the intensity of the transmitted light I , the extinction coefficient ε , the concentration of the sample c and the thickness/path length of the light d . For all measurements, a blank sample (pure solvent) was measured as background correction and the diluted particles with a concentration of 50 $\mu\text{g mL}^{-1}$ were measured in a Suprasil[®] quartz cuvette.

3.4 Atomic absorption spectrometry

The quantitative and qualitative detection of certain elements can be performed by atomic absorption spectroscopy (AAS). The to-be determined elements are dissolved, atomized and transferred into the analysis chamber. The atoms are irradiated with light of the exact wavelength which is needed to induce an electron transition in the sample. This wavelength can either be generated by using a hollow-cathode lamp of the same element or by a gas-filled tube which emits all needed wavelength. The absorption is proportional to the concentration of the atomized species according to the Lambert-Beer law (6). Previously to the measurement, a calibration curve of known concentrations is generated to correlate the absorption of the sample to the concentration.

Silver/silver-palladium digestion:

A certain volume of nanoparticle dispersion was mixed with 1 mL of nitric acid. The solution was then further diluted with ultra-pure water. Detection limits: silver 50 ppb, palladium 200 ppb.

Silver-gold/silver-iridium digestion:

A certain volume of silver-gold or silver-iridium nanoparticle dispersion was mixed with 2 mL of nitric acid and heated to 120 °C for 30 minutes. The dispersion was then diluted with ultra-pure water and filtered with a syringe PTFE-filter with a pore size of 0.45 µm. To determine the gold content the procedure was performed the same way but with exchanging nitric acid by aqua regia. Since iridium could not be dissolved with accessible methods it could not be determined by AAS.

All measurements were carried out by Kerstin Brauner and Robin Meya in the Laboratory of Microanalysis, University of Duisburg-Essen.

3.5 X-ray photoelectron spectroscopy

X-ray photoelectron spectroscopy (XPS) is a technique where a sample surface is irradiated by an X-ray beam while measuring the energy and number of escaped electrons from inelastic collision. The penetration depth of the method is typically in a range between 0 to 10 nm. The electrons can be used to obtain information about the empirical formula, chemical state or the electronic state of the detected elements. In a typical XPS spectrum, the intensity is plotted against the energy in eV. Because electrons are counted, the technique needs to be carried out in vacuum or ultra-high vacuum to prevent interference of electrons with atmosphere molecules. Since the energy of the used X-ray with a particular wavelength is known, the electron binding energy of each electron can be determined by an equation based on the work of Ernest Rutherford:^[106]

$$E_{binding} = E_{photon} - (E_{kinetic} + \phi) \quad (7)$$

Where $E_{binding}$ is the binding energy of the electron, E_{photon} is the energy of the used X-ray photon and $E_{kinetic}$ is the detected energy of the electron by the instrument. The work function term ϕ corresponds to the electron energy loss caused by the detector absorption. The resulting peaks at certain energies correspond to the orbital energy of which the electron has escaped. Since this energy differs with the electronic state, it is possible to determine the oxidation state of the element contained in the sample.

The XPS measurements and data evaluation was carried out by Dr. Ulrich Hagemann in the Center for Nano Integration at the University of Duisburg-Essen.

3.6 X-ray powder diffraction

X-ray powder diffraction (XRPD) is used to determine the phase purity and the crystallographic structure of a crystalline powder. Since the wavelength of the radiation needs to be in the same range as the atomic distances of the compound, high energetic X-rays are used. The formed crystalline lattice of the compound leads to constructive or destructive interference based on the angle the X-rays hit the sample. The interference of a crystalline sample with X-rays is shown in Figure 9.

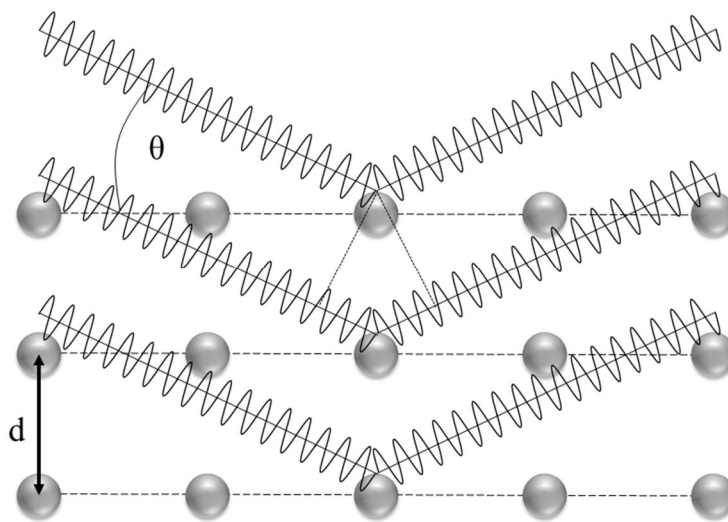


Fig. 9: Schematic drawing of X-rays constructively interfering with crystallographic lattice planes with θ the Bragg angle and d the distance of single lattice planes.

The beam is diffracted at the electron shell of the atoms. In the right angle, the scattered waves from different planes do interfere constructively. In other angles, the waves start to interfere destructively. The occurrence of interference consequently depends on a geometrical relationship and can be described by the Bragg equation (8):

$$n \cdot \lambda = 2 \cdot d \cdot \sin(\theta) \quad (8)$$

With n an integer, the X-ray wavelength λ , the lattice plane distance d and the Bragg angle θ . Consequently, the path difference between two diffracted waves needs to be an integral multiple to yield constructive interference. Smaller crystallites like observed in nanomaterials only

possess few crystallographic lattice planes. Furthermore, nanoparticles contain lots of surface defects which directly corresponds to their high surface area to volume ratio. Therefore, the few lattice planes show a high deviation of the ideal distance d . This leads to a peak broadening which can be used to calculate the mean crystallite size of all lattice planes or of single crystallographic planes by the Scherrer equation (9):^[107]

$$D_{hkl} = \frac{K \cdot \lambda}{\beta_{hkl} \cdot \cos(\theta)} \quad (9)$$

Where D_{hkl} is the extension of the corresponding crystallographic lattice plane, K is the Scherrer form factor which differs depending on the habitus of the particles and the used fit function^[108], β_{hkl} is the full width at half maximum of the corresponding reflex of the lattice plane, λ the wavelength of the X-rays and θ the corresponding Bragg angle. Since not only the crystallite size, but also micro strain leads to peak broadening, the micro strain can be calculated by the Stokes-Wilson equation (10):^[106]

$$\varepsilon = \frac{\beta_{hkl}}{4 \cdot \tan(\theta)} \quad (10)$$

With ε for the micro strain, β_{hkl} for the full width at half maximum and θ for the corresponding Bragg angle. Because both equations (9, 10) use the half width of the peak maximum (β_{hkl}) they are only approximations. The contribution of micro strain and crystallite size to the peak broadening can be identified by using the Williamson-Hall plot. This is possible because the micro strain has a higher influence on the high indexed crystallographic planes and consequently on lower d values of the reciprocal space. The Williamson-Hall plot is performed with the following equation (11):

$$\beta_{hkl} \cdot \cos(\theta) = \left(\frac{K \cdot \lambda}{D} \right) + (4 \cdot \varepsilon \cdot \sin(\theta)) \quad (11)$$

This linear plot leads to the micro strain ε as the slope, the crystallite size D as the y axis section by inserting β_{hkl} for the full widths at half maximum, θ for the corresponding Bragg angles, K

for the Scherrer form factor and λ the wavelength of the used X-ray radiation. Since the peak broadening is calculated proportionately, the Williamson-Hall plot leads to more accurate results. This equation (11) is consequently used by the program TOPAS which was used to calculate crystallite sizes in this work. The last factor which can result in peak broadening is the instrumental aberration where the instrumental setup and the used geometry lead to a peak broadening. This factor can be subtracted by the Debye-Scherrer equation (12):

$$D_{hkl} = \frac{K \cdot \lambda}{(\beta_M^2 - \beta_S^2)^{1/2} \cdot \cos(\theta)} \quad (12)$$

To correct the instrumental aberration, the half width at full maximum (β_S) of a high crystalline standard, like LaB₆ or silicon powder in a comparable peak position, is subtracted from the half width of the sample peak (β_M). The modified Scherrer equation can also be applied to the Williamson-Hall plot.

3.6.1 Synchrotron radiation

Synchrotrons are used to generate high energetic electromagnetic radiation from infrared up to hard X-rays. This is done by accelerating bunches of electrons to relativistic speeds. If those electrons are forced by electric fields to leave their trajectory they emit electromagnetic radiation known as synchrotron radiation.^[109] The emitted radiation is perpendicular to the electron motion. The high flux of the synchrotron radiation leads to strongly increased intensities and consequently to sharp peaks investigating nanomaterials with hard X-ray radiation. Furthermore, it is possible to generate powder patterns of particles in solution which creates the possibility of *in-situ* investigations during synthesis.^[47, 110] The generated beam often possesses a high degree of polarization and high brightness with a small cross section.^[109] The experiments in this work were measured with a wavelength (λ) = 0.20703 Å.

3.7 Scanning electron microscopy and energy dispersive X-ray spectroscopy

The resolution of visible light is limited by the used wavelength. The resolution of optical microscopes is described by the Abbé limit with the following equation (13):

$$d = \frac{\lambda}{2n \cdot \sin(\alpha)} = \frac{\lambda}{2NA} \quad (13)$$

Where d being the resolution, λ the wavelength of the light, n the refractive index of the immersion media, α the aperture angle and NA the numerical aperture. To overcome this limit, scanning electron microscopy (SEM), where an electron beam with a short wavelength scans the surface of objects smaller than the wavelength of the visible light, is used. The electrons are generated by a field emission gun. The released electrons are focused by electric coils and lenses and accelerated with a voltage of 5-30 kV. The resulting focused electron beam (primary electrons, PE) is then moved in a lateral order over the sample surface. The electrons do now interact in two different ways with the sample. Firstly, the electrons can be elastically scattered resulting in backscattered electrons (BSE) which do not experience an energy loss. Since denser materials yield more BSE, the high energetic electrons generate a material contrast where denser materials appear brighter than less dense materials. Secondly, secondary electrons (SE) are generated by inelastic scattering. SE are generated by electron removal from the inner shell of the material. Consequently, these electrons possess a low energy and can only leave the sample from depths down to 5 nm. Since edges and higher parts do not have that much material where the SE can be intercepted these areas appear brighter. If the sample is not conductive it needs to be sputtered with a conductive material.

The removal of SE also induces the generation of X-ray quants by filling the hole with an electron of the outer shell. The energy difference between both shells is emitted as X-ray quant. This quant has a characteristic energy corresponding to the element from which it is generated. Consequently, the detected energy of the quant can be used to perform qualitative and quantitative determination of the elements in the sample. This technique is called energy dispersive X-ray spectroscopy (EDX) and is often coupled with SEM or TEM. High resolution EDX allows to map small sample regions to generate intensity distributions of small areas like single nanoparticles if coupled with TEM.

3.8 Transmission electron microscopy

Another method to visualize small objects is the transmission electron microscopy (TEM). In contrast to SEM, the sample must be thin enough for the electron beam to pass through. The electron beam is focused onto the sample and the transmitted electrons are detected by a bright field detector. Since the electron beam must pass through the sample, the accelerating voltage lies in a range between 40-300 kV. This results in a higher resolution. Different modifications can be applied to the method. The sample can either be scanned (scanning transmission electron microscopy, STEM) or a dark field detector can be used to detect electrons in different angles. For example high-angle annular dark field imaging (HAADF) can be performed to generate high atomic number contrast to generate detailed EDX maps of samples or single particles.^[111]

The samples are prepared by dropping a highly diluted dispersion onto a carbon-coated copper grid which is dried afterwards. The measurement is performed under high vacuum. The performed *in-situ* heating experiments were carried out with the wildfire system of DENS solutions where the dispersion is applied on a graphene thin film via drop casting. The used chip can be electrically heated.

All TEM/STEM/HAADF/EDX measurements and data analysis were carried out by Dr. Kataryna Loza under the supervision of Dr. Mark Heggen in the Ernst Ruska-Center and Peter Grünberg Institute, Forschungszentrum Jülich GmbH, Germany.

3.9 Differential scanning calorimetry

Differential scanning calorimetry (DSC) is a technique in which the energy differences to heat a sample compared to a reference is measured. The energy corresponds hereby to a certain temperature. The resulting thermogram gives information about phase transition, recrystallization processes, glass transitions and if those are of an exothermic or endothermic nature. Additionally, oxidation processes or other chemical reactions can be monitored. Furthermore, the total amount of energy of the process can be calculated by integration of the resulting peak area.

4. Experimental section

4.1 Software/databases used

Table 2: Listing of the software and databases used in this thesis. The databases are marked with an asterisk (*).

Software/database*	Purpose	Reference/editor
ChemDraw	Molecular formula design	PerkinElmer Informatics, Inc.
Endnote X7, X8	Citation manager	Thomson Reuters
DIFFRAC.EVA	Phase analysis	Bruker
Topas 5.0	Rietveld refinement	Bruker
Mercury 3.9	Visualization of crystal structures	CCDC
Powder 3D	Visualization of 3D X-ray diffraction powder data	B. Hinrichsen, R. Dinnebier, M. Jansen
Fit2D	Integration of synchrotron TIF files	Hemmersley, A., ESRF
jEdit	Processing of .inp files	jEdit.org
Dioplas 0.3.0d	Processing of multiple synchrotron TIF files	C. Prescher
ImageJ	Graphical particle size analysis	Wayne Rasband, National Institutes of Health, USA
Photoshop CS4 V 11.0	Graphic design	Adobe
Microsoft Office	Graphic design, textualization	Microsoft
American Mineralogist crystal structure database (AMSCD)*	Crystallographic data	[112-113]
Crystallographic open database (COD)*	Crystallographic data	[114-118]
ICDD*	Crystallographic data	International center for diffraction data

4.2 Chemicals used

Chemical	Producer	Purity
Diethylene glycol	Sigma-Aldrich	> 99.0 %
Ethylene glycol anhydrous	Sigma-Aldrich	99.8 %
Hydrochloric acid	Bernd Kraft	p.a.
Nitric acid	Bernd Kraft	p.a.
Palladium nitrate (ICP standard)	Bernd Kraft	> 99.9 %
Poly(N-vinylpyrrolidone) (MW = 40,000 g mol ⁻¹)	Fluka	p.a.
Poly(N-vinylpyrrolidone) (MW = 55,000 g mol ⁻¹)	Sigma-Aldrich	p.a.
Potassium hydroxide	FWR	p.a.
Sodium borohydride	Sigma-Aldrich	> 96 %
Sodium chloride	FWR	p.a.
Silver nitrate	Carl Roth	> 99.9 %
Tetrachloridoauric acid	Self-made from Au-powder	
Trisodium citrate dihydrate	AppliChem	p.a.

4.3 Devices used

Device	Producer
Atomic absorption spectrometer	ThermoElectron M-Series
Centrifuge	Hettich Rotofix 32A
Disc centrifuge	CPS Instruments Disc Centrifugation DC24000
Differential scanning calorimeter	Netzsch DSC 204 Cell
Dynamic light scattering	Malvern Nano ZS
Lyophilizer	Christ Alpha 2-4 LSC
Microwave reactor (synchrotron)	Anton Paar Mono 300
Microwave reactor (lab)	CEM Discover SP
Potentiostat	SP-300 BioLogic
Rotary evaporator	Buechi Rotavapor R-114
Scanning electron microscope coupled with EDX	FEI Titan 80-300, EDAX ^[119]
Scanning transmission electron microscope coupled with EDX and HAADF	FEI Titan G2 80-200 CREWLEY ^[120]
Sonotrode	Heilscher UP50H
Ultracentrifuge	SORVALL WX Ultra Series
Ultrasonic bath	Elmasonic S10
UV/Vis spectrometer	Varian Cary 300
Vortex	Scientific Industries Vortex-Genie 2
X-ray powder diffractometer	Bruker D8 Advanced (Bragg-Brentano geometry)
X-Ray photoelectron spectrometer	PHI 5000 Versaprobe II
Synchrotron source	DESY, Beamline P02.1

4.4 Synthesis of silver nanoparticles with glucose

In solution, D- and L- glucose exists in equilibrium with several cyclic isomers. Especially in water more than 99 % of the glucose molecules exist in the cyclic form α -D-glucopyranose.^[121]

The redox reaction of the synthesis of metallic ions with glucose is consequently as follows:^[122]

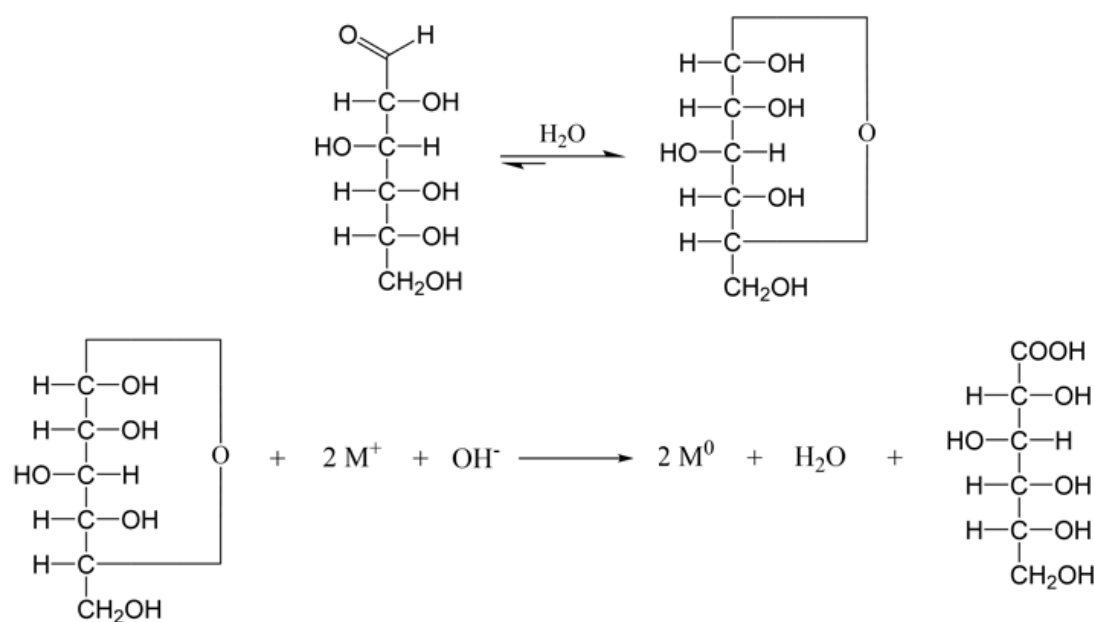
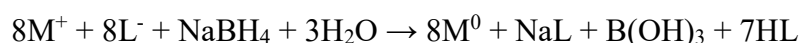


Fig. 10: Reaction scheme of the reduction of metal ions by glucose. The cyclic form of glucose is strongly favored in aqueous solutions.

In a typical synthesis, 2.00 g of D-glucose (11.10 mmol) and 1.00 g of poly (N-vinylpyrrolidone) (9 mmol based on the molar mass of the monomer; $M_w = 40,000 \text{ g mol}^{-1}$) were dissolved and stirred in 40 mL ultra-pure water and heated to 90 °C. The temperature was maintained for 45 min. Following this step, 1 mL of freshly prepared silver nitrate solution (2.94 M) was added quickly to the stirred solution. After 60 minutes the received dispersion was quickly cooled to room temperature with an ice bath. The purification was performed by triple ultracentrifugation at 20,000 rpm (66,000 g) for 30 minutes. After each centrifugation, the supernatant was removed and the particles were redispersed in ultra-pure water using an ultrasonic bath.

4.5 Metallic nanoparticles from reduction with sodium borohydride

In the general redox reaction of sodium borohydride, eight electrons are released which can potentially reduce metal ions. Depending on the oxidation state of the used metal precursor, different numbers of metal ions can be reduced to their elemental form. The general reaction mechanism of sodium borohydride consequently looks as follows:



The metal ion (M) and the corresponding ligand of the metal ion (L) can differ depending on the used metal precursor. In this work either sodium hexachloridoiridate (Na[IrCl₆]) or silver nitrate (AgNO₃) were reduced using sodium borohydride.

4.5.1 Synthesis of silver nanoparticles

In a typical synthesis, 18 mg silver nitrate (0.06 mmol) and 22 mg trisodium citrate (0.10 mmol) were dissolved in 330 mL water. The reaction mixture was then cooled down in an ice bath and stirred with a velocity of 700 rpm. In the following step, 10 mL of a freshly prepared 10 mM sodium borohydride solution, obtained from pre-cooled water (stored in a fridge), was rapidly added. One minute after the addition of sodium borohydride, a solution of PVP (25 mmol, based on the molar mass of the monomer; $M_w = 40,000 \text{ g mol}^{-1}$) was injected to the solution. The reaction mixture was further stirred for 3 hours. Afterwards, the reaction volume was reduced to 50 mL in a rotary evaporator (60 °C bath temperature, 95 mbar pressure). The purification was performed by triple ultracentrifugation at 20,000 rpm (29,400 g) for 30 minutes. The formed particle pellet should not be redispersed and can hence be discarded. Particles obtained are stored under argon atmosphere and light exclusion at 8 °C.

4.5.2 Synthesis of iridium nanoparticles

In a typical synthesis, 6.35 mL of sodium hexachloridoiridate (metal content 0.719 g L^{-1} (0.02 mmol)) and 22 mg trisodium citrate (0.10 mmol) were added to 300 mL of boiling ultra-pure water. After 1 minute, 10 mL of a 0.4 M solution of sodium borohydride were added. After another 1 minute, 5 mL of a 0.1 M NaOH solution were added. The reaction was stirred for 1 hour under reflux and was then cooled down to room temperature in an ice bath. The resulting dispersion was neutralized with 4 M hydrochloric acid and the volume was reduced by a rotary evaporator. The purification was performed by triple ultracentrifugation at 20,000 rpm (29,400 g) for 30 minutes. After each centrifugation, the supernatant was removed and the particles were redispersed in ultra-pure water using an ultrasonic bath.

4.5.3 Synthesis of porous iridium/iridium dioxide nanostructures

In a typical synthesis, 6.35 mL of sodium hexachloridoiridate dissolved in water (metal content 0.719 g L^{-1} (0.02 mmol)) were neutralized with 20 μL of 1 M sodium hydroxide solution. The metallic precursor was then diluted in 250 mL of ultra-pure water and heated until reflux. Then, 35 mg trisodium citrate were added to the reaction mixture. Subsequently 150 mg of sodium borohydride were dissolved in 10 mL cold ultra-pure water and instantly added to the suspension. After 1 minute, 120 mg poly-(N-vinylpyrrolidone) (PVP, $M_w = 40,000 \text{ g mol}^{-1}$) dissolved in 10 mL water were added to the resulting slightly brown dispersion. The mixture was stirred for further 35 minutes under reflux. After this period, 150 mg sodium borohydride were added for a second time. The whole reaction was boiled for additional 55 minutes. Following this step, the mixture was brought to room temperature with an ice bath. The dispersion was stirred for further 48 hours. The resulting blue-black dispersion was reduced to a volume of 50 mL using vacuum. The particles were purified by fourfold ultracentrifugation using 29,400 g (20,000 rpm) for 30 minutes.

4.5.4 Synthesis of silver-iridium core-shell systems

In a typical synthesis, 18 mg silver nitrate (0.06 mmol) and 22 mg trisodium citrate (0.10 mmol) were dissolved in 330 mL water. The reaction mixture was then cooled down in an ice bath and stirred with a velocity of 700 rpm. In the following step, 10 mL of a freshly prepared 10 mM sodium borohydride solution, obtained from pre-cooled water (stored in a fridge), was rapidly added. One minute after the addition of sodium borohydride, a solution of PVP (25 mmol, based on the molar mass of the monomer; $M_w = 40,000 \text{ g mol}^{-1}$) was injected to the solution. Eight minutes later, 1.5 mL of 1M NaOH were added to the solution to adjust the pH value to 11. The ice bath was removed and 4 mL of sodium hexachloroiridate (metal content 0.719 g L^{-1} (0.02 mmol)) were added to the stirring solution. A second time, 10 mL of freshly prepared 20 mM sodium borohydride solution were added. The resulting red-brown dispersion was stirred overnight. Afterwards, the reaction volume was reduced to 50 mL in a rotary evaporator (60 °C bath temperature, 95 mbar pressure). The purification was performed by triple ultracentrifugation at 20,000 rpm (29,400 g) for 30 minutes. After each centrifugation, the supernatant was removed and the particles were redispersed in ultra-pure water using an ultrasonic bath. Particles obtained are stored under argon atmosphere and light exclusion at 8 °C.

4.6 Metallic nanoparticles from the polyol process

The polyol process uses poly alcohols which fulfill the role of the reducing agent as well as the solvent at the same time. Furthermore, polyols can stabilize forming metal nanoparticles. The improved reaction scheme purposed by Meléndrez et al. for ethylene glycol looks as follows.^[90]

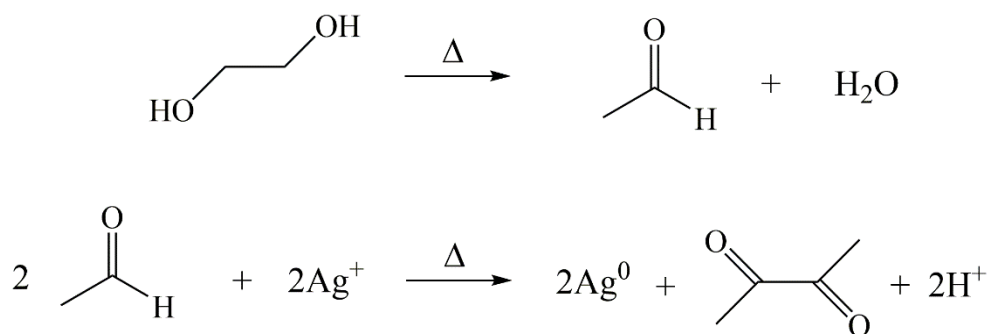


Fig. 11: Reaction scheme of the reduction of silver by ethylene glycol. As side products, water and protons appear.

The thermal decomposition of two ethylene glycol or diethylene glycol molecules provides the reaction with two usable electrons for the reduction of metal ions.

4.6.1 Synthesis of silver nanocubes (oxidative etching)

6 ml of anhydrous ethylene glycol were heated up to 140 °C in a 50 mL open round bottom flask for one hour. Next, 30 μL of a 0.1 M of aqueous hydrochloric acid solution were added to the mixture. Meanwhile 80 mg silver nitrate (0.47 mmol) and 80 mg poly-(N-vinylpyrrolidone) (0.72 mmol, based on the molar mass of the monomer, $M_w = 55,000 \text{ g mol}^{-1}$) were dissolved in ethylene glycol. The resulting solutions were mixed, and 6 mL of the resulting mixture was rapidly added to the heated ethylene glycol. The flask was then sealed air tight with PTFE-paste. After 20 hours, the reaction was cooled to room temperature in an ice bath. The purification was performed by triple ultracentrifugation at 20,000 rpm (66,000 g) for 30 minutes. After each centrifugation, the supernatant was removed and the particles were redispersed in ultra-pure water using an ultrasonic bath. In the end, the resulting dispersion was filtered with a syringe cellulose filter (pore size 0.45 μm).

4.6.2 Synthesis of silver nanowires (seed and growth)

334 mg of poly-(N-vinylpyrrolidone) (3.00 mmol, based on the molar mass of the monomer, $M_w = 55,000 \text{ g mol}^{-1}$) were dissolved in 20 mL ethylene glycol. The mixture was then heated up to 180 °C in an open round bottom flask. The needed silver chloride seeds were generated by adding 50 μL of 0.43 M silver chloride and silver nitrate solution each simultaneously to the stirring mixture. The seed containing mixture was further stirred for 25 minutes at 180 °C. The growth of the particles is initiated by dropwise addition of 0.12 M silver nitrate solution with an addition rate of 25 mL h^{-1} via a syringe pump. After the complete addition the dispersion is further stirred for 15 min. In the end, the mixture is cooled down to room temperature in an ice bath. To dissolve the silver chloride seeds, 200 μL of ammonia were added and the dispersion was centrifuged with 2000 rpm (666 g). The supernatant was removed and the particles again were three times washed with ultra-pure water by centrifugation (2000 rpm, 666 g).

4.6.4 Synthesis of iridium nanoparticles in a microwave

In a typical experiment, 30 mg of sodium hexachloridoiridate (0.18 mmol) and 60 mg poly (N-vinylpyrrolidone) (0.27 mmol, based on the molar mass of the monomer, $M_w = 55,000 \text{ g mol}^{-1}$) were completely dissolved in 5 mL diethylene glycol at room temperature. The vial was then sealed with a PTFE cap and transferred to the microwave reactor (CEM Discover SP). After stirring for 2 min at room temperature, the solution was rapidly heated to 200 °C by the microwave at the maximum possible rate. The reaction was finished after 30 minutes. The solution was quickly cooled to room temperature with compressed air in the microwave within about 120 s and then added to cold (25 °C) ultrapure water. The nanoparticles were purified by triple ultracentrifugation (30,000 rpm, 66,000g) and redispersed in ultrapure water.

4.6.3 Synthesis of silver nanoparticles in a microwave

In the performed experiments, 30 mg or 90 mg of silver nitrate (0.18 mmol or 0.53 mmol) and 20 mg or 60 mg poly(N-vinylpyrrolidone) (0.27 mmol or 0.81 mmol, based on the molar mass of the monomer, $M_w = 55,000 \text{ g mol}^{-1}$) were completely dissolved in 5 mL diethylene glycol at room temperature. The solution took on a light-yellow colour (due to plasmon resonance), indicating the formation of small Ag seeds. The vial was then sealed with a PTFE cap and transferred to the microwave reactor (Anton Paar Monowave 300; 200 W). After stirring for 2 minutes at room temperature, the solution was rapidly heated to 160 °C or 200 °C by the microwave at the maximum possible rate. This heating took about 30-40 s for each experiment. XRPD was measured within 20 s frames with 3 frames a minute directly after the maximum reaction temperature was reached. To stop the reaction at a defined endpoint, the solution was quickly cooled to room temperature with compressed air in the microwave within about 120 s and then added to cold (25 °C) ultrapure water. The nanoparticles were purified by triple ultracentrifugation (30,000 rpm, 66,000g) and redispersed in ultrapure water. All measurements were performed at the beamline P02.1 at the DESY synchrotron source in Hamburg, Germany. The used wavelength (λ) was 0.20703 Å.

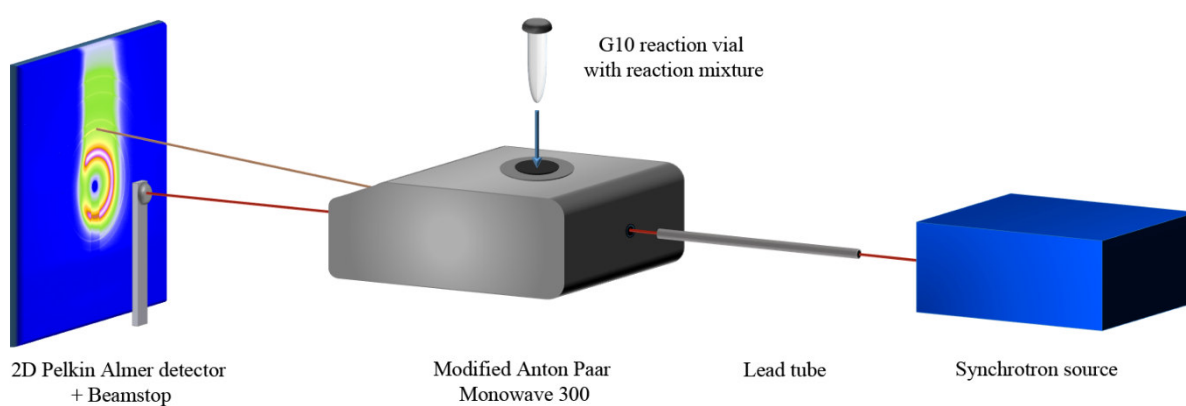


Fig. 12: Scheme of the experimental setup. The orange beam implies one of the scattered X-rays. The synchrotron source is just a simple geometrical shape due to simplification reasons.

4.7 Synthesis of core-shell particle (seed and growth)

To generate core-shell systems, 0.2 mg of silver nanoparticle (independently of morphology or size used) were diluted in 15 mL ultra-pure water. To the stirring dispersion, 400 μL of a 0.1 M ascorbic acid solution and the required amount of 1 M NaOH solution to set the pH to 11 were added. The mixture was stirred for 2 minutes. To initiate the shell growth, 0.06 mM metal precursor solution (based on the metal amount) was added with a rate of 0.2 mL min^{-1} via a syringe pump. After the complete addition the dispersion was further stirred for an hour. The nanoparticles were ultracentrifuged twice for purification (20,000 rpm, 29,600 g) and redispersed in ultrapure water.

The instructions for this experiment need to be executed exactly the way described. Higher concentrations of metal precursor or too low pH values lead to galvanic replacement reactions which results in a loss of the particle morphology.

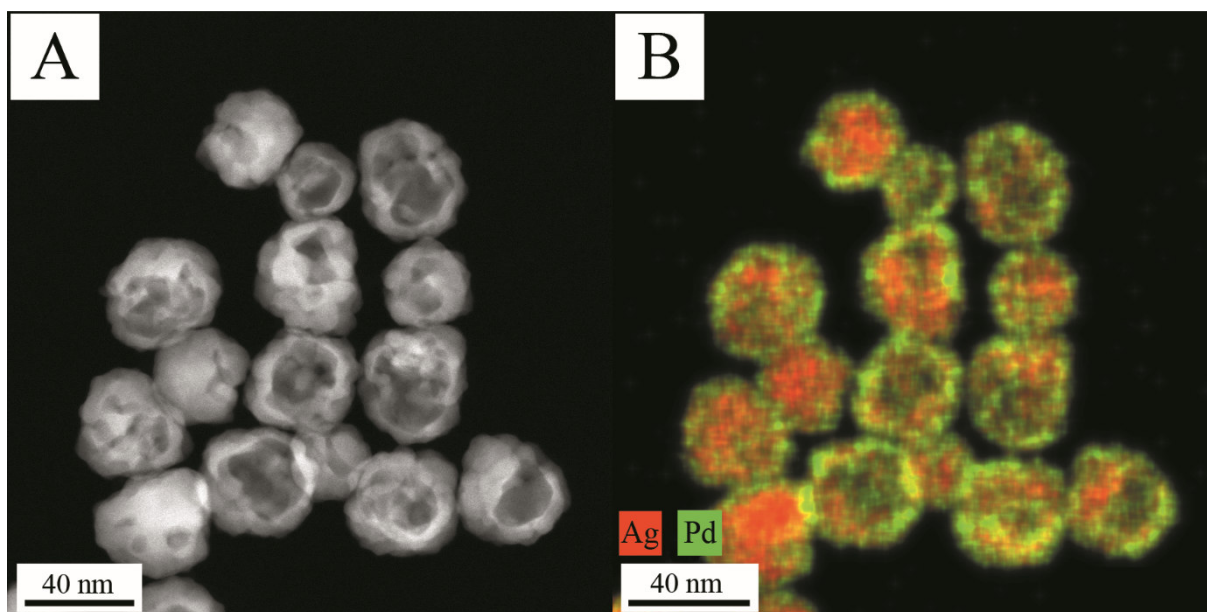


Fig. 13: Results from a poorly executed synthesis of silver-palladium nanospheres. The pH value of the synthesis was not well controlled. The particles show a partially galvanic replacement leading to a combination of hollow alloyed structures and core-shell nanoparticles.

4.8 Experimental setup of the dissolution experiments

The nanoparticles used (compare chapter 5.4) were prepared as former described. For the experiments, 5 mL of nanoparticle dispersion with a silver concentration of $50 \mu\text{g mL}^{-1}$ were added to the upper part of an Amicon[®] Ultra – 15 centrifugal filter (MWCO = 3,000 Da). The filters are immersed in 28 mL of ultra-pure water. At certain time intervals, 3 mL of the 28 mL of the lower part were taken and refilled with 3 mL fresh water. The removed 3 mL were mixed with 0.1 ml concentrated nitric acid and the silver content was determined by AAS.

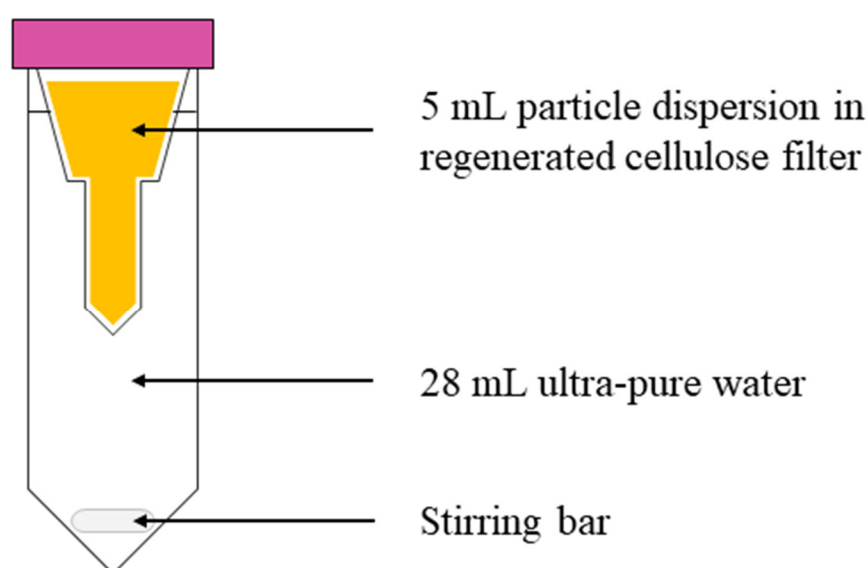


Fig. 14: Schematic setup of the performed dissolution experiments. The cellulose filter of the Amicon[®] tube is filled with 5 mL particle dispersion and immersed in ultra-pure water while stirred.

As a control and to determine the diffusion of silver ions through the filter material, silver nitrate solution was also tested. The results showed that the complete diffusion is finished after 21 days into the experiments. Furthermore, the silver nitrate solution was filtered through the cellulose by centrifugation to exclude possible interactions of the membrane and the silver ions. The determination by AAS showed that unfiltered and filtered solutions had the same concentrations. Consequently, no interaction between ions and membrane occur. The described setup is adapted from experiments performed by Dr. Viktoria Grasmik.^[24]

5. Results and discussion

5.1 Synthesis of silver nanoparticles from glucose

The synthesis of “spherical” silver particles using glucose as reducing agent is most likely one of the best investigated silver nanoparticle syntheses. Originally, the synthesis was established by Wang *et al.*^[122] to investigate the influence of PVP as a capping agent. The system has since been investigated in terms of crystallite growth in dependence of reaction time^[123] and furthermore, the internal structure of the nanoparticles has been examined.^[82, 91] Hence, the particles have found application *in vivo* and *in vitro* experiments^[124] and their dissolution kinetics are well studied.^[21-22, 91] Therefore, the system was perfectly suited to realize possible core-shell particles with silver serving as core material.

5.1.1 Characterization of nanoparticles synthesized with glucose

The synthesized particles used in this work were characterized using different analytical methods. All analyses were performed with particles dispersed in ultra-pure water if not noted otherwise.

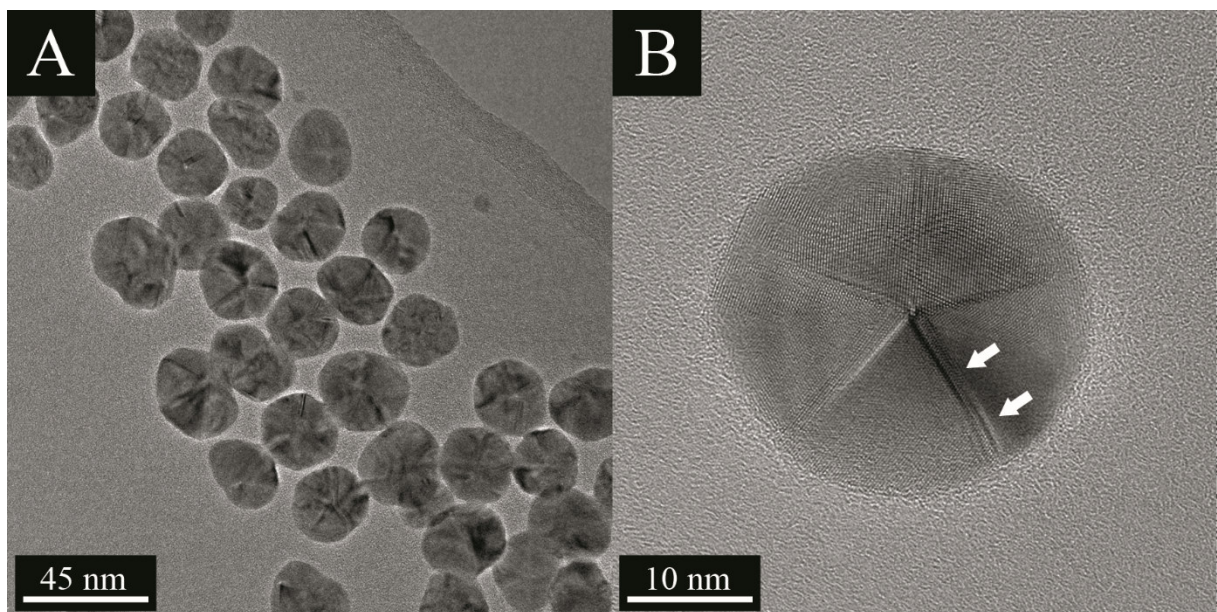


Fig. 15: HRTEM image of silver nanoparticles obtained from the glucose synthesis after 30 minutes (A) and an image of a single particle showing a penta-twinned crystalline structure with twin defects and stacking faults at the grain boundaries marked by white arrows (B).

5.1 Synthesis of silver nanoparticles from glucose

The transmission electron microscopy images shown in Figure 16 were recorded with an accelerating voltage of 300 kV. For the quantification via SEM images (not shown), overall 100 particles were digitally measured. This measurement resulted in an average particle size of $54 \text{ nm} \pm 9 \text{ nm}$ with a PDI of 0.17. Overall, the particles appear to be spherical but in addition several particles with anisotropic structures, like rods and platelets, are observed.^[91] Moreover, the spherical particles appear to be slightly deformed. This deformation can be explained by the in-depth investigation of the internal structure. Particles obtained from the glucose synthesis do mostly grow in penta-twinned crystalline structures which develop a decahedral assembly. This assembly is constructed of five tetragonal crystallites with angles of 70.53° which generate a gap of 7.35° . This gap is closed by defects at the grain boundaries (compare Fig. 15, B). Due to geometrical principals the particles can only develop a disc like shape (Fig. 16).^[82, 91]

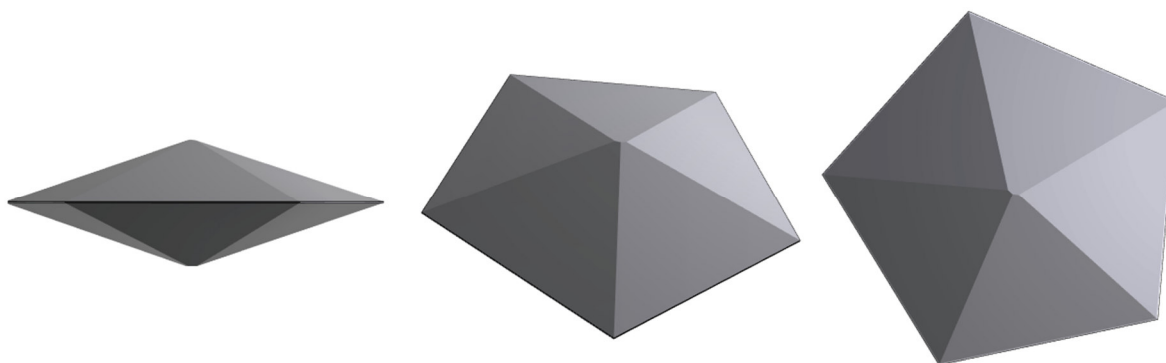


Fig. 16: Schematic geometrical 3D model of a silver particle obtained from the glucose synthesis. The Figure depicts various angles for a better overview. The particle was constructed with a relation of particle width to particle high of 3:1. This ratio was determined by AFM measurements.^[91]

Therefore, particles obtained from the glucose synthesis are not spherical but have a disc like, anisotropic structure. To investigate the colloidal stability and the size distribution in dispersion dynamic light scattering (DLS) measurements were performed. DLS measurements regarding the glucose synthesis frequently show a bimodal size distribution in terms of intensity versus size plots. This observation is regularly explained by a second fraction of smaller particles. However, taken into consideration that the particles are not spherical (compare Fig. 16), two different diffusion coefficients result from the anisotropic shape. This phenomenon has often been observed during analyses of anisotropic particles like rods, wires, platelets and prisms during this work. All those particles have generated bimodal size distributions. The used autocorrelation function which leads to the diffusion coefficient can be modified to fit the

anisotropic shape. Moreover, additions to the technique itself like a higher flux of the used laser or multiple measuring angles can be made to describe anisotropic particles.^[125-128] Unfortunately, this kind of modifications could not be realized during this work.

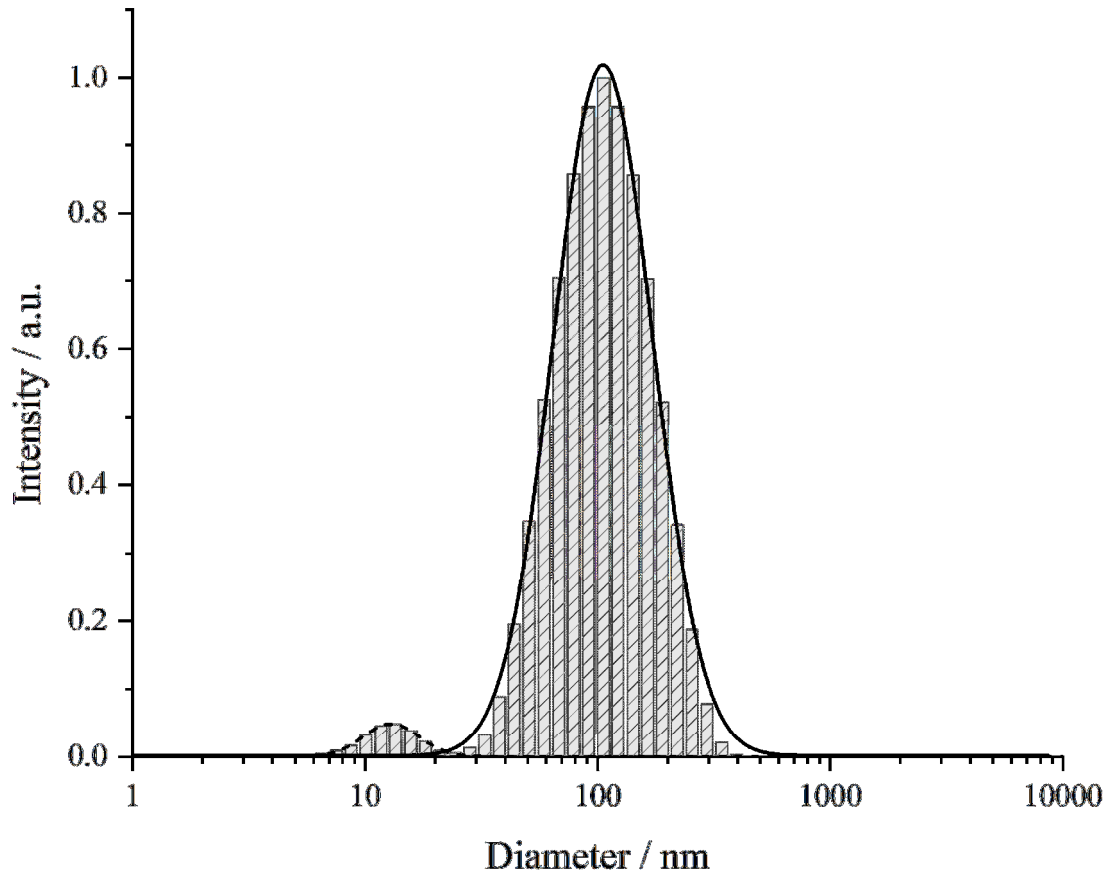


Fig. 17: DLS measurement of particles synthesized with the glucose synthesis. The graph shows the intensity (a.u.) as a function of the diameter (nm). The bimodal size distribution can be explained by the anisotropic form of the particles.

Hence the DLS results in a bimodal size distribution with a mean particle size of 92 nm and an artefact at 14 nm. The PDI of the sample, with a value of 0.28, is in the range of a monodisperse system. The high difference in PDI compared to the SEM analysis is because the DLS results in a bimodal distribution. The overall size increase compared to the SEM images is based on the method. The DLS measures the hydrodynamic shell additionally to the metallic core and hence overestimates the size. Normally, the size distribution by number would lead to accurate values for particles sizes. But since the intensity shows an artefact caused by the anisotropic character the distribution by number leads to wrong results. The scatter intensity is proportional to the radius to the power of six ($I \sim r^6$). This relationship is taken into consideration for the calculation of the distribution by number. Therefore, the small peak will be highly

overestimated in the number-based distribution which results in too small mean particle sizes. The distribution by number could hence not be used.

The particles have a ζ -potential of -23 mV which can be explained by adsorbed molecules of neutral charged PVP and negatively charged counter ions like NO_3^- from the synthesis. This leads to an overall negative ζ -potential which stabilizes the particles sterically and electrostatically. The size of the particles was further determined using disc centrifugation sedimentation (DCS).

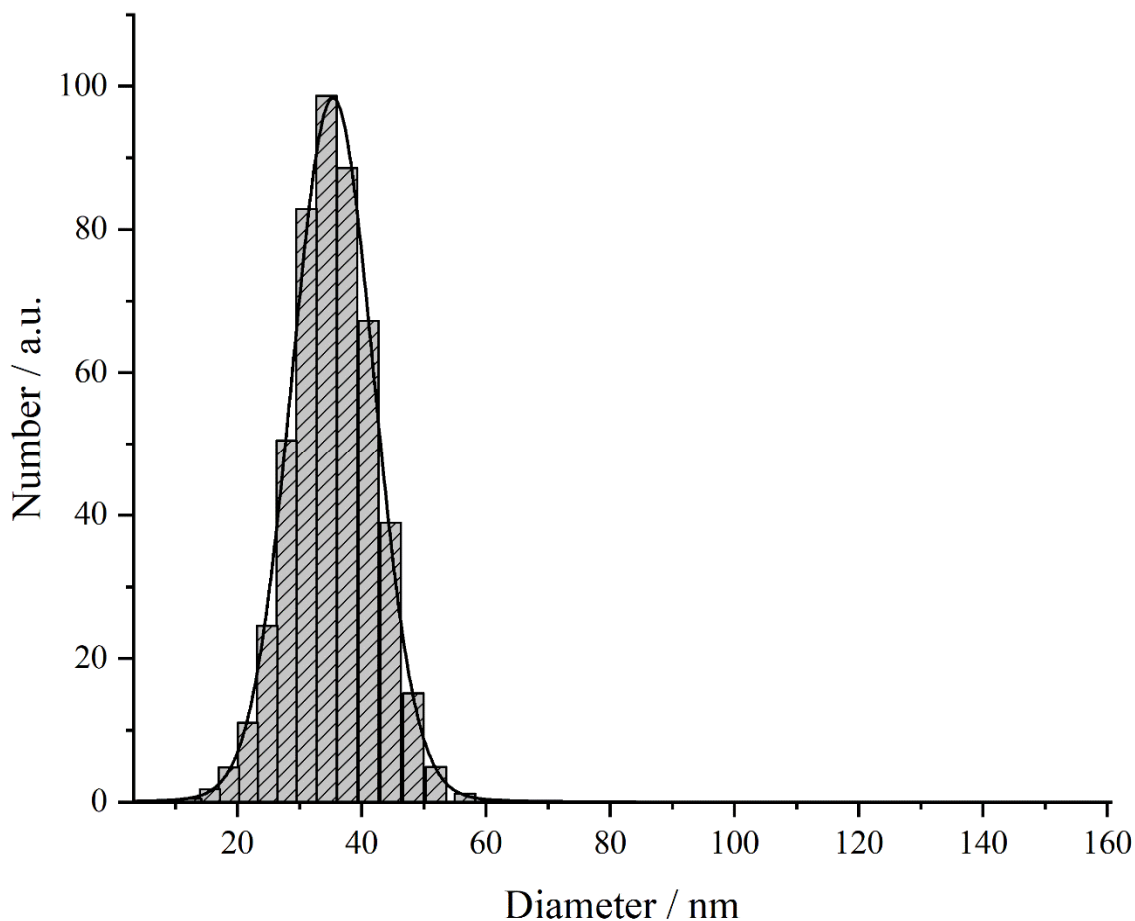


Fig. 18: DCS measurement of the synthesized silver nanoparticles with glucose. The graph shows the number (a.u.) as a function of the particles diameter (nm).

The DCS measurement shows a particle size distribution with a maximum at 53 nm and a standard deviation of ± 12 nm as well as a PDI of 0.25. The data set does not contain any visible peaks of particles with a diameter less than 20 nm and therefore confirms that the observed artefact in the DLS measurement (Fig. 17) is due to the anisotropic shape and not to a fraction of smaller particles. The discrepancy between both methods is due to the different measuring

principles. The DCS requires the relative density of the particles to calculate their size. However, the theoretical density of the metal particles will differ from the real density because of the polymeric shell. Consequently, the particles have a lower effective density which leads to a size underestimation. Taken the advantages and disadvantages of all size determining methods into consideration, the methods are in good agreement with each other. An overview of the data is shown in Table 3.

Table 3: Size distribution, standard deviation, polydispersity index (PDI) and the coefficient of determination (COD) for the applied Gauss-fits for all size determining methods.

Method	SEM	DLS	DCS
Diameter / nm	50	92	53
Standard deviation (σ) / nm	14	48	12
PDI	0.17	0.28	0.25
COD (R^2)	0.9848	0.9968	0.9788

The optical properties of silver nanoparticles can be studied using UV/Vis spectroscopy. The form as well as the position of the absorption band contains a lot of different information. Information like polydispersity of spherical systems can be investigated by examining the broadness of the band. Furthermore, the position of the maximum is directly related to the particles size. Bigger particles will therefore undergo a red shift in absorption compared to smaller particles.

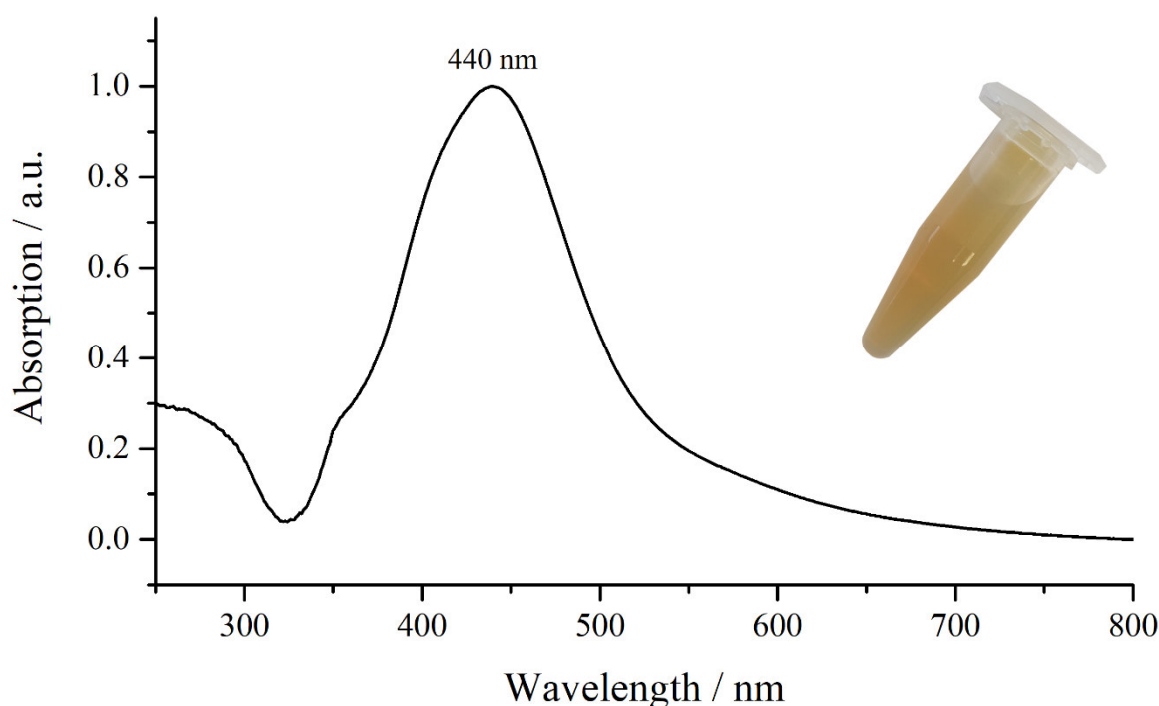


Fig. 19: UV/Vis spectrum of silver nanoparticles synthesized with glucose and an additional image of the actual sample. The graph depicts the absorption (a.u.) as a function of the wavelength (nm).

The spectrum shows a relatively narrow absorption band with a FWHM of 106 nm and a maximum absorption at 440 nm. This absorption is comparable to particles with a size of 60 nm described in the literature.^[122, 129] The data was obtained from a Gaussian fit. A further characterization regarding the crystallographic properties has not been performed because of already existent extensive studies in the literature.^[82, 123, 130]

The synthesized particles possess a high quality and reproducibility. They do develop monodisperse size distributions in ranges between 40-70 nm. The particles themselves do not have a spherical but an anisotropic disc like shape. However, the yield of the synthesis is by any standard low. Investigations by *Dr. Jens Helmlinger* have revealed a yield of only 1.3 % based on the used amount of silver.^[91] Investigations of the yield by AAS in this work have shown values around 5-8 % depending on the synthesis. This might be related to the relatively weak reducing agent glucose. Anyhow, the particles have good properties to perform further synthesis to generate core-shell structures and were therefore used for further experiments.

5.1.2 Bimetallic nanoparticles based on the glucose synthesis

The purified particles from the glucose synthesis were used as seeds for the synthesis of bimetallic systems. These seeds were dispersed in ultra-pure water and ascorbic acid as the reducing agent was added. The corresponding metal precursor, either tetra chloridoauric acid or palladium nitrate, were then added in a specific ratio to the stirring solution via a syringe pump. The ratios of both metals will be given in mole percentage if not noted otherwise.

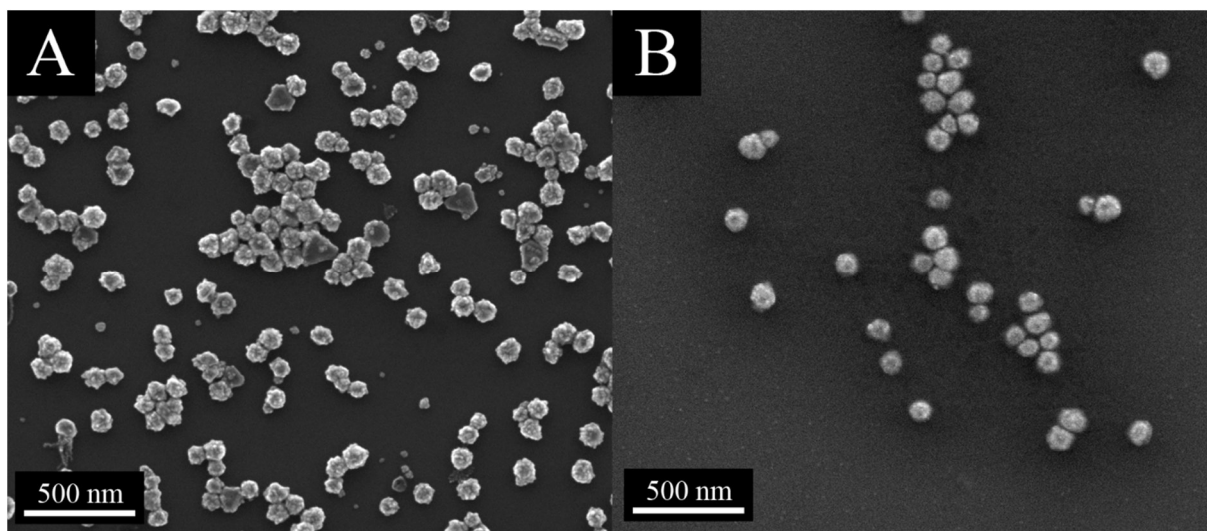


Fig. 20: SEM images of the synthesized bimetallic particles with gold (A) and with palladium (B) in a molar ratio of 50:50. Both images were taken with an accelerating voltage of 25 kV and a 100000 times magnification.

Most particles obtained from both reactions show a spherical morphology. Other particle morphologies like prisms and rods can also be observed (Fig. 20, A). This was expected since the seeds were taken from the glucose synthesis. As formerly described, the glucose synthesis generates a certain amount of non-homogeneous structures (compare chapter 5.1.1). To estimate the size distribution of each sample, the diameters of 100 particles were digitally measured. The obtained histogram for the reaction with tetra chloridoauric acid resulted in a bimodal size distribution with a maximum at $90 \text{ nm} \pm 12 \text{ nm}$ and a second maximum at $29 \text{ nm} \pm 8 \text{ nm}$ (Fig. 21, B). The synthesis from the reaction with palladium nitrate reveals a narrow, unimodal size distribution with a peak maximum at 66 nm and a standard deviation of 9 nm (Fig. 21, D). The PDI for the synthesis with gold is 0.16 and 0.10 in the case of palladium. Therefore, both systems exhibit a higher monodispersity than the used seeds which have a PDI of 0.17.

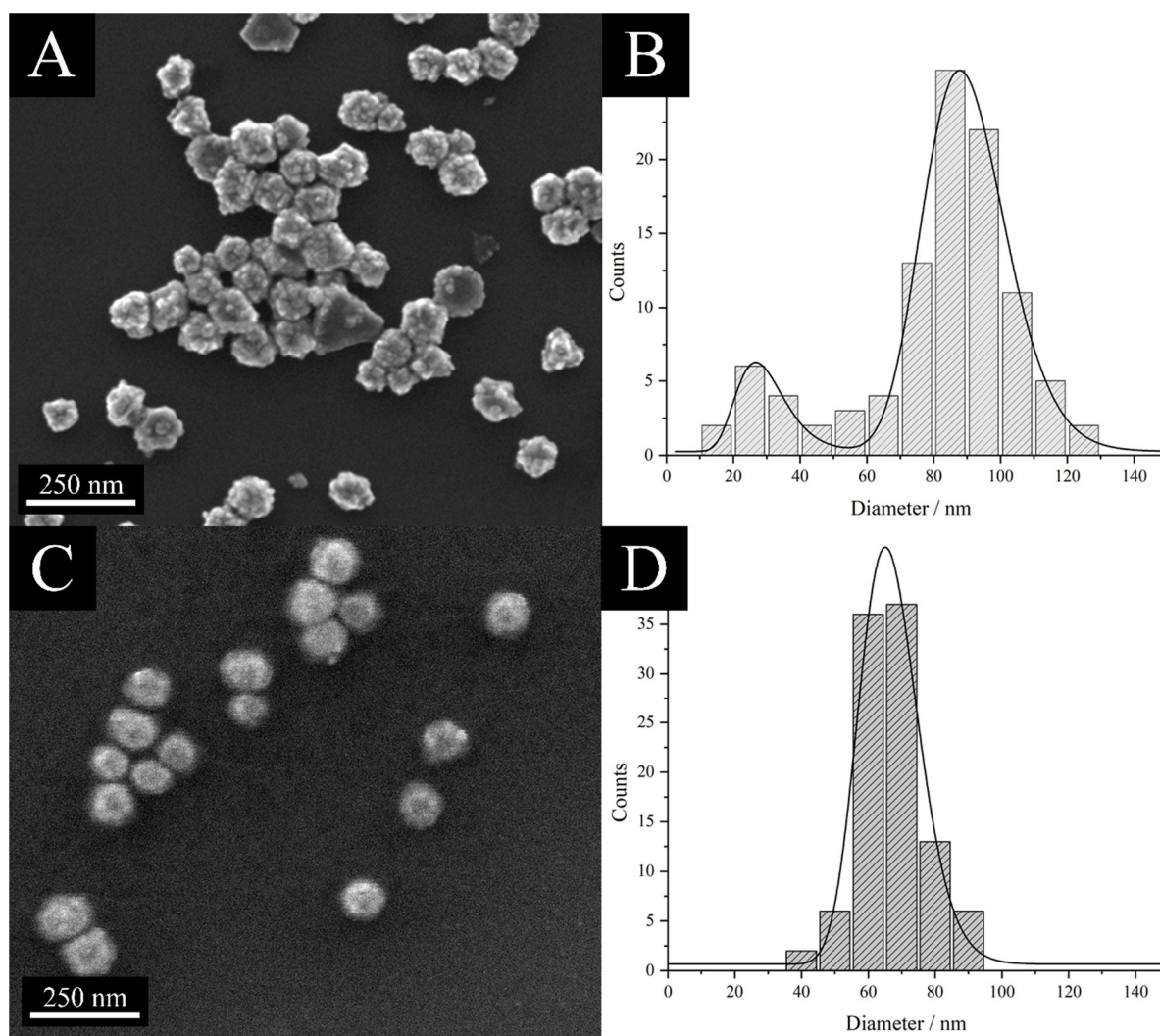


Fig. 21: SEM image with a higher magnification of the obtained bimetallic particles with gold (A) and palladium (C) and the corresponding histograms for the synthesis with gold (B) and palladium (D). Both Histograms have been calculated using a bin size of 10.

The size difference between both syntheses is quite high taken into consideration that both particles were synthesized using the same seeds as well as the same parameters regarding precursor addition rate and concentration of reducing agent. Taking a closer look, the particles synthesized with gold reveal a spherical form but have a rough, irregular surface. This surface seems to be built of small crystallites which might have formed on the silver seeds (Fig. 21, A). Particles obtained from the synthesis with palladium have a much smoother surface which might partially explain the difference in size (Fig. 21, C). Additionally, EDX spectra were taken to gain more information about the particle composition. The nominal compositions of the analyzed syntheses were 50:50 (Ag:M) ratios. The EDX revealed a 44:56 (Ag: Au) composition for the gold containing particles and a ratio of 57:43 (Ag: Pd) for the particles with palladium. Therefore, certain amounts of silver and palladium must have reacted otherwise during the

syntheses. Those values however must be evaluated with care. EDX measurements taken by SEM have a normal error between 1-5 % for elements contents >10 At%.^[131] However, differences between both syntheses might be explained by different reaction pathways.

To investigate the observed differences between both syntheses in more detail, HAADF images were taken by Ms. Dr. Katarzyna Loza at the Ernst-Ruska centrum in Jülich. The images were captured with an accelerating voltage of 300 kV. Additionally, EDX maps of single particles were performed to verify and investigate the loss of silver and palladium along with the composition of the particles.

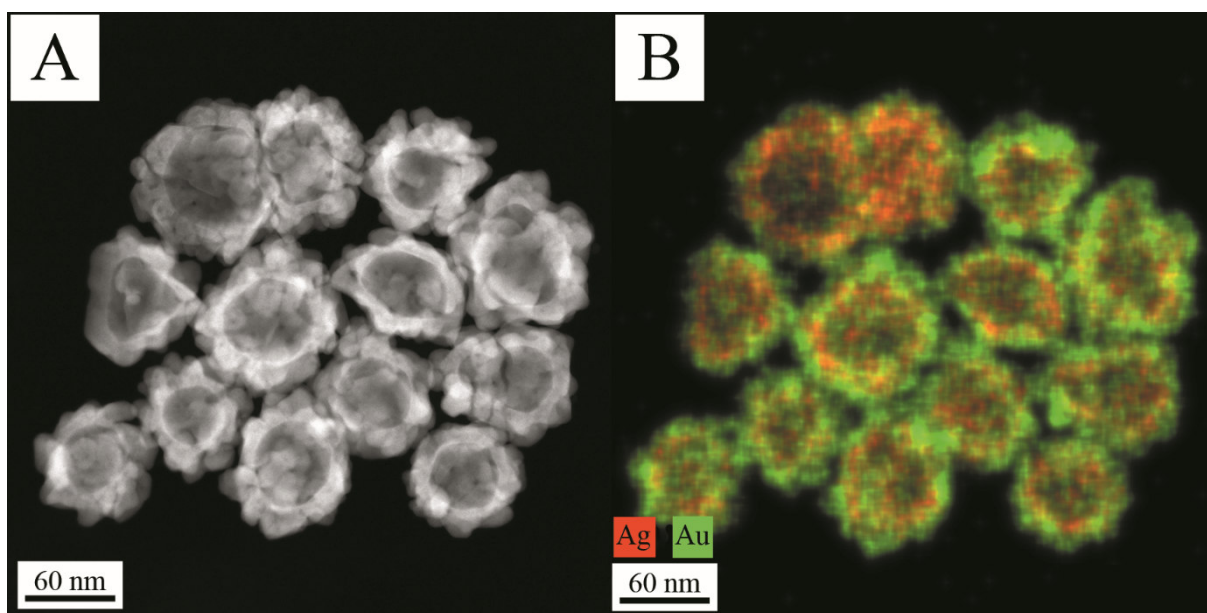


Fig. 22: HAADF images of silver particles after the reaction with chloridoauric acid (A) and the corresponding EDX map for the same particles (B). Energy corresponding to silver is marked with a red and gold with a green color.

The HAADF images reveal that the generated structures of silver particles which reacted with tetrachloridoauric acid result in hollow spheres. This can be explained by a galvanic replacement reaction where the gold cations are reduced with “sacrificed” electrons of the silver atoms.^[29-31, 34] In further considerations, those hollow spheres reveal several small pores where dissolved silver ions have diffused through (Fig. 22, A). The EDX map shows that the inner sphere is built of an alloy of both metals with an enrichment of silver. The outer layer of the structure is mostly constructed of phase-pure gold (Fig. 22, B). Therefore, the particles build a kind of core-shell structure during the synthesis. The core is consequently a hollow alloyed sphere of silver and gold with a highly gold-enriched shell.

5.1 Synthesis of silver nanoparticles from glucose

The former described galvanic replacement of silver with gold is due to their dissimilar standard potentials (E°). The standard potential for the Au^{3+} -ion is +1.50 V while it is +0.80 V for the Ag^{+} -ion. The reduction potential of the used ascorbic acid (-0.55 V)^[132] at pH 7 is not sufficient to protect the metallic silver against the oxidation by Au^{3+} cations. Hence, three silver atoms will be oxidized to reduce one gold atom. The surface atoms of the particle will therefore be oxidized by the gold ions in the solution (Fig. 23, A). Following, the silver ions will be reduced by the ascorbic acid and crystallize as an alloy with the formed gold atoms. This newly formed crystallites will conceivably form a connection to the surface of the silver seed (Fig. 23, B). The work of Grasmik *et al.* has shown that the standard potential for silver becomes more shifted to gold, and hence nobler, if an alloy is formed.^[28] Consequently, silver incorporated in those alloyed crystallites will not be further oxidized by gold ions. Based on this, the gold atoms will be reduced by the electrons of non-alloyed silver atoms in the seed core. This will lead to a hollow core (Fig. 23, C). After all silver ions are incorporated in the alloy, the remaining gold ions will be reduced by the remaining ascorbic acid, what will result in a gold shell around the newly arose hollow core (Fig. 23, D).

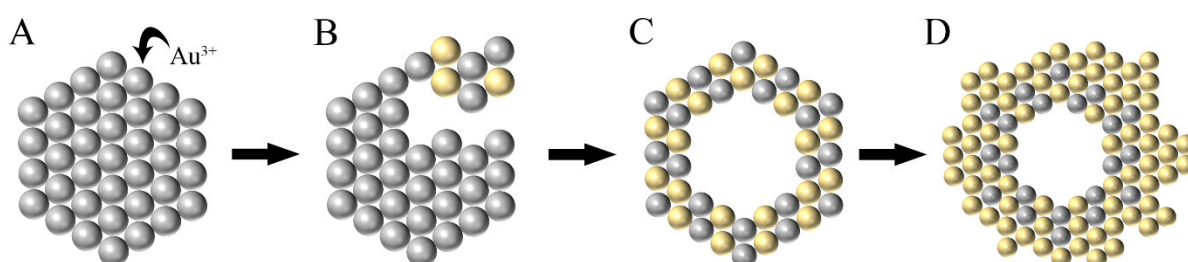


Fig. 23: Schematic mechanism of the growth of hollow bimetallic silver-gold nanoparticles with a gold shell. The yellow spheres represent the gold atoms and the gray spheres represent the silver atoms.

The EDX map of the particles shows a composition of 38:62 (Ag: Au) and thus confirms the loss of silver during the synthesis. A formation of silver chloride could explain the mass loss of silver. Chloride ions of the used precursor, tetra chloridoauric acid, will most likely have intercepted some ions of silver and leave an oversupply of gold ions in the solution which form the gold shell. This will lead to an instantaneous precipitation of silver chloride. Since the particles were washed with a certain amount of ammonia, the silver chloride was washed out during purification. The smaller particles which are observed in the size distribution calculated

from SEM images could be newly formed alloyed crystallites which have lost connection to the main particle and are therefore much smaller.

The sample synthesized with palladium has also been investigated using HAADF and EDX maps (Fig. 24).

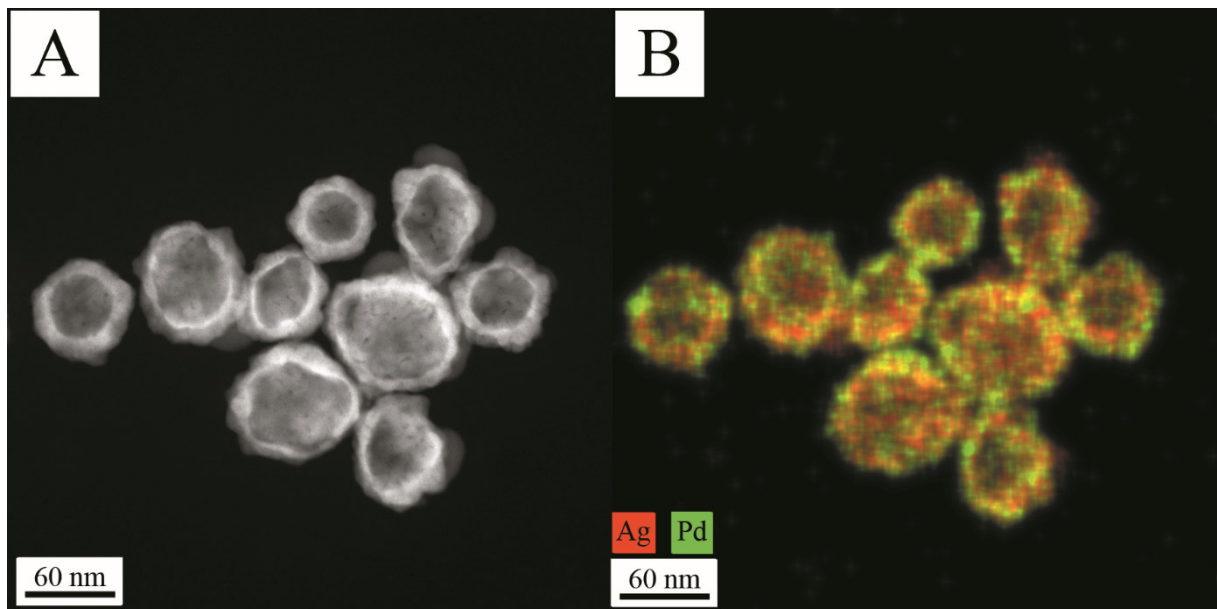


Fig. 24: HAADF image of the synthesized silver-palladium nanoparticles (A) and an EDX map taken from the same spot (B). Energy densities corresponding to silver are marked with a red and to palladium with a green color.

The system has developed a similar structure in comparison to the former described particles with gold. The synthesis also results in hollow spheres which occurrence can be explained by a galvanic replacement reaction by palladium for silver. However, there is a prominent difference between both samples. The EDX map shows that all particles have developed an alloyed structure. In contrast to the sample synthesized with gold, no shell of palladium around the particles is observed. This observation also explains the former described smoother surface of the particles. The difference in both syntheses is thus to the standard potentials of silver (+0.80 V) and palladium (+0.85 V) which are quite similar. After the hollow sphere of the alloy has been formed, both metal ions will consequently be reduced simultaneously.

The EDX map of the sample reveals a composition of 65:35 (Ag:Pd) and therefore confirms the loss of palladium during the reaction already detected by EDX during SEM. This loss can be explained by the formation of small palladium particles during the reaction. Those smaller particles were indicated during purification, where the supernatant remains a slightly brown

5.1 Synthesis of silver nanoparticles from glucose

color. Based on this observation, it becomes clear that a competition between newly formed seeds and the incorporation of the palladium into the alloy is occurring.

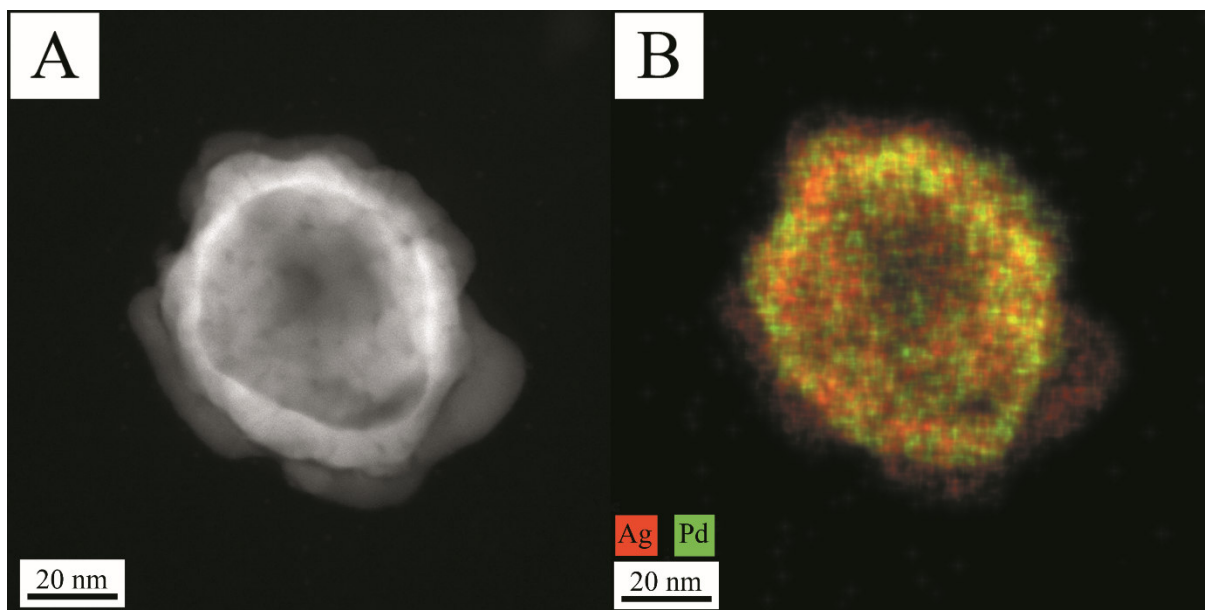


Fig. 25: HAADF image (A) and EDX map (B) of a single particle obtained from the synthesis with palladium. A halfway formed shell of silver can be seen in the EDX map.

Taken an even closer look into the internal structure, the particles have an enrichment of silver on the outer surface (compare Fig. 25). The steps of the formation of the silver-palladium particles is quite like the formation of silver-gold particles.

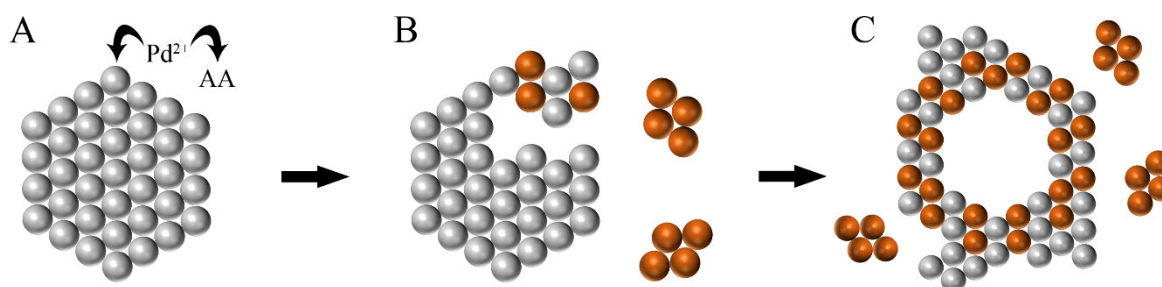


Fig. 26: Schematic mechanism of the growth of silver-palladium hollow spheres. Silver atoms are marked with a gray color. Palladium atoms are marked with a red-brown color.

Already at the beginning of the synthesis the palladium ion concentration is lowered because of the formation of small palladium seeds (Fig. 26, A+B). The seeds might either be formed by oxidation of ascorbic acid or silver atoms. At a certain point, only silver will be available and will hence crystallize to the hollow spheres forming an outer layer around the alloy

(Fig. 26, C). Furthermore, no chloride is present during the synthesis. The amount of accessible silver during the reaction remains unchanged. This explains the difference in the molar ratio of both nanoparticle species. The discrepancy in the composition of both systems is thereby caused by two dissimilar effects. Both hollow spheres result because silver is the less noble metal in the synthesis and will therefore be oxidized. In the newly formed alloys, silver will become nobler due to an increase of the standard potential. However, the chloride which is present during the gold synthesis will lower the silver content and will thereby lead to an enrichment of gold in the outer shell. In the case of palladium, the concentration of palladium will decrease due to formation of palladium nanoparticles. This directly leads to an outer layer which has a high amount of silver. The recrystallization of both systems leads to a more homogenous size distribution. That was confirmed by the calculated PDIs for both syntheses.

To further characterize the crystallographic properties of both systems, XRPD patterns were recorded. Bimetallic systems which develop alloys or solid solutions can be identified because of their alteration in lattice parameter based on the percentage composition of both metals.

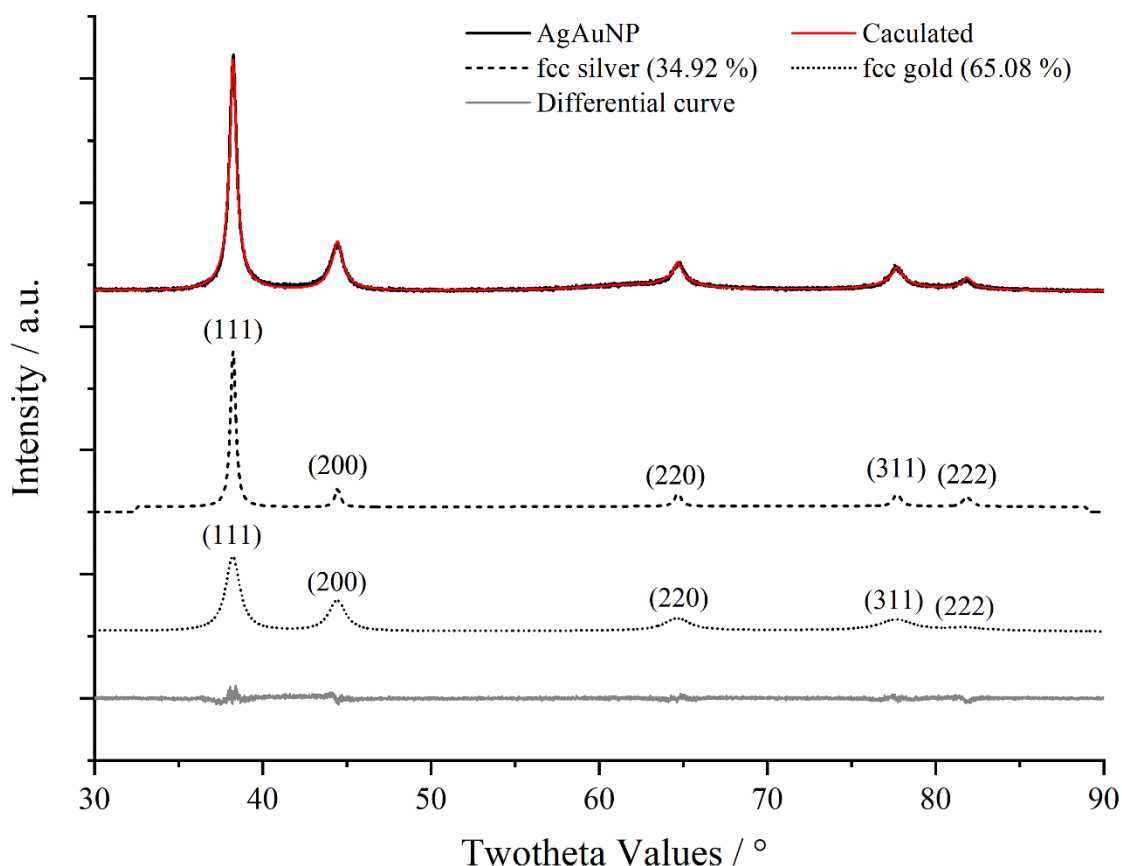


Fig. 27: Rietveld refinement of the synthesized hollow silver-gold nanospheres. The peak profile was calculated using fcc-phases of silver and gold.

5.1 Synthesis of silver nanoparticles from glucose

The obtained data from the XRPD measurement of hollow silver-gold nanoparticles was used to determine the lattice parameter as well as the composition by Rietveld refinement. The data treatment reveals that overall two different phases are present. Besides the fcc-phases of silver and gold, a third amorphous halo between 55-70° can be seen (Fig. 27). The halo is only low in intensity and is related to the used sample holder. This could be verified by several measurements. The cumulative fit data of both fcc-phases shows that the material has a composition of 65.1 % gold and 34.9 % silver. Those values are in good agreement with the former described composition by EDX of 38:68 (Ag:Au). The lattice parameters obtained from both metal phases as well as the data obtained from the cumulative fit is shown in Table 4.

Table 4: Lattice parameters and crystallite sizes obtained from Rietveld refinement. The table shows the parameters of silver, gold and the cumulative fit which describes the alloy formed by the hollow core.

Phase	Lattice Parameter / Å	Crystallite size / nm
fcc silver	4.0754 (1)	22.4 (3)
fcc gold	4.0779 (2)	8.2 (1)
Cumulative Fit (Alloy)	4.0735 (2)	17.4 (1)

The lattice parameter of gold is shifted to the value of silver. Normally, alloys develop a shift of the lattice parameters. This shift will be stronger towards the lattice parameter of the material which is more present in the alloy and will have a linear dependency over all possible mixtures. Therefore, alloys with a 50:50 composition will end up with a lattice parameter in between the lattice parameters of both metals. This dependency is called Vegard's law.^[133] Silver-gold alloys however do develop an irregularity to other alloy systems. The alloys of silver and gold show a deviation from this linear dependency whereby the highest deviation occurs in the 50:50 composition.^[134] A polynomial fit of known lattice parameters of different compositions from the literature can be used to calculate the composition of an alloy. Therefore the lattice parameter obtained from Rietveld refinement is plotted to the polynomial fit. The received x-value equals the composition of the system (Fig. 28). The calculation with the obtained lattice parameter from the cumulative fit by the Rietveld refinement of the sample leads to a silver amount of 85.6 % (Fig. 28). This composition may be considered with caution, since nanoparticulate systems already have smaller lattice parameters and the fit is obtained from the bulk alloys. The huge deviation in composition derived by Rietveld refinement and EDX in comparison to the calculated composition by the lattice parameter can be explained. In a closer look, the XRPD data shows that the calculated peak profile of gold is broadened in comparison to the silver reflexes (Fig. 27). This broadening in the refinement indicates smaller crystallites

of gold. Hence, the broadening might be caused by the irregular growth of gold around the hollow alloyed cores which leads to smaller crystallites of 8.2 nm. The irregular growth can also be seen in HAADF images (compare Fig. 29, A).

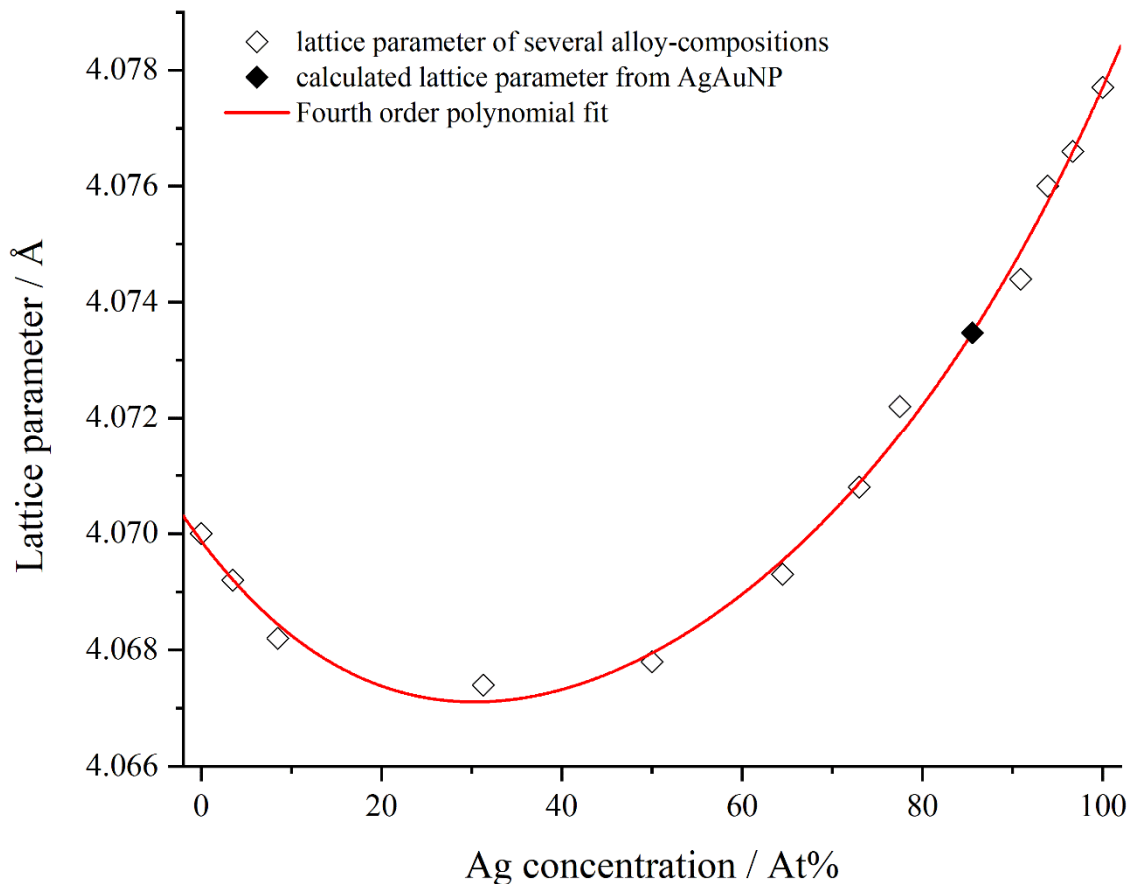


Fig. 28: Nonlinear regression of lattice parameters for silver-gold alloys obtained from bulk material.^[134] The lattice parameter is shown as a function of the silver concentration (at%). The fit was obtained from a polynomial fit of the fourth order with the following formula: $y = A_0 + A_1 \cdot x + A_2 \cdot x^2 + A_3 \cdot x^3 + A_4 \cdot x^4$ and a COD of 0.9948.

The Peak profile which is obtained by XRPD shows thereby a mixture of smaller crystallites of the gold phase (8.2 nm) and bigger crystallites of the generated alloy (17.4 nm). This leads to the conclusion that the alloyed core has a higher degree of crystallinity and consequently contributes more to the peak position. The performed EDX map shows a high amount of silver in the alloyed core (Fig. 29, B). Hence, the composition of the inner core is enriched in silver which directly correlates to the extrapolated amount of 85.6 % silver by the lattice parameter. This enrichment can be explained by the occurring chemical reaction. For the reduction of one Au^{3+} -ion three silver atoms will be oxidized.

5.1 Synthesis of silver nanoparticles from glucose

The newly formed silver ions will diffuse into the solution and will be reduced by ascorbic acid. Based on this mechanism always three silver atoms will be formed when only one gold atom is generated. This will lead to an enrichment of silver in the alloyed core.

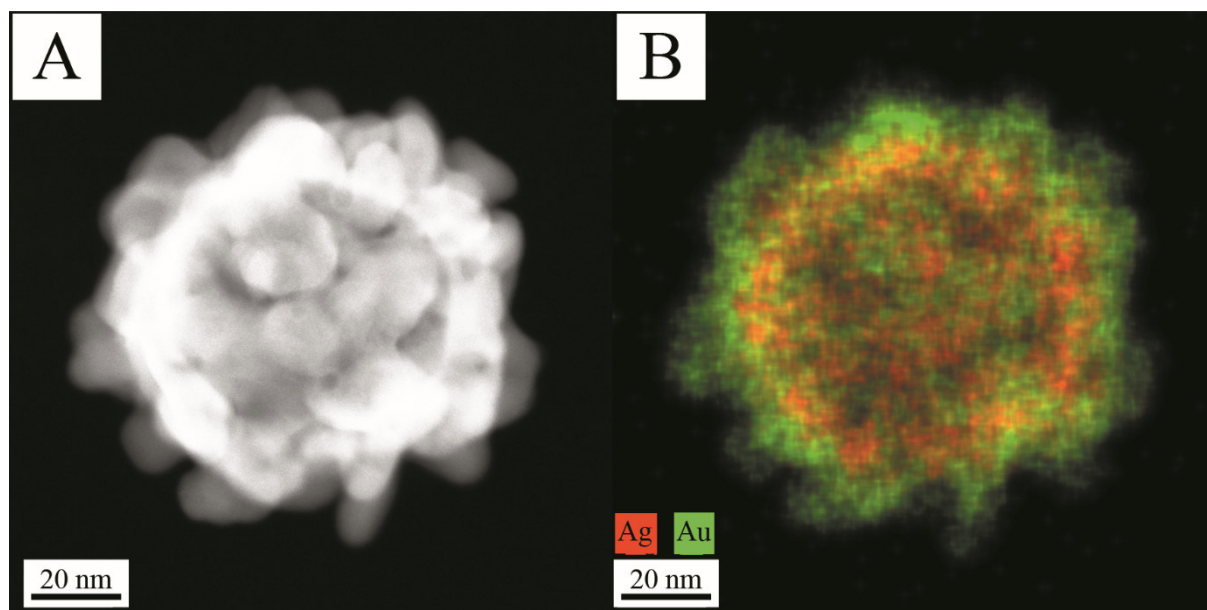


Fig. 29: HAADF image (A) and EDX map (B) of a single particle obtained from the synthesis with gold. A rough irregular surface of gold which might contain only small crystallites has grown around the hollow alloyed core.

Additionally, the standard potential of silver will increase as soon as gold atoms crystallize into the structure right next to them. This leads to a certain amount of silver which will not be oxidized at all. These two effects will consequently lead to a strong enrichment of silver in the alloyed core. The investigation by XRPD of the hollow silver-gold nanoparticles shows that the core of the particles is an alloy with a high amount of silver. Compared to the inner core, the sizes of the outer gold crystallites (shell) are drastically decreased. This difference in crystallite sizes of the silver-gold alloy (core) and the phase pure gold (shell) directly influences the mean lattice parameter of the Rietveld refinement. The XRD could therefore be used to investigate the difference of the crystallographic properties of the shell and the core which occur during the reaction.

The hollow particles obtained from the synthesis with palladium were also investigated using X-ray powder diffraction as well as Rietveld analysis (Fig. 30).

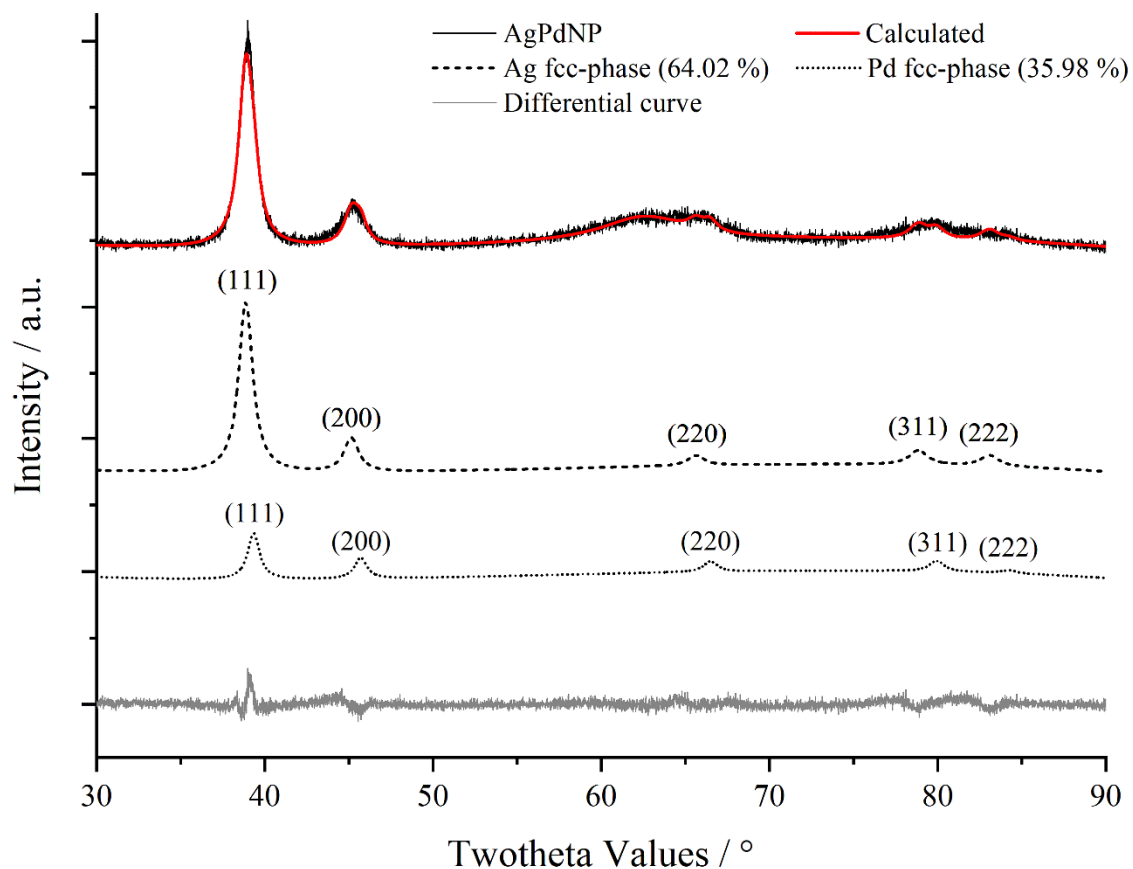


Fig. 30: Rietveld refinement of the synthesized hollow silver-palladium nanospheres. The peak profile was calculated using fcc phases of silver and palladium. Additionally, an amorphous phase was found.

The refined pattern shows a mixture of palladium and silver with a percentage atomic distribution of 64.0 % silver to 36.0 % palladium. Furthermore, an amorphous halo between 55-70° is observed. The maximum count rate for the reflex with the highest intensity, corresponding to the (111)-lattice plane, is only 800 and consequently very low. Amorphous spots of the used sample holder are the cause of this amorphous halo based on the low sample/background-signal ratio. Anisotropic stacking faults or a high micro strain of higher indexed planes could be excluded as an explanation for the amorphous halo. Former refinements without the amorphous phase have shown that neither the position nor the intensity can be correlated to any other phase of one of the present metals. The refinement is done by fitting the two separate phases of both fractions to gain a cumulative fit that describes the obtained pattern. The shift of the lattice parameter of single phases in the formed alloy can

5.1 Synthesis of silver nanoparticles from glucose

hence be calculated. The parameter obtained from both metal phases as well as the data obtained from the cumulative fit is shown in Table 5.

Table 5: Lattice parameters and crystallite sizes obtained from Rietveld refinement. The table shows the parameters of silver, palladium and the cumulative fit which describes the alloy formed by the hollow core.

Phase	Lattice Parameter / Å	Crystallite size / nm
fcc silver	4.0383 (3)	9.5 (1)
fcc palladium	3.9914 (3)	11.7 (5)
Cumulative Fit (Alloy)	4.0046 (1)	9.6 (1)

The data shows a direct shift from the silver phase to the lattice parameter of palladium and vice versa. Alloys from palladium and silver follow strictly Vegard's law. Thus, the lattice parameters of the alloys will have a linear dependency with the increase of one metal's fraction. This dependency can be used to calculate the composition from the lattice parameter.

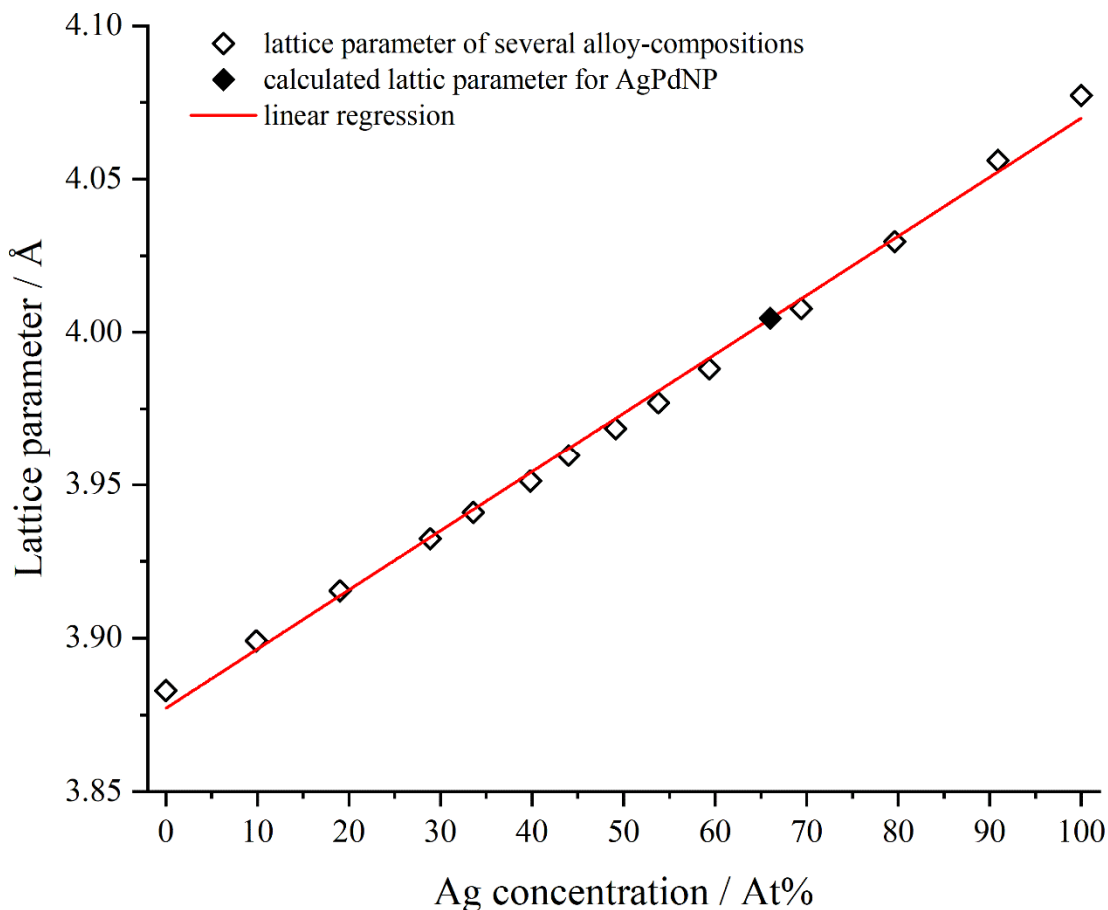


Fig. 31: Vegard-plot for silver-palladium alloys from bulk material.^[134] The lattice parameter is shown as a function of the silver concentration (at %). The linear fit has a COD of

The obtained composition reveals a mixture of 66.03 at% silver to 33.97 at% palladium. Those values are in perfect agreement with the parameters obtained from Rietveld refinement as well as the distribution determined by EDX. The small fraction of non-alloyed silver on the outside of the particles will somewhat influence the lattice parameter of the cumulative fit. A slightly lower content of silver in the alloyed core is consequently expected. Since a certain amount of silver is crystallized phase-pure on the outer surface, the hollow core must be somehow enriched in palladium. The Rietveld refinement could be used to calculate the crystallite size of both phases. The value obtained for the silver phase is 9.5 nm and for palladium it is 11.7 nm. The crystallite size of the cumulative fit is 9.5 nm and reveals that both phases have the same crystallinity. Since both phases have comparable crystallite sizes, the influence of the alloyed core on the XRD measurements is less noticeable than compared to the hollow silver-gold nanoparticles.

The XRPD measurements could show that both alloyed cores have different compositions because both precursors are present in different oxidation states. The silver-gold core has a huge amount of silver (85.5 %) whereas the composition of the alloy in the palladium containing particles is ~60:40 (Ag:Pd). Therefore, both systems differentiate in their reaction pathway as well as their internal structure.

To confirm the colloidal stability of both systems the particles were investigated using DLS and DCS. Furthermore, the optical characteristics were investigated using UV/Vis spectroscopy. The obtained data from DCS and DLS were evaluated using Gaussian fits.

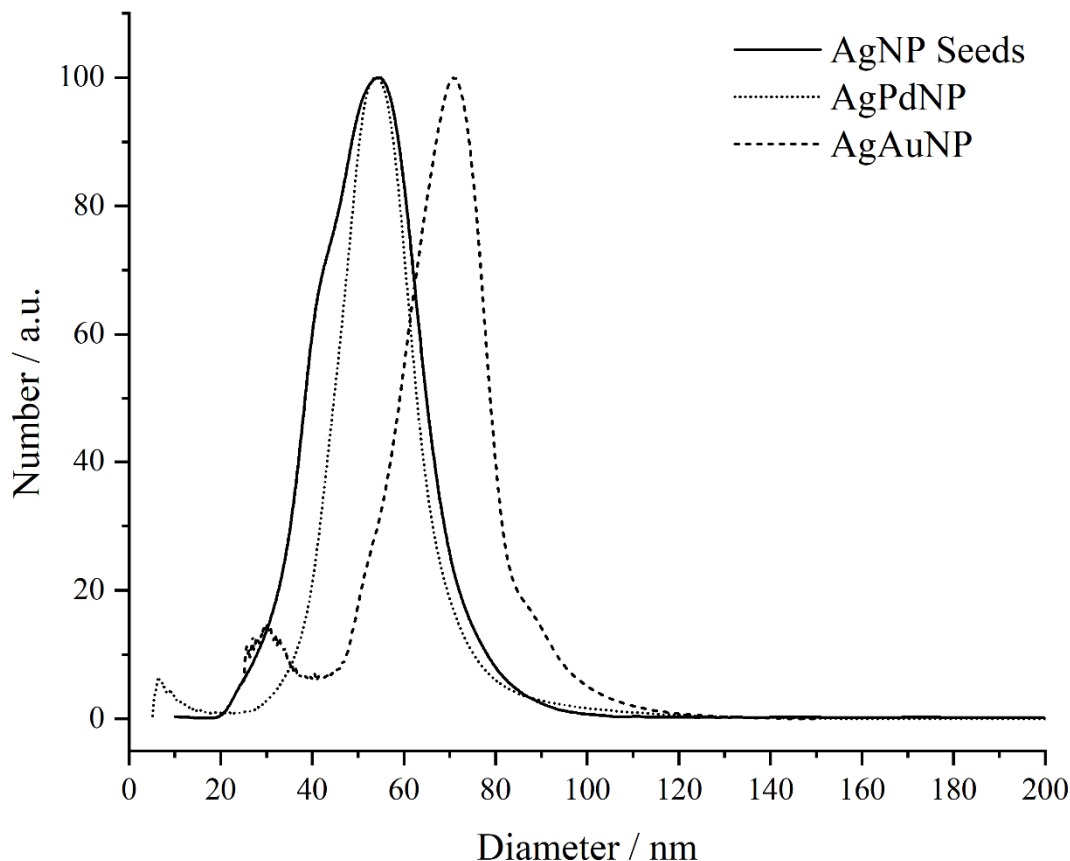


Fig. 32: Size comparison by DCS between the seeds from glucose and the obtained hollow bimetallic nanoparticles. The number (a.u.) is depicted as a function of the diameter (nm).

The comparison of the collected DCS distributions reveals that the silver-gold particles are the largest and have a bimodal size distribution. The first maximum of the distribution is at $70 \text{ nm} \pm 9 \text{ nm}$. The peak shape has an irregular form which might be interrelate with the rough surface of the particles. The second maximum of the size distribution occurs at 30 nm and has a standard deviation of 10 nm. The measurement of the silver-palladium particles shows a unimodal, narrow size distribution with only one maximum at 54 nm and standard deviation of 9 nm. The distribution is even narrower than the one measured from the seeds. This is most likely related to the fact that the particles undergo a recrystallization process which leads to a more monodisperse system.

For the measurements of both bimetallic particles a 50:50 mixture of the densities of silver and the corresponding metal were taken to determine the size. This, however, does not match with the real composition of the particles. Furthermore, the particles have a hollow core which has a direct influence on the real density of the system. The particle diameter is therefore strongly underestimated in comparison to the seeds as well as the SEM measurements. However, taken these facts into consideration, the distributions are quite comparable to the SEM measurements regarding the size distribution as well as the dispersity of the bimetallic particles (compare Fig. 21, B+D).

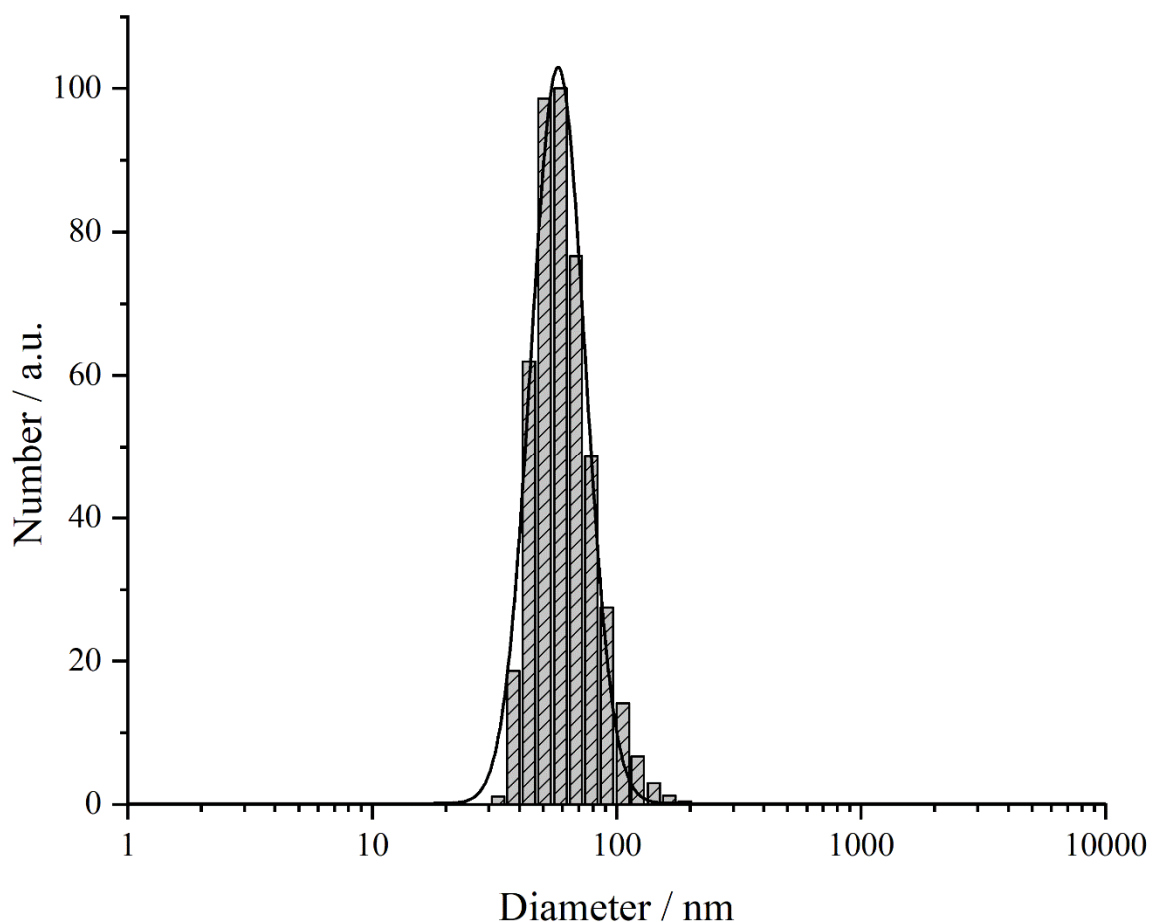


Fig. 33: DLS size distribution for the synthesized silver-gold nanoparticles. The number (a.u.) is shown as a function of the diameter (nm).

The DLS intensity distribution (not shown) for the bimetallic systems, in comparison to the used seeds, do not show a bimodal size distribution in both cases. This is since the anisotropic structures of the seeds have completely recrystallized into spherical alloyed particles. The smaller fraction of particles (compare SEM and DCS) in the case of silver-gold is completely masked by the fraction of larger particles based on the $I \sim r^6$ dependency.^[135]

5.1 Synthesis of silver nanoparticles from glucose

Hence, the bimetallic particles show unimodal size distributions by number with a PDI of 0.13 (Fig. 33). The obtained ζ -potentials for both syntheses are around -10 mV to -23 mV and result from a combination of neutral adsorbed PVP as well as adsorption of counter ions like chloride and nitrate.

A comparison of all size determining methods is shown in Table 6. All performed methods are in good agreement and confirm a high colloidal stability. No aggregates or agglomerates occur during measurements or storage.

Table 6: Comparison of the diameters obtained from different colloidal characterization methods. All datasets were obtained using Gaussian fits to evaluate the data.

Method	Diameter	AgNP Seeds	AgAuNP	AgPdNP
SEM	By number	50 ± 14	90 ± 12 nm 29 ± 8 nm	66 ± 9 nm
DLS	By number	-	71 ± 17 nm	65 ± 14 nm
	By intensity	92 ± 48 nm	120 ± 49 nm	115 ± 45 nm
DCS	By number	53 ± 12 nm	70 ± 9 nm	54 ± 8 nm
			30 ± 10 nm	

The bimetallic particles were further characterized using UV/Vis spectroscopy to determine the optical properties.

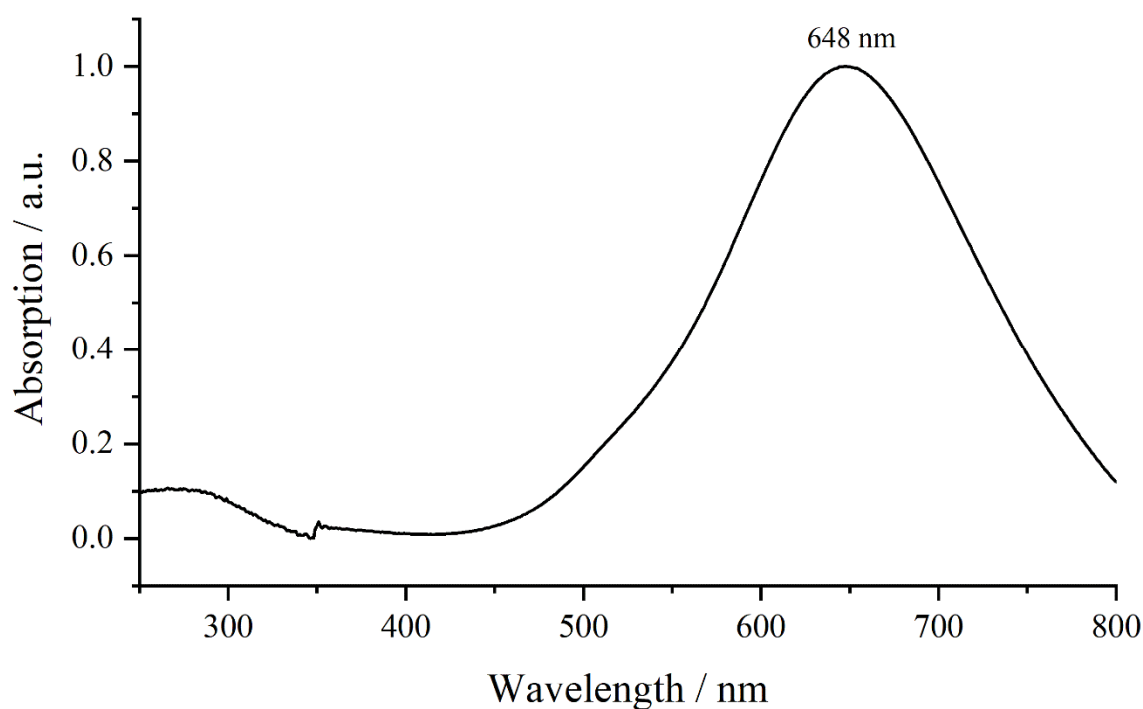


Fig. 34: UV/Vis spectrum obtained of the silver-gold particles synthesized with Ag-seeds from the glucose synthesis. The absorption (a.u.) is shown as a function of the wavelength (nm).

The UV/Vis spectrum of the bimetallic silver-gold spheres shows a broad absorption band with a FWHM of 169 nm and a maximum at 648 nm (Fig. 34). A typical gold absorption maximum for particles with a diameter of 90 nm occurs normally around 540-560 nm.^[136-137] Because the shell of the particles mostly contains gold, a comparable value was expected. The high red shift however could be explained by the rough surface of the particles (compare Fig. 22). Anisotropic structures like rods can be tuned in terms of plasmon resonance to have an absorption maximum between 600-900 nm.^[138-139] Therefore, the anisotropic surface might be an explanation.

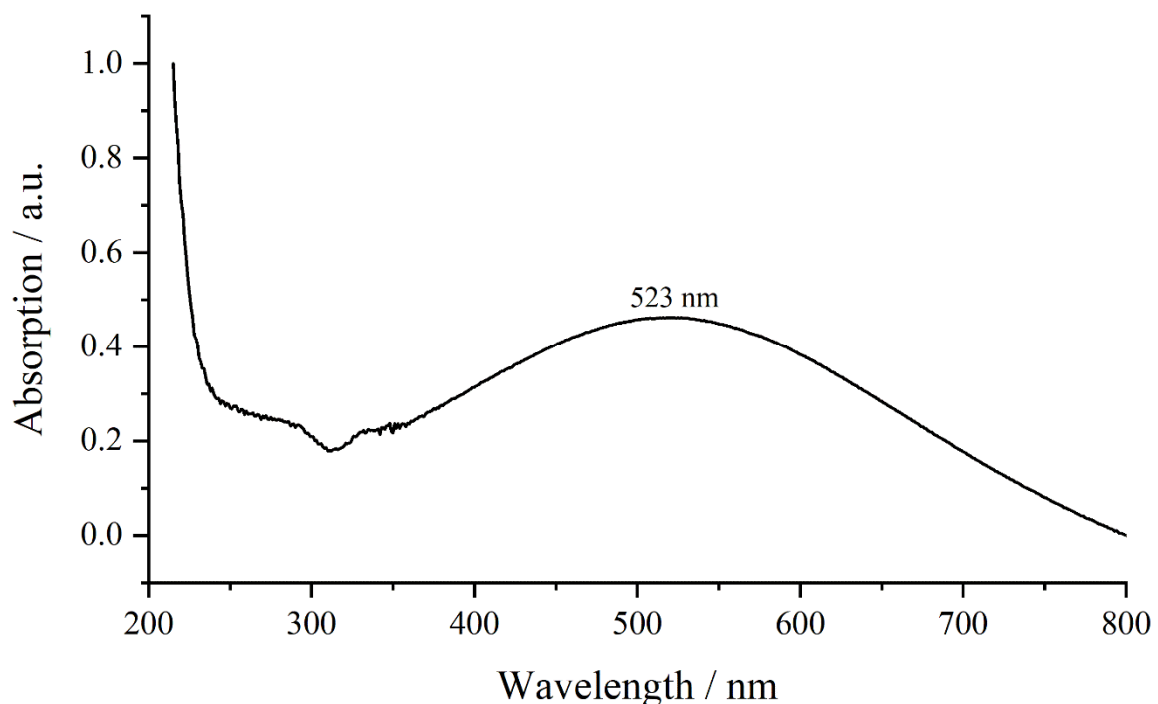


Fig. 35: UV/Vis spectrum obtained of the silver-palladium particles synthesized with Ag-seeds from the glucose synthesis. The absorption (a.u.) is shown as a function of the wavelength (nm).

The UV/Vis spectrum of the obtained silver-palladium nanoparticles reveal an even broader absorption band with an FWHM of 372 nm and a maximum at 523 nm. Palladium nanoparticles do absorb evenly over the whole visible range with a maximum absorption in the UV region.^[11] This leads to reduction of silver absorption if palladium is incorporated into nanoparticles with silver. An additional explanation might be the formation of silver rich zones on the surface of the spherical particles. These zones have no regular shape and will therefore have a variety of different surface plasmons. This results in a broad absorption. Similar observations can be made regarding anisotropic structures of silver e.g. prisms or rods.^[92, 102, 140]

In summary, the seed and growth method to synthesize spherical core-shell particles has shown that the direct reduction with ascorbic acid will not lead to the expected core-shell particles. The formed particles are constructed of an alloyed-core of silver and the corresponding metal (gold or palladium). The shell of the particles is either enriched with gold or, in the case of palladium, with silver.

An in depth structural investigation showed that this is because of their unequal standard potentials. Silver will therefore always undergo a galvanic replacement with the nobler metal. Furthermore, the precursors as well as the fact that palladium forms new monometallic palladium seeds lead to different outcomes of both syntheses. The investigation by X-ray powder diffraction and Rietveld refinement revealed that the hollow core of the silver-gold particles is highly enriched in silver (86:14 Ag: Au), whereas the hollow cores of the particles obtained from the synthesis with palladium have a composition around 66:34 (Ag: Pd). This observation is directly related to the oxidation states of the corresponding metal precursor as well as their electrochemical standard potentials. Additionally, the particles could be characterized in terms of their colloidal stability. The formed shell of gold in the silver-gold synthesis leads to larger particles with a highly anisotropic surface. In comparison bimetallic particles from the silver-palladium synthesis yield particles with a smoother surface and a silver enriched shell which are smaller in diameter. Both systems experience a recrystallization process which results in better PDIs in comparison to the used seeds from the glucose synthesis.

The irregular surface has a direct influence on the optical properties of the particles. The silver-gold system shows a maximum absorption at 648 nm and is therefore blue in dispersion. The irregular deposition of gold and silver on the outer shells of the particles and the anisotropic character leads to a broad absorption band which corresponds to different optical properties compared to the alloys as well as the monometallic particles of same size.

Especially the observations regarding the growth and the corresponding structure as well as an in-depth search in the literature have helped to set the foundation for the synthesis of core-shell nanoparticles with the desired internal structure. Furthermore, future planned experiments regarding the dissolution of the here described particles could help to influence the silver ion release rate to find possible applications.

5.1.3 Core-Shell nanoparticles based on the glucose synthesis

This section of the work will describe the characterization of synthesized core-shell particles in detail. The obtained particles were produced using a seed and growth method. As seeds, former characterized silver nanoparticles obtained from the glucose synthesis were used (see chapter 5.1.1).

A deposition of a metal on preformed metal nanoparticles can be done quite easily if the used core metal is nobler than the shell metal. Less noble particles, like silver, will undergo a galvanic replacement reaction if another nobler metal, like gold, is present (compare chapter 5.1.2). There are lots of examples in the literature of core-shell systems with silver as shell material.^[95, 97-99, 141] Based on former characterizations of hollow structures, a search of the literature revealed that core-shell particles with a silver core can be synthesized by adjusting the pH-value during the reaction. An increase of the redox potential of the used reducing agent, ascorbic acid, will happen if a higher pH-value is adjusted.^[38-39] This leads to a situation where the reduction potential of the added reducing agent becomes stronger than the galvanic reaction rate ($G_{\text{red}} > G_{\text{gal}}$).

However, even with the knowledge the realization is not that simple. Various experiments regarding the adjustment of the pH in this work have shown that not only the pH, but also other parameters like the precursor addition rate, the concentrations of the precursor and reducing agent, and the seed amount play major roles for a successful synthesis with a silver core.

For the present work, the syntheses of core-shell nanoparticles with a silver core were optimized to be used for several particle morphologies. The particle cores were previously generated and purified. The shell was realized by adjusting the pH to a value of 12 and an addition of a certain amount of ascorbic acid. The particles were stabilized using PVP and characterized using different methods. The present chapter will only refer to the data obtained for silver-gold core-shell systems. However, every conclusion and observation made can be adopted to syntheses with other shell-materials like palladium.

5.1 Synthesis of silver nanoparticles from glucose

After the synthesis the particles were characterized using HAADF, EDX mapping, DCS, DLS, UV/Vis spectroscopy and the ζ -potentials of the particles were determined. As a verification of the core-shell structure as well as to investigate the composition of the system, the inner structure was disclosed by HAADF and EDX maps.

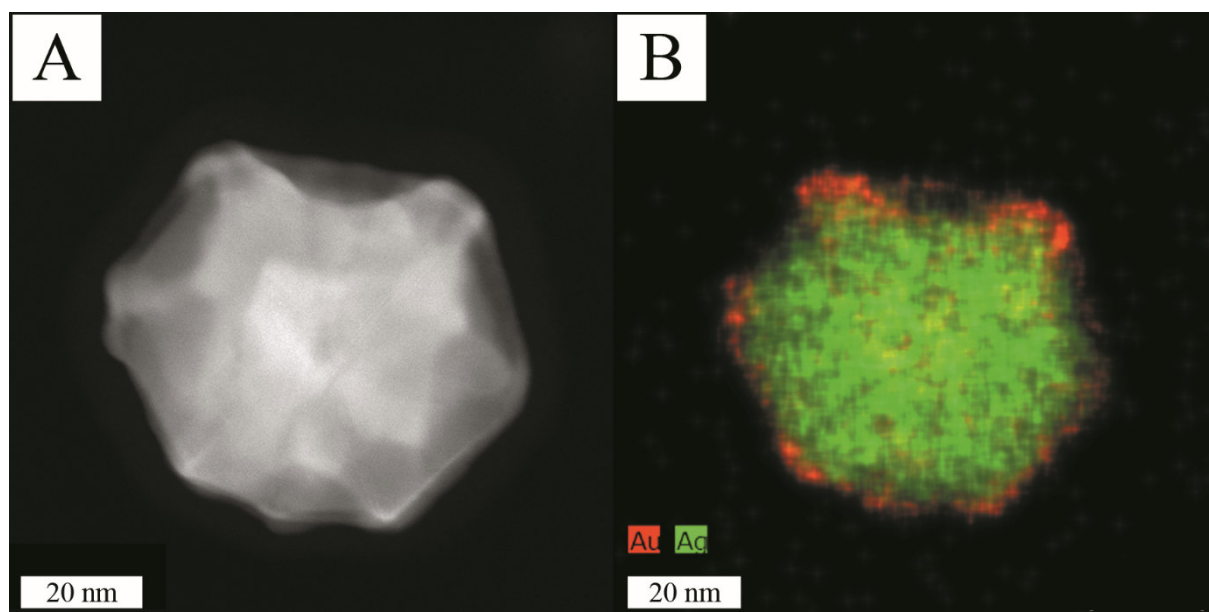


Fig. 36: HAADF image (A) and the corresponding EDX map (B) of a silver-gold nanoparticle. The EDX map shows a shell of gold around the silver core (seed were generated by the glucose synthesis).

The Fig. 36 shows a representative HAADF image and an EDX map of a particle obtained from a synthesis with gold. The nominal molar ratio of the synthesis was 90:10 (Ag:Au). The particles have maintained their morphology. No holes or hollow regions can be observed in the structures. This indicates that no galvanic replacement has taken place during the reaction. The outer shell of the displayed particle consists of gold atoms only. The grown shell is relatively thin compared to the particle diameter. Furthermore, the shell is not completely developed. Digital measurements revealed a shell thickness around 3-5 nm in the dominant regions. The higher accretion of atoms in those regions might be related to distinct crystallographic surfaces of the nanoparticle. Those crystallographic surfaces have different free surface energies because the energy corresponds to the density of atoms as well as the amount of bonds. Therefore, the surface energy of the low indexed planes will be differing as follows^[82]: $\gamma_{\{111\}} < \gamma_{\{100\}} < \gamma_{\{110\}}$ and gold atoms will preferably grow on the (110)-plane to lower the system energy. Furthermore, the used capping agent PVP complexes the (100) lattice planes and induces a directional growth in (111) and (110) direction. This might be an explanation for the irregular surface growth.^[142-143]

The EDX map shows a composition of 87:13 (Ag:Au). The distribution for the mapped particles might differ to the nominal composition but is still in good agreement with the used ratio.

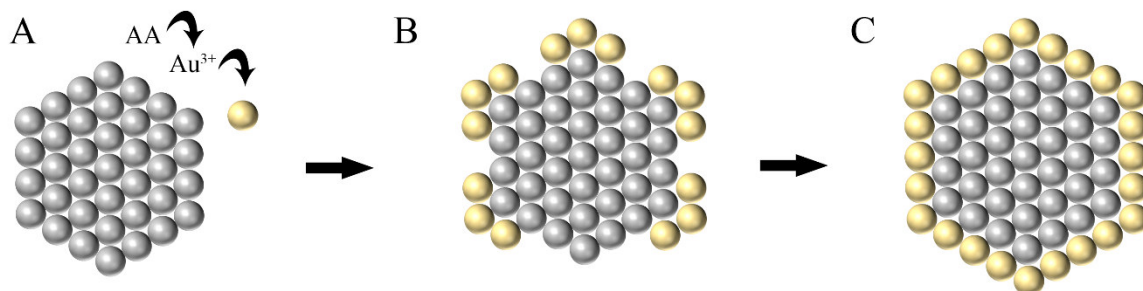


Fig. 37: Schematic mechanism of the growth of silver-gold core-shell spheres. Silver atoms are marked with a gray color. Gold atoms are marked with a yellow color. AA abbreviates ascorbic acid.

The optimized reaction conditions prevent an occurrence of a galvanic replacement reaction and therefore lead to a reduction of gold only by the reducing agent ascorbic acid (AA) (Fig. 37, A). The formed gold atoms will now start to grow on the present seeds of silver. Since the concentration of gold atoms is always below the supersaturation, the spontaneous formation of gold nuclei does not occur.^[76] This will lead to an onward growing formation of the shell. The accretion of gold atoms to the particle surface will be affected by the diverse energies of the different lattice planes and the complexation of the (100)-facets by PVP. Therefore, the shell starts a directional growth at specific regions of the particle surface (Fig. 37, B). If enough gold is added to the reaction mixture, a fully developed shell will be formed (Fig. 37, C).

To confirm the colloidal stability and the size of the particles in dispersion, the synthesized silver-gold core-shell systems were examined with DLS. Additionally, the ζ -potential was determined.

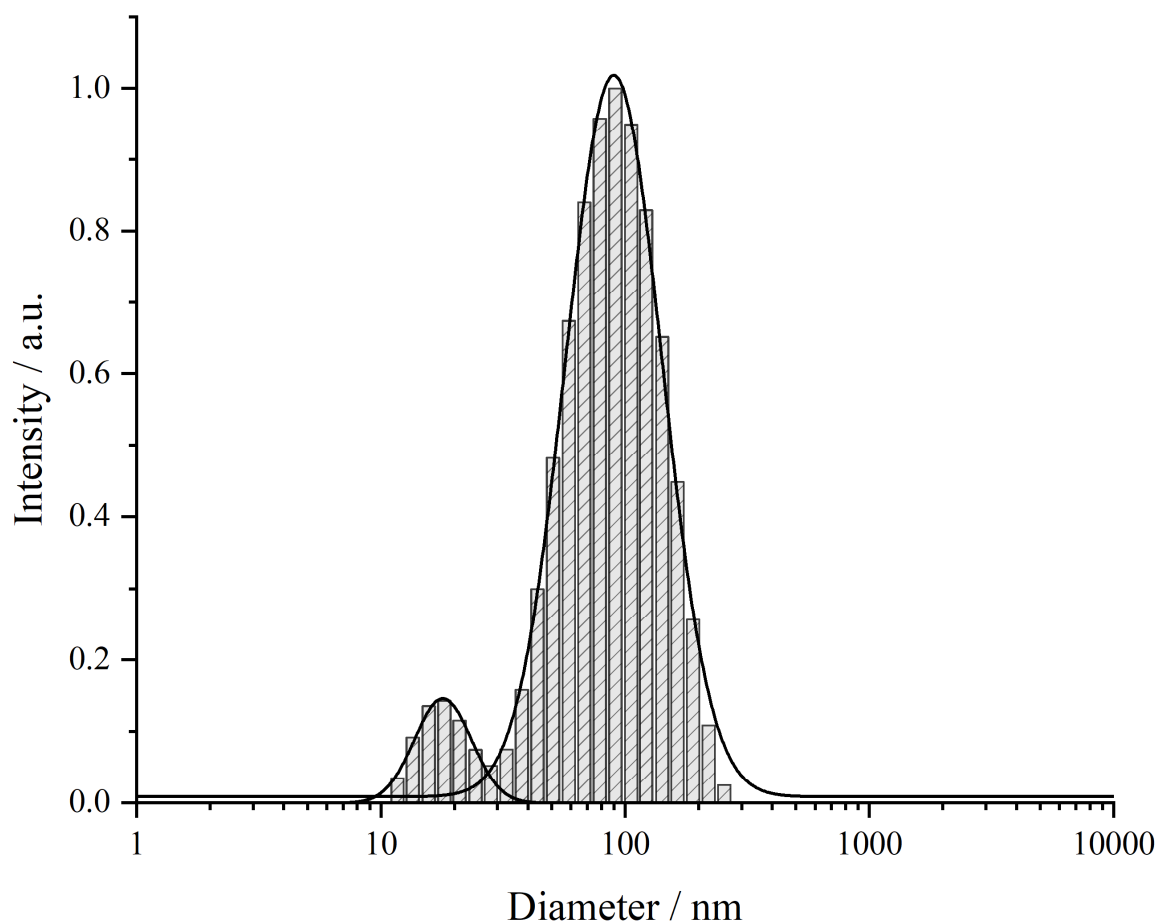


Fig. 38: Representative DLS measurement of the silver-gold core-shell particles obtained from experiments with glucose particles as seeds. The graph depicts the Intensity (a.u.) as a function of the diameter (nm).

Taking a closer look, the data reveals that the DLS measurement results in two different sized fractions (Fig. 38). The first fraction is 97 nm sized with a standard deviation of 43 nm. The second fraction has a size of $19 \text{ nm} \pm 6 \text{ nm}$. The existence of the second fraction is based on the anisotropic nature of the used seeds, which was discussed in detail in chapter 5.1.1. Depending on the fact that the particles only develop a thin gold shell and no galvanic replacement takes place, the seeds keep their anisotropic nature. The overall size increase compared to the used seeds is 5 nm. The bimodal distribution prevents the use of the size distribution by number due to the measuring principle and the corresponding overestimation of the smaller fraction.

The PDI of the measurement is 0.26 and shows a monodisperse system with no agglomeration or aggregation effects. To further investigate the size distribution in ultra-pure water, the particles were measured by disc centrifugation sedimentation (DCS).

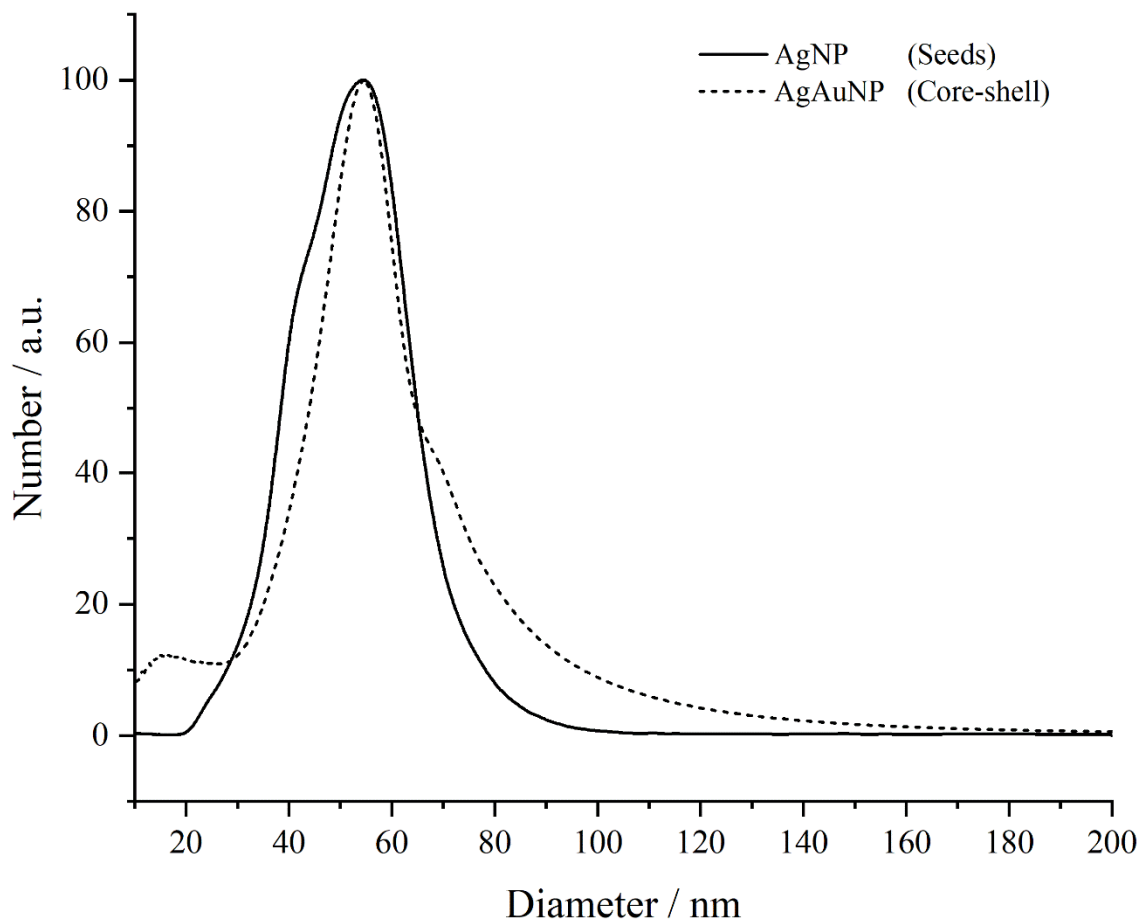


Fig. 39: DCS measurement of the obtained AgAu core-shell system in comparison with the size obtained by DCS for the used seeds. The number (a.u.) is shown as a function of the diameter (nm).

The size distribution obtained for the AgAu core-shell particles shows a high similarity to the measurement of the used seeds. To determine the maximum size and the standard deviations of both systems, Gaussian-fits were applied. The maximum size determined for the core-shell systems is at 56 nm with a standard deviation of 12 nm. Those values are quite comparable to the seeds (53 nm \pm 12 nm). A size increase of only 3 nm is observed. This is in good agreement with the data obtained from the DLS. The PDI is 0.22 and therefore the same as the PDI of the seeds. Already the HAADF image had shown that the formed shell has only a small influence on the size of the particles. Therefore, all performed techniques are in good agreement. A direct

5.1 Synthesis of silver nanoparticles from glucose

comparison between the core-shell system and the used seeds of all applied size determining methods is shown in Table 7.

Table 7: Size distribution, standard deviation (SD), polydispersity index (PDI) and the coefficient of determination (COD) for the applied Gaussian-fits for all size determining methods. The table shows a comparison between the obtained core-shell particles and the used seeds.

Method	SEM		DLS		DCS	
	Ag	AgAu	Ag	AgAu	Ag	AgAu
Particles	Ag	AgAu	Ag	AgAu	Ag	AgAu
Diameter / nm	50	60	92	97	53	56
SD (σ) / nm	14	9	48	43	12	12
PDI	0.23	0.12	0.26	0.26	0.25	0.22
COD (R^2)	0.9848	0.9486	0.9968	0.9858	0.9788	0.9572

To investigate the optical properties of the obtained core-shell system, the particles were characterized using UV/Vis spectroscopy. The absorption of electromagnetic radiation by the surface of nanoparticles strongly depends on the surface composition as well as its size.

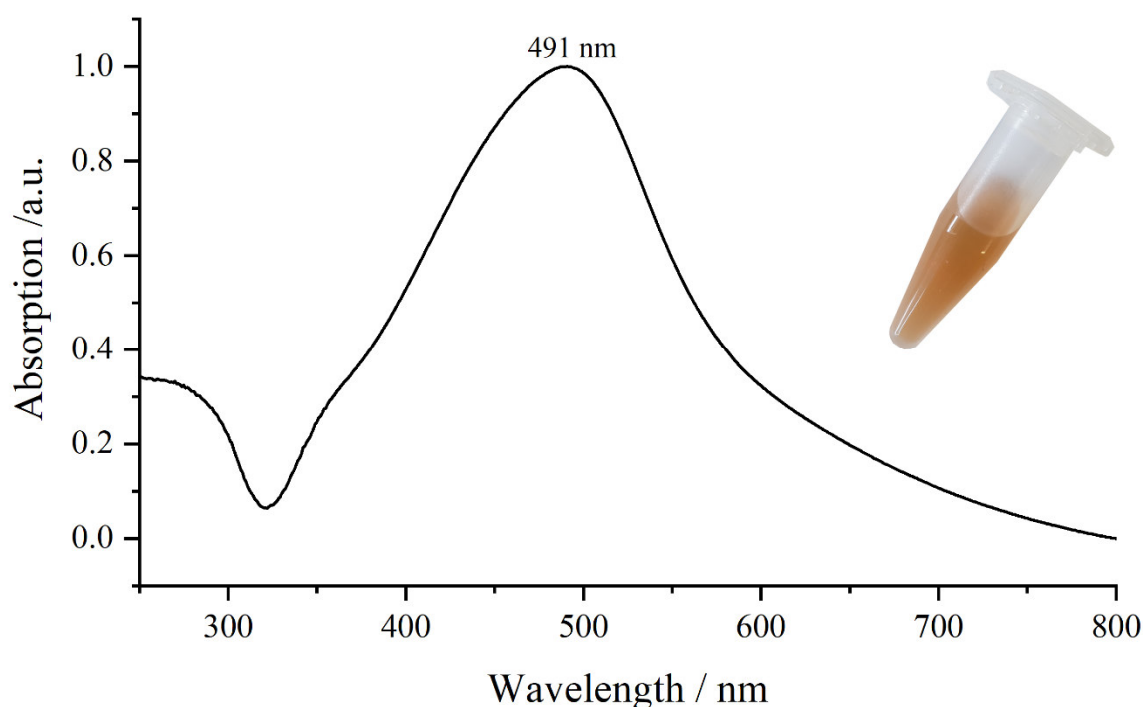


Fig. 40: UV/Vis spectrum obtained of the silver-gold core-shell particles synthesized with seeds from the glucose synthesis and an additional image of the actual sample. The absorption (a.u.) is shown as a function of the wavelength (nm).

The absorption maxima of silver particles in solution will experience a bathochromic shift when the particle diameter increases. The absorption of bimetallic particles based on gold and silver will differ depending on their composition. Alloyed particles containing more gold will show a

plasmon resonance shifted to the main gold absorption and silver richer particles will be more shifted to the main absorption peak of pure silver.^[27-28, 100] The synthesized core-shell particles show a relatively broad absorption band with a FWHM of 150 nm and a maximum absorption at 491 nm. The particles in dispersion therefore possess an orange color (see Fig. 40). Despite profound investigations regarding the literature, no UV/Vis spectra of spherical core-shell systems of silver-gold could be found. However, the comparison between the collected UV/Vis spectrum and alloyed particles of roughly the same size with a composition of 70:30 (Ag:Au) shows that the absorption band of the core-shell particles is much redder shifted even with a smaller amount of gold. The maximum absorption of the alloyed particle system already occurs at 436 nm.^[25] The core-shell system contains much more gold atoms on the particle surface and has therefore an absorption peak with a strong bathochromic shift compared to monometallic gold nanoparticles. Gold particles with a size of 60 nm show a surface plasmon resonance peak at 540 nm.^[81]

In summary, the data show that core-shell particles could be synthesized. In this process, the morphology of the seeds was maintained. Further, the investigations show that the particles have a high colloidal stability. The obtained data from DLS and DCS reveal that the particles do not aggregate or agglomerate. The optical properties of the particles are more gold-like than silver-like. A clear shift in absorption makes it possible to distinguish between core-shell and alloyed particles of the same elements and size by UV/Vis spectroscopy. Because of their high quality the synthesized particles could be used for dissolution experiments (compare chapter 5.4).

5.2 Synthesis of silver nanoparticles with sodium borohydride

As part of a cooperation, certain requirements were set to the synthesized particles described in this section. Those needed to be spherical, colloidal stable, functionalized with PVP, highly monodisperse and in a size range of 5-10 nm in diameter. Silver nanoparticles can be synthesized in a lot of different ways resulting in different shapes and sizes. Bottom up syntheses of those particles can either be performed in organic solvents (ethylene glycol (EG), oleylamin (cis-1-amino-9-octadecene, OAm))^[144], or in aqueous solutions. Depending on the additives and the reaction conditions, a quantity of different shapes and sizes can be realized.^[23, 142-143, 145-147]

However, the generation of small silver nanoparticles (3-6 nm) is often only performed to generate seeds as a preliminary state of certain morphologies.^[93, 148] These seeds provide no long-term stability due to their weak colloidal stabilization with trisodium citrate and are therefore not suitable for the asked requirements. In the literature, there are a few examples of syntheses regarding sizes around 5-10 nm.^[149-150] Unfortunately, those syntheses do not meet the former formulated requirements either.

For the present work, silver nanoparticles were synthesized using sodium borohydride as a reducing agent. The stabilization of the system was realized using PVP as capping agent. After the purification by ultracentrifugation, the particles were characterized using several analytical methods like HRTEM, DLS, DCS, TG, XRPD and electron diffraction.

5.2.1 Characterization of silver nanoparticles from sodium borohydride

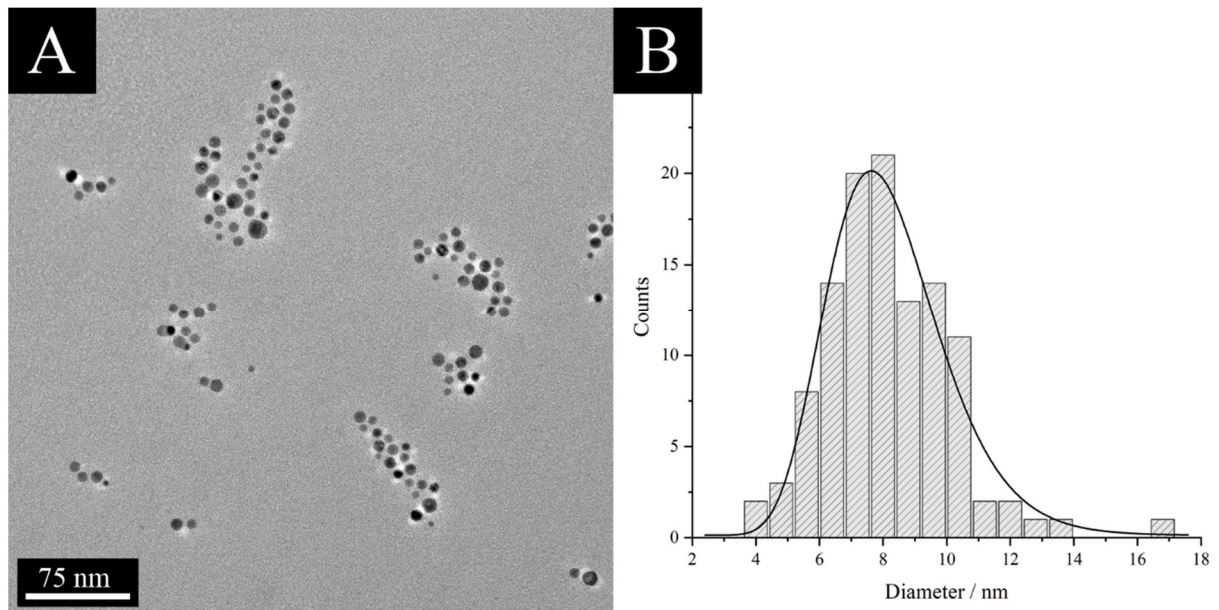


Fig. 41: HRTEM overview image of silver nanoparticles synthesized with sodium borohydride (A) and the corresponding histogram (B).

Figure 41 (A) shows a HRTEM image of the synthesized particles. The images were taken in cooperation with Dr. Marc Heggen and Dr. Kataryna Loza in the Ernst-Ruska-Zentrum of the research centre in Jülich with an accelerating voltage of 300 kV. All observed particles show a spherical morphology. No branched structures or anisotropic particle morphologies are observed. The sizes of the particles were digitally measured resulting in a histogram which was fitted using a Gauss function (Fig. 41, B). Concerning the size and monodispersity, the particles show a narrow size distribution with a mean size of 7.9 nm and a standard deviation of ± 1.8 nm. The measurement results in a PDI of 0.28 and confirms that a monodisperse system was generated. To further investigate the crystallographic structure of single particles, images with higher magnification were taken.

It deeper consideration, two kinds of particles can be identified. On the one hand there are particles which appear to be single crystalline (Fig. 42, A), on the other hand there are particles with massive numbers of stacking faults and clear visible grain boundaries (Fig. 42, B). To quantify the amount of those stacking faults, the areas of 20 particles as well as the areas of the visible stacking faults were digitally measured. This measurement resulted in an 83.7 % to 16.3 % ratio of regularly grown area to stacking faults.

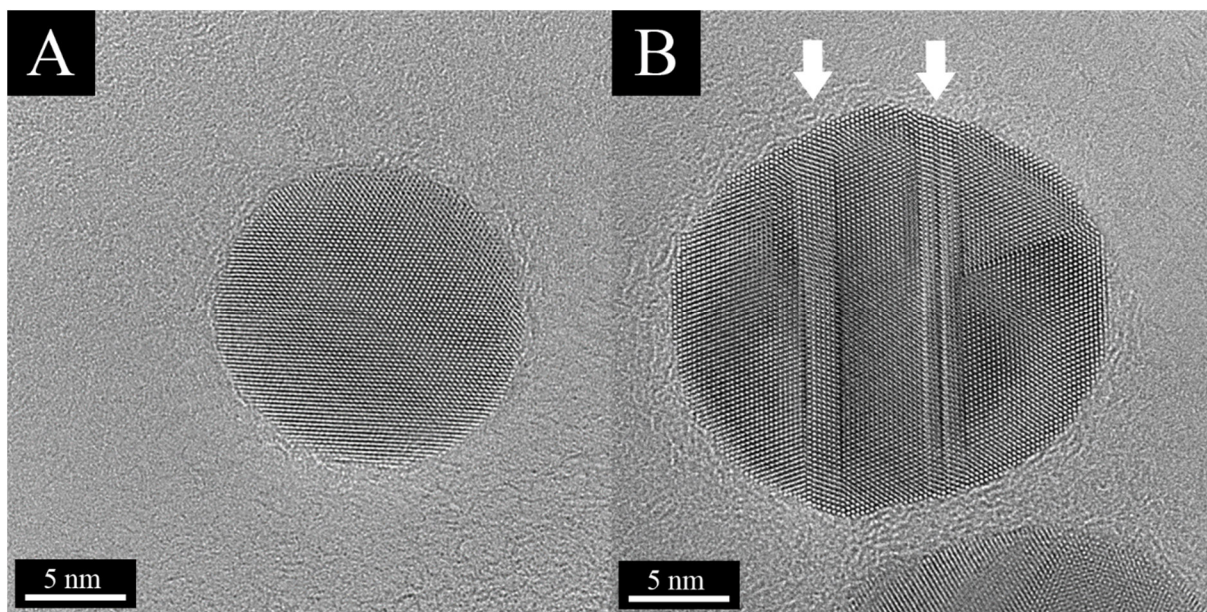


Fig. 42: HRTEM image of a single crystalline silver nanoparticle synthesized with sodium borohydride (A) and a particle of the same sample with a high amount of stacking faults marked with white arrows (B).

These stacking faults might occur because of the brisk crystallization using sodium borohydride. Based on the fact that sodium borohydride with its substantial reduction potential^[151-154] will lead to a high concentration of silver atoms, the nucleation and crystallization of the particles is a tremendous fast process. The crystallization will therefore be driven kinetically. Fast crystallization processes likely lead to copious stacking faults.

To further analyze the crystallographic properties and the phase purity, an XRPD pattern of a freeze-dried sample was measured. The procedure was carried out with a step width of $0.01^\circ \text{ min}^{-1}$ to obtain a high resolution. Besides that, the sample was prepared on a silicon wafer to reduce background scattering of the sample holder. As a part of the performed phase analysis, the sample showed the expected reflexes of the fcc-phase of the silver lattice. All five lattice plane reflections in the selected 2θ range, which was measured with copper radiation, could be associated to the literature (compare Table 8).

Table 8: Assignment of the measured crystallographic silver reflex positions to the literature (ICDD-PDF database (00-004-0783)).

Reflex position measured $2\theta / ^\circ$	Reflex position Literature $2\theta / ^\circ$	Lattice plane (hkl)
38.182	38.110	(111)
44.249	44.281	(200)
64.509	64.438	(220)
77.503	77.464	(311)
81.671	81.529	(222)

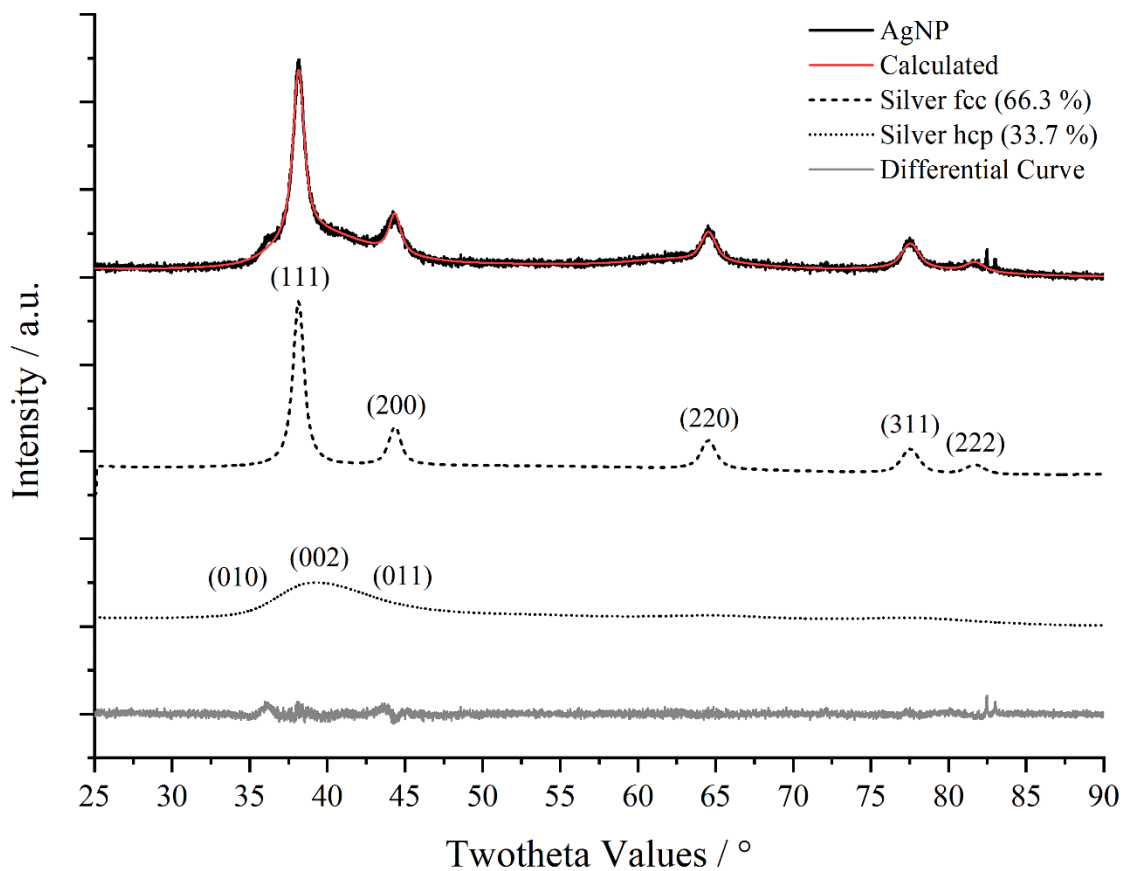


Fig. 43: Rietveld refined XRPD pattern of particles synthesized with sodium borohydride. The pattern shows all expected reflexes of the fcc-phase. Additionally, the previous described stacking faults can be identified as shoulders of the (111)-lattice plane reflex. A model fitting of an additional hcp phase leads to a quantification of the defect amount.

During the Rietveld refinement, using only one phase to fit the data was not sufficient. This was due to shoulders of the (111)- and the (200)-reflex which are caused by the large numbers of stacking faults (Fig. 43). To obtain better refinement results, a second phase of silver needed to be used to model the anisotropic reflex shape. Similar approaches have already been carried out in the literature using an hcp-phase which is quite common in silver particles.^[155-159] Even if it is not totally clear that the crystallite defects develop a strict hcp-phase, the modeling during the refinement leads to good results. A bct-phase, which can also cause peak shoulders, was also taken into consideration, but led to worse results during the refinement.

The introduction of an hcp-phase during the refinement also allows a quantification of the percentage appearance of stacking faults. The obtained ratio of 66.3 % to 33.7 % of the two phases strongly differs to the graphically obtained data (83.7% to 16.3 %). Since HRTEM images only provide 2D datasets, a deviation to the obtained powder data was expected. Furthermore, the graphical data was evaluated from 20 particles, hence the statistical relevance of the powder data is much higher. The strongest deviation from the fcc-phase is in the region between 32-47° and therefore located on the (111) and (200) reflexes. Exactly in this region, the reflexes with the highest intensity of the hcp-phase are located (compare Table 9).

Table 9: Overview of the silver hcp reflex positions between 32-45° from Rietveld refinement in comparison to the literature. The literature reflex position of the hcp-phase were calculated using single crystal diffraction data.^[112]

Reflex position observed $2\theta / ^\circ$	Reflex position Literature $2\theta / ^\circ$	Lattice plane (hkl)
36.205	36.077	(110)
37.883	37.520	(002)
40.967	40.462	(101)

The shifted of the calculated reflex positions to higher twotheta values shows a decrease of the lattice parameters. This observation is well documented for metallic nanoparticles. The lattice parameter will decrease with a reduction of lattice planes.^[160-161] The space groups as well as the calculated lattice parameters and cell volumes of the two observed silver phases are shown in Table 10.

Table 10: Space groups, calculated cell volumes and lattice parameter for the hexagonal (hcp) and cubic (fcc) phases derived from Rietveld refinement.

Phase	Space group	LP ($a / \text{Å}$)	LP ($c / \text{Å}$)	Cell volume / Å^3
Ag fcc	<i>Fm-3m</i>	4.0816 (5)	-	67.996 (25)
Ag hcp	<i>P63/mmc</i>	2.8615 (82)	4.7067 (18)	33.377 (233)

Crystallographic defects, like they are observed, are energetically disfavored because they increase the lattice energy of the system. These defects might therefore decrease or completely vanish during a thermal treatment. Applying addition thermal energy, the system should undergo a phase transition leading to a high crystalline fcc-phase which is thermodynamically favored compared to the hcp-phase. To gain a deeper insight into the thermal behavior of the sample, a DSC measurement with freeze dried particles was performed. For the measurement, 4.8 mg of material were heated to 350 °C with a heating rate of 2 K/min. The final temperature was then maintained for 30 minutes. Afterwards, the sample was cooled down to room

temperature with a cooling rate of 2 K/min. The experiment was performed under atmospheric oxygen. The obtained thermogram shows a small increase of energy density in the beginning of the measurement between 25-75 °C. This might be caused by desorption of gases or the evaporation of maintained solvent or moisture. After this point, an exothermic peak arises in the measurement. It develops over a temperature range from 75-257.4 °C (Fig. 44).

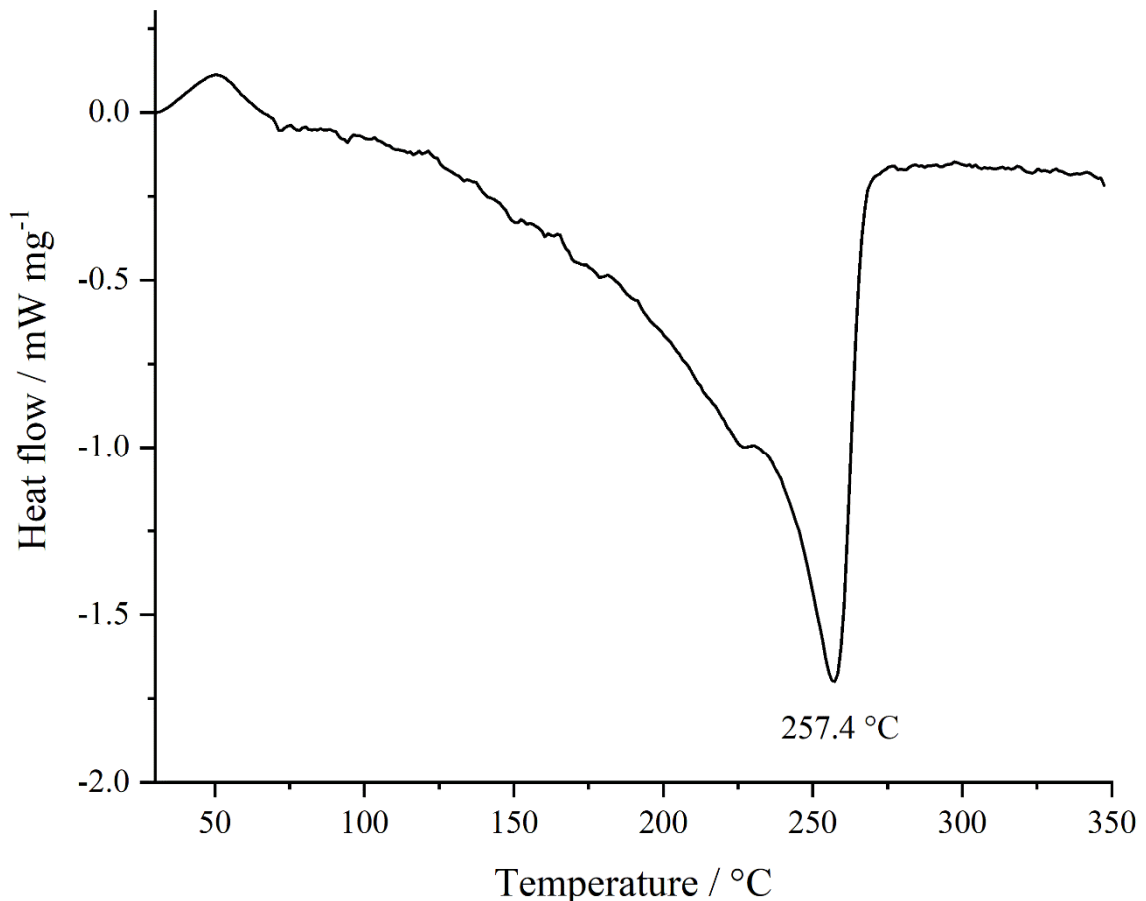


Fig. 44: DSC measurement of silver nanoparticles under atmospheric conditions. The heat flow (mW mg^{-1}) is shown as a function of the temperature ($^{\circ}\text{C}$).

After the maximum at 257.4 °C is reached, the heat flow returns to the starting level. This endothermic peak course indicates a phase transition. The integration of the peak leads to the quantity of specific energy released in the process. The whole specific energy obtained from integration is -282.7 kJ/mol (-2621 J/g) and therefore corresponds to a mass related overall energy release of 12.58 J. This exothermic event is related to the recrystallization of the former described stacking faults as well as the increase of the crystallite size and the partial decomposition of PVP. To confirm the indicated transition to a pure fcc-phase, the sample was measured via XRPD afterwards (Fig. 45).

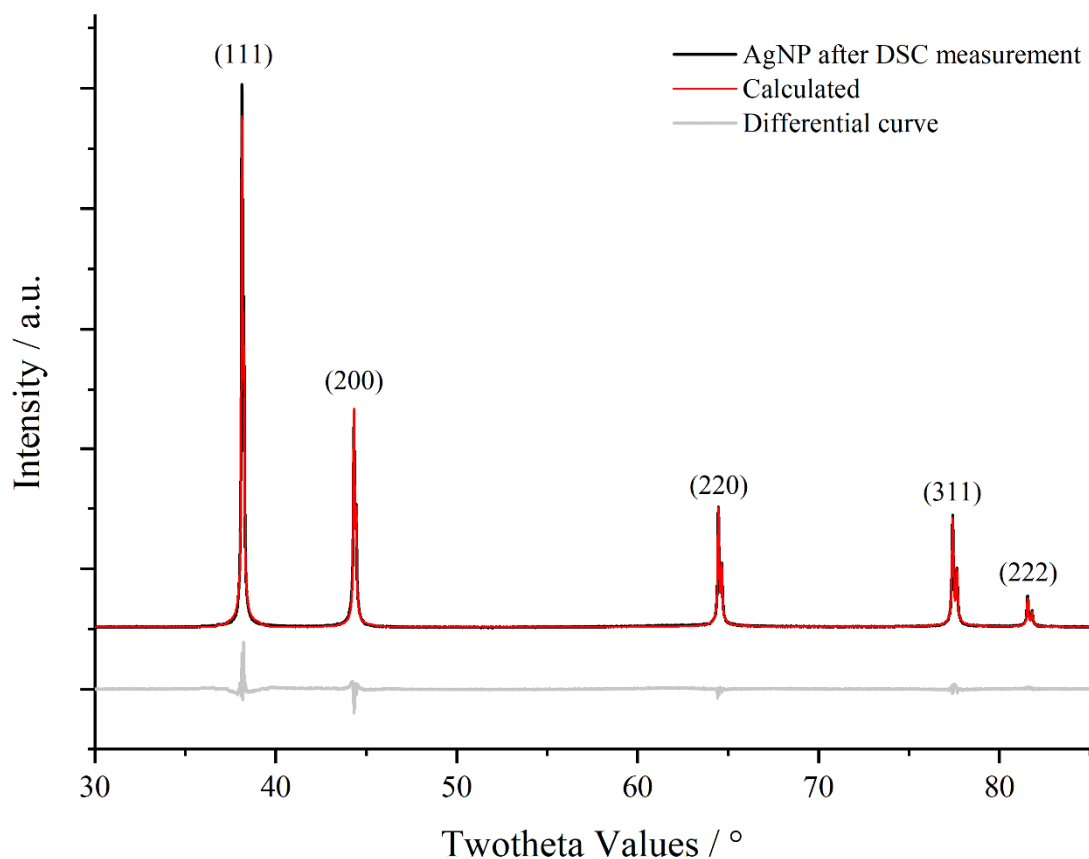


Fig. 45: XRPD pattern obtained from particles after DSC treatment under atmospheric conditions ($K\alpha_2$ radiation was not stripped). The sample shows no shoulders, but an increase of the crystallite size which confirms the assumptions based on the thermogram obtained from DSC.

The powder pattern obtained after the heat treatment reveals a pure fcc-phase without any foreign phases or reflex shoulders. This shows that the shoulders, which were observed before, were caused by the occurring hcp-phase which has passed through a solid-solid phase transition to the more stable fcc-phase. Furthermore, crystallite sizes (CS) and lattice parameters (LP) could be obtained from the refinements of the sample before and after heat treatment (Table 11).

Table 11: Comparison of the lattice parameter and the crystallite size of silver nanoparticles before and after the DSC heat treatment under atmospheric conditions. The lattice parameter of bulk silver for a better comparison was obtained from a single crystal measurement at room temperature.

Sample	LP_{fcc}	CS_{fcc}	CS_{hcp}
AgNP	4.0837 (6)	7.5 (1)	1.2 (1)
AgNP after DSC	4.0865 (2)	128.8 (15)	-
Bulk Silver	4.0860 ^[113]	-	-

As can be seen, the lattice parameter from the sample before the heat treatment is smaller than the bulk lattice parameter. The effect that the lattice parameter of nanostructures is reduced, is mostly explained by the surface effect and has been described using several models.^[162-164] The sample which was heat treated has a lattice parameter comparable to the bulk material. The crystallite size has grown significantly which results in much sharper reflexes with higher count rates and a dramatic change of the reflex profile (Fig. 46).

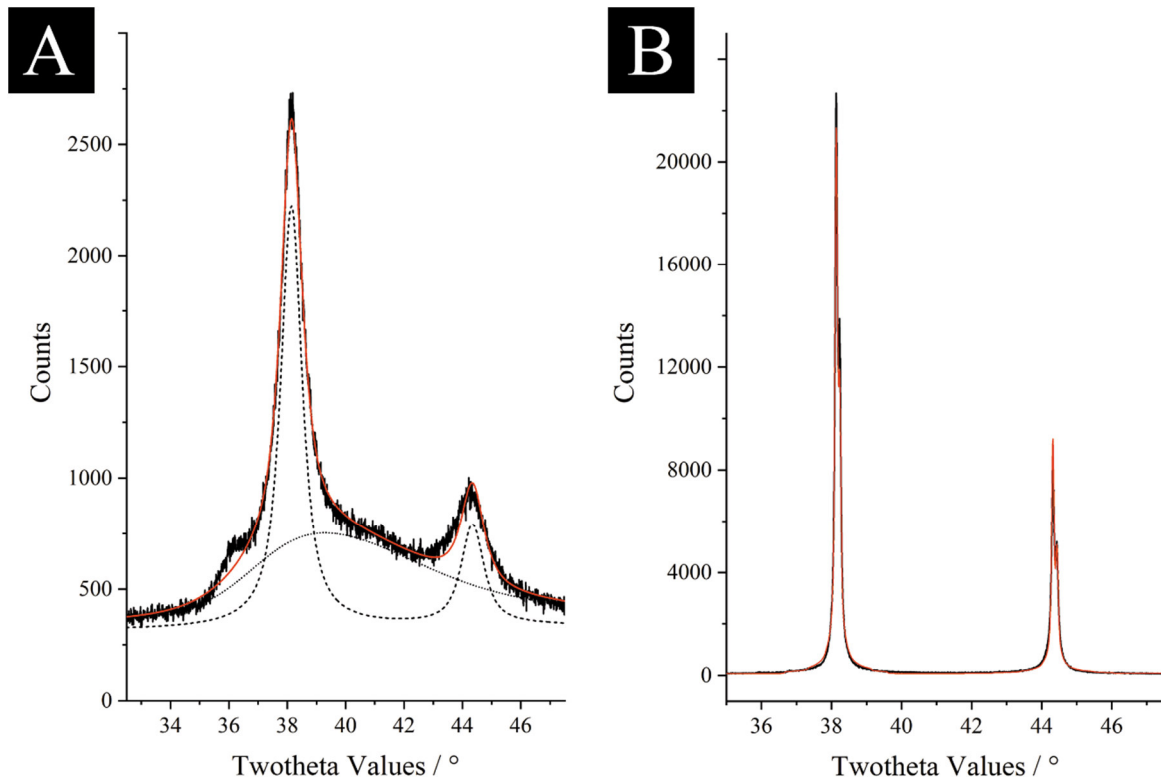


Fig. 46: Reflex profile of the (111) and (200) crystallographic planes obtained from XRPD before (A) and after (B) the heat treatment in the DSC (patterns are not $K\alpha_2$ stripped).

To confirm that the stacking faults are constructed of a hexagonal phase, electron diffraction patterns were created from HRTEM images by Dr. Kateryna Loza. Furthermore, this technique was used to distinguish between the stacking faults and the normally occurring fcc-phase. The red and yellow squares in Figure 47 show spots from which electron diffraction patterns were generated. Inside the red square the lattice plane orientation in Z-direction is (110) corresponding to an fcc-silver lattice. The atom-atom distance in the crystallographic (111) direction is 2.31 Å and hence in good agreement with the literature value (2.36 Å). Furthermore, the investigation of the atom-atom distance in (002) lateral dimension is with 2.04 Å the same as the literature value (2.04 Å).^[112]

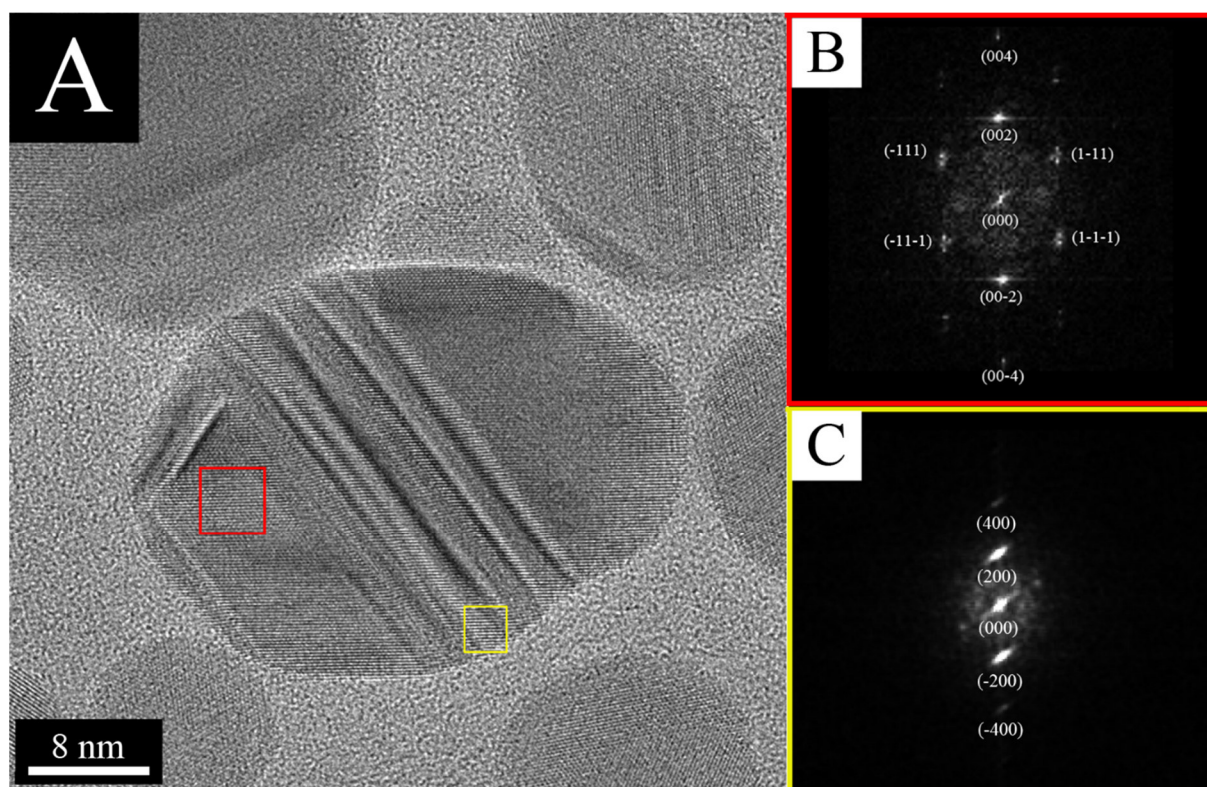


Fig. 47: HRTEM image of a single silver nanoparticle obtained from the synthesis with sodium borohydride (A). The colored squares indicate the spots where the electron diffraction patterns were generated. The red color shows the electron diffraction pattern of the fcc-phase (B) and the yellow square leads to a diffraction pattern of the formed stable hcp-phase (C).

The investigation by electron diffraction of the stacking faults (yellow squares, Fig. 47) shows that the orientation in Z-direction is (011) and corresponds to an hcp silver lattice. The assumption of an hcp-phase by XRPD could consequently also be proved by HRTEM. To strengthen the result, the atom-atom distances in (1-11) and (-100) direction were measured. The measurements resulted in $d_{1-11} = 1.38 \text{ \AA}$ and $d_{-100} = 2.50 \text{ \AA}$ and are consequently slightly different than the values from literature ($d_{1-11} = 1.40 \text{ \AA}$, $d_{-100} = 2.54 \text{ \AA}$). To visualize the recrystallization of the stacking faults, *in-situ* heating HRTEM experiments, which were carried out with a wildfire system (DENSSolutions), were performed by Dr. Kateryna Loza. With this system, real-time imaging of thermal dynamics can be performed. The sample is applied on a graphene thin film via drop casting and can be heated with integrated electrodes. The experiments were carried out with a heating rate of 10 K/min. A single particle was imaged in 50 K steps. In theory, a visualization over the whole temperature range is possible but silver nanoparticles recrystallize under application of energy by the electron beam. To minimize this beam damage, a segmented measurement technique was chosen.

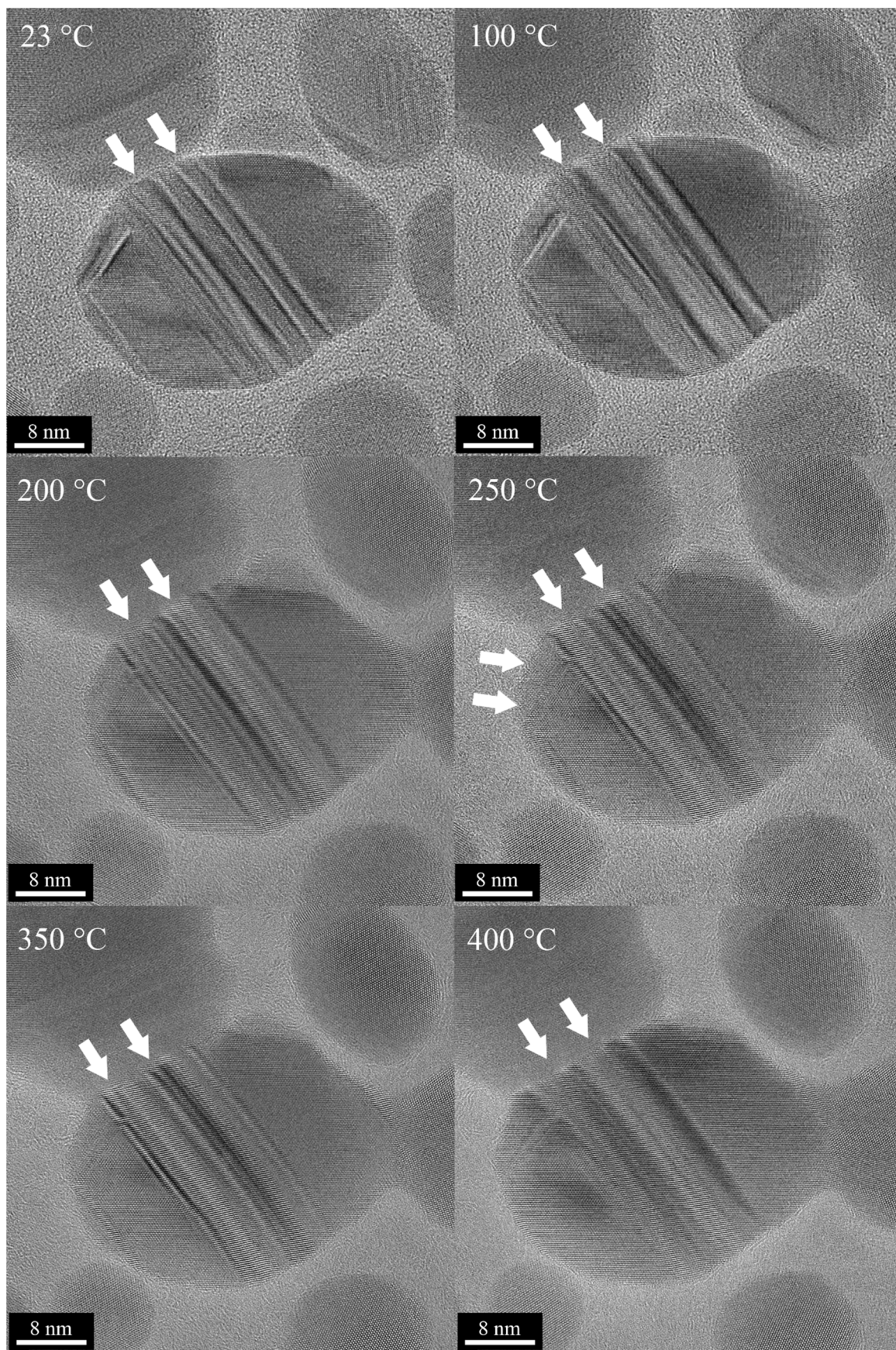


Fig. 48: HRTEM images of a silver nanoparticle at various temperatures visualizing phase transitions and changes in crystallinity of the stacking faults. The white arrows mark intense stacking faults.

The areas that are described correspond to the white arrows of the images taken at different temperatures in Figure 48. The increase of temperature has a direct effect on the observed stacking faults. The clear visible grain boundaries at room temperature (23 °C) are starting to get more diffuse when the temperature is increased to 100 °C. If the temperature is even further increased to 200 °C, the grain boundaries become less visible. The observed defects start to fuse together resulting in larger connected areas of an hcp-phase on the particle surface. If a temperature of 250 °C is applied, smaller energetically disfavored defects start to vanish. At a temperature of 350 °C grain boundaries become more visible again indicating a starting phase transition in the described areas. The DSC indicated that the recrystallization process should have been completed with an applied temperature of 257.4 °C (compare Fig. 44), but even at 400 °C the particle still show less dominant defects with an hcp-structure. To confirm that the hexagonal phase is still present, electron diffraction patterns at 400 °C were generated. This investigation showed that both phases (hcp, fcc) with identical orientations to the ones at room temperature are still present. To explain the occurring discrepancies between both methods (TEM, XRPD) a second DSC under inert conditions with a higher comparability to the used vacuum during HRTEM was performed.

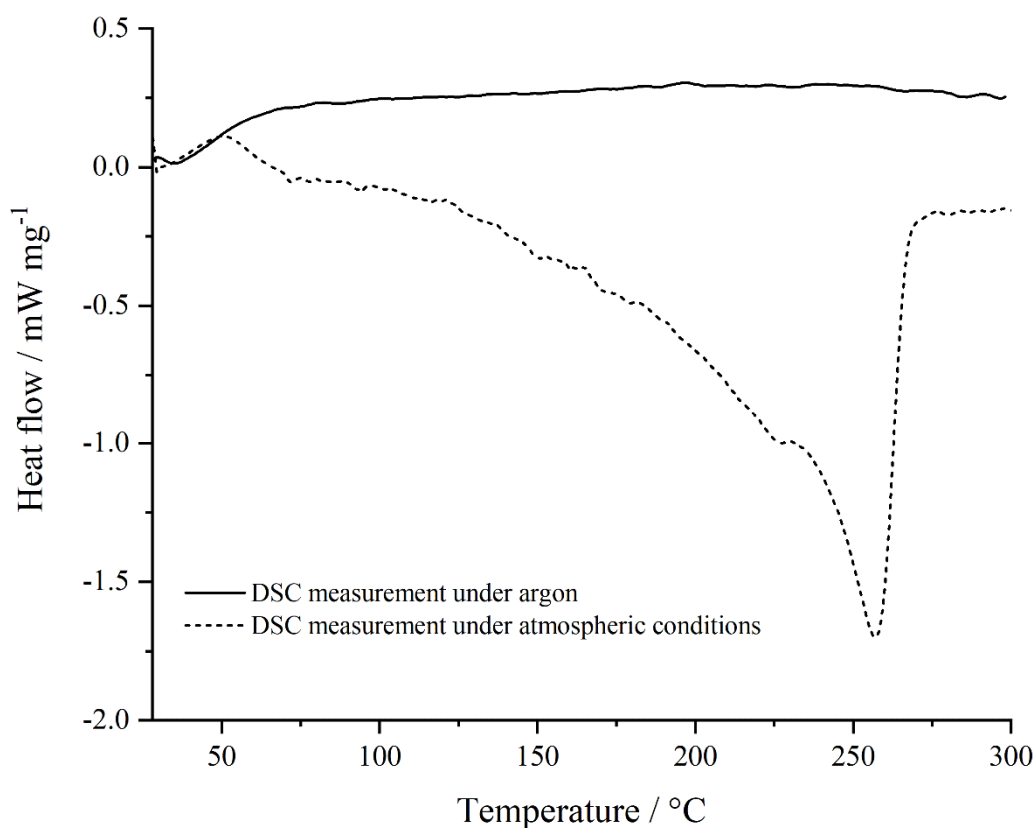


Fig. 49: DSC measurement of silver nanoparticles under atmospheric conditions in comparison with a measurement under argon. The heat flow (mW mg⁻¹) is shown as a function of the temperature (°C).

The DSC measurement under inert conditions strongly differs from the one performed under atmospheric conditions. The exothermic peak with a maximum at 257.4 °C is not observed. Furthermore, the energy density curve shows a flat linear course which indicates that only small changes inside the sample occur. This observation is in better agreement with the data from the *in-situ* heating experiment received with the high-resolution transmission electron microscope. As part of this work, the thermal decomposition of PVP was investigated by thermogravimetric measurements. These experiments have shown that a mass loss of ~31 % in the temperature range between 25-350°C is observed in oxygen. The decomposition is completed after a temperature of 610 °C is reached. Consequently, the endothermic peak in the DCS experiment under oxygen might be partially caused by the decomposition of PVP. This leads to the conclusion that the recrystallization is directly correlated to oxygen species as well as an intact polymeric functionalization. To confirm this assumption a XRPD measurement of the sample after thermal treatment in argon atmosphere was prepared.

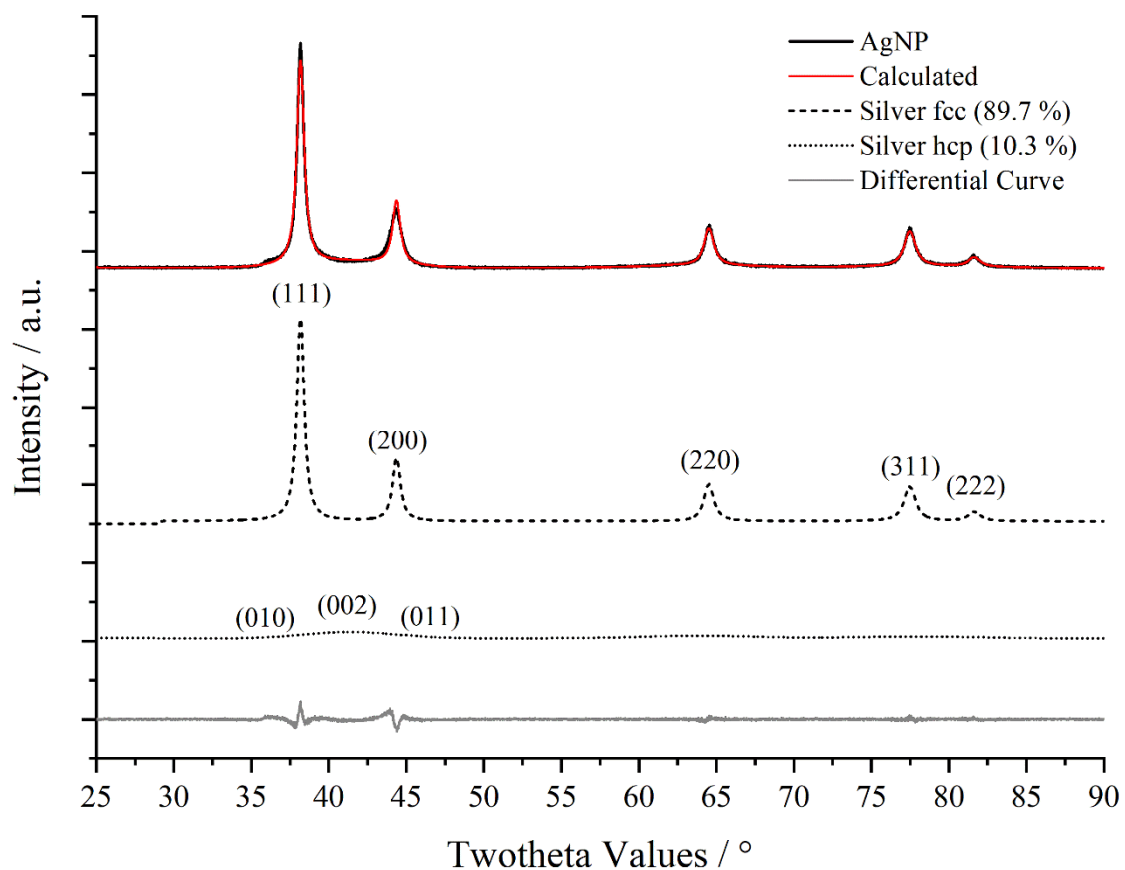


Fig. 50: XRPD pattern obtained from AgNP after thermal treatment under argon atmosphere ($K\alpha_2$ radiation was not stripped). The sample still shows shoulders with a decreased intensity and a small increase of the crystallinity.

In comparison to the diffractogram of the particles obtained from the heat treatment in presence of oxygen (Fig. 45), the peak profile obtained from the inert atmosphere still shows shoulders in the region between 34-48°. Since the shoulders are caused by the hcp-phase, a complete phase transition did not occur. Please note that both measurements were performed with different samples. Hence the amount on stacking faults can vary. The increase in crystallinity is not that dominant in comparison to the sample which was thermally treated in the presence of oxygen. For a better overview of the data the crystallite sizes and the lattice parameters calculated by Rietveld refinement are compared.

Table 12: Comparison of the lattice parameters and the crystallite sizes of silver nanoparticles before and after heat treatment under normal and inert atmosphere in the DCS.

Sample	LP_{fcc}	CS_{fcc}	CS_{hcp}
AgNP	4.0837 (6)	7.5 (1)	1.2 (1)
AgNP after DSC (Oxygen)	4.0865 (2)	128.8 (15)	-
AgNP after DSC (Argon)	4.0842 (5)	22.1 (5)	1.3 (2)

The increase of crystallite size shows that the particles still undergo a sintering process, but the process is drastically decreased. For a better overview of the stacking faults the (111)- and (200)-reflexes of the heat-treated sample (argon) and a sample as synthesized are depicted (see Fig. 51).

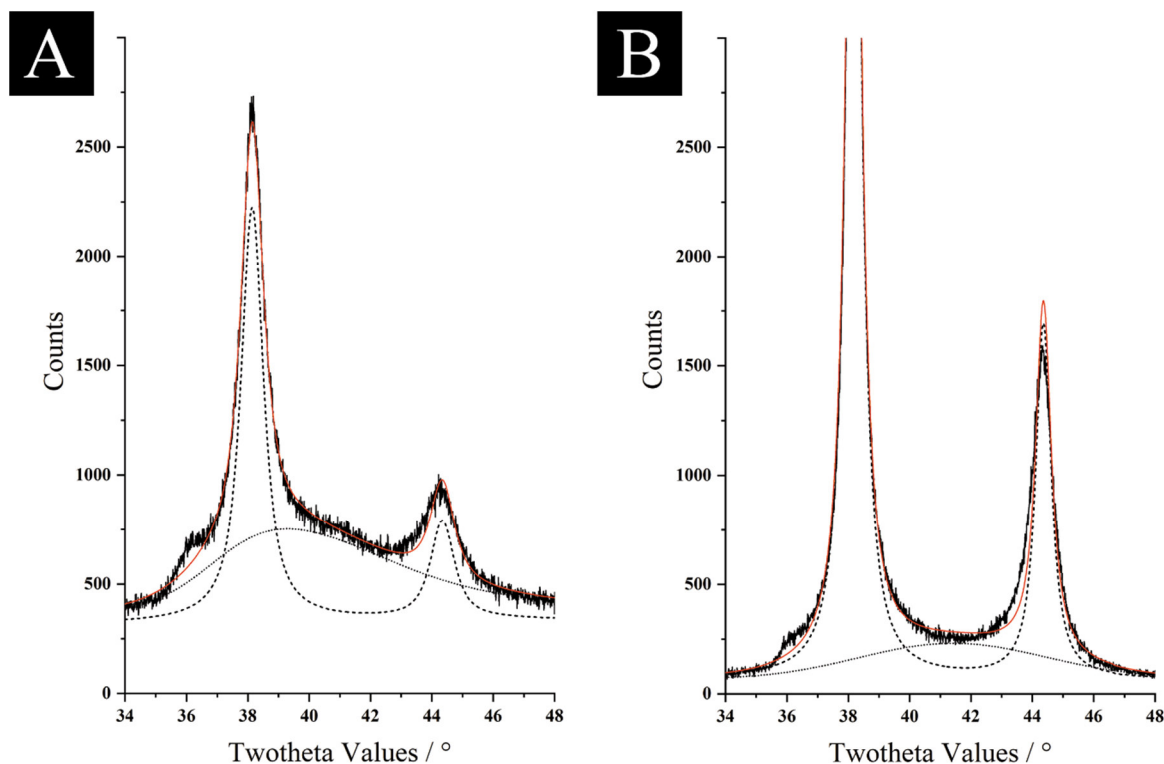


Fig. 51: Reflex profile of the (111) and (200) crystallographic planes obtained from XRPD after (B) and before (A) heat treatment under inert conditions (patterns are not $K\alpha_2$ stripped).

The colloidal stability of the system was verified using several methods. The silver nanoparticles have been characterized using DLS, DCS, UV/Vis and by determination of the ζ -potential.

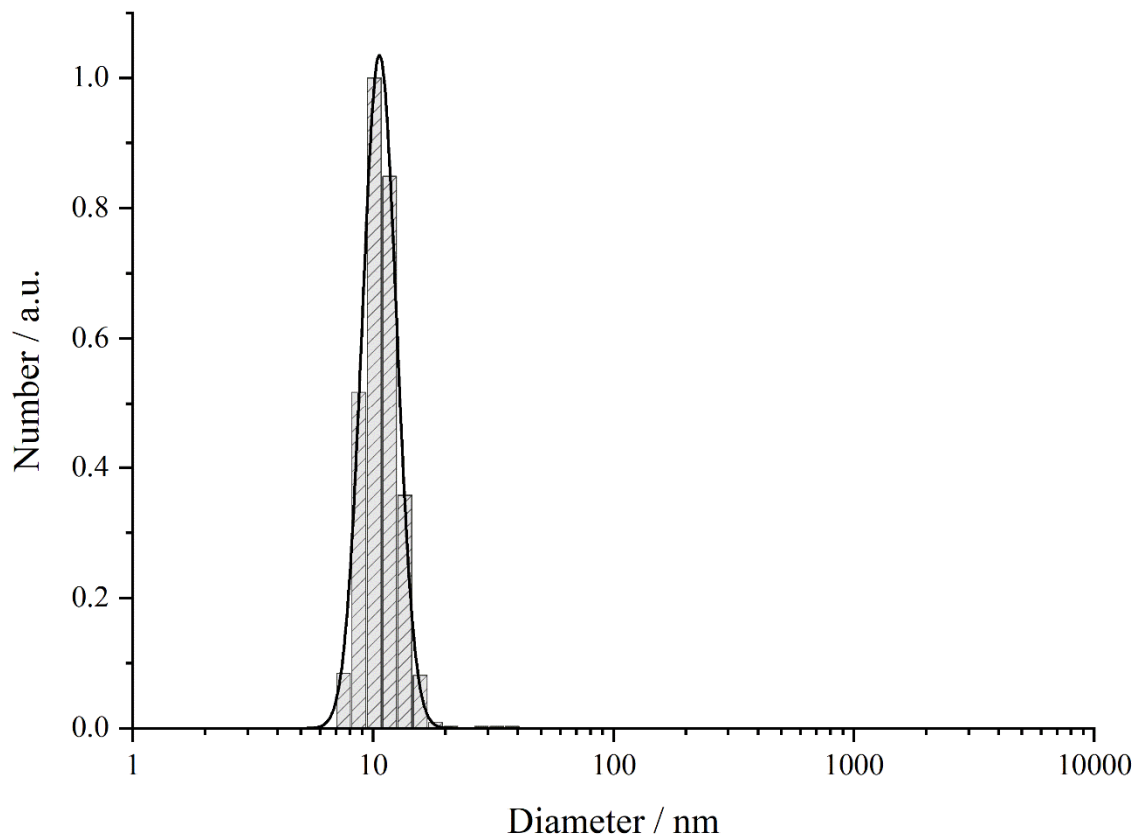


Fig. 52: DLS measurement of silver nanoparticles. The graph shows the number (a.u.) as a function of the particles diameter (nm).

To analyze the obtained data from DLS, the dataset was fitted using a Gaussian function (Fig. 52). The determined size by DLS is 10.9 nm with a standard deviation of ± 1.8 nm. The obtained PDI for the measurement is 0.16 and confirms a monodisperse particle system. The size increase compared to the histogram of the HRTEM images (Fig. 41, A+B, (8.0 ± 1.9) nm) can be explained by the principle of the method. The DLS measures the metallic core including the hydrodynamic shell by measuring a time dependent scatter intensity caused by Brownian motion and will therefore result in overestimated particle sizes (compare Chapter 3.1). The narrow size distribution obtained from DLS also confirms that there are no agglomerates. The ζ -potential of -15 mV can be interpreted by an absorption of PVP as well of trisodium citrate on the particle surface. In the beginning of the synthesis, the seeds are stabilized using only trisodium citrate to inhibit the growth.

The addition of the neutral polymer PVP, which absorbs with the free electron pair of the oxygen, only replaces the trisodium citrate partially during trans-functionalization. Therefore, the particles are stabilized with a combination of steric and electrostatic effects. The particles size in ultra-pure water has further been investigated by DCS (Fig. 53).

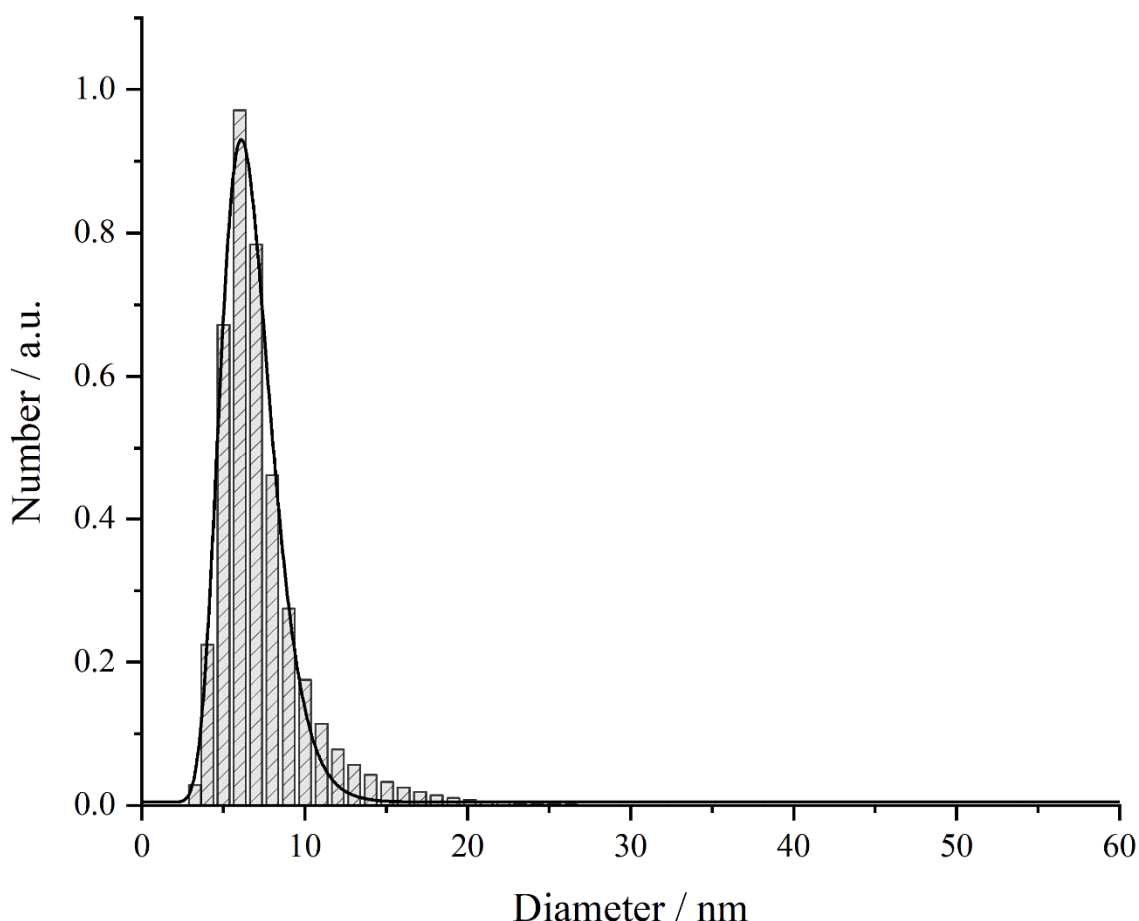


Fig. 53: DCS measurement of silver nanoparticles synthesized with sodium borohydride. The graph shows the number (a.u.) as a function of the particles diameter (nm). The whole measurement was performed up to 200 nm but cut for clarity. In the cutout region, no other signals were observed.

The mean size determined by DCS is 6.5 nm with a standard deviation of ± 1.7 nm. The values were received by a Gaussian peak profile to fit the data. DCS uses the relative density to calculate the particle size. Since the particles have a stabilizing polymeric shell, the real density will be lower in comparison to the literature value of the metal density used in the program. As a result, the particle size is underestimated. The PDI obtained by the fit is 0.22 and is therefore comparable to the DLS data.

With all limitations of each method taken into consideration, the obtained sizes from the applied methods are in good agreement. All measurements confirm that the particles obtained from the reduction with sodium borohydride lead to well defined particles having a narrow size distribution.

Table 13: Size distribution, standard deviation, polydispersity index (PDI) and the coefficient of determination (COD) for the applied Gauss-fits for all size determining methods.

Method	TEM	DLS	DCS
Size / nm	8.0	10.9	6.5
Standard deviation (σ) / nm	1.9	1.8	1.7
PDI	0.22	0.16	0.22
COD (R^2)	0.9578	0.9988	0.9914

Optical properties of silver nanoparticles can be investigated using UV/Vis spectroscopy. The obtained spectra contain a lot of information regarding the examined system. The size increase of silver particles leads to a red shift in the main absorption band. Furthermore, a broad absorption band can indicate a polydisperse systems. Anisotropic particles will lead to multiple absorption bands caused by different surface plasmon energies related to the free path length of the plasmons. Also, the functionalization of the particles must be taken into consideration, since adsorbed molecules will increase the surface electron density.

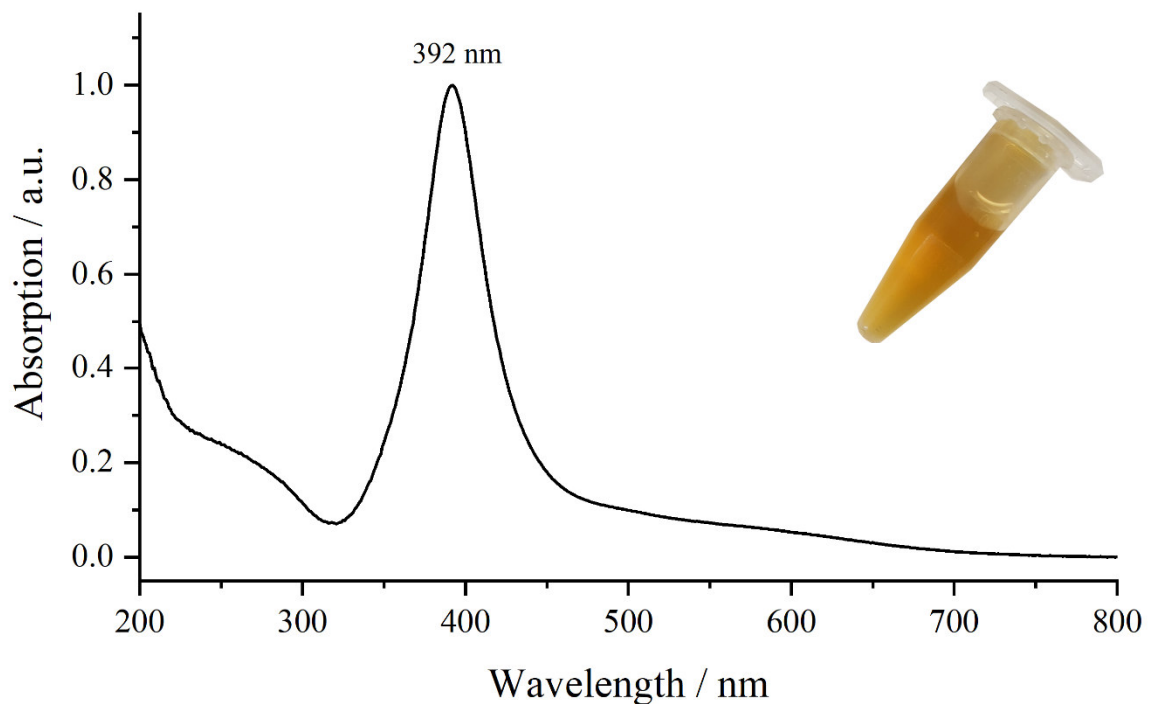


Fig. 54: UV/Vis spectrum of silver nanoparticles synthesized with sodium borohydride and an additional image of the actual sample. The graph depicts the absorption (a.u.) as a function of the wavelength (nm).

The main absorption band for the synthesized particles appears at 392 nm. Comparable particles in the same size range from literature have shown similar absorption maxima. Silver nanoparticles capped with PEI (polyethyleneimine) or PPA (peracetic acid) show both absorption bands around 410 nm.^[149-150] Nonetheless, these syntheses result in much broader peaks. The FWHM of the absorption band regarding the sodium borohydride synthesis is only 47 nm and therefore confirms the narrow size distribution already described by TEM, DCS and DLS.

To investigate the yield of the synthesis, Ag^+ contents for several experiments were determined. Further investigation which were carried out by *Dr. Jens Helmlinger* had shown that a reduction of silver cations with glucose results only in a yield of 1.3 %.^[91] This makes this synthesis inefficient and uneconomical. To quantify the amount of silver for the described synthesis, AAS measurements of three different fractions were taken. Namely the supernatant, the pellet and the suspension of nanoparticles. The pellet, which develops after centrifugation, cannot be dispersed because the particles aggregate irreversibly. This could be shown by UV/Vis spectroscopy (Fig. 55) as well as DCS measurements (not shown). Due to this fact, the synthesis undergoes a certain loss of silver.

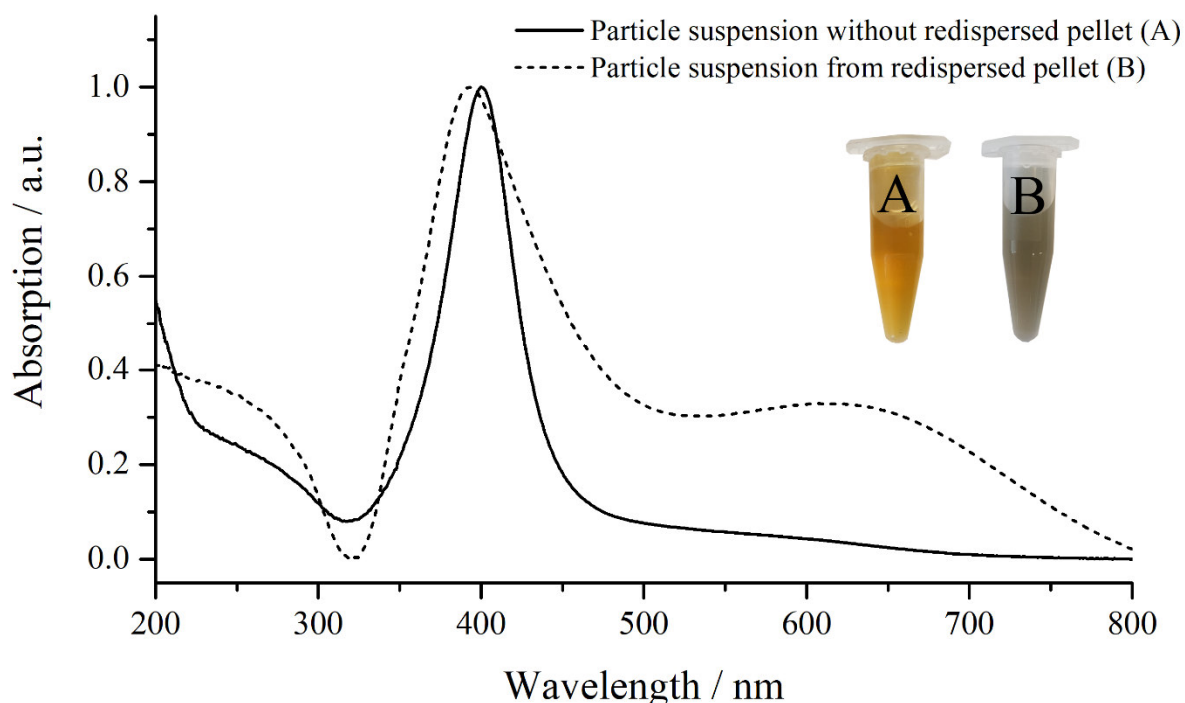


Fig. 55: UV/Vis spectra of silver nanoparticles with and without dispersed pellet. The graph depicts the absorption (a.u.) as a function of the wavelength (nm).

The supernatant after centrifugation remains yellow-colored, which indicates particles that did not sediment. The silver precursor amount used differs slightly with every investigated synthesis but was an average of 18 mg silver nitrate resulting in a theoretical total silver nanoparticle amount of 11.4 mg.

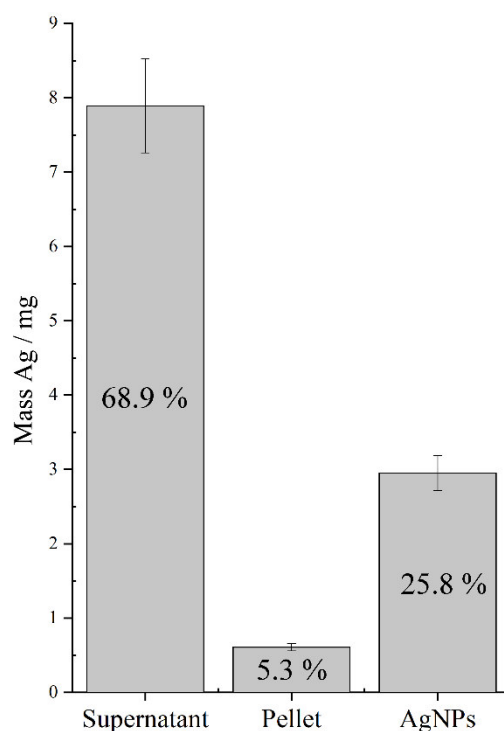


Fig. 56: Silver mass (mg) of the different investigated fractions and the corresponding percentages obtained from AAS.

After the complete purification process an overall silver content of 3.0 mg could be isolated in the particle suspension. This leads to a yield of 25.8 % and hence to a nearly 20 times higher yield than obtained from the glucose synthesis. Most of the silver content is lost in the supernatant. This might be reduced by longer centrifugation times or higher rotation speeds but would also lead to broader size distributions of the system. Thus, the purification method is suitable for this synthesis.

Table 14: Comparison between the yields of the glucose synthesis and the synthesis with sodium borohydride.

Synthesis	Theoretical mass of silver / mg	Experimental mass of AgNP /mg	Yield / %
Sodium borohydride	11.4	3.0	25.8
Glucose ^[91]	318.0	4.2	1.3

5.2.2 Reproducibility and long-term stability

Silver nanoparticle synthesis show often a lack of reproducibility throughout the literature. This observation was detailed in the work of *Dr. Jens Helmlinger*.^[91] To verify the reproducibility of the sodium borohydride synthesis, the first successful 22 experiments were monitored by DCS measurements (Table 15).

Table 15: Maximum size, standard deviation, PDI as well as the average size and averaging deviation of those values. 22 synthesis using sodium borohydride as reducing agent were validated. The data was obtained using Gaussian fits.

Synthesis number	Size / nm	Standard deviation (σ) / nm	PDI
004	7.3	± 1.6	0.21
005	9.6	± 2.7	0.27
006	8.2	± 2.2	0.25
007	9.8	± 2.4	0.24
008	9.5	± 2.2	0.22
009	9.1	± 2.4	0.25
010	8.9	± 1.9	0.20
011	8.5	± 2.8	0.30
012	11.0	± 3.4	0.29
013	9.5	± 2.6	0.26
014	8.9	± 1.9	0.20
015	9.3	± 3.3	0.33
016	9.8	± 2.7	0.26
017	10.8	± 3.2	0.28
018	7.6	± 2.0	0.25
019	7.5	± 2.0	0.26
020	6.3	± 1.6	0.25
021	7.4	± 2.0	0.26
022	6.5	± 1.6	0.24
023	6.5	± 1.7	0.25
024	6.5	± 0.8	0.13
025	6.8	± 1.4	0.20
026	8.8	± 2.0	0.21
Average size	8.4	± 2.2	0.24
Standard deviation	± 1.2	± 0.5	0.03

The absence of the syntheses 001-003 is due to optimizations of the experimental conditions. Therefore, these syntheses resulted in particle distributions with broad peak profiles and were only to develop and improve the synthesis. The experimental description is based on the synthesis 004. From the data in Table 15, it can be seen that the synthesis has a high reproducibility resulting in particles with an average size of $8.4 \text{ nm} \pm 1.2 \text{ nm}$ and a PDI of 0.24. There are no strong deviations either in particle size nor PDI.

The long-term stability of the particles was confirmed by storing two particle aliquots of the same sample with a concentration of 50 $\mu\text{g/mL}$ for 1 month and for 2 years. The particles were measured with DCS as well as UV/Vis spectroscopy after the elapsed time. The concentration was chosen because the upper concentration limit for the silver content in biological tests is 50 $\mu\text{g/mL}$ at maximum.

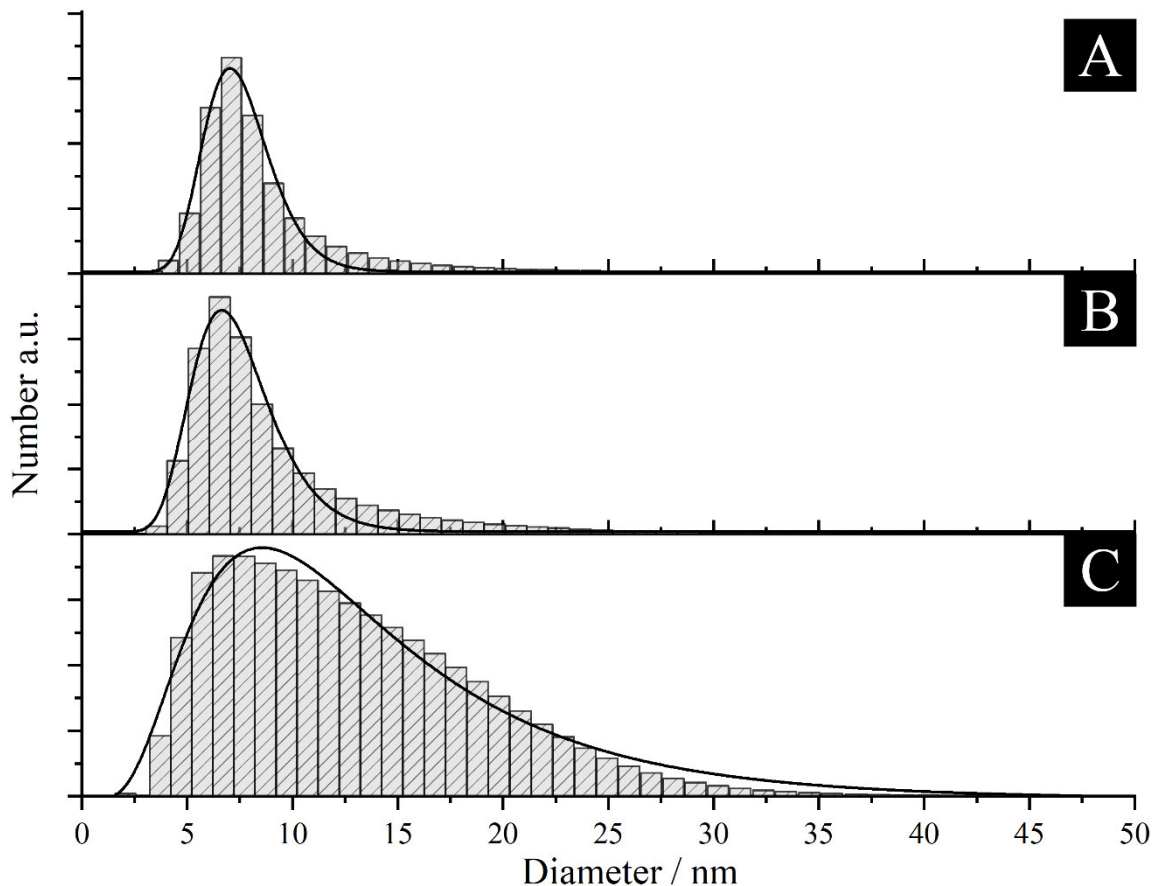


Fig. 57: DCS measurements of the sample 004 with a concentration of 50 $\mu\text{g/mL}$ after synthesis (A), after 4 weeks (B) and after 2 years (C). The number (a.u.) is depicted as a function of diameter (nm).

The comparison of the DSC measurements performed directly after the synthesis (Fig. 57, A) and after storage for 4 weeks (Fig. 57, B) show no difference in size or distribution. The mean size for the particles directly after synthesis is $7.4 \text{ nm} \pm 1.7 \text{ nm}$ whereas the size after 4 weeks is $7.2 \text{ nm} \pm 2.0 \text{ nm}$. The small deviation in the mean size is in the error of the method. Therefore, a storage of the particles obtained from the sodium borohydride synthesis are stable for at least 28 days. The investigation of the particles after 2 years shows a broad but unimodal size distribution with a maximum at 12.1 nm and a standard deviation of 9.2 nm. The PDI of the measurement is 0.59 and therefore reveals that the long storage time has created a

polydisperse system. The broad size distribution occurs because of Oswald ripening. Smaller particles are thermodynamically less stable than bigger particles since the free surface energy directly correlates with the specific surface area. One requirement for the occurrence is a low solubility of the particles in the used solvent.^[72] The small particles will dissolve and redeposit on larger crystals to minimize the system's energy. The overall particle size will therefore increase. In early stages of the ripening, the particle distribution will become more polydisperse. However, the particles maintained their color and no bigger aggregates or agglomerates were observed. The data obtained from DCS and UV/Vis spectroscopy is summarized in Table 16.

Table 16: Size distribution, standard deviation and polydispersity index (PDI) for the applied Gauss-fits for the DCS measurements. Additionally, the absorptions maxima obtained from UV/Vis spectroscopy are shown.

Time of measurement after the synthesis	Mean DCS diameter / nm	Standard deviation / nm	PDI	UV/Vis maximum absorption / nm
1 Day	7.4	1.7	0.22	392
28 Days	7.2	2.0	0.27	392
730 Days	12.1	9.2	0.59	402

The observed shift in plasmonic resonance for the sample after 730 days is correlated to the size increase of the particles. The investigations regarding the stability and the reproducibility show that the developed synthesis and the resulting product is perfectly suitable for biological experiments. The particles show a high stability over at least 28 days. Hence, the system could be used in different biological studies.

In summary the synthesis of silver nanoparticles with sodium borohydride leads to monodisperse particles within a size range of 5-10 nm. Investigations by HRTEM revealed that the particles possess a high amount of stacking faults. In addition, single crystalline particles can be observed. The defects consist of a stable hexagonal silver phase (hcp) which could be quantified by XRPD in combination with Rietveld refinement. The amount of stacking fault might vary but shows a mean percentage amount of 25-30 % and is consequently quite high. A study by DSC and XRPD could show that these defects undergo a phase transition when oxygen is present. The capping agent PVP will be decompose under heat treatment in an oxygen containing atmosphere and will hence not be able to protect the particle against sintering and recrystallization processes.

The recrystallization can partially be visualized by *in-situ* heating experiments via HRTEM which are performed under ultra-high vacuum. The number of defects still decreases, but a certain quantity of defects, which consist of the hexagonal silver phase, remain even after application of 400 °C and the corresponding thermal energy. This observation is confirmed by XRPD were the irregular peak profile of the (111) and (200) crystallographic reflexes still shows shoulders after a thermal treatment in inert atmosphere. These shoulders confirm the ongoing existence of the hexagonal phase.

The particles obtained from the synthesis show a high colloidal stability which was confirmed by narrow size distributions derived from DLS as well as DCS. The particles absorb visible light at 398 nm corresponding to their plasmonic resonance. The yield is an average of 25.8 % and hence much better compared to the synthesis of quasi spherical particles obtained from reduction with glucose (1.3 %). Long-term stability experiments have shown that the particles are stable in solution for at least 28 days and show a good reproducibility. The generated system hence fulfills the requirements set and could henceforward be used for biological experiments.

5.2.3 Core-shell particles based on the synthesis with sodium borohydride

The influence of bimetallic systems of the physical and chemical properties was already shown in the scope of this work. The incorporation of two metals in an alloy for example leads to an increase of the noble nature of silver. However, studies by Köller *et al.* have shown that sputtered dots of silver on a nobler substrate like gold can induce a sacrificial anode effect which will increase the silver ion release rate.^[25] Especially a system based on iridium sputtered with silver dots showed an enormous release of silver ions compared to systems based on gold or palladium.^[26]

Hence, a transfer of this principle into a nanoparticulate system to enhance the silver ion release rate was an aim of this work. The enhanced dissolution would overall decrease the concentration of needed particles in possible medical applications. Investigations of alloyed systems have shown that those particles are not suitable for this application due to the fact the standard potential of silver will rise in a case of an incorporation.^[28] Following from this, the release of silver ions would decrease due to the fact that the oxidizing species, which cause the ion release^[22], would be less efficient. Therefore, particles with a core-shell structure with only a thin incomplete shell were needed to generate a system where both metals remain in their pure phase and are still accessible. Those needed to be spherical, colloidal stable, functionalized with PVP, highly monodisperse and in a size range of 5-10 nm in diameter to compare them to the former synthesized monometallic silver particles. For further comparison and to perform dissolution kinetic experiments, several core-shell systems with gold and palladium as well as iridium were synthesized. Only syntheses with compositions of 90:10 and 80:20 (Ag:M) were performed since higher concentrations of metal will develop a full shell and therefore seal the silver core against oxidizing species. This would have been contra productive to our initial intention.

The particles containing iridium were synthesized using a one pot synthesis because the seed and growth mechanism could not be applied, since the precursor can not efficiently be reduced with ascorbic acid. Therefore, a modified version of the sodium borohydride synthesis was developed. Further, silver-palladium and silver-gold systems in different ratios were synthesized by the seed and growth approach which is described in detail in chapter 5.2.1. But different to these particles the used seeds were taken from the synthesis with sodium borohydride.

To characterize the bimetallic silver-iridium particles, different analytical methods such as HAADF, EDX mapping, DLS, DSC, UV/Vis spectroscopy and the determination of the ζ -potential were used. To confirm the spherical morphology and to determine the size of the metallic core HRTEM images were taken.

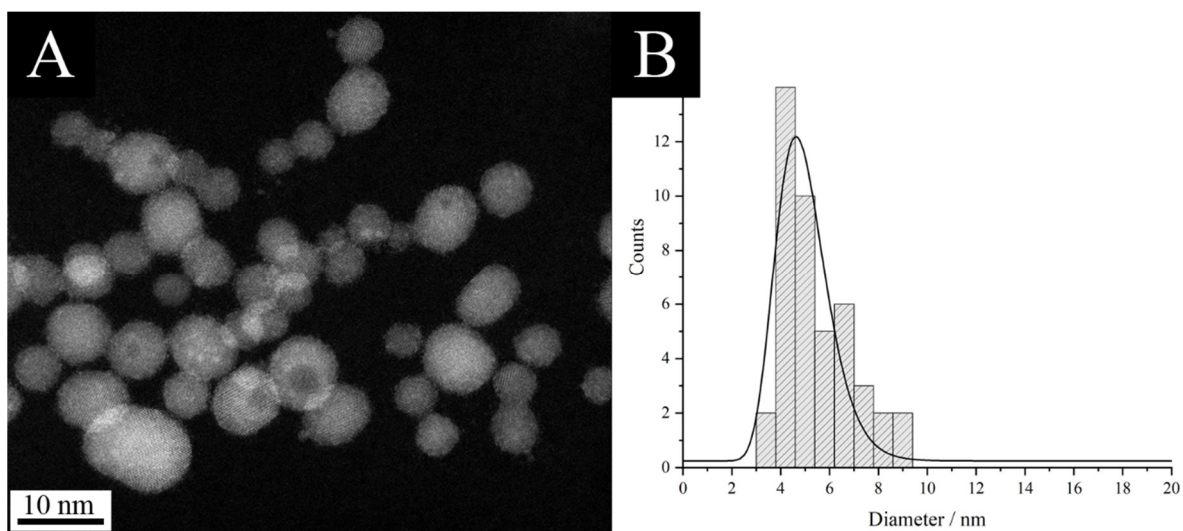


Fig. 58: HAADF of the obtained silver-iridium nanoparticles (A) and the corresponding histogram of the particle size (B). The graph shows the counted particles as a function of the particle size (nm).

The majority of observed particles shows a spherical morphology. Additionally, around ~20 % of the particles show a slightly elongated oval morphology with an aspect ratio of 1:1.3. The mean diameter derived from the histogram which was fitted with a Gaussian peak profile is 4.9 nm with a standard deviation of ± 1.1 nm (PDI = 0.17). The distribution results in a slightly smaller mean size compared to the monometallic silver particles. The early addition of iridium stabilizes the particles. This assumption was made due to different observations. The particles obtained from the bimetallic synthesis are much more stable than monometallic silver particles against beam damage in HRTEM while processing. Furthermore, the silver-iridium particles could be stirred over 20 hours. Particles from the monometallic synthesis will grow after this time if not purified and will reach a size of ~30 nm. This shows, that the particles are stabilized when iridium is incorporated in the system. Moreover, the resulting pellet after centrifugation could be dispersed without occurring aggregation. This treatment cannot be performed with the monometallic particles (compare chapter 5.2.1). All those observations confirm a more stable product as an outcome of the bimetallic synthesis. To further investigate the internal structure and the bimetallic nature, an EDX map of single particles was performed.

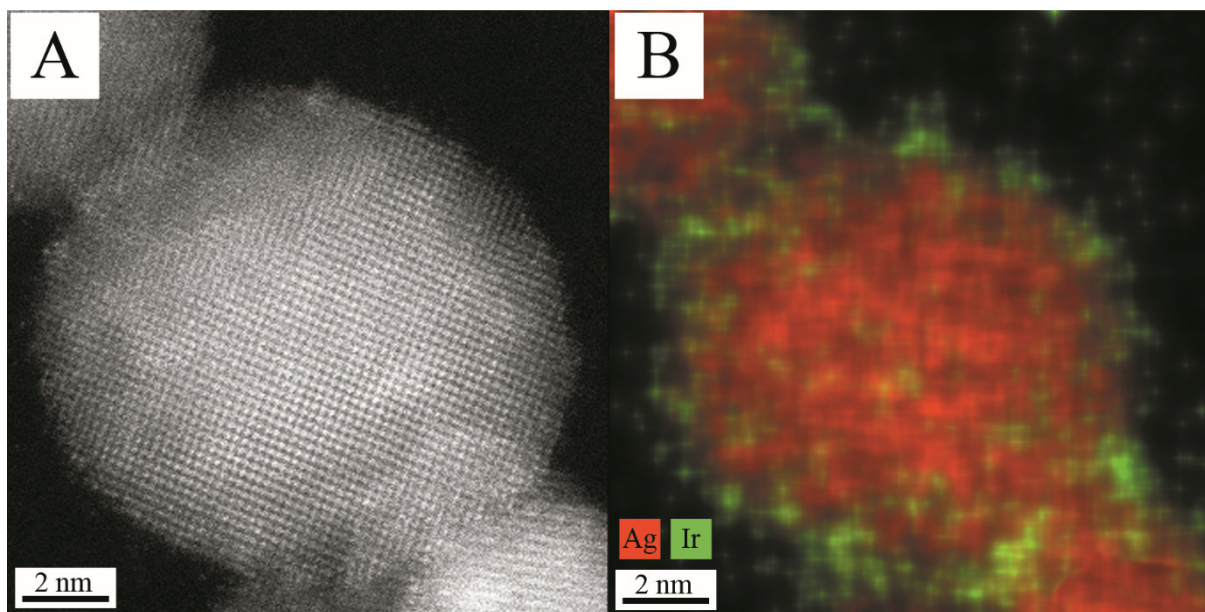


Fig. 59: HAADF image of a single bimetallic silver-iridium nanoparticle (A) and the EDX map of the same particle (B). The energy of silver is marked with a red color while the energy corresponding to iridium is marked in green.

The EDX map shows that a shell of iridium has grown around the spherical silver core. The shell is not completely developed and shows pilings of iridium in certain regions of the particle surface. The element distribution of the particles determined by EDX is 92:8 (Ag:Ir) and therefore slightly differs to the nominal composition (88:12 (Ag:Ir)). Since only one particle was mapped, the data has no statistical relevance. The silver cores show no signs of galvanic replacement reactions. This is quite astonishing. Especially taken into consideration that the synthesis was performed at a pH of 12 and that the used reducing agent was sodium borohydride. Former syntheses as well as the literature have shown that a higher pH value increases the reduction potential of the reducing agent ascorbic acid and therefore prevents a galvanic replacement reaction. Taken into consideration that the reduction potential of sodium borohydride will be lowered at higher pH values, a galvanic replacement reaction becomes likelier under the present conditions.^[165] This leads to two possible explanations for the formation of a core-shell system. Firstly, the used metal precursor complex of iridium, the hexachloridoiridate(IV) ($[\text{IrCl}_6]^{2-}$), might become less stable in alkaline conditions. Actually, the complex is reduced under basic conditions and decomposes to $[\text{IrCl}_6]^{3-}$ under evolution of oxygen: $2 [\text{IrCl}_6]^{2-} + 2 \text{OH}^- \leftrightarrow 2 [\text{IrCl}_6]^{3-} + \frac{1}{2} \text{O}_2 + \text{H}_2\text{O}$ (Fig. 60, A).^[4]

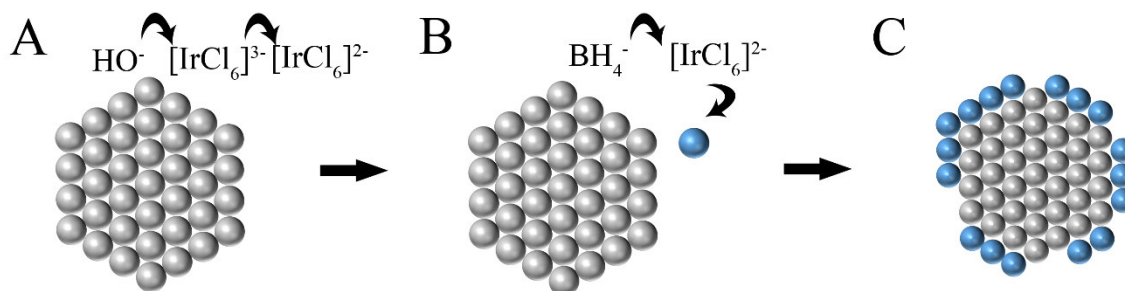


Fig. 60: Scheme of a possible reaction for the formation of the silver-iridium core-shell system. The blue spheres represent iridium atoms and the grey spheres represent silver atoms.

The former standard potential $E^\circ = +0.835$ V of the precursor complex will therefore decrease to $E^\circ = +0.77$ V of the newly formed Ir(III)-Complex. This standard potential is lower than E° of silver (+0.80 V). Hence, no galvanic replacement reaction will occur, and a shell of iridium is formed around the particles (Fig. 60, B+C). The balanced half reactions of the different complex anions are shown in Table 17.

Table 17: Standard potentials of balanced half-reactions of hexachloridoiridate in different oxidation states^[50, 166] in comparison with the standard potential of silver and silver oxide.^[166-167]

Balanced half-reaction	E° / V
$[\text{IrCl}_6]^{2-} + e^- \leftrightarrow [\text{IrCl}_6]^{3-}$	+0.867
$[\text{IrCl}_6]^{2-} + 4 e^- \leftrightarrow \text{Ir} + 6 \text{Cl}^-$	+0.835
$[\text{IrCl}_6]^{3-} + 3 e^- \leftrightarrow \text{Ir} + 6 \text{Cl}^-$	+0.77
$\text{Ag}^+ + e^- \leftrightarrow \text{Ag}$	+0.80
$2 \text{Ag}^+ + 2 \text{OH}^- \rightarrow 2 \text{AgOH} \leftrightarrow \text{Ag}_2\text{O} + \text{H}_2\text{O}$	+0.342

The second explanation might be a formation of Ag_2O on the surface of the preformed silver nanoparticles. Silver ions which might be still present in the synthesis or positively charged silver on the particle surface will form silver hydroxide which will decompose to silver oxide: $2 \text{Ag}^+ + 2 \text{OH}^- \rightarrow 2 \text{AgOH} \leftrightarrow \text{Ag}_2\text{O} + \text{H}_2\text{O}$ (Fig. 61, A). This reaction could in theory form a thin layer around the particles which leads to a surface passivation (Fig. 61, B). Consequently, the layer will protect the silver nanoparticles from further oxidation and a shell of iridium atoms will be formed (Fig. 61, C). Both theories provide a possible explanation for the formation of silver-iridium core-shell nanoparticles. An investigation of the oxidation state of silver via XPS might help to reveal the right answer. Unfortunately, in this work this question remains unanswered since no XPS was performed.

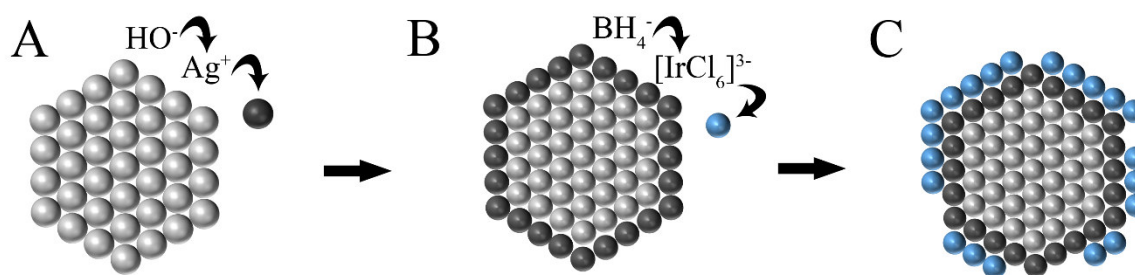


Fig. 61: Schematic reaction for a passivation of silver nanoparticles by a Ag_2O layer. The passivation protects the metallic core of a galvanic replacement reaction. Ag_2O is simplified as black spheres. Iridium atoms are depicted in blue and silver in grey.

To investigate the crystallographic structure of the formed particles, XRPD measurements were performed and evaluated with Rietveld refinement. The evaluation of the pattern reveals that three different phases are present (Fig. 62). Silver shows a mixture of an fcc- and an hcp-phase.

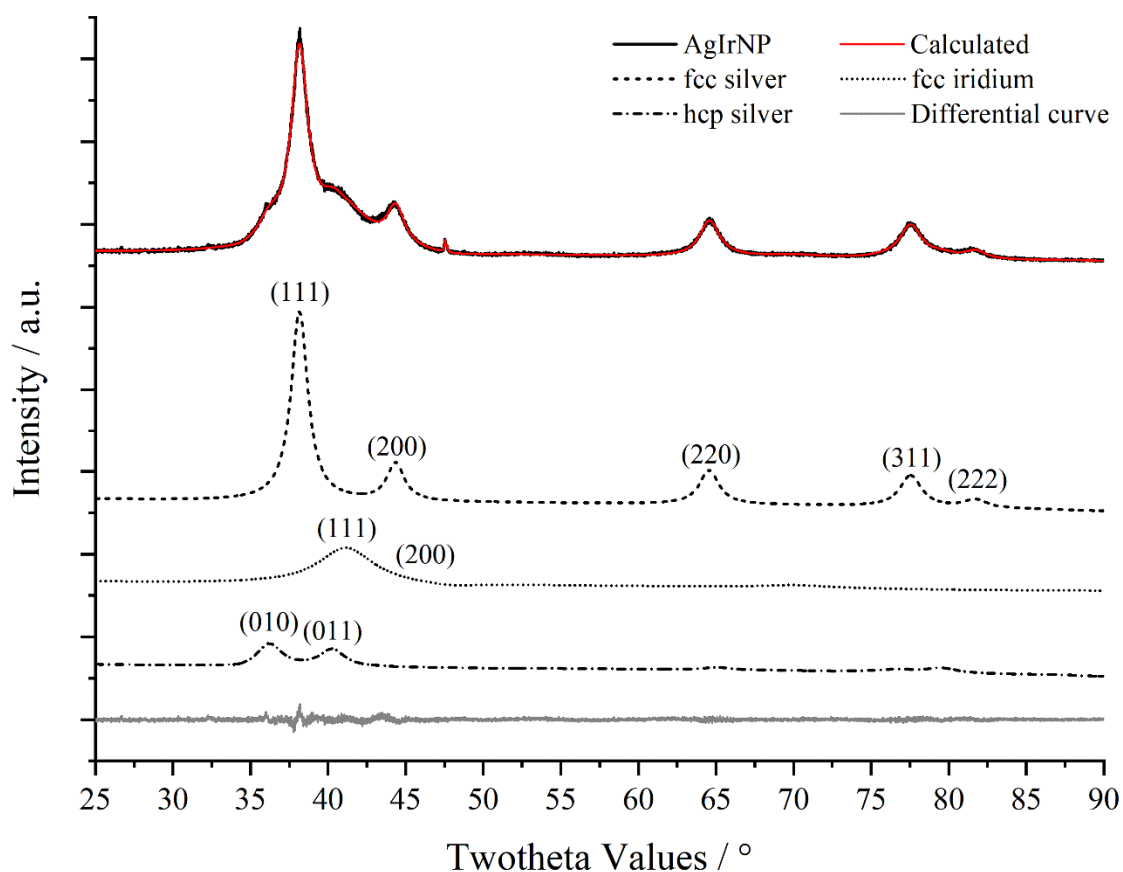


Fig. 62: Rietveld refined XRPD pattern of bimetallic silver-iridium particles synthesized with sodium borohydride. Two phases of silver fcc, hcp as well as iridium fcc-phase are fitted to describe the pattern.

This observation is in accordance to prior investigation regarding the structure of monometallic silver nanoparticles (see chapter 5.2.1).

Table 18: Space groups and calculated cell volumes and lattice parameters for the observed phases of silver and iridium derived from Rietveld refinement

Phase	Space group	$LP (a / \text{Å})$	$LP (c / \text{Å})$	Cell volume / Å^3
Ag fcc	$Fm-3m$	4.0811 (3)	-	67.974 (17)
Ag hcp	$P6_3/mmc$	2.8607 (7)	5.2200 (9)	36.994 (68)
Ir fcc	$Fm-3m$	3.7965 (21)		54.719 (9)

A phase quantification shows that only 0.95 % of silver possess an hcp structure. This is around 30 times less compared to the monometallic particles. Furthermore, the hcp phase has a distinct preferred orientation of the (010) and (011) crystallographic planes. Both silver phases sum up to a total amount of 89.29 at%. Therefore, a composition of silver-iridium of 89:11 (Ag:Ir) is determined by Rietveld refinement. This is 3 at% more than obtained from EDX. The distribution by Rietveld refinement has a high statistical relevance since it sums up over all particles in the measured sample. However, the method has certain limitations, especially with irregular peak profiles and cumulative reflex shapes which leads to an error of ± 2 %. The observed lower amount of hcp stacking faults of the silver core is in good agreement with the HRTEM images. They show less stacking faults of the silver cores in the bimetallic system compared to the monometallic silver particles.

To further characterize the bimetallic system in dispersion the particles were characterized using DLS, DCS and the ζ -potential was determined. All procedures were carried out in ultra-pure water as dispersion medium.

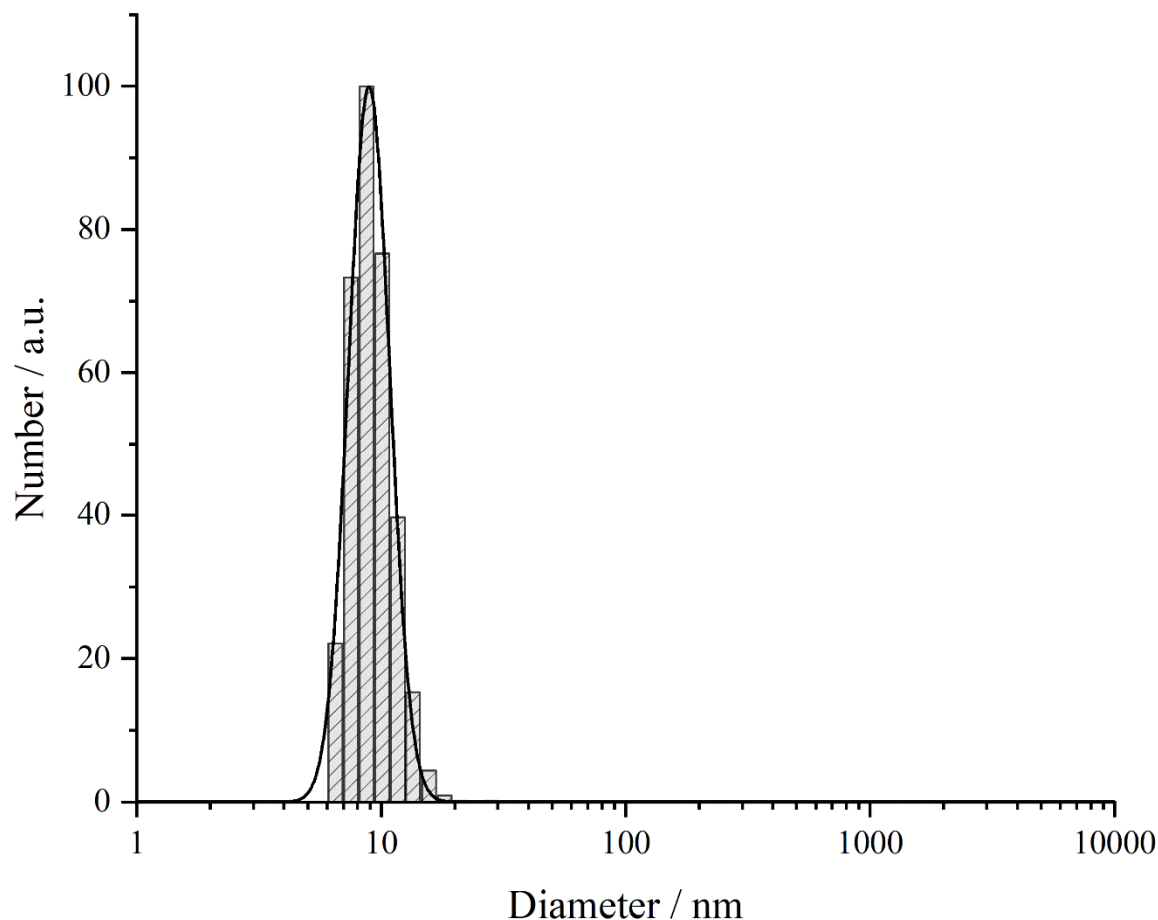


Fig. 63: DLS measurement of the bimetallic silver-iridium particles. The graph shows the particle number (a.u.) as a function of the diameter (nm).

The DLS reveals a mean particle diameter of 9.3 nm with a standard deviation of ± 1.9 nm. The obtained PDI from the applied fit is 0.18 and confirms the monodisperse nature of the system. The mean particle diameter is slightly higher than obtained from the histogram measured from HRTEM images. This deviancy is because the DLS gives the hydrodynamic diameter of the particles. Only one maximum occurs during the measurement. This shows that no agglomeration or aggregation of the particles occurs. To confirm the data obtained from DLS additionally a DCS measurement was carried out.

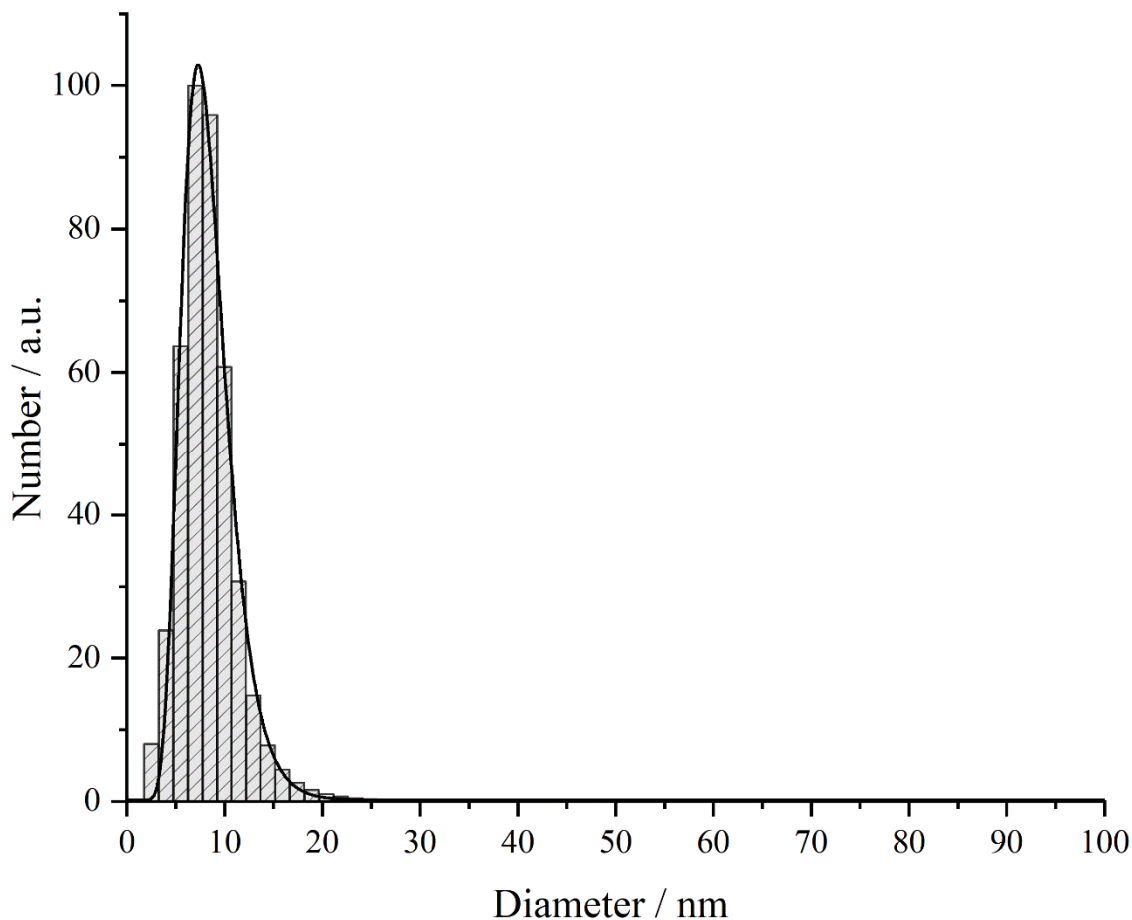


Fig. 64: DCS measurement of silver-iridium nanoparticles synthesized with sodium borohydride. The graph shows the number (a.u.) as a function of the particles diameter (nm). The whole measurement was performed up to 200 nm but cut for clarity. In the cutout region, no other signals were observed.

The DCS also shows a monodisperse system. The mean particle diameter is $8.0 \text{ nm} \pm 2.6 \text{ nm}$ which leads to a polydispersity index of 0.29. The determination was performed using a Gaussian fit to describe the dataset. All methods confirm the formation of monodisperse nanoparticles with a high colloidal stability. To characterize the optical properties, UV/Vis spectroscopy was performed. Iridium nanoparticles absorb wavelengths of the visible section over the whole range with a maximum absorption in the UV region.^[11] The application of iridium as shell material leads to a decrease in absorption of the silver SPR peak compared to monometallic silver nanoparticles of the same size. Furthermore, the general form of the absorption band compared to monometallic silver particles is drastically changed. The absorption is much broader and exists in the region from 316-660 nm which leads to a red-brown dispersion (Fig. 65). The main absorption maximum is slightly blue shifted to a value of 394 nm.

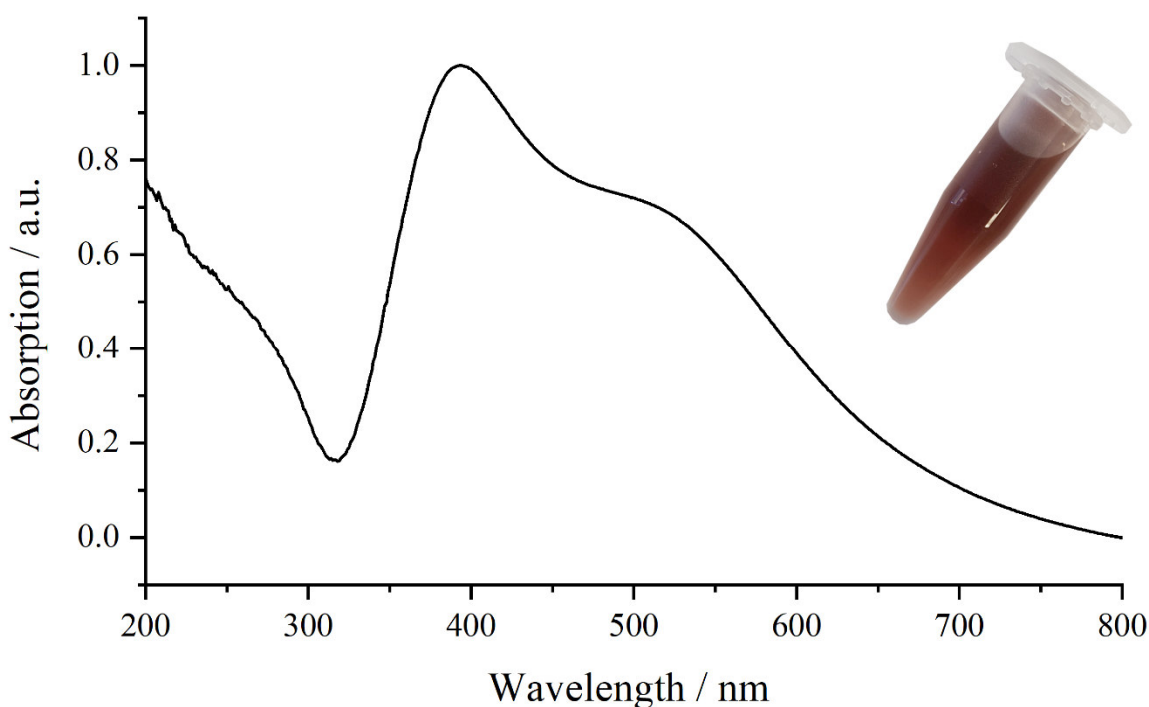


Fig. 65: UV/Vis spectra of the synthesized core-shell silver-iridium nanoparticle and a photograph of the actual sample. The absorption (a.u.) is shown as a function of the wavelength (nm).

Since the particles are monodisperse, the broad absorption band might be caused by other reasons. The size determination by HRTEM has revealed that around $\sim 20\%$ of the particles in the sample have a slightly anisotropic structure. This might be a possible explanation for the shoulder of the absorption band. Supplementary, the shell of iridium is not fully developed which can lead to a strong deviation in plasmon energies and consequently result in a broad absorption band. Comparable observations could already be made in section 5.1.2 where hollow spherical with an irregular surface have developed unusual SPR peaks.

The same synthesis can be adapted to generate other nominal ratios of both metals. Other syntheses with the nominal ration of 80:20 (Ag:Ir) have been investigated to validate that the generated particles do fulfill the same requirements. The synthesis formed particles with a mean diameter of 10 nm whereby they are marginally bigger than particles obtained from the 90:10 molar ratio. Furthermore, the particles show a lower number of spherical particles. Anisotropic oval structures are present in amounts of up to $\sim 75\%$. Those structures have the same aspect ratio of 1:1.3 like in the sample with the 90:10 compositions. A consequence of the higher anisotropy is that the former observed shoulder in the UV/Vis spectrum of the composition

90:10 (compare Fig. 65) has now fully developed to a broad absorption band between 320-560 nm (Fig. 66, C).

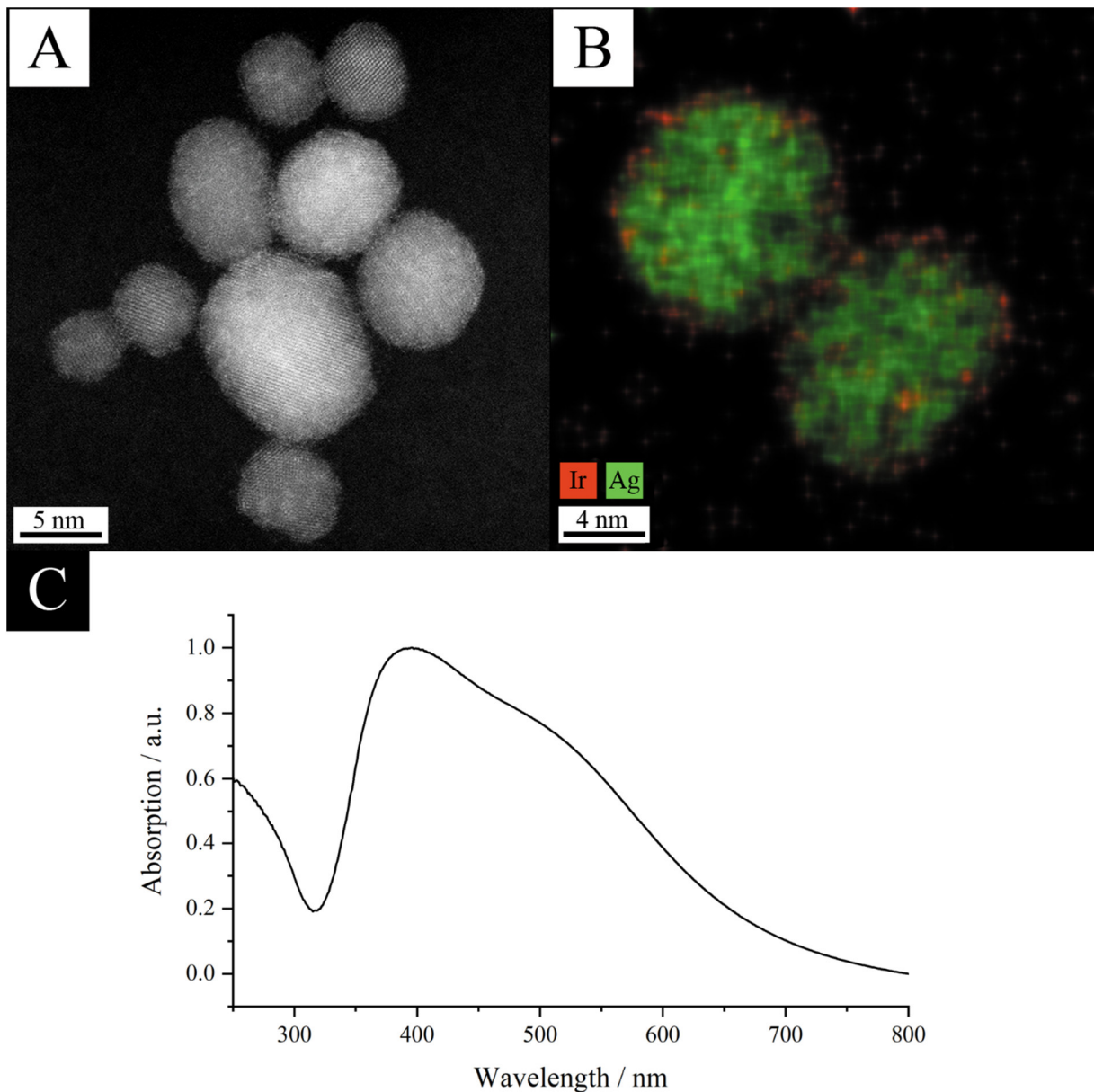


Fig. 66: Dark Field HRTEM image of silver-iridium particles with a nominal ratio of 80:20 (A), EDX mapping of the same sample (B) and the obtained UV/Vis spectrum (C).

The EDX map reveals a composition of 86:14 (Ag:Ir) and hence a relatively strong deviation from the nominal composition. Further colloidal characterization methods were performed to compare both syntheses. All size determining measurements show a size increase if the amount of iridium is increased. The obtained system with the nominal composition of 80:20 (Ag:Ir) still results in a monodisperse system. All data is compared in Table 19. This leads to the assumption that the same synthesis can be used for a variety of nominal compositions.

Table 19: Comparison between silver-iridium nanoparticles syntheses with different nominal compositions.

Synthesis	TEM / nm	Composition EDX	Composition Rietveld	DLS / nm	DCS / nm
AgIr90:10	4.9 ± 1.1	92:8	89:11	9.3 ± 1.9	8.0 ± 2.6
AgIr80:20	7.5 ± 1.9	86:14	82:18	13.2 ± 3.2	11.0 ± 3.2

Additionally, to the silver-iridium particles, other shell materials were applied to the silver nanoparticles obtained from the synthesis with sodium borohydride. For an application of gold and palladium as shell material, the procedure using ascorbic acid and a pH of 12, which was formerly described, was used (compare chapter 5.1.3). A size determination by DCS reveals that the particle increase in size after the second material is applied.

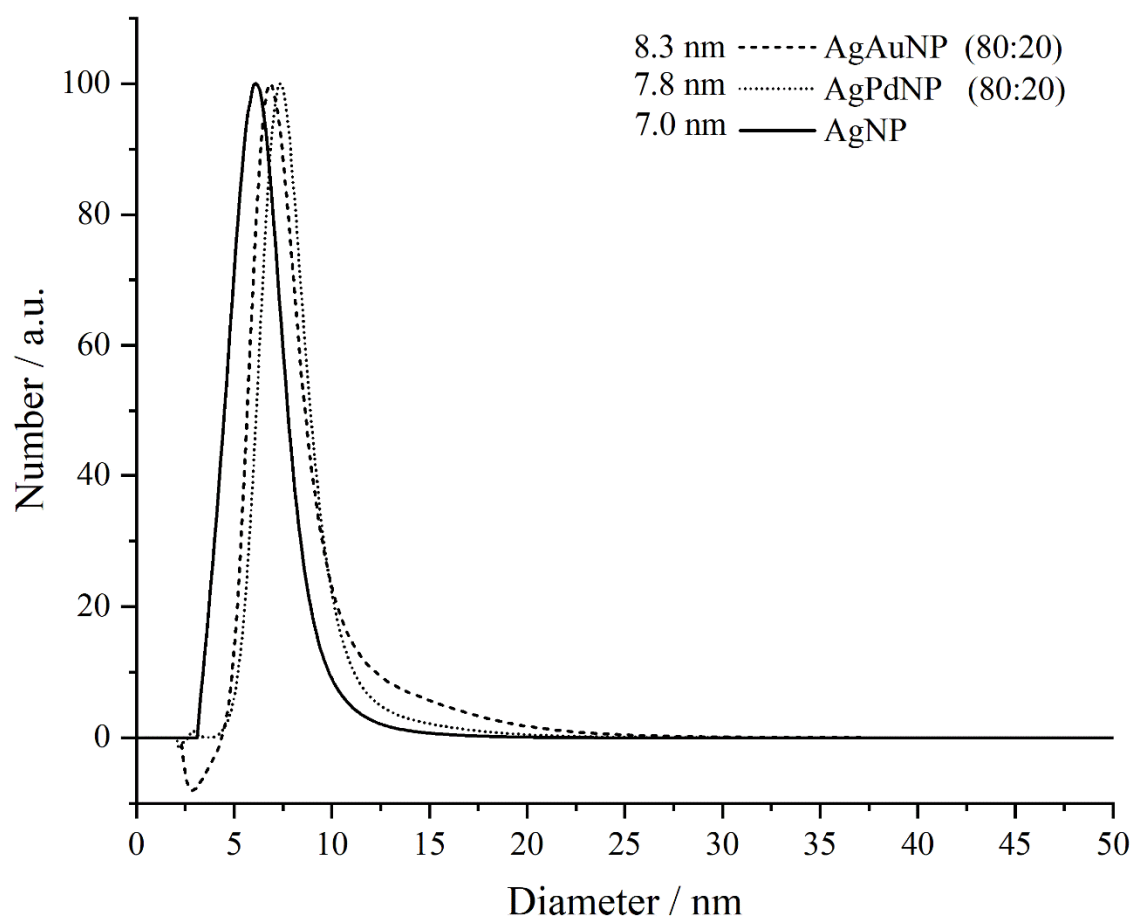


Fig. 67: DCS measurements of synthesized core-shell systems with palladium and gold in comparison with the used silver seeds from the synthesis with sodium borohydride. The number (a.u.) is shown as a function of the diameter (nm).

Overall four syntheses with different compositions could be realized using this method. These are the compositions 90:10 and 80:20 for both bimetallic configurations ((AgPd), (Ag:Au)). The data for all realized core-shell systems are compared to the seed data (see Table 20).

Table 20: Mean size, standard deviation, polydispersity index (PDI) and the coefficient of determination (COD) for the applied Gaussian-fits for all size determining methods for the compositions 90:10 and 80:20 for silver-palladium and silver-gold core-shell nanoparticles. The data is compared to the data of the used seeds. Furthermore, the maximum absorption band of the UV/Vis spectra and the composition determined by AAS is depicted.

AgNP (Seeds)				
Method	DLS	DCS	UV/Vis absorption / nm	(Ag:M) AAS composition
Diameter / nm	10.4	7.2		
Standard deviation (σ) / nm	2.1	1.7		
PDI	0.18	0.22	397	100:0
COD (R^2)	0.9872	0.9573	FWHM: 58	
AgAuNP (90:10)				
Method	DLS	DCS	UV/Vis absorption / nm	AAS composition
Diameter / nm	10.9	7.7		
Standard deviation (σ) / nm	1.8	1.8		
PDI	0.17	0.22	405	91:9
COD (R^2)	0.9875	0.9747	FWHM: 101	
AgAuNP (80:20)				
Method	DLS	DCS	UV/Vis absorption / nm	AAS composition
Diameter / nm	11.4	8.3		
Standard deviation (σ) / nm	2.2	1.8		
PDI	0.19	0.25	410	81:19
COD (R^2)	0.9921	0.9837	FWHM: 117	
AgPdNP (90:10)				
Method	DLS	DCS	UV/Vis absorption / nm	AAS composition
Diameter / nm	11.8	7.4		
Standard deviation (σ) / nm	2.8	1.3		
PDI	0.23	0.20	392	95:5
COD (R^2)	0.9856	0.9678	FWHM: 134	
AgPdNP (80:20)				
Method	DLS	DCS	UV/Vis absorption / nm	AAS composition
Diameter / nm	11.2	7.8		
Standard deviation (σ) / nm	2.0	1.2		
PDI	0.18	0.24	387	86:14
COD (R^2)	0.9952	0.9140	FWHM: 147	

The data shows that all ratios could be realized. The bathochromic shift in plasmon resonance for the core-shell particles with gold is expected because of the optical properties of gold nanoparticles.

Furthermore, the intensity of the main absorption band of both compositions with palladium is reduced. This indicates that a shell of palladium has grown. The broadening of the absorption bands in all syntheses is expected, due to the inhomogeneous growth of the shell. The directional growth which occurs is caused by the complexation of the (100) crystallographic lattice plane by PVP (compare chapter 5.1.3) and results in a multiplication of SPR peaks which form a broad absorption band.

In summary, core-shell particles with sizes of 5-10 nm could be synthesized for all intended compositions. All systems are monodisperse and show no signs of aggregation or agglomeration. Silver-iridium particles are slightly smaller compared to monometallic silver nanoparticles. The synthesis with hexachloridoiridate as precursor in presence of sodium borohydride as a reducing agent can only occur because the core of silver is protected against a galvanic replacement reaction. But different to the core-shell growth mechanism with ascorbic acid, the protection is not based on the reduction potential increase of the reducing agent. Two different explanations are possible based on chemical reactions under basic conditions. Firstly, the iridium precursor is previously reduced by hydroxide ions under the formation of oxygen or second, silver ions are oxidized to a passivating oxide layer which protects the particles (Fig. 60, Fig. 61). The EDX maps for the particles show that not all iridium has been reduced and therefore the ratios of both metals slightly differ to the nominal compositions. An investigation of the composition by AAS of silver-iridium particles was not possible since the dissolution of the elemental iridium could not be performed under given circumstances. However, EDX maps and Rietveld analysis are in good agreement.

Furthermore, the core-shell synthesis via a seed and growth approach resulted in bimetallic silver-gold and silver-palladium core-shell nanoparticles. The particles show a size increase in comparison to the used seeds. Additionally, all dispersions show an expected behavior in terms of optical properties (compare Table 20). The particles could therefore be used for dissolution kinetic experiments to determine their silver ion release rate.

5.3 Synthesis of silver nanoparticles with the polyol process

To adapt the synthesis of core-shell systems to other morphologies of silver nanoparticles and possibly tune their dissolution kinetics, two morphologies of silver nanoparticles were synthesized using a polyol process. This type of synthesis uses an organic alcohol like ethylene glycol (EG) or diethylene glycol (DEG) to perform three different tasks at the same time. Those compounds can be the solvent, the reducing agent as well as the stabilizer. In the reaction of ethylene glycol two electrons become utilizable to reduce silver ions.^[37, 90] The relatively slow reduction of silver ions in combination with suitable ligands that complex certain crystallographic facets makes this method useful to initiate a kinetic controlled growth of particles with various morphologies (compare chapter 2.5). Different approaches like oxidative etching or seed-induced growth mechanisms can hence be used to generate nanowires or nanocubes of silver.^[37, 89] Those morphologies were generated and will be characterized and described in detail.

Studies about the dissolution behavior for different morphologies have shown that the ion release rate directly correlates with the effective surface of the particles.^[23] Hence an applied shell of a second metal might influence this kinetic to tune the dissolution in terms of long-term ion release. The combination of particle shape and shell-influenced dissolution kinetics could consequently be used to address several time spans. This concept could in theory lead to a release of silver ions over the whole healing process of a patient if using nanoparticles as coatings for implants. The former described synthesis for core-shell systems can also be applied to nanowires as well as nanocubes. The obtained results will be described in detail in the following segment.

5.3.1 Characterization of silver nanocubes generated by oxidative etching

Silver nanocubes can be generated by selective etching of twinned particles using an acid. In the growth process of the seeds, single-crystalline and twinned particles arise. The twinned structure possesses a lower surface energy, but this energy gain results in a trade-off to stronger lattice distortion and increased surface defects. The twinned particles will therefore have a greater susceptibility and higher reactivity towards etching.^[37] Consequently, applying an acid during the reaction, twinned particles will dissolve to silver ions whereas only the single-crystalline particles will remain. Those will further grow to nanocubes (Fig. 68). A key role plays the polymer PVP which interacts more strongly with the $\{100\}$ -facets of the forming crystals and inhibits the growth of those planes. This leads to a directed growth.^[143]

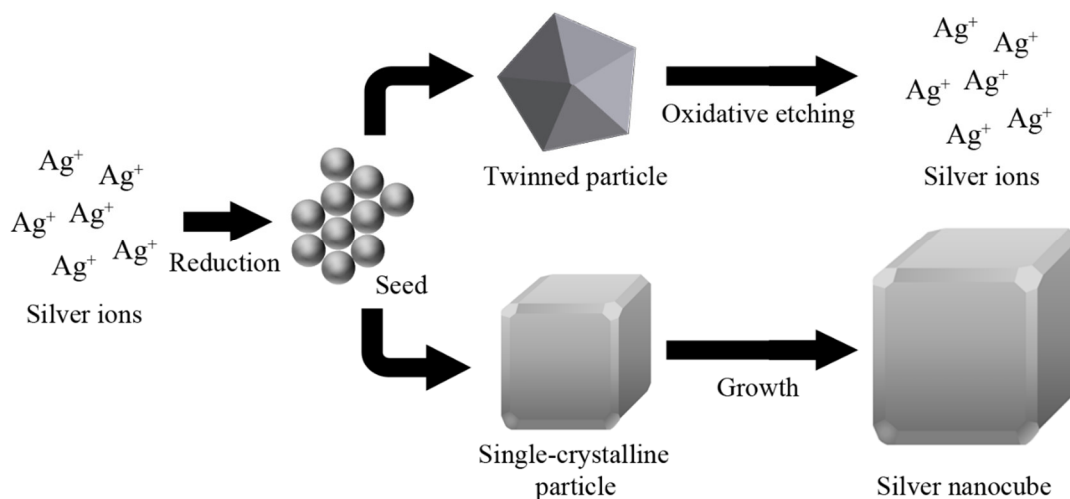


Fig. 68: Schematic reaction mechanism of the oxidative etching process to generate silver nanocubes proposed by Xia et al.

In this work, a synthesis by Xia et al. which was modified by Dr. Helmlinger was used.^[91] The following two steps were added:

1. Ethylene glycol was heated up to 160 °C and stirred with an open flask for 60 minutes.
2. Before the reaction starts, the solutions of silver nitrate and PVP are freshly prepared and will only be mixed immediately before the reaction.

The particles obtained from the modified synthesis result in a mostly cubical morphology. Additionally, a certain number of nanowires is generated (Fig. 69). The formation of those wires is the consequence of an incomplete etching process of twinned seeds. Those nanowires can be

separated from the silver nanocubes by filtration via a cellulose-syringe filter with a pore size of $0.45\ \mu\text{m}$.

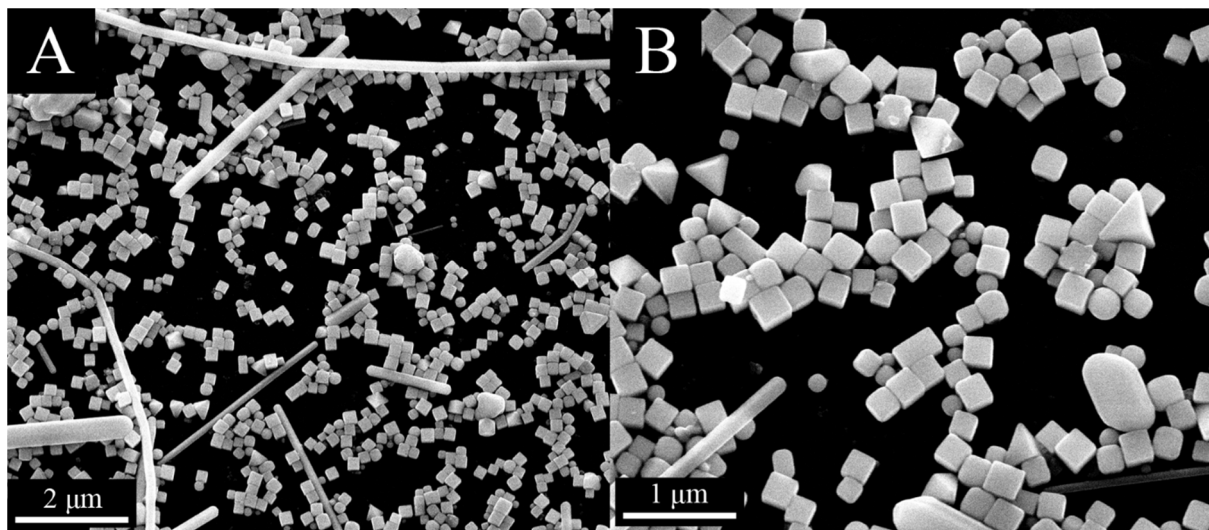


Fig. 69: Mixture of silver nanocubes and nanowires obtained by the modified synthesis after Helmlinger. The images were taken with an accelerating voltage of 15 kV and a magnification of 25000 times (A) and 50000 times (B).

The wires are longer than $1\ \mu\text{m}$ and consequently only the smaller particles remain in the dispersion after filtration of the product. SEM images taken after filtration were used to generate a histogram (Fig. 70). This treatment resulted in the determination of the mean size (199 nm), the standard deviation ($\pm 19\ \text{nm}$) and the PDI (0.05). The synthesized silver nanocubes show a narrow size distribution and can henceforth be classified as a monodisperse system.

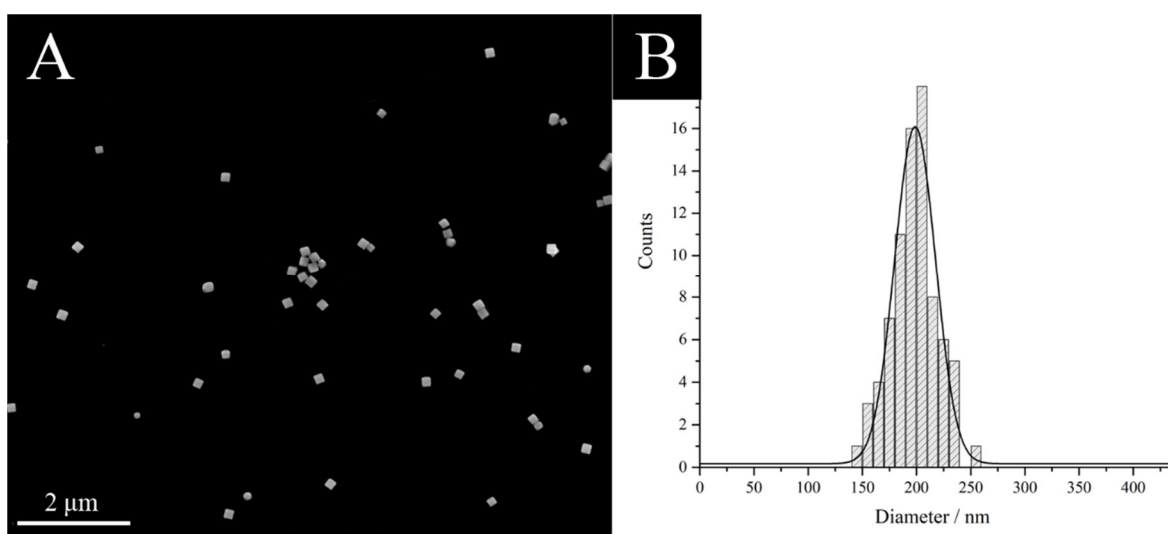


Fig. 70: Silver nanocubes after the filtration over a cellulose filter with a pore size of $0.45\ \mu\text{m}$ (A) and the obtained histogram from SEM (B). The images were taken with an acceleration voltage of 10 kV.

To verify the colloidal stability in ultra-pure water, DLS and DCS measurements were performed.

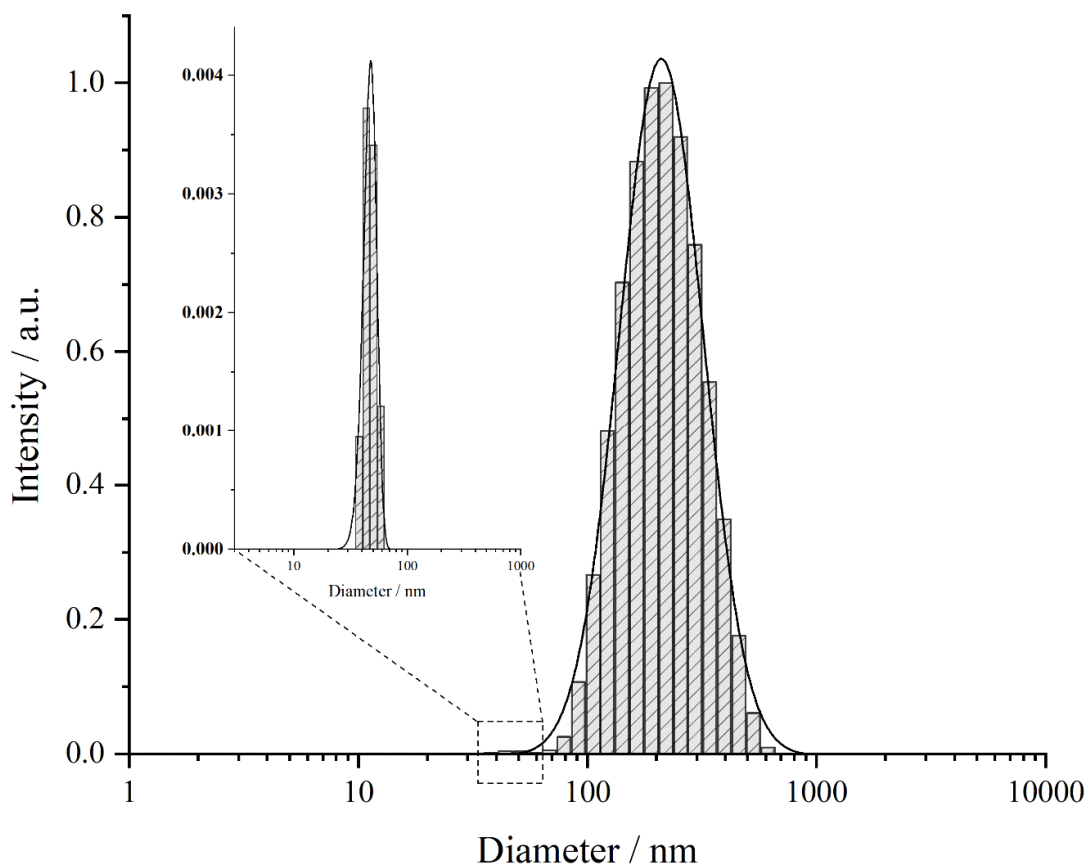


Fig. 71: DLS measurement of silver nanocubes obtained by oxidative etching. The graph shows the intensity (a.u.) as a function of the diameter (nm). If the data is evaluated with care the graph shows a bimodal size distribution with a small second signal.

The size distribution obtained from intensity seems to be unimodal at first glance. An attentive evaluation of the data leads to the uncovering of a second much smaller signal. The investigations by SEM have shown that the sample has a narrow, unimodal size distribution with a low standard deviation, therefore an alternative explanation needs to be found to interpret the data. The SEM images reveal not only a pure-phase of silver nanocubes, but additionally other morphologies like cuboids (Fig. 72, A), tetrahedra (Fig. 72, B) and spheres (Fig. 72, C) are present. Those morphologies only occur in small amounts, but they can be found. These particle types will not be separated by filtration and consequently remain in the solution. The morphologies have different diffusion coefficients than the nanocubes and will hence lead to a smaller fraction in the DLS measurement. The influence of anisotropic structures on DLS measurements was already discussed in detail in chapter 5.1.1. However, the

amount of those structures determined by SEM is about ~3-8 % and hence comparatively low. This leads to a weak signal in the distribution by intensity.

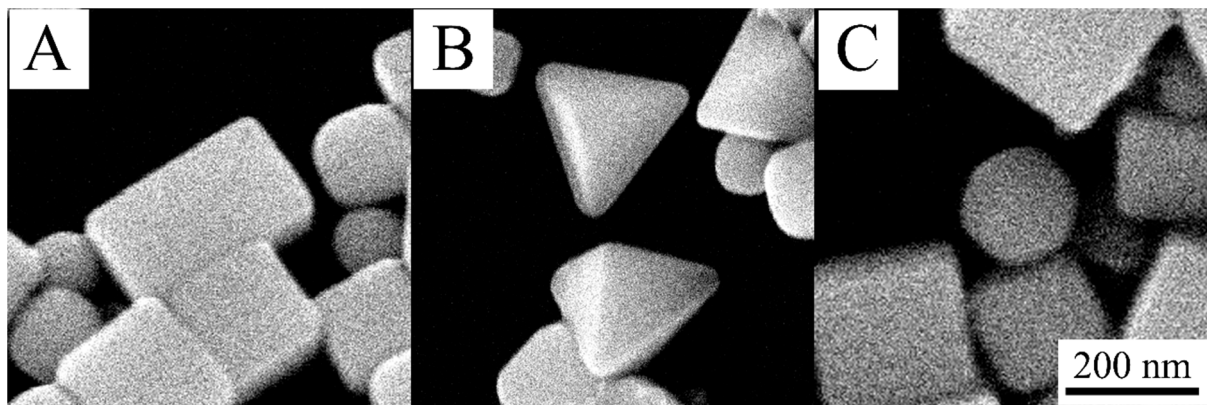


Fig. 72: Morphological byproducts from the synthesis of silver nanocubes by oxidative etching. The Figure depicts cuboids (A), tetrahedral (B) and spheres (C).

The small second signal has a direct influence of the calculated distribution by number. The maximum of the main signal in the distribution by intensity is at $227 \text{ nm} \pm 90 \text{ nm}$ with a PDI of 0.16 (Fig. 71). In comparison, the distribution by number (not shown) results in a strong bimodal size distribution. The first peak in the distribution by number appears at $142 \text{ nm} \pm 58 \text{ nm}$ and the second appears at $46 \text{ nm} \pm 9 \text{ nm}$. This distribution shows no correlation to the findings of the SEM data and could hence not be used. The determined ζ -potential was -40 mV and shows a strong absorption of NO_3^- ions on the (100)-facets surfaces of the nanocubes.

To confirm that the distribution by number is strongly influenced by other morphologies a DCS measurement was performed. The measurement reveals also a bimodal size distribution, but in comparison to the data obtained from DLS the mean size of the first peak is at $204 \text{ nm} \pm 19 \text{ nm}$ and the second maximum has a mean size of 167 nm with a standard deviation of 24 nm (Fig. 73). The first maximum however has only an intensity of 7.9 % in comparison to the second maximum. Hence only a small fraction is observed. This fraction could also be caused by the irregular structures of some particles in the sample. Since the particles diffuse through a gradient of different densities, the morphology can influence the sedimentation time and might lead to a second fraction. The average PDI of a bimodal size distribution can be calculated by weighting the percentage number contribution (PND) of single peaks by their PDI. Hence the following formula (14) can be used:^[168]

$$\text{PDI}_{\text{Average}} = (\text{PDI}_{\text{Peak 1}} \cdot \text{PND}_{\text{Peak 1}}) + (\text{PDI}_{\text{Peak 2}} \cdot \text{PND}_{\text{Peak 2}}) \quad (14)$$

The PDI obtained by the size distribution by the DCS measurements is 0.02 and thus even smaller than calculated by SEM.

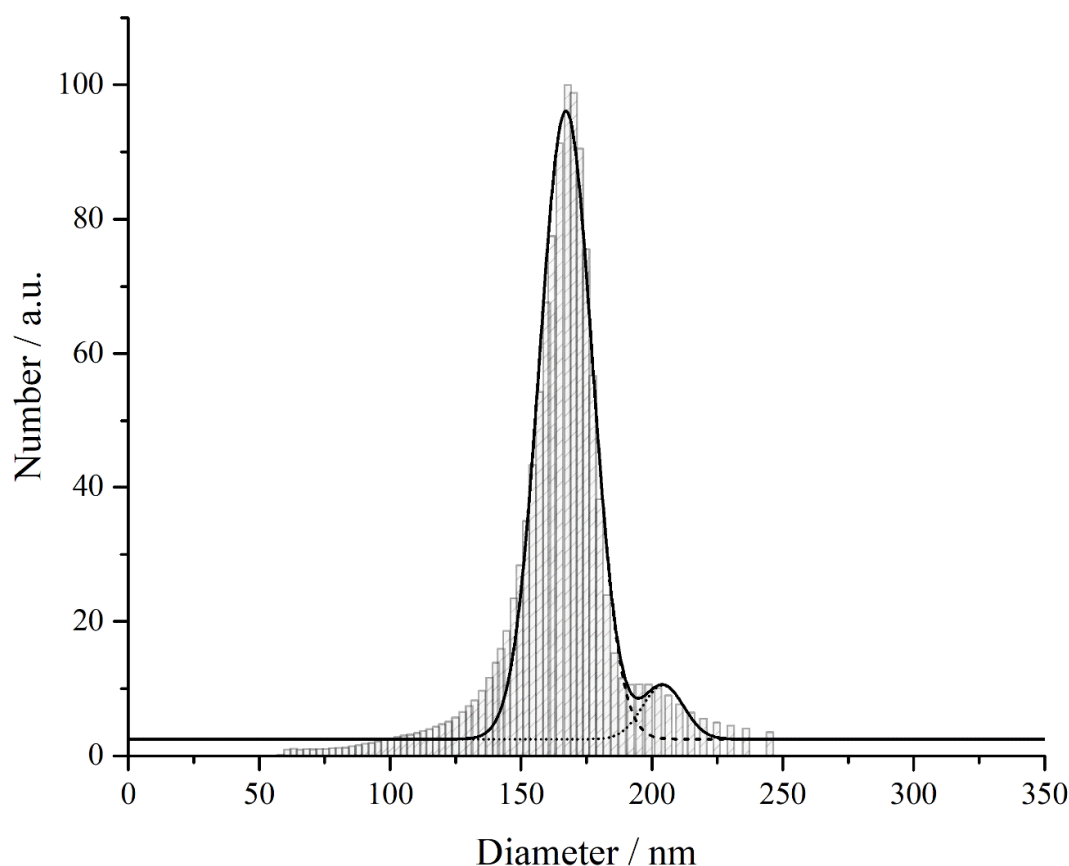


Fig. 73: DCS measurement of silver nanocubes synthesized with ethylene glycol. The graph shows the number (a.u.) as a function of the particle diameter (nm).

Particle size distributions determined by DCS will result in underestimated particle diameters because the density of the system is overestimated. The polymeric shell has a direct influence on the real density. The determination by the used size-defining procedures is in good agreement.

Table 21: Comparison of the mean size, standard deviation, polydispersity index (PDI) and the coefficient of determination (COD) for the applied Gauss-fits for all size determining methods.

Method	SEM	DLS by intensity	DCS by number	
Size / nm	199	227	204	167
Standard deviation (σ) / nm	19	90	19	24
PDI	0.05	0.16	0.01	0.02
COD (R^2)	0.9545	0.9988	0.9787	0.9783

Furthermore, the optical properties of the obtained silver nanocubes were characterized by UV/Vis spectroscopy. These properties are well investigated since silver nanocubes do find applications in surface enhanced Raman spectroscopy (SERS).^[44, 169-171]

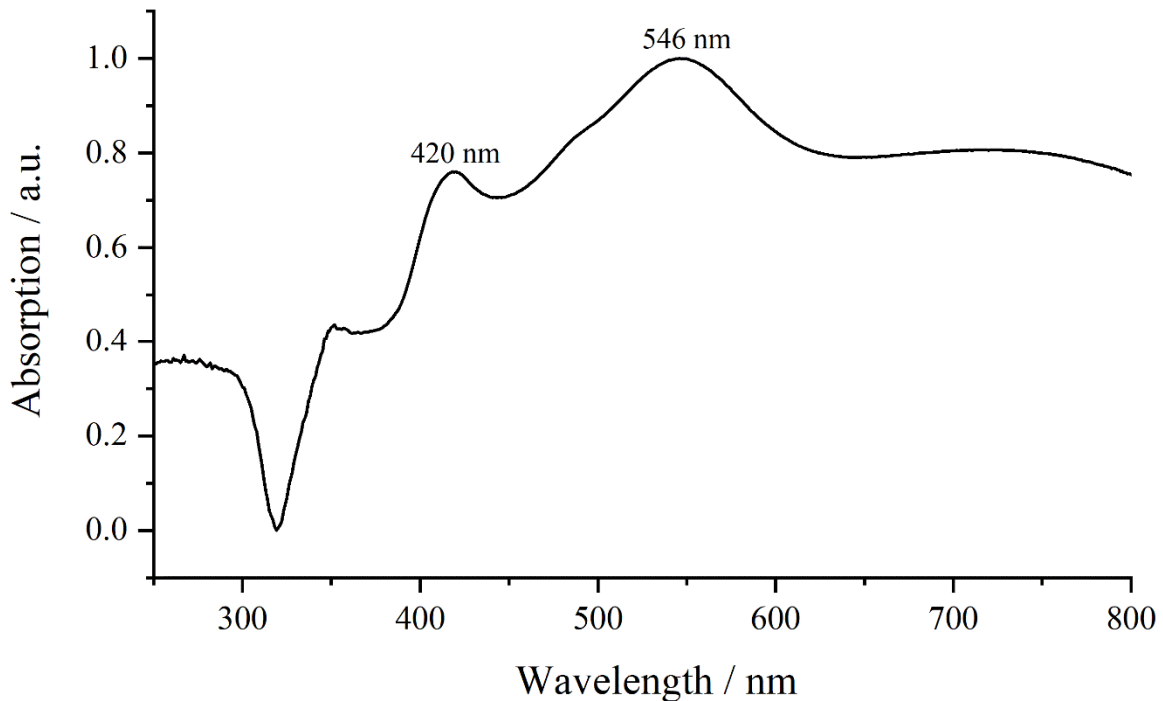


Fig. 74: UV/Vis spectrum of silver nanocubes. The graph depicts the absorption (a.u.) as a function of the wavelength (nm).

The absorption spectrum shows two different maxima. The first maximum occurs at a wavelength of 546 nm. The different polarized electric charge distributions for silver nanocubes were calculated by Zhou et al. and show that the plasmon resonance is mostly caused by the edges, and hence the (110) facets of the cubes. The maximum at 546 nm is caused by a dipole resonance mode that is induced by a (110) polarized incident electric field. The other maximum arise due to evenly distributed contributions of quadrupole and dipole resonances.^[170] The position of the maximum at 546 nm is comparable with silver nanocubes in the same size range from the literature.^[84] An investigation of the crystallographic structure of the silver nanocubes was not performed due to the extensive characterization by available literature.^[83, 130, 142-143, 172]

In summary, it was possible to synthesize monodisperse silver nanocubes with an average PDI of 0.06 and sizes around 170-200 nm. The generated particles were suitable to perform further core-shell synthesis and dissolution kinetic experiments.

5.3.2 Core-Shell particles based on silver nanocubes

To investigate core-shell nanocubes towards their dissolution kinetics and properties in solution, different molar compositions of silver-gold (70:30, 80:20, 90:10) and silver-palladium (80:20, 90:10) were synthesized. The variation of the shell thickness was carried out to investigate the growth behavior of the shell and the associated changes in optical properties of the different compositions. The particles were examined by HRTEM, EDX mapping, SEM, DLS, DCS, UV/Vis spectroscopy and their ζ -potential was determined. Additionally, the real composition of the system was identified by AAS.

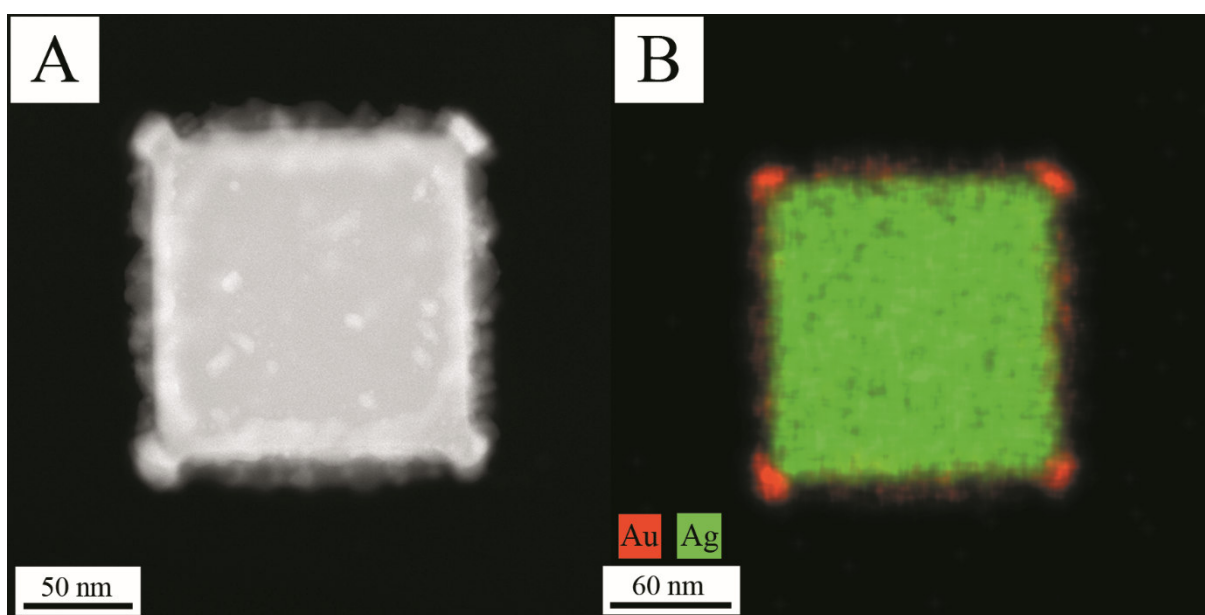


Fig. 75: HAADF image of a silver-gold core-shell nanocube with a nominal composition of 90:10 (A) and the corresponding EDX map (B). The images were taken with an accelerating voltage of 300 kV.

To verify a shell formation, the nanocubes were imaged by high-angle annular dark-field imaging (HAADF). Furthermore, an EDX map of the 90:10 (Ag:Au) composition was performed. The high Z-contrast of the method allows to distinguish between both materials. It becomes noticeable that the shell material has not grown regularly to the surface. Some facets show higher amounts of gold with thicknesses around 11.5 nm. This leads to the conclusion that gold atoms have crystallized to specific crystallographic surfaces of the particle. An enrichment of gold is observed on the $\{111\}$ -facets which form the corners of the nanocubes. Furthermore, the edges of the cubes are heavily loaded with gold atoms: These edges consist of $\{110\}$ -facets. The indices of the different surfaces of silver nanocubes are shown Fig. 76.

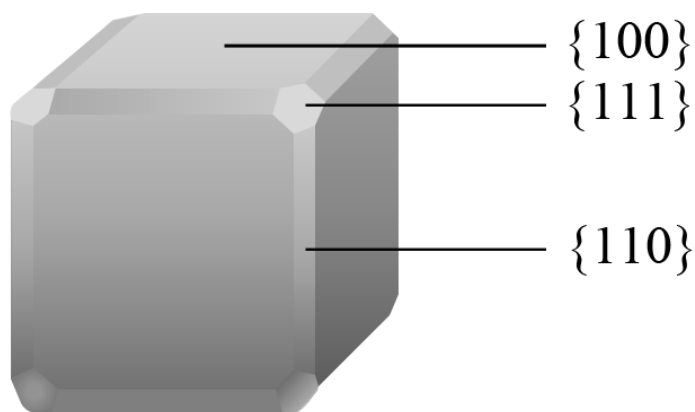


Fig. 76: Crystallographic orientation of the different surfaces of silver nanocubes derived by electron diffraction.^[142-143]

The polymer PVP plays a key role in the directional growth of the nanocubes. It complexes the {100}-facet and hence leads to the formation of silver nanocubes.^[37] In the case of a shell material addition, the complexed PVP still inhibits the growth of gold atoms at those facets. This leads to an increased accretion of gold atoms at the energetically better accessible facets and consequently an irregular growth. The sufficient increase of gold, for example a 70:30 (Ag:Au) composition, leads to a completely grown shell around the silver nanocubes. The investigated sample however showed signs of galvanic replacement due to a too high addition rate of gold precursor (Fig. 77, A+B).

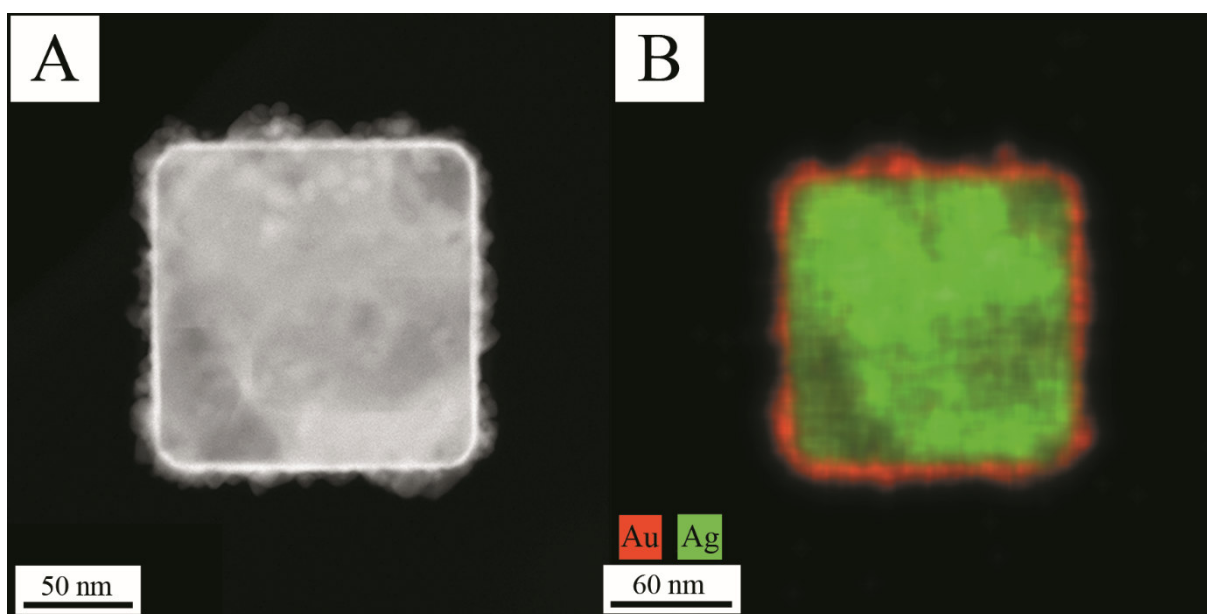


Fig. 77: HRTEM image of a silver-gold core-shell nanocube with a nominal composition of 70:30 (A) and the corresponding EDX map (B). The images were taken with an accelerating voltage of 300 kV.

The shell still shows irregularities but is fully developed. Consequently, the growth remains directional till a definite amount of shell material has crystallized at the preferred facets. Later, the growth will also take place at the $\{100\}$ -facets which leads to a shell closure. The nominal compositions slightly differ to the determination by EDX. The amount of gold is always slightly less than the nominal composition (92:8, 76:24). The directional growth using varying gold quantities has a direct influence of the nanoparticle optical properties. Since dipole and quadrupole resonances of the (110)-lattice planes lead to the absorption maxima of the phase-pure silver nanocubes, the directional growth of a gold layer at those facets directly influences the absorption of the corresponding excitation wavelengths.

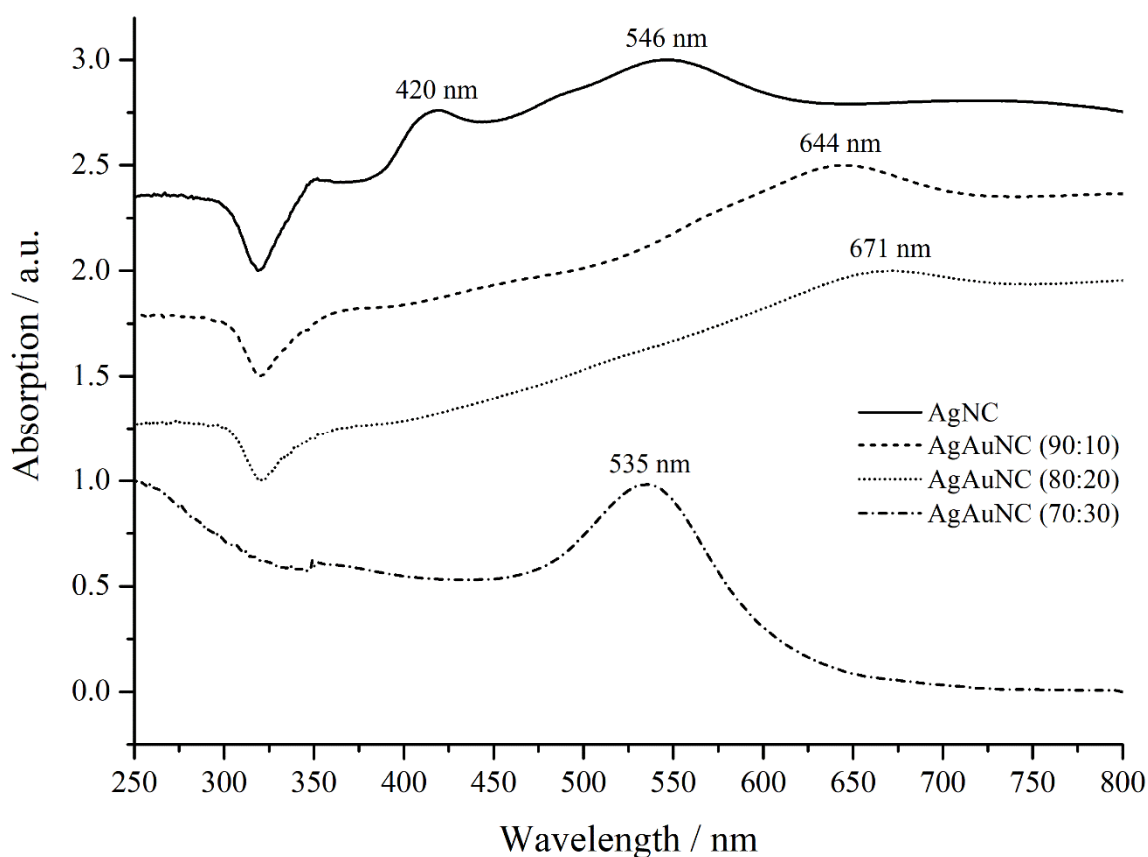


Fig. 78: UV/Vis spectra of phase-pure silver nanocubes (NC) and core-shell systems based on gold in different compositions. The absorption (a.u.) is shown as a function of the wavelength (nm). The graphs have been stacked for a better overview.

This effect can be visualized by UV/Vis spectra. When a quantity of 10 mol% gold is added, the absorption band at 420 nm completely vanishes caused by the formation of a gold shell at the $\{110\}$ -facets. The growth of gold crystallites hence has a huge influence on the induced quadrupole moment of the structure. Furthermore, the absorption band at 546 nm, which is

caused by the induced dipole moment becomes redshifted to 644 nm. If the composition is varied to 80:20 this shift is even more dominant (Fig. 78). The general curve shape of the spectra is still comparable to the spectrum of silver nanocubes. If the amount of gold is further increased (70:30), the shell will be fully developed (compare Fig. 77). This leads to an absorption spectrum with a maximum at 535 nm and a completely different curve (Fig. 78, B). The data corresponds to the spectrum of phase-pure gold nanocubes.^[173-174] Consequently, a complete formation of a shell can be verified using UV/Vis spectroscopy. Furthermore, this observation supports the concept of selective growth of gold on seeds generated by the glucose synthesis (see chapter 5.1.3). To verify that the synthesized core-shell systems retain their unimodal size distribution and their colloidal stability, the particles were investigated by DLS, DCS and the ζ -potential was determined.

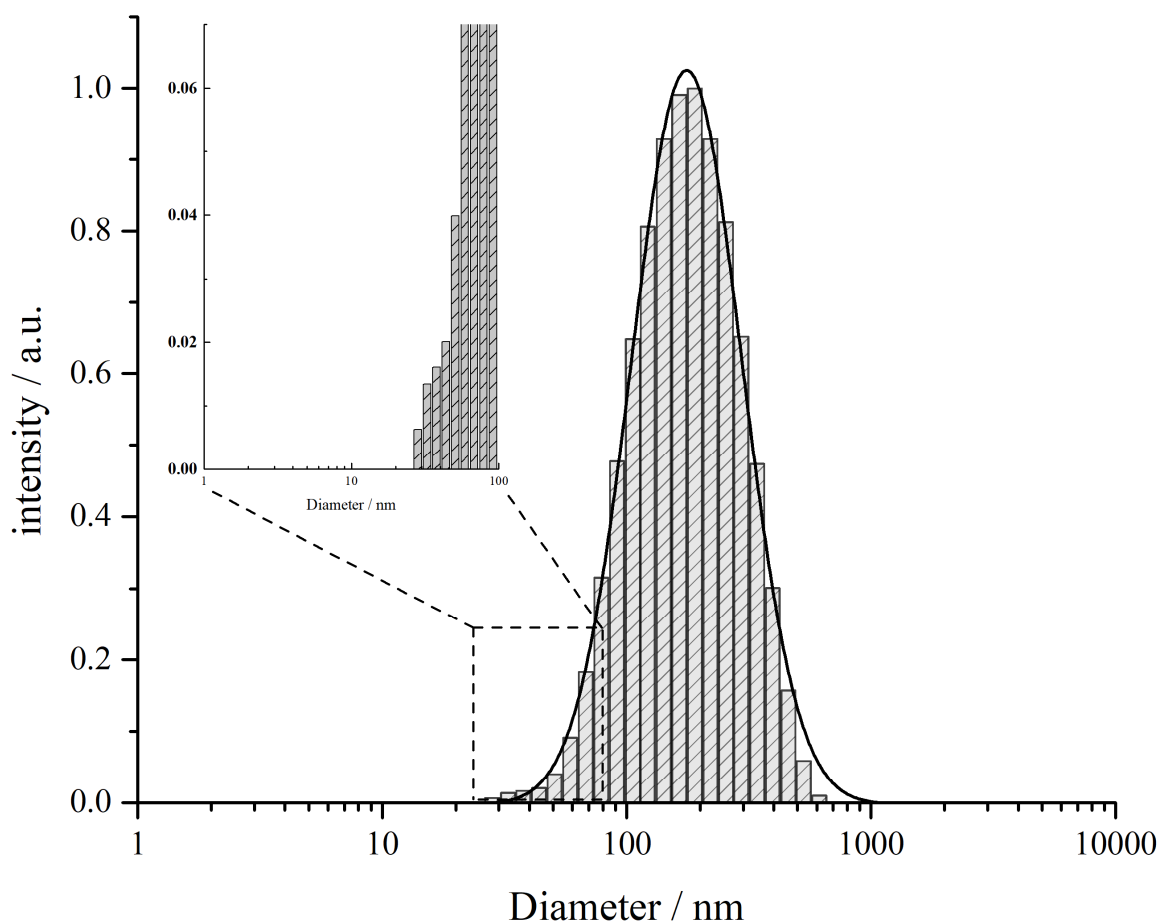


Fig. 79: DLS measurement of silver nanocubes and an applied gold shell. The graph shows the intensity (a.u.) as a function of the diameter (nm). If the data is evaluated with care the graph shows intensity in the region between 25-55 nm.

The size distribution by intensity obtained from DLS also reveals a signal for particles with a size around 25-55 nm (compare Fig. 71). By addition of the shell the particle morphology is maintained which leads to the conclusion that the same effects made for silver nanocubes are the case for those signals (see chapter 5.3.1). The intensity in this region is increased compared to the single-phased silver nanocubes. The directional growth of the shell along the (111)- and (110)-crystallographic planes (compare Fig. 75 and Fig. 76) will have a strong influence of the diffusion coefficient of the system. Based on the understanding that the small signal is generated by anisotropic structures and not by small particles, the anisotropic character of the system has increased. The main signal of the measurement is at $230 \text{ nm} \pm 126 \text{ nm}$ and therefore comparable to the data obtained by single silver nanocubes. The increase in the standard deviation is most likely also an effect of the increase in anisotropy. The PDI obtained by DLS is 0.19 and hence confirms a monodisperse system after the addition of the shell. The ζ -potential with -40 mV is in the same magnitude of the used cubic seeds. To confirm that no smaller particles are present, a DCS measurement was performed.

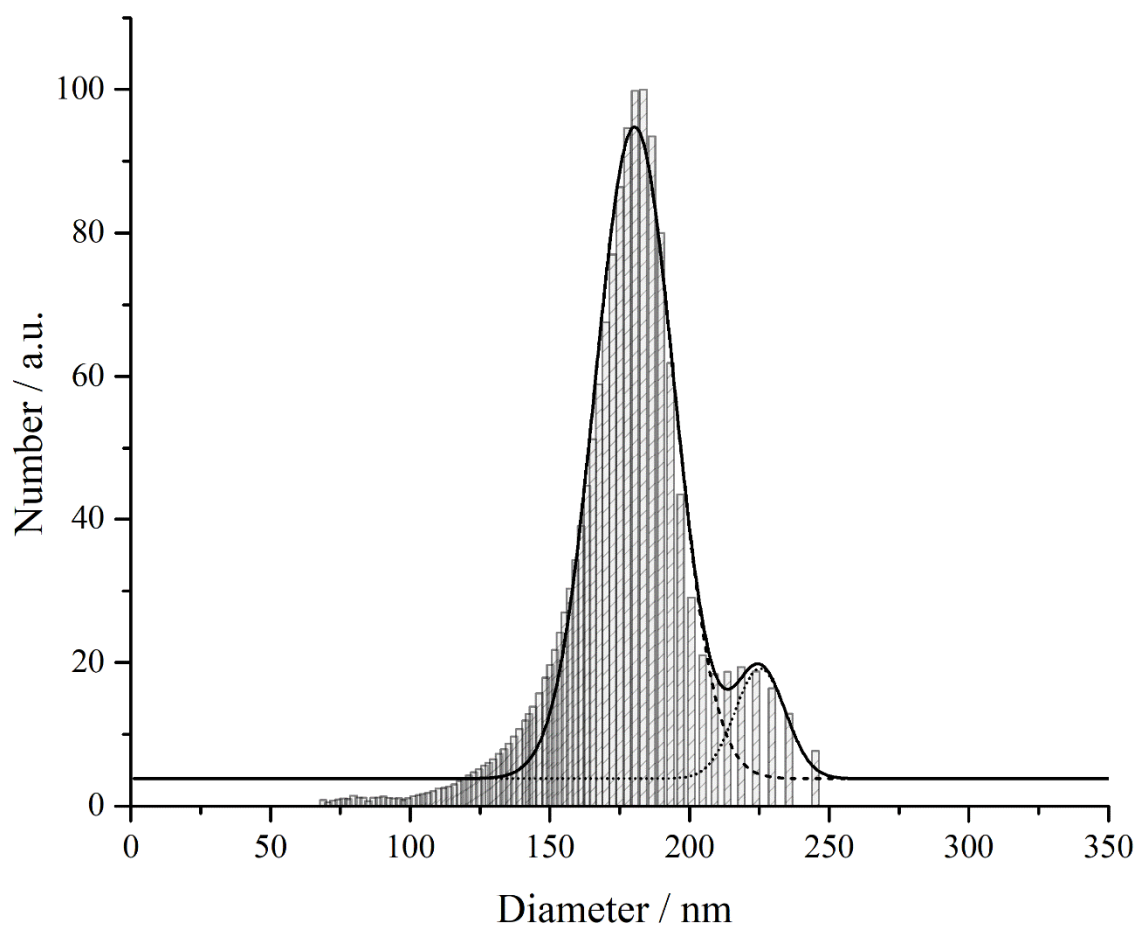


Fig. 80: Representative DCS measurement of silver-gold nanocubes with a nominal composition of 90:10 (Ag:Au). The graph shows the number (a.u.) as a function of the particle diameter (nm).

After the shell application, the system still results in a bimodal size distribution with a small maximum at $225 \text{ nm} \pm 14 \text{ nm}$ and a second main maximum at $180 \text{ nm} \pm 9 \text{ nm}$. This overall size increase compared to the seeds is in accordance to the formed shell and its thickness. The size distribution is maintained but slightly shifted to higher maximum mean sizes. The calculated PDI of the core-shell system is with 0.02 the same as the PDI of phase-pure silver nanocubes. Comparable datasets were obtained for all other synthesized compositions. The performed synthesis can also be used to generate silver nanocubes with a shell of palladium.

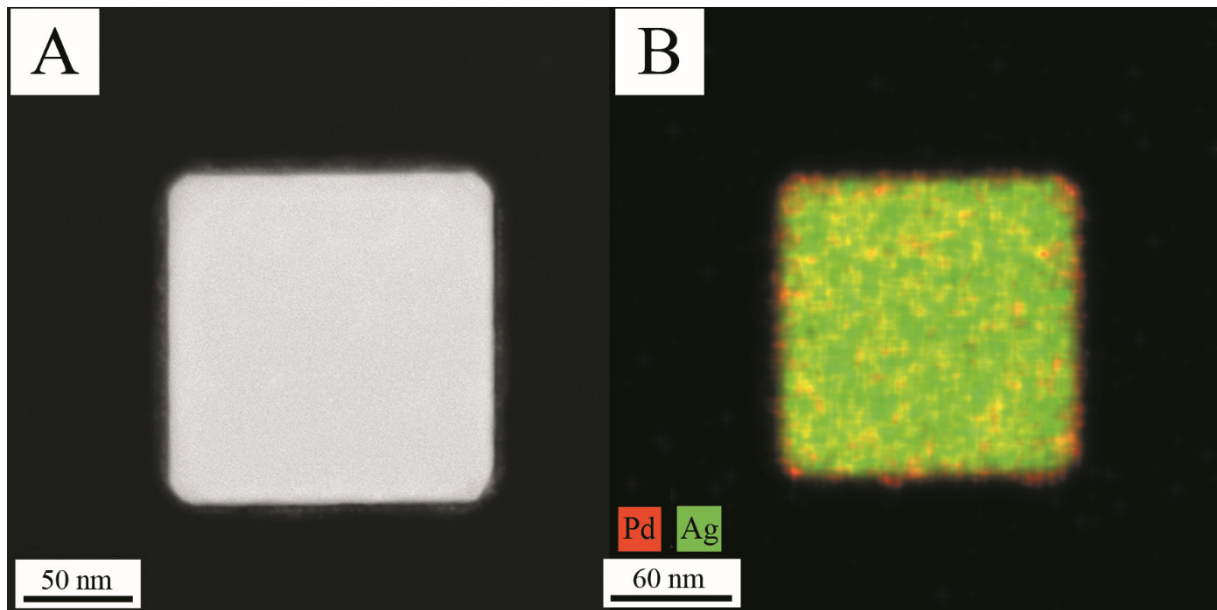


Fig. 81: HAADF image of a silver-palladium core-shell nanocube with a nominal composition of 90:10 (A) and the corresponding EDX map (B). The images were taken with an accelerating voltage of 300 kV.

The silver-palladium nanocubes with a nominal composition of 90:10 show a shell formation of palladium around the used silver seeds. The amount of palladium determined by EDX in comparison to gold in the same nominal composition is much smaller. The distribution derived by EDX is 98:2 (Ag:Pd). The determination by AAS revealed a real composition of 95:5 (Ag:Pd). Consequently only $\sim 50 \%$ of the used palladium have been incorporated as shell material. This observation is in good agreement with former investigations of bimetallic nanoparticles of silver and palladium in this work (compare chapter 5.2.3, Table 20). All experiments with palladium as shell material have led to reduced amounts of palladium in the investigated systems. An explanation is based on the competition between accretion and nucleation of the emerging palladium atoms. Consequently, palladium atoms will form new spherical nanoparticles which are separated by centrifugation in the purification process. An accumulation of palladium at the $\{111\}$ - and $\{110\}$ -facets is still observable. The directional

growth of palladium has the same effects on the absorption spectra as the gold-shell. The decrease in quadrupole resonance however is not as strong, since the palladium shell is much thinner, and the electron density of palladium is smaller compared to gold (see Fig. 82).

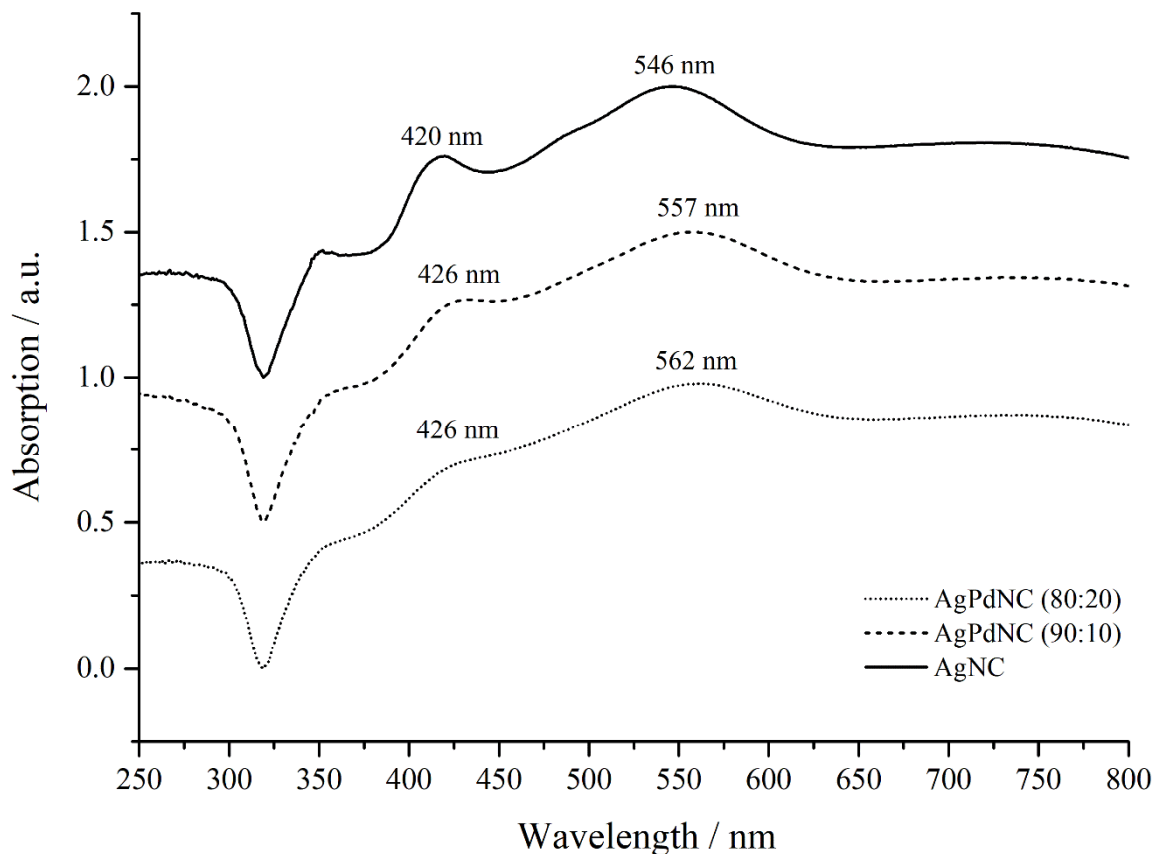


Fig. 82: UV/Vis spectra of phase-pure silver nanocubes (NC) and core-shell systems with a palladium shell in different compositions. The absorption (a.u.) is shown as a function of the wavelength (nm).

The nominal composition of 80:20 (Ag:Pd) led to a real composition of 90:10 (Ag:Pd). In closer consideration the application of additional palladium also leads to a minor effect on the quadrupole resonance compared to gold. The absorption band at 426 nm is still visible if 10 mole percentage of palladium is applied (Fig. 82, dotted line). Furthermore, the redshift for all compositions is less dominant compared to gold. This leads to the conclusion that a material with no plasmon resonance in the visible range has a reduced impact on the quadrupole resonance of silver nanocubes if applied as shell material. A complete characterization of all synthesized compositions was performed by DLS, DCS, AAS and UV/Vis spectroscopy. The data is summarized in Table 22.

Table 22: Mean size, standard deviation, polydispersity index (PDI) and the coefficient of determination (COD) for the applied Gauss-fits for all size determining methods of all synthesized compositions. The data is compared to the data of the used seeds. Additionally, the maximum absorption band of the UV/Vis spectra and the composition determined by AAS is depicted.

AgNC (Seeds)				
Method	DLS	DCS	UV/Vis absorption / nm	(Ag:M) AAS composition
Diameter / nm	227	204/167		
Standard deviation (σ) / nm	90	19/24		
PDI	0.16	0.02	420	100:0
COD (R^2)	0.9988	0.9798	546	
AgAuNC (90:10)				
Method	DLS	DCS	UV/Vis absorption / nm	(Ag:Au) AAS composition
Diameter / nm	230	225/180		
Standard deviation (σ) / nm	126	14/9		
PDI	0.19	0.02	644	92:8
COD (R^2)	0.9873	0.9811		
AgAuNC (80:20)				
Method	DLS	DCS	UV/Vis absorption / nm	(Ag:Au) AAS composition
Diameter / nm	232	228/184		
Standard deviation (σ) / nm	120	18/12		
PDI	0.18	0.02	671	86:14
COD (R^2)	0.9749	0.9758		
AgAuNC (70:30)				
Method	DLS	DCS	UV/Vis absorption / nm	(Ag:Au) AAS composition
Diameter / nm	233	228/184		
Standard deviation (σ) / nm	118	20/11		
PDI	0.18	0.02	535	76:24
COD (R^2)	0.9924	0.9863		
AgPdNC (90:10)				
Method	DLS	DCS	UV/Vis absorption / nm	(Ag:Pd) AAS composition
Diameter / nm	228	204/168		
Standard deviation (σ) / nm	90	20/24		
PDI	0.16	0.02	420	95:5
COD (R^2)	0.9987	0.9678	557	
AgPdNC (80:20)				
Method	DLS	DCS	UV/Vis absorption / nm	(Ag:Pd) AAS composition
Diameter / nm	230	204/168		
Standard deviation (σ) / nm	110	20/24		
PDI	0.17	0.02	420	90:10
COD (R^2)	0.9887	0.9873	562	

In summary, silver nanocubes and core-shell nanocubes using different compositions could be synthesized. The silver nanocubes have explicit optical properties with two absorption bands. Those are caused by induced dipole and quadrupole moments of the {110}-facets of the nanoparticles. The used polymer PVP induces a directional growth by complexing the (100)-crystallographic planes of the forming silver nanoparticles leading to a cubic habitus. The nanocubes have a mean size of 200 nm and a narrow size distribution resulting in a PDI of 0.06. In addition to the nanocubes small amounts of other morphologies like cuboids, tetrahedrons and spheres are observed. Those morphologies lead to a small second fraction by intensity in the DLS measurement. The divergent diffusion corresponding to the morphology leads to a second signal in the size distribution by intensity. Due to the high quality of the generated silver nanoparticles they could be used to perform further syntheses of core-shell structures with gold and palladium.

The investigation of the core-shell structures by HRTEM, EDX mapping and UV/Vis spectroscopy reveals a directional growth of the shell material at the {111}- and {110}-facets. The PVP-complexed {100}-facets of the particles cause an inhibited growth and lead to increased accretion at the remaining facets. This accretion leads to a vanishing of the absorption maximum of the silver nanocubes at 420 nm in the UV/Vis spectrum and has hence a direct influence of the quadrupole resonance of the particles. Furthermore, the application of gold leads to a bathochromic shift of the main maximum at 546 nm. This effect intensifies with the increase of gold regarding the used compositions (compare Table 22). If the amount of gold is increased to a composition of 70:30 (Ag: Au), the UV/Vis spectrum changes to the appearance of gold nanocubes. The attenuation of the absorption maxima as well as the bathochromic shift can also be observed for an addition of a palladium shell. However, the effects are notably reduced. The particles obtained after the shell addition maintain their morphology. The mean size distributions of the core-shell systems show a size increase corresponding to the applied amount of the second material. The ζ -potential and the PDI remain comparable to those of the used cubic seeds and hence lead to monodisperse, colloidal stable systems.

The use of palladium as shell material reveals a competition between nucleation and accretion by the formed palladium atoms. This leads to a reduced amount of palladium in the product.

5.3.3 Characterization of silver nanowires synthesized with hetero seeds

A common technique to generate silver nanowires is a hetero nucleation of silver at silver chloride seeds. The formed cubic silver chloride particles will be used as crystallization seeds, where penta-twinned silver nanoparticles will grow at the corners.^[89] The addition of PVP leads to a complexation of the $\{100\}$ -facets of the growing silver nanoparticles (compare chapter 5.3.1) and induces a directional growth to nanowires. Besides syntheses with hetero seeds like platinum^[87, 175] or silver chloride^[86], nanowires can also be realized without addition of other additives except silver nitrate and PVP.^[88] However, all those methods are seed and growth approaches. The slow addition of silver precursor leads to a kinetic growth in $\{110\}$ direction with an inhibited growth on the $\{100\}$ -facets and hence to an elongated wire-like morphology.

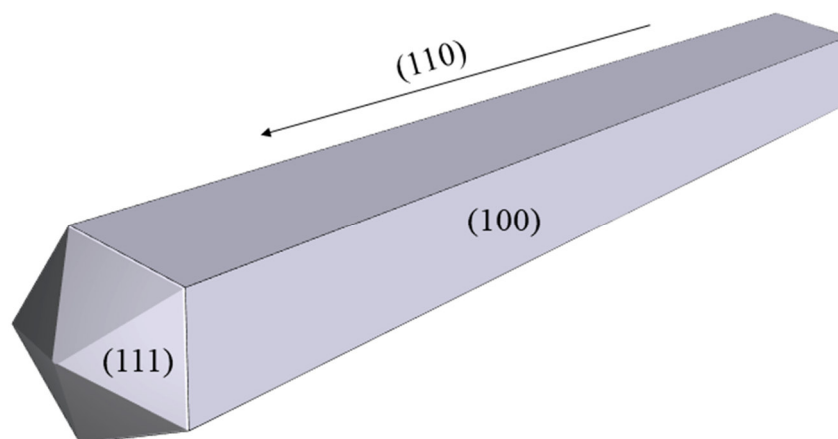


Fig. 83: Schematic geometrical 3D model of a silver nanowire obtained from the polyol process using hetero seeds of silver chloride. The Figure depicts the low indexed crystallographic planes of a particle and was adapted from Sun et al.^[176]

The synthesis was performed after Buhro et al. and consequently used hetero seeds of silver chloride. The formed silver chloride seeds are dissolved with ammonia after completion of the reaction. The used solvent, ions and free polymer are separated from the particles by purification via centrifugation. After purification the particles were characterized by SEM, XRPD, UV/Vis spectroscopy, DLS and the ζ -potential was determined.

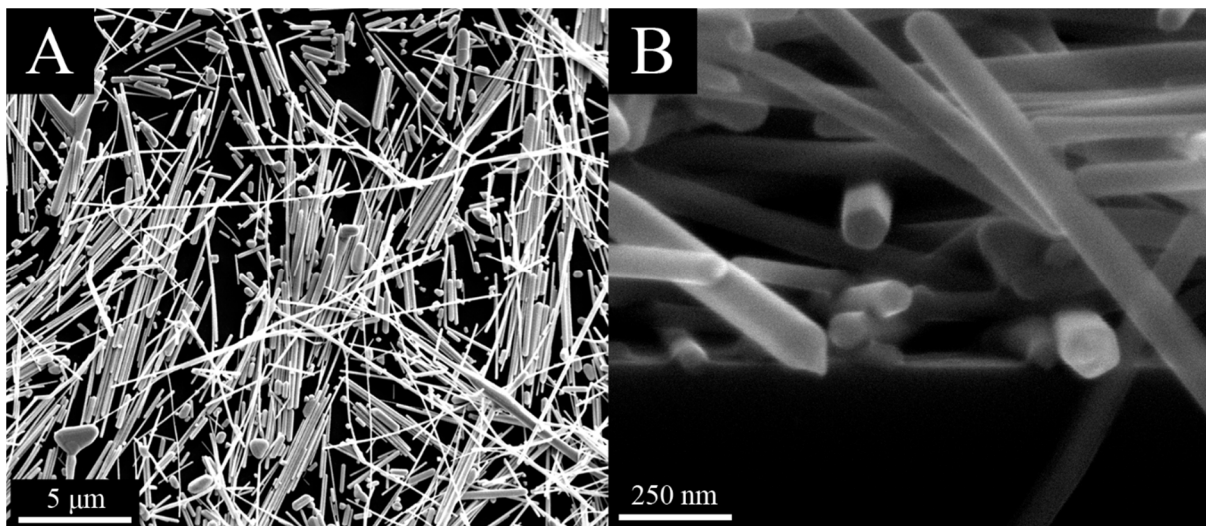


Fig. 84: SEM images of the synthesized silver nanowires with a magnification of 10000 (A) and a magnification of 200000 showing the dodecahedral structure of the cross-section (B). The images were taken with accelerating voltages of 8 kV (A) and 25 kV (B).

The SEM images show that mostly nanowires have been generated. In addition, few particles with other morphologies can be observed. Furthermore, shorter wires with an increased thickness can be found. The aspect ratio of length and width is relatively high. Most particles show a length of around 15-20 μm whereas the width lies at $97 \text{ nm} \pm 23 \text{ nm}$. The former described decahedral structure of the particle ends can be visualized with SEM (see Fig. 84, B).

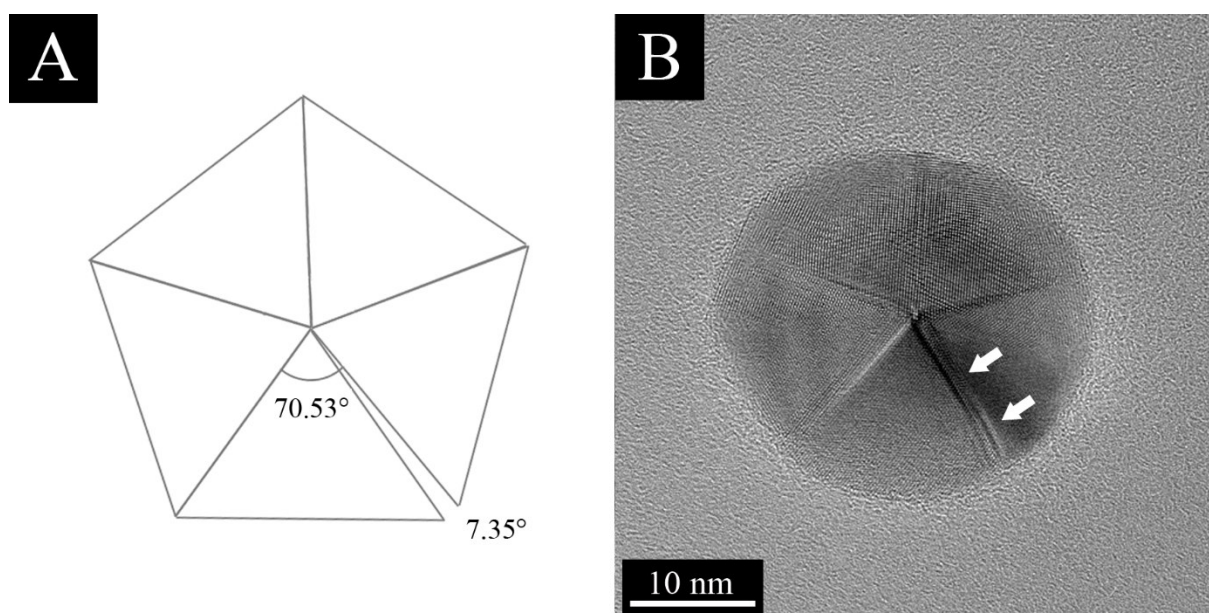


Fig. 85: Geometrical model of penta-twinned tetrahedral (A) and a single penta-twinned particle obtained from the glucose synthesis (B). The white arrows indicate stacking faults and twin defects at the grain boundaries caused by the generated gap of 7.53° .

To identify if phase-pure silver was generated, and all seeds of silver chloride have been removed, the product was analyzed by XRPD. The dodecahedral seed structure has a direct influence of the system's crystallography. Due to certain geometrical reasons corresponding to the opening angle of the five tetrahedrons of 70.53° , a gap of 7.35° results (see Fig. 85). Investigations by Sun et al. have shown that the defects, which develop along the (110)-axis of the silver fcc-structure, form a stable bct-phase with a highly preferred orientation along the (002)-crystallographic plane. Those defects have a direct influence on the XRPD pattern and will cause a shoulder at the (200)-reflex of the silver fcc-pattern (Fig. 86).

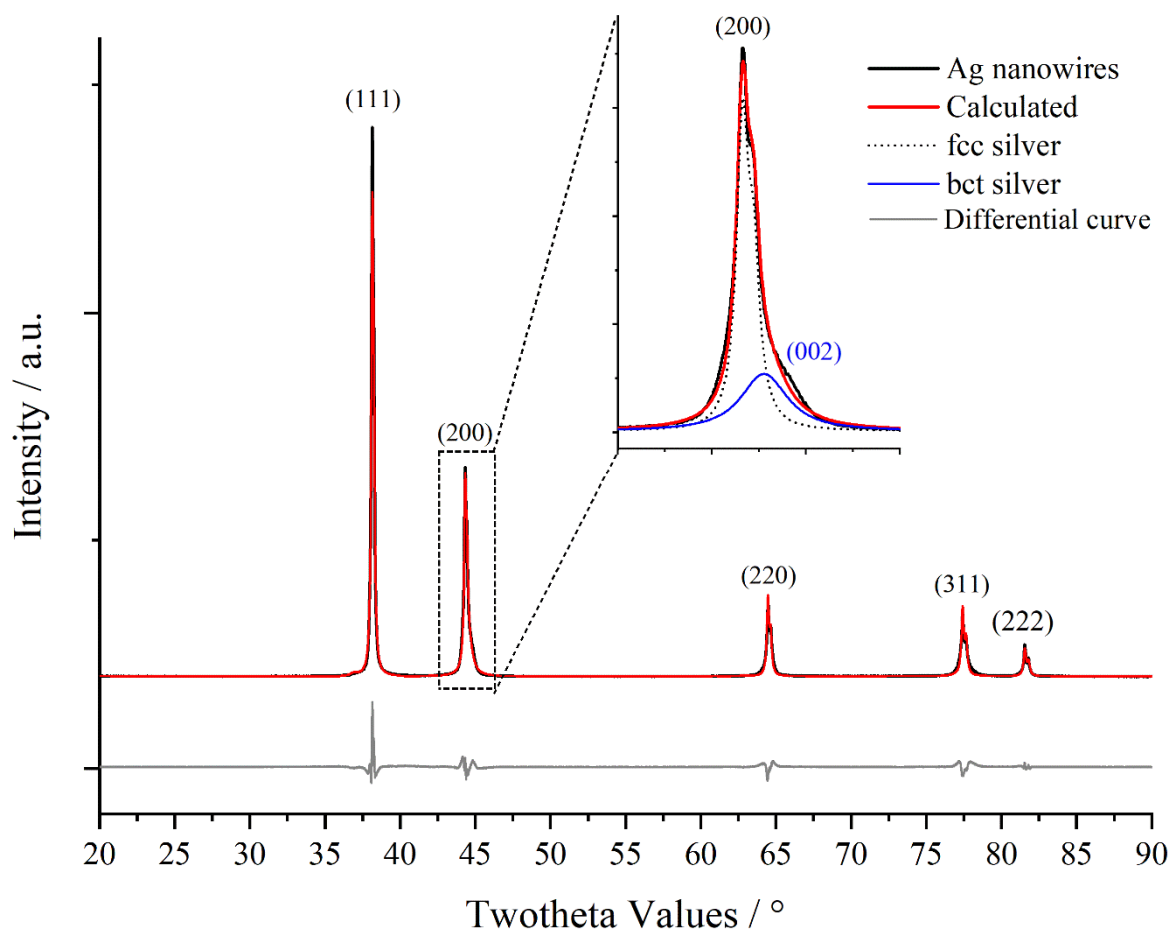


Fig. 86: Rietveld refined pattern of silver nanowires obtained from powder X-ray diffraction. The measurement was performed using Bragg-Brentano geometry and reveals a strong preferred orientation along the (200)-crystallographic plane of the silver fcc-pattern (not $K_{\alpha 2}$ stripped).

The pattern shows no additional reflexes for silver chloride which was consequently completely removed. The refinement using a bct-phase additional to the fcc-phase leads to much better results and shows that a stable tetragonal phase is present. A tetragonal phase of palladium was already identified by Xia et al. applying high pressure to nanocubes and nanoplates.^[177] However, the induced phase transition was only stable at 12-25 GPa and vanished completely

5.3 Synthesis of silver nanoparticles with the polyol process

after the pressure was removed. Sun et al. could show that this phase is also present in silver nanowires.^[176] Stacking faults and twin defects at the grain boundaries caused by the former described gap of the penta-twinned structure is the cause of the formation. The parameters obtained from the refinement for both phases are shown in Table 23.

Table 23: Space groups, calculated lattice parameters (*LP*) and cell volume of the cubic and the tetragonal silver phases compared to the literature (lit.).

Phase	Space group	<i>LP</i> (<i>a</i> / Å)	<i>LP</i> (<i>c</i> / Å)	Cell volume / Å ³
Ag fcc	<i>Fm-3m</i>	4.0830	-	68.0660
Ag bct	<i>I4/mmm</i>	3.0009	4.0519	64.1067
Ag fcc lit. ^[113]	<i>Fm-3m</i>	4.0860	-	68.2174
Ag bct lit. ^[176]	<i>I4/mmm</i>	2.8990	4.0580	n.a.

The lattice parameter of the fcc-phase with 4.0830 Å is decreased in comparison to bulk silver. This effect is caused by small domain sizes, high amounts of stacking faults and the increase of surface defects due to the nano-crystalline nature (compare chapter 5.2.1). The lattice parameters of the bct-phase are also slightly shifted but are in good agreement with the literature values.^[176] A single peak analysis of the pattern can be used to determine the extension of the lattice planes of single crystallites of the corresponding indices. This analysis can additionally be utilized to investigate the anisotropic growth. The crystallite domain size is calculated by the Scherrer equation.

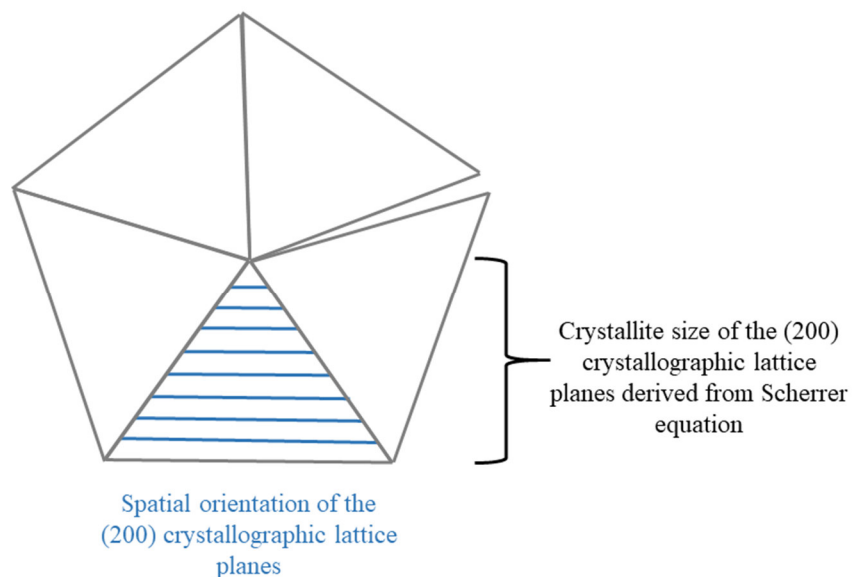


Fig. 87: Cross-section of a dodecahedral silver nanowire and spatial orientation of the (200)-lattice planes inside the nanowire.

Since the nanowires are constructed of penta-twinned crystals, the average radius of the particle cross-section corresponds to the calculated extension of the (200)-crystallographic lattice planes (compare Fig. 87). Hence the doubling of the calculated crystallite size leads approximately to the mean diameter of the silver nanowires.

Table 24: Crystallite sizes for domains of different lateral dimensions of silver nanowires derived from Scherrer equation.

Phase	Domain (hkl)	Crystallite size / nm
Ag fcc	111	38
Ag fcc	200	35
Ag bct	002	14

The crystallite size obtained for the (200)-lattice plane is 35 nm and leads to a mean diameter of the silver nanowires of 70 nm. This value is in good agreement with the $97 \text{ nm} \pm 23 \text{ nm}$ obtained from SEM measurements. The crystallites in (111)-direction have a size of 38 nm and verify the anisotropic growth of the particles. The crystallites of the bct-phase have a mean size of 14 nm and are much smaller compared to the evaluated crystallites of the fcc-phase.

The anisotropic nature of the obtained particles constitutes a problem with the typically executed characterization methods to determine the colloidal stability and size in solution. Because of the enormous length of the particles, the sedimentation rate using DCS is too fast to gain evaluable data. This leads to incorrect results which are consequently not usable. Furthermore, has the high anisotropic character on the wires a direct influence of the scatter intensity measured by DLS. The particles will have different diffusion coefficients regarding the length and the width. Additionally, a rotational movement can take place and will also lead to a modified diffusion as well as a different scattering. Hence, particles with high anisotropic character show a bimodal size distribution in DLS intensity measurements (compare Chapter 5.1.1). This second signal at smaller sizes will increase with the anisotropic character.

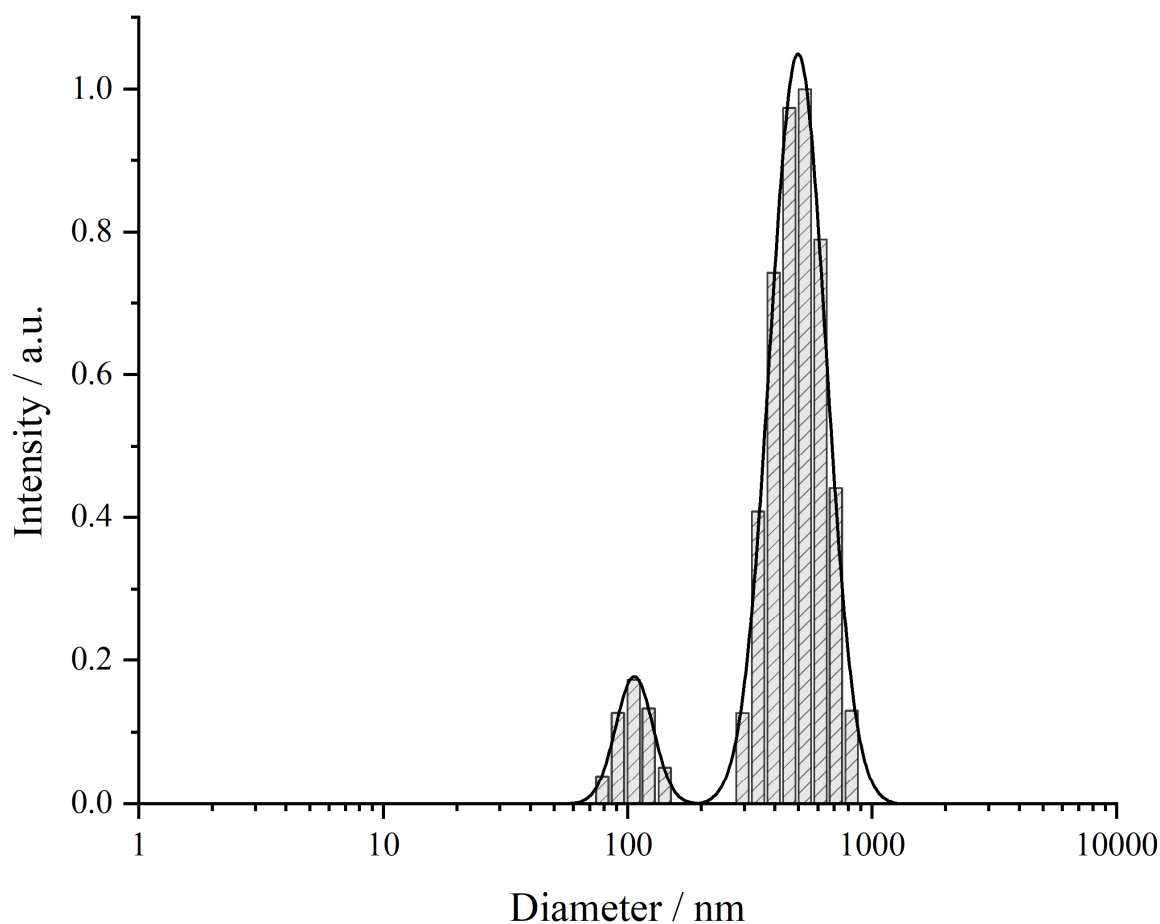


Fig. 88: DLS measurement of silver nanowires. The graph shows the intensity (a.u.) as a function of the diameter (nm). The bimodal size distribution results from the anisotropic structure and the corresponding differences in diffusion coefficients.

The bimodal size distribution reveals two different maxima for the executed measurement on silver nanowires. The first maximum has a mean size of $511 \text{ nm} \pm 123 \text{ nm}$ and the second

maximum has a mean size of 108 nm with a standard deviation of 17 nm. However, the data is strongly afflicted with errors due to the limited measurement geometry and missing adaptations of the methods. The determination of the ζ -potential leads to a value of -37.5 mV. This indicates an additional electrostatically stabilization by the absorption of NO_3^- -ions from the used metal precursor silver nitrate.

To characterize the optical properties of the synthesized nanoparticles, UV/Vis spectroscopy was performed. Silver nanowires have distinct optical properties which can be characterized by their absorption of visible light. Consequently, an absorption spectrum has been recorded.

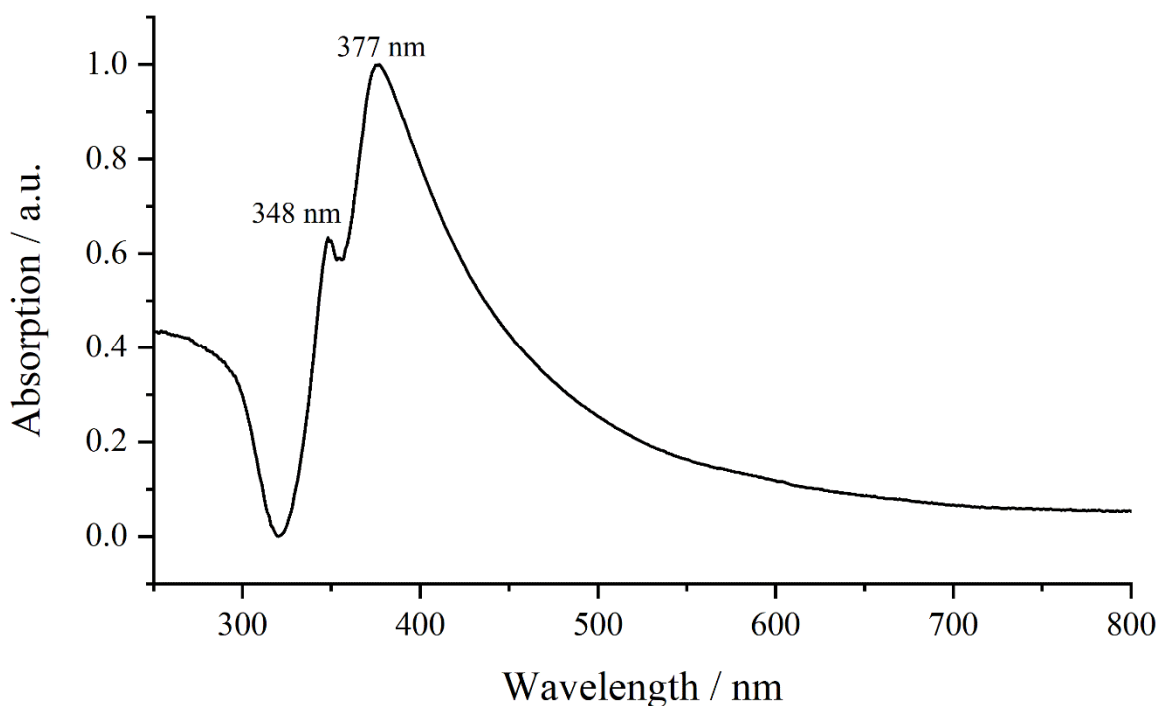


Fig. 89: UV/Vis spectrum of silver nanowires. The graph depicts the absorption (a.u.) as a function of the wavelength (nm).

Due to the high anisotropic character of the particles, two kinds of energetically different surface plasmons are present. Those can be excited by specific visual light wavelengths and will induce an *out-of-plane* quadrupole resonance with an absorption maximum at 377 nm. Furthermore, an *out-of-plane* dipole moment of the $\{100\}$ -facets, which can be excited by a wavelength of 348 nm, will be induced (see Fig. 89).^[88] The obtained spectrum is in accordance with spectra from the literature.^[87-88]

In summary it was possible to synthesize silver nanowires with high quality. The generated particles were suitable to perform further core-shell experiments.

5.3.4 Core-shell particles based on silver nanowires

To generate core-shell particles from previously synthesized silver nanowires, the same parameters as for silver nanocubes and spheres were applied. The systems were synthesized in the compositions of 80:20 (Ag:M) with palladium and gold as shell materials. Furthermore, experiments with compositions of 50:50 (Ag:Pd) were produced to investigate the optical properties after the shell has fully developed. All discussions about the systems will be made with the data from palladium hence the silver-gold system showed comparable results. The different compositions were characterized using SEM, HAADF, EDX mapping, AAS, DLS and the ζ -potential was determined.

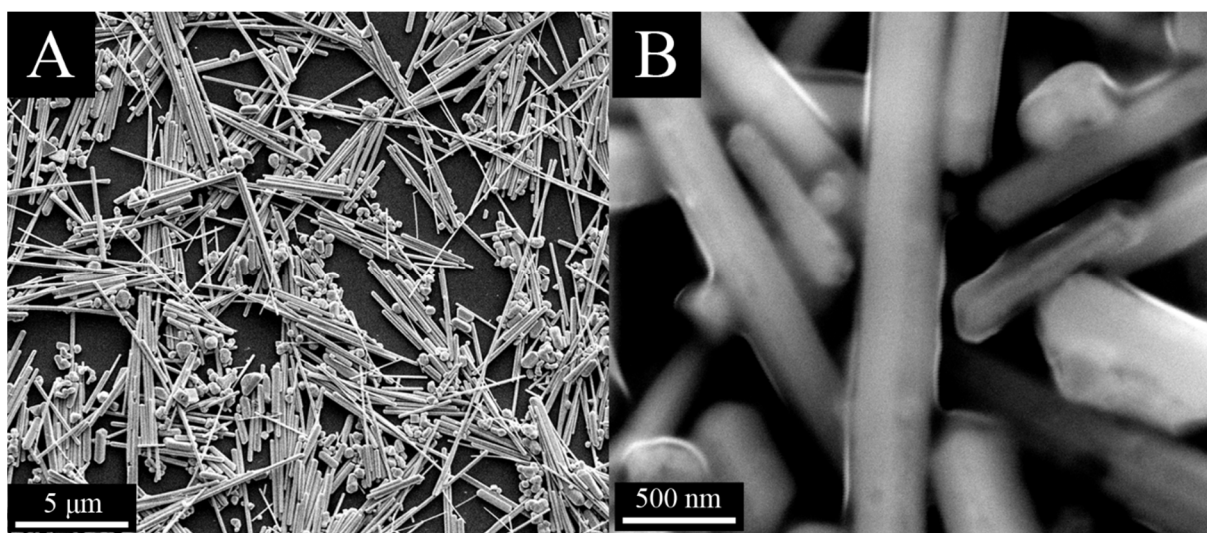


Fig. 90: SEM images of the synthesized silver-palladium nanowires (50:50) with a magnification of 10000 (A) and a magnification of 100000 (B). The images were taken with an accelerating voltages of 10 kV (A) and 20 kV (B).

The SEM images of core-shell silver-palladium nanowires with a nominal composition of 50:50 (Ag:Pd) reveal that the morphology after shell application is maintained (Fig. 90). The average particle width lies in a range between 70-130 nm and is therefore increased compared to phase-pure silver nanowires. The length of the particles remains in a high varying size range between 5-15 μm and is hence still comparable but shortened compared to the used seeds. Since the particles are washed two more times after shell application, a shortening by breaking structures is a possible explanation. Former syntheses of core-shell systems with palladium have shown that the used amount of palladium differs from the real composition. In general, around 50 % of palladium will nucleate to small spherical palladium particles which will be

separated by the purification process. To determine the real composition of the system, an AAS measurement for the concentrations of silver and palladium was carried out. The determined composition by AAS was 70:30 (Ag:Pd) and consequently shows a 40 % loss of palladium. To confirm a shell formation and the composition determined by atomic absorption spectroscopy, the particles were further investigated by HAADF imaging and an EDX map was generated.

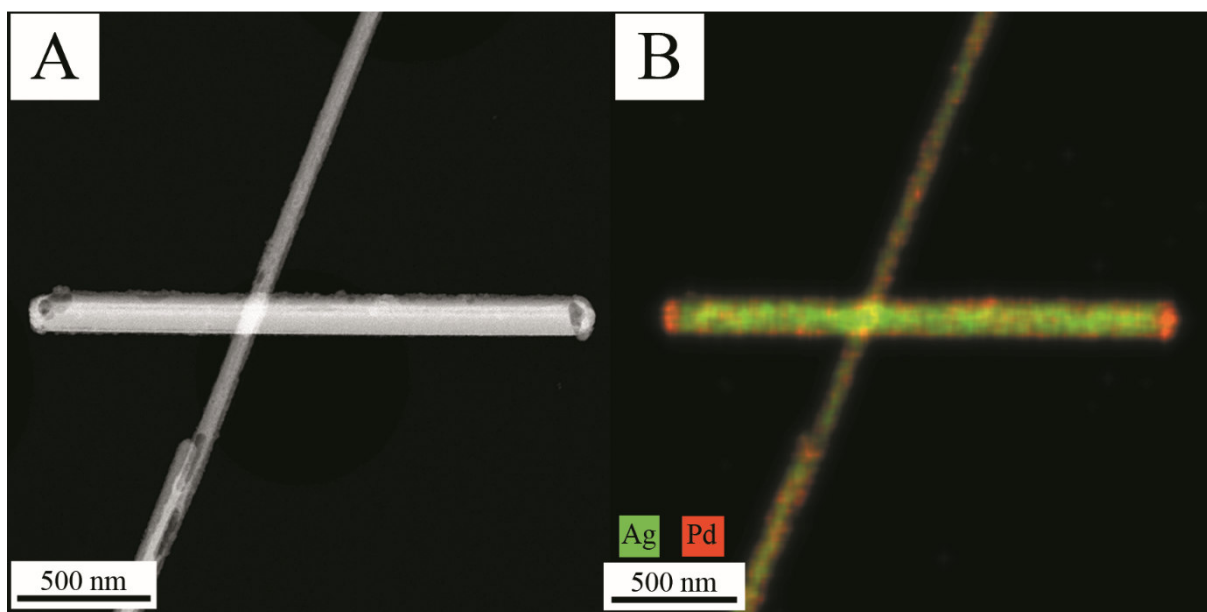


Fig. 91: HAADF image of a silver-palladium core-shell nanowires synthesized with a nominal composition of 50:50 (A) and the corresponding EDX map (B). The images were taken with an accelerating voltage of 300 kV.

The mapping of single particles (Fig. 91, B) leads to a composition of 76:24 and is therefore in good agreement with the values obtained from AAS (70:30). A shell of palladium has developed while the morphology is maintained. The EDX map reveals an enrichment of palladium at the end of the wires with a thickness of 55-70 nm. Since those are constructed of $\{111\}$ -facets (compare Fig. 83, chapter 5.3.3), a directional growth of the shell is a reasonable explanation. Hence PVP complexes the $\{100\}$ -facets, a growth in this crystallographic plane is inhibited. In addition, palladium can also be found at the $\{100\}$ -facets which indicates a beginning shell closure. To gain a deeper insight in the directional growth and the corresponding changes in the crystallography of the system, an XRPD pattern was generated.

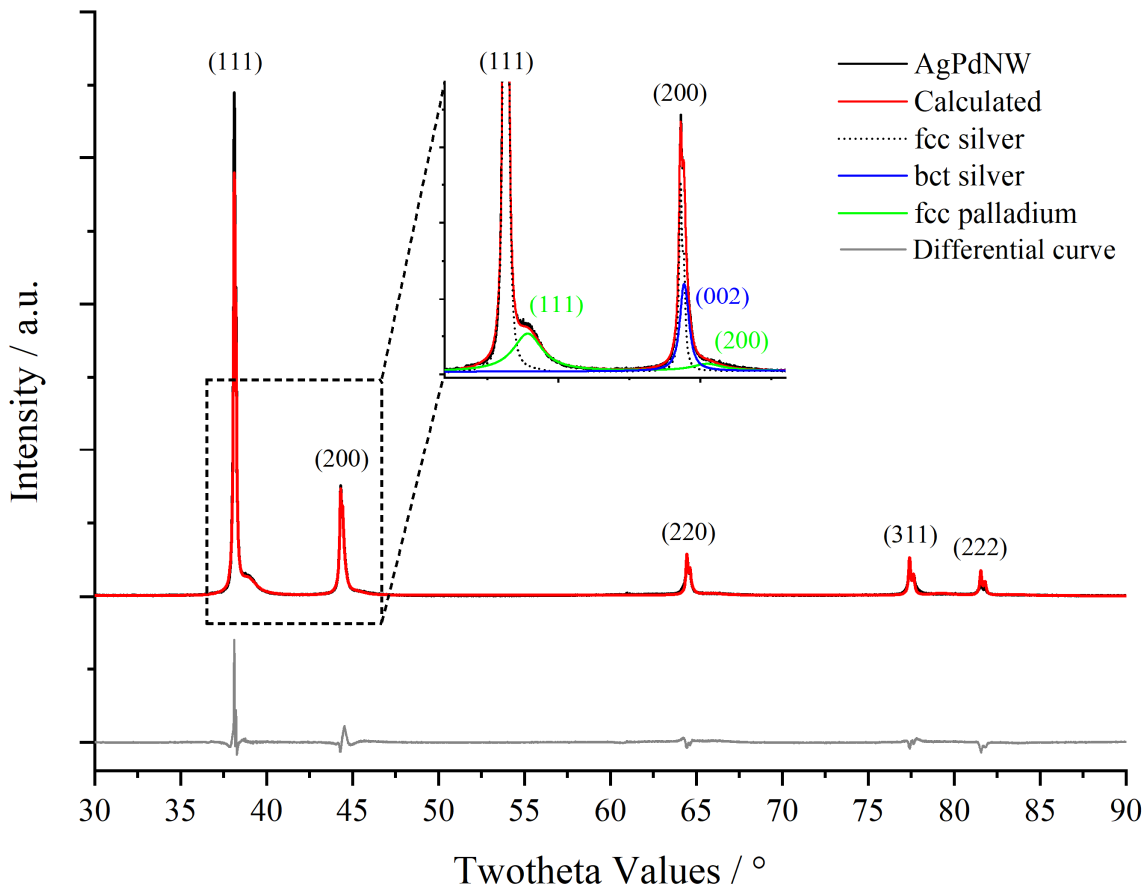


Fig. 92: Rietveld refined pattern of silver-palladium nanowires obtained from powder X-ray diffraction. The measurement was performed using Bragg-Brentano geometry and hence shows a strong preferred orientation along the (111)- and (200)-crystallographic planes.

Since the further analyzed sample of silver nanowires were used as seeds to generate the core-shell system, the XRPD data can be compared. The refinement was again used to calculate the lattice parameter and the cell volumes (Table 25).

Table 25: Space groups, calculated lattice parameters (LP) and cell volumes of the cubic and the tetragonal silver phases of silver-palladium and pure silver nanowires compared to literature values.

Phase	Space group	LP (a / Å)	LP (c / Å)	Cell volume / Å ³
Ag fcc (AgPd)	$Fm-3m$	4.0877	-	68.3041
Pd fcc (AgPd)	$Fm-3m$	4.0089	-	64.4290
Ag bct (AgPd)	$I4/mmm$	3.2688	4.0629	39.2909
Ag fcc (Ag)	$Fm-3m$	4.0830	-	68.0660
Ag bct (Ag)	$I4/mmm$	3.0009	4.0519	37.6998
Ag fcc lit. ^[113]	$Fm-3m$	4.0860	-	68.2174
Pd fcc lit. ^[178]	$Fm-3m$	3.9910	-	63.5690
Ag bct lit. ^[176]	$I4/mmm$	2.8990	4.0580	n.a.

The powder pattern after shell applications reveals that the shoulder of the (200)-reflex is still present and has even risen in intensity. Additionally, a second intensity increase corresponding to the (111) reflex of the palladium fcc-phase can now be observed. It arises as a shoulder of the (111)-reflex of the fcc-silver. Since palladium has been added to the system, the signals of the silver bct-phase and the palladium fcc-phase overlap. A calculation is still possible since the refinement gives reasonable values. However, the values for the bct-phase must be treated with care due to the strong overlap. The lattice parameters and volumes of both fcc-phases could be determined. The silver fcc-phase still shows comparable values to the used silver seeds. A single reflex analysis was carried out to determine the extension of the (111) and (200) lattice planes of both fcc-lattices (Ag, Pd). The results are compared to the former calculated extensions of the pure silver nanowires (Table 26).

Table 26: Crystallite sizes for domains of different lateral dimensions of silver and silver-palladium nanowires derived from Scherrer equation.

Phase	Domain (hkl)	Crystallite size / nm
Ag fcc (Ag)	111	38
Ag fcc (Ag)	200	35
Ag bct (Ag)	002	14
Ag fcc (AgPd)	111	39
Ag fcc (AgPd)	200	37
Ag bct (AgPd)	002	23
Pd fcc (AgPd)	111	7
Pd fcc (AgPd)	200	7

The investigation shows that all lateral dimensions have grown after the shell is applied. Since phase-pure palladium has grown on certain facets both phases can be clearly distinguished in the pattern. The domain size increase also shows that the nanowires did not experience a galvanic replacement reaction. The increase of the (111) and (200) lateral dimensions as well as the appearance of the corresponding palladium reflexes are in good agreement to the EDX map of single particles. Since the most palladium is added to the (111) and (200) facets palladium also shows a strong intensity for the corresponding reflexes. This shows that a directional growth of a shell material can be identified by XRPD. Interestingly, the significant size increase of the (110) lattice plane of the bct-phase might indicate strong directional growth of palladium at this specific surface. However, the method has certain limitations regarding stacked reflex profiles and hence the data should not be over interpreted. The differences in intensity of the (220), (311) and (222) reflexes compared to the pattern of the used seeds is related to the sample preparation. The core-shell sample was directly applied from solution whereas the sample of pure silver was previously lyophilized. The freeze-dried particles often

build granules which leads to a random spatial distribution of the particles reducing a preferred orientation on the sample holder.

To investigate the influence of the applied shell on the optical properties, UV/Vis spectra of different compositions were prepared. The amount and kind of applied shell material regarding silver nanocubes (chapter 5.3.2) has shown that the forced directional growth has a huge influence on the resulting absorption spectra. For a better comparability the spectra of different compositions of silver-palladium nanowires were labeled with the real composition determined by AAS. This was done because the nominal and real compositions differ significantly.

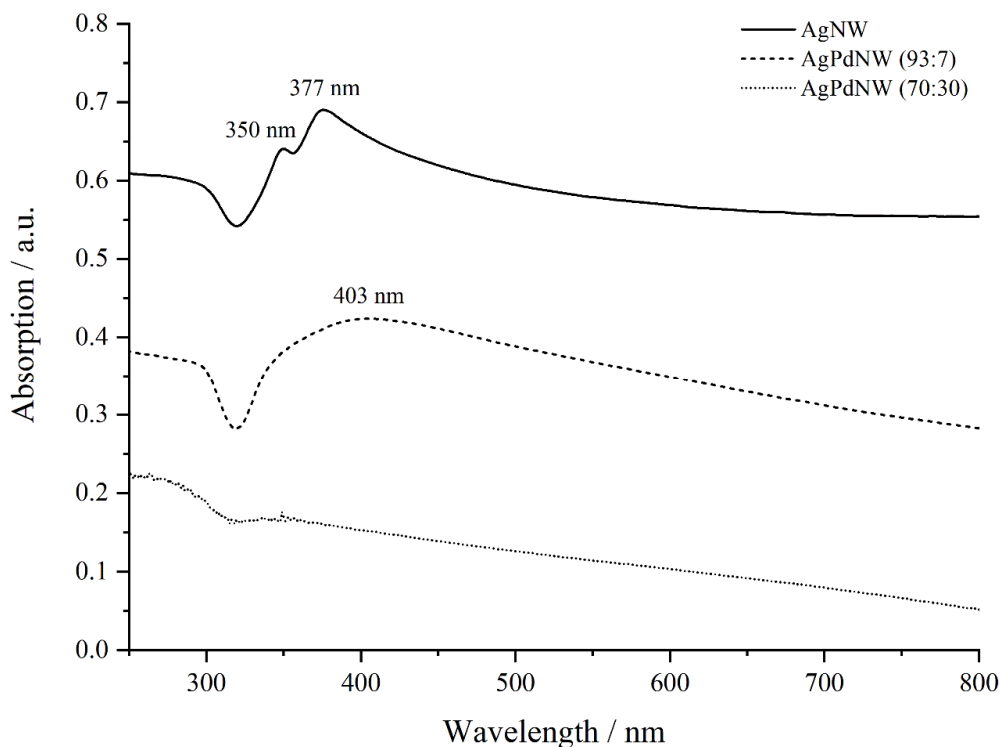


Fig. 93: UV/Vis spectra of phase-pure silver nanowires (NW) and core shell systems with palladium in different real compositions. The absorption (a.u.) is shown as a function of the wavelength (nm). The graphs have been stacked for a better overview.

The induced *out-of-plane* dipole moment of silver nanowires at a maximum of 350 nm completely vanishes after 7 mole percentage of palladium (nominal 80:20 (Ag:Pd)) is applied. Furthermore, the absorption band at 377 nm has undergone a redshift to 403 nm. The main absorption band also broadens. Normally, this absorption is caused by the induced dipole moment of the {100}-facets of the crystal. Since it was shown that a directional growth happens along the {110}- and {111}-facets, the induced dipole moment must also depend on the nature of those facets to explain the gathered data. Consequently, the addition of another metal

completely changes the electrical nature of the particle. If enough shell material (30 mole %) is applied, the absorption spectrum will be the same as for dispersed palladium nanoparticles and will not develop any absorption bands in the visible region of the spectrum (Fig. 93).^[11]

In summary, silver nanowires could be synthesized. Furthermore, the addition of shell materials like palladium and gold was successful using different compositions. Silver nanowires are sustained using hetero seeds of silver chloride where penta-twinned seeds crystallize at the corners. Based on the relatively weak reducing agent ethylene glycol and the application of PVP, which complexes the (100)-crystallographic planes, a directional kinetic growth leads to the desired nanowires. The penta-twinned seeds have a resulting geometrical gap (compare Fig. 85, A) which leads to a high amount of twin defects and stacking faults (Fig. 85, B). Investigations by X-ray powder diffraction could show that those defects are caused by a stable tetragonal silver phase (bct) which grows along the (110)-axes and hence has anisotropic orientation in the direction of the (002)-lattice planes (Fig. 86). Additionally, the particles possess distinct optical properties which are attributable to the induced *out-of-plane* dipole and quadrupole moments of the (100)-crystallographic plane which result in absorption maxima at 348 nm and 377 nm. The characterization showed that the obtained particles were suitable to perform further experiments to generate core-shell structures with silver as core material.

The attachment of palladium or gold as shell material is directional if only 10-20 mole percentage are used. The directional growth of the shell was shown by the EDX map where increased amounts of shell material is observed at the $\{111\}$ -facets (Fig. 91, B). The directional growth was further confirmed by UV/Vis measurements of different compositions (Fig. 93) which show a direct influence of the absorption maxima caused by the induced *out-of-plane* dipole and quadrupole moments. The absorption maximum at 350 nm completely vanishes after an addition of 7 mole percentage palladium. Furthermore, a bathochromic shift of the absorption maxima at 377 nm is observed. A complete shell formation (real composition of 70:30 (Ag:Pd)) leads to an absorption spectrum which is comparable to phase-pure palladium nanoparticles in dispersion. The syntheses of core-shell nanowires with a silver core and either gold or palladium as shell material was successful. The obtained particles could therefore be used for dissolution kinetic experiments.

5.4 Dissolution of silver-based nanoparticle systems

The investigation of the dissolution of silver and bimetallic nanoparticles based on silver are quite interesting due to the antibacterial effects of silver ions.^[19-20, 179-180] Silver nanoparticles are able to diffuse through the cell membrane of bacteria and the released ions bind on specific sulfur, oxygen or nitrogen containing groups. This will lead to the loss of functionality of certain amino acids and enzymes containing the targeted groups. A resulting increased membrane permeability leads to loss of the proton motive force, leakage of cellular content and disrupted DNA replication.^[18]

Former investigations regarding the dissolution of silver nanoparticles have shown that the ion release rate directly correlates with the surface area and consequently with the size of the nanoparticles. The ion release occurs under oxygen containing atmospheres where active oxygen species oxidize the present particles.^[22] Additionally, the ion release rate can be correlated with the particle morphology. Consequently, morphologies with a high surface area to volume ratio, like platelets, will release more silver ions based on the used silver amount compared to morphologies like spheres, cubes or wires.^[23]

Supplementary studies of Köller et al.^[25-26] showed that silver nanodots sputtered on a novel substrate like gold exhibit an increased cytotoxicity. Especially silver dots sputtered on iridium revealed a significant increase cytotoxicity compared to palladium or gold surfaces.^[25-26] The former described syntheses in this work were carried out to combine both findings to eventually generate bimetallic particles of different morphologies and sizes with “designed” ion release rates. The used metals were chosen to match the systems of Köller et al. A mixture of different bimetallic and monometallic particles could in theory be applied to medical substrates like implants to provide a controlled silver ion release over the whole healing process.

To investigate the silver ion release rate, the concentrations of the synthesized particles were determined by AAS. All particle dispersion concentrations were set to 50 $\mu\text{g mL}^{-1}$ for a better comparability. The dispersions were then filled into the upper part of an Amicon[®] Ultra centrifugal filter where the lower part was filled with ultra-pure water. Consequently, the released silver ions diffused through the membrane into the lower part where they were quantified by AAS (for more details see experimental chapter 4.8).

5.4.1 Evaluation of the dissolution experiments

The setup and evaluation of the data was adapted from Dr. Viktoria Grasmik.^[24] For the experiments, overall 17 different particle systems were synthesized. These core-shell systems are based on former synthesized and characterized silver nanoparticles of different morphologies (spheres (different sizes), cubes and wires) as seeds. The pure silver nanoparticles were also compared as reference material. All synthesized systems are shown in Table 27.

Table 27: List of nanoparticles with nominal and real compositions (mol%, determined by AAS) for the performed dissolution experiments. The molar ratio of iridium containing samples were determined by EDX. The silver concentration could still be measured by AAS.

Synthesis	Morphology / size	Nominal molar ratio / Ag:M	real molar ratio / Ag:M (AAS)
Sample 1	Spheres / > 10 nm	(88:12) Ag:Ir	(92:8) Ag:Ir (EDX)
Sample 2	Spheres / > 10 nm	(80:20) Ag:Ir	(86:14) Ag:Ir (EDX)
Sample 3	Spheres / > 10 nm	(80:20) Ag:Au	(81:19) Ag:Au
Sample 4	Spheres / > 10 nm	(80:20) Ag:Pd	(86:14) Ag:Pd
Sample 5	Wires / < 2 μ m	(80:20) Ag:Pd	(93:7) Ag:Pd
Sample 6	Spheres / > 40 nm	(80:20) Ag:Pd	(89:11) Ag:Pd
Sample 7	Spheres / > 10 nm	(100:0) Ag	-
Sample 8	Wires / < 2 μ m	(80:20) Ag:Au	(88:12) Ag:Au
Sample 9	Spheres / > 40 nm	(80:20) Ag:Au	(81:19) Ag:Au
Sample 10	Spheres / > 40 nm	(100:0) Ag	-
Sample 11	Wires / < 2 μ m	(100:0) Ag	-
Sample 12	Cubes / > 200 nm	(80:20) Ag:Au	(86:14) Ag:Au
Sample 13	Cubes / > 200 nm	(80:20) Ag:Pd	(90:10) Ag:Pd
Sample 14	Spheres / > 10 nm	(88:12) Ag:Ir	-
Sample 15	Cubes / > 200 nm	(100:0) Ag	-
Sample 16	Spheres / > 40 nm	(90:10) Ag:Pd	(95:5) Ag:Pd
Sample 17	Spheres / > 10 nm	(90:10) Ag:Au	(91:9) Ag:Au

If iridium or gold are used as shell material, the systems nearly have the intended nominal molar ratios. In the case of palladium however approximately half of the used metal is lost to the former described formation of small palladium nanoparticles during the reaction (compare shapers 5.1-5.3). All particles were characterized by AAS, DCS and DLS. The results showed that all particle systems were monodisperse and colloidal stable. The particles could hence be used for the dissolution experiments. To ensure that the diffusion of silver ions does not influence the dissolution kinetic of the nanoparticles, a sample containing silver nitrate solution was also monitored. The amount of silver was 44.81 μ g and consequently refers to a concentration of ~ 9 μ g/mL in the upper part of the setup (determined by AAS). After the experiment was finished, the total amount of silver was calculated by formula 15.

$$Ag_{total} = Ag_{Diff} + Ag_{loss} + Ag_{up} \quad (15)$$

Where Ag_{total} is the sum of silver determined by AAS after the experiment, Ag_{Diff} is the diffused amount of silver in the lower part of the setup at the last measurement point, Ag_{loss} is the amount of silver which was removed from the system for the AAS measurement at every single measurement point and Ag_{up} is the remaining silver in the upper part of the setup. The sum equals $43.91 \mu\text{g}$ which corresponds to 97.98 % of the starting value.

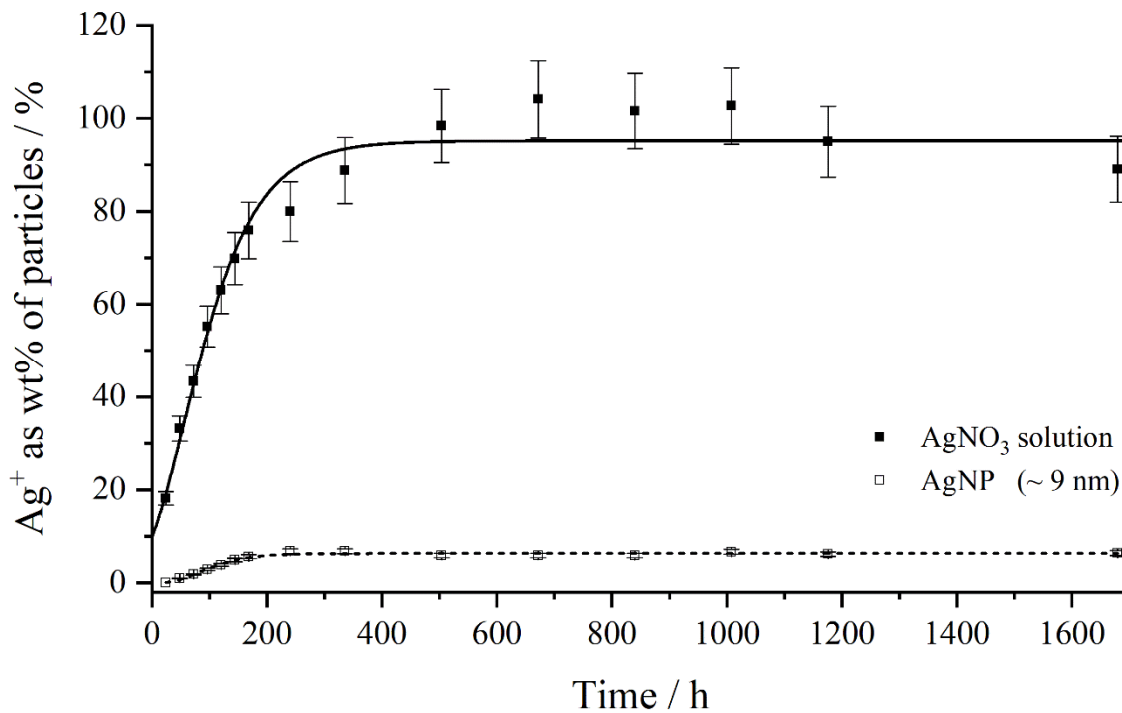


Fig. 94: Comparison of the silver amount (%) of silver nitrate and the fastest dissolving particles in the experiment (AgNP ~ 9 nm) determined by AAS. The diffusion rate of silver ions is much faster than the dissolution rate of the particles. The data was evaluated using Gompertzian fit functions.

Figure 94 shows that the diffusion of silver ions is much faster than the dissolution of the particles. To calculate the rate constants, the data was evaluated using a Gompertzian function (formula 16). With the asymptote a , the Euler's number e , the rate constant k , the time x and the inflection point x_c .

$$f(x) = ae^{-e^{-k(x-x_c)}} \quad (16)$$

This formula is used in the literature to describe the dissolution of APIs and has hence also been used by Dr. Grasmik.^[24, 181] The average rate constant k_a is calculated by dividing the asymptote (a (μg)) by the time at which the maximum dissolution occurs (t_{md} (h)).

$$k_a = \frac{a \text{ (}\mu\text{g)}}{t_{md} \text{ (h)}} \quad (17)$$

The diffusion of the silver ions leads to an average rate constant ($k_{a(\text{diffusion})}$) of 191.54 ng h^{-1} whereas the average rate constant ($k_{a(\text{dissolution})}$) for the fastest dissolving silver nanoparticles is 19.82 ng h^{-1} . Consequently, this leads to the assumption that $k_{a(\text{diffusion})} \gg k_{a(\text{dissolution})}$ and the rate constant of the dissolution is not influenced by the diffusion of the silver ions. To confirm this assumption, a former accomplished non-diffusion based experiment with particles from the same synthesis performed by Dr. Kateryna Loza was compared to the new dataset (Fig. 95, black points).

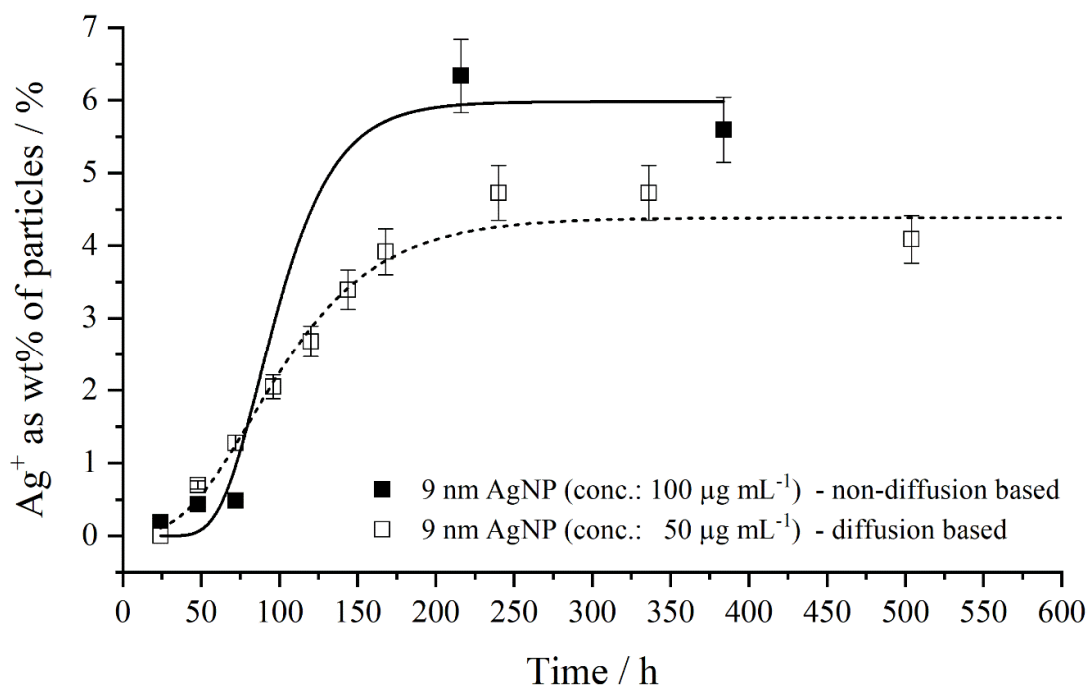


Fig. 95: Comparison of the dissolution of ~ 9 nm silver nanoparticles synthesized with sodium borohydride. Both datasets were obtained from different diffusion and non-diffusion based experimental setups. The non-diffusion based experiment was carried out by Dr. Loza.

In this experiment particles were stirred in dispersion. Aliquots were taken after certain intervals. Those aliquots were filtrated in Amicon[®] Ultra centrifugal filters (MWCO = 3,000 Da) and the silver content of the resulting solution was determined by AAS. To exclude the possibility of attractive interactions of silver ions with the filter membrane, a

silver nitrate solution was filtrated beforehand. Afterwards the contents of the filtered and not filtered sample were determined by AAS. Both samples showed the same concentration. A positive interaction between silver ions and the membrane can consequently be excluded. The evaluation of the datasets shows that the dissolution in both executed experiment show similarities. The average rate constant and percentage dissolution for the non-diffusion based experiment performed by Dr. Loza ($k_a = 22.65 \text{ ng h}^{-1}$, 6.0 %) are in good agreement with the rate constant and percentage dissolution with the diffusion dependent experiment in this work ($k_a = 19.82 \text{ ng h}^{-1}$, 4.4 %). An increase in dissolution like it is observed for the sample with the higher concentration ($100 \mu\text{g mL}^{-1}$) is also described in the literature.^[21] Consequently, the performed experiments in this work are not affected by diffusion and are perfectly suitable to calculate rate constants and maximum diffusion of metallic nanoparticles. In the beginning AAS measurements were taken every day for the first 7 days. This was done because cell experiments are normally performed in the same time range. The dissolution was further tracked up to 70 days (1680 hours). For a better overview, only experiments that showed detectable silver contents are shown in Fig. 96.

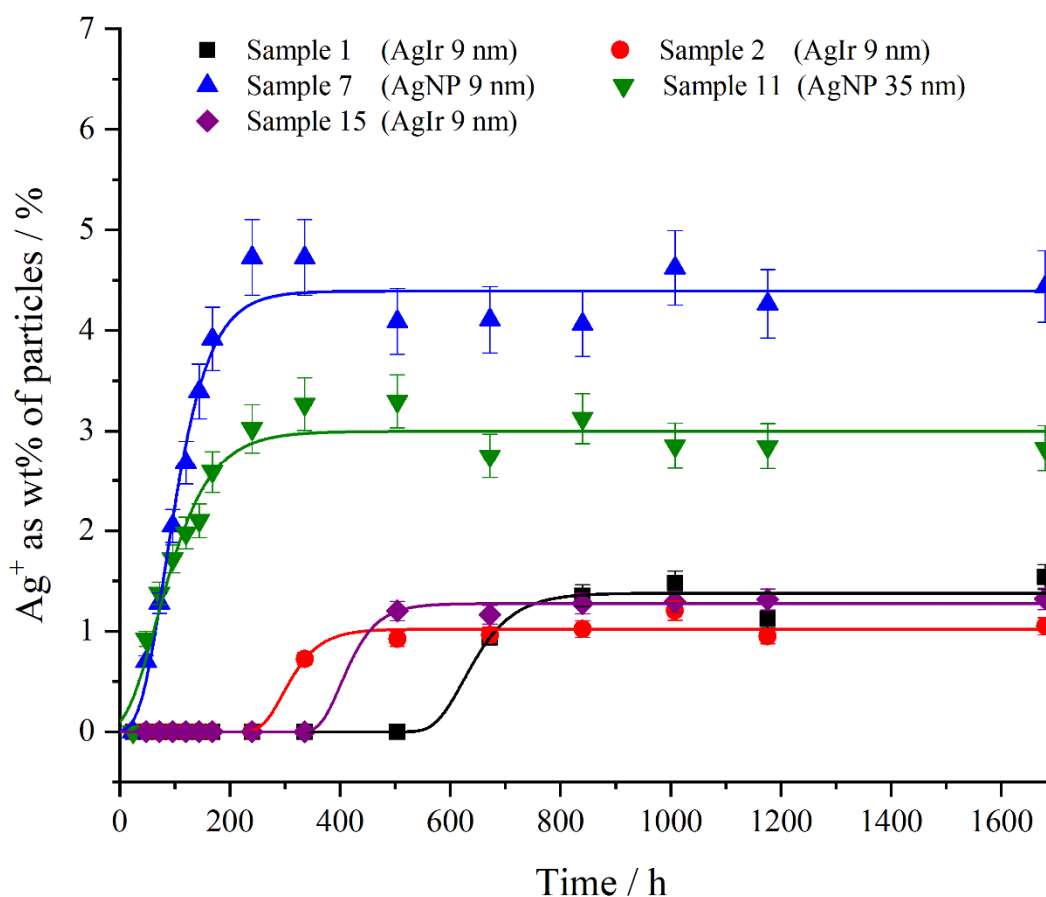


Fig. 96: Dissolution of the total silver mass (%) as a function of the time (hours). Only samples with detectable amounts of silver are shown. The removed summed up amount of silver at each measuring point was added to the next detected point.

Samples that are not depicted did not show any dissolution. The data reveals that only particles containing iridium and pure spherical silver particles show dissolution over the investigated time range. All other systems and consequently all core-shell systems using gold or palladium as shell material do not release silver ions in a detectable range. Even if these particles are in the same size ranges. This shows that the shell material is an important factor for the dissolution of silver.

Table 28: Silver dissolution rates, asymptotes and inflection points determined by the used Gompertzian fits to describe the dissolution of the samples 1, 2, 7, 11 and 15. All examined samples had the same silver concentration of 50 $\mu\text{g mL}^{-1}$.

Sample	Dissolution rate k of silver / ng h^{-1}	Asymptote a / μg	Time at inflection point x_c / h	Average dissolution rate k_a of silver / ng h^{-1}
1	12.34 ± 0.89	3.19 ± 0.03	614.46 ± 4.69	3.16
2	25.52 ± 12.18	2.20 ± 0.07	296.39 ± 19.40	2.62
7	21.21 ± 2.38	10.03 ± 0.21	85.53 ± 3.89	19.82
11	17.26 ± 2.32	6.61 ± 0.17	67.84 ± 5.41	9.82
15	24.25 ± 8.40	2.78 ± 0.05	404.48 ± 33.31	3.33
Sample	Diffusion rate k of silver / ng h^{-1}	Asymptote a / μg	Time at inflection point x_c / h	Average diffusion rate k_a of silver / ng h^{-1}
AgNO ₃	12.13 ± 1.13	38.54 ± 1.23	59.60 ± 4.22	191.54

The data evaluation by the Gompertzian fitting shows that pure silver nanoparticles with a size of ~ 9 nm (sample 7) show the highest average dissolution rate of 19.82 ng h^{-1} . Furthermore, those particles show the most released silver ions in the first 240 hours (~ 10 days) which leads to the conclusion that small spherical particles are the best to use for their antibacterial effects in this period. After 506 hours (~ 21 days), the dissolution reaches the saturation limit. The silver ion release of bigger silver particles with a size of ~ 35 nm starts in the same time interval, but the amount of the released silver is smaller compared to sample 7. The dissolution reaches a saturation after 670 hours (~ 25 days). Both samples with a nominal composition of 88:12 (Ag:Ir, sample 1 and 15) show comparable average silver release rates of 3.16 ng h^{-1} for sample 1 and 3.33 ng h^{-1} for sample 15. The time at which the dissolution of both particles starts notably differs (compare Table 28, inflection points). The dissolutions of silver-iridium particles with a nominal composition of 80:20 (Ag:Ir) is the slowest compared to the other samples. An average dissolution rate of 2.62 ng h^{-1} is observed. Consequently, the amount of released silver ions differs as follows: AgNP (9 nm) > AgNP (35 nm) > AgIrNP (9 nm, 88:12) > AgIrNP (9 nm, 86:14) whereas sample 7 and 11 show the fastest dissolution.

The data show that a sacrificial anode effect, like it was observed by Köller et al., cannot be observed using core-shell nanoparticles. The experiments reveal that particles with a shell of a nobler metal decrease the silver ion release rate even if the shell is not completely developed around the particles (compare chapters 5.1-5.4). However, the trend that systems containing iridium release more ions when compared to systems of palladium and gold can be confirmed. Only silver-iridium core-shell systems showed dissolution of silver ions. Neither nanocubes nor wires showed any dissolution in the time interval of the experiment (1680 hours). The investigation of silver nitrate as a standard, shows that the silver ion transfer through the cellulose filter material is delayed. The saturation occurs only after 21 days were the maximum is reached. However, the rate constant for the diffusion for silver nitrate (191.54 ng h^{-1}) is much higher compared to the rate constant for the dissolution of the tested particles (19.82 ng h^{-1}) ($k_{a(\text{diffusion})} \gg k_{a(\text{dissolution})}$). Since the ion transfer through the membrane is a much faster process than the dissolution of the nanoparticles, the kinetic dissolution experiments are not influenced. This could also be testified by the comparison to an experiment using the same nanoparticles which was not diffusion dependent. Both experiments showed comparable average rate constants (k_a) as well as percentage dissolutions.

A major discovery is that the particles which have a shell of iridium still show a dissolution of silver but with a significant delay in time. This observation could be used to mix nanoparticles and assure a silver ion release over a broader time interval.

5.5 *In-situ* powder diffraction of silver nanoparticles

The growth mechanisms and kinetics of a polyol-based silver nanoparticle reduction were studied *in-situ* by combining a laboratory microwave reactor and high-flux X-ray powder diffraction performed at a synchrotron beamline (DESY P02.1). Nanomaterials, especially based on silver, are of great interest in a lot of applications and fields. Colloidal silver is already used in many products such as biocides, pigments, catalysts as well as consumer products and medical devices.^[15, 182] Due to the high interest, reliable and high yield syntheses are required. Since the silver ions are the active species in the system the dissolution of the AgNP plays a key role.^[19-20, 179-180]

Former works and studies have shown an influence of size and shape on the dissolution of the particles.^[21-23, 183] Therefore, a deeper insight into the kinetics and growth processes of those reactions is required. Data obtained from these measurements could be used to optimize reaction parameters and lead to a better reproducibility of those systems. Especially microwave syntheses with their high energy efficiency and their homogenous heat distribution are an interesting synthesis way to study.^[184-185] Our workgroup and particular the work of Helmlinger et al. has investigated two polyol based syntheses comparing ethylene glycol (EG) and diethylene glycol (DEG). The use of DEG revealed significantly better results regarding dispersity and particle shape and was consequently also used in our experiments.^[186] Overall three different experiments with altered parameters were investigated.

The received data sets were evaluated by auto sequential Rietveld refinement to calculate crystallite sizes, peak areas and lattice parameters. After the syntheses, the obtained particles were purified by ultracentrifugation and characterized by SEM, TEM, DLS as well as DCS and AAS. The colloidal characterization methods confirm mechanistic changes obtained from *in-situ* X-ray powder diffraction.

The experiments were performed in cooperation with Prof. Dr. Robert E. Dinnebier and Luzia S. Germann from the Max-Planck-Institute for solid-state research in Stuttgart. The evaluation of the high crystalline standard as well as the determination of the instrumental aberrations were hereby performed by Luzia S. Germann. In addition, Luzia was a huge help and mentor for the introduction in the used programs for the performed data evaluation.

5.5.1 Characterization of silver nanoparticles from a polyol process in a microwave

For a deeper insight into the influence of the metal precursor concentration as well as the temperature on the crystallographic growth of the silver nanoparticles, three different syntheses were performed (Table 29).

Table 29: Experimental conditions and used chemical concentrations for the three-different performed silver nanoparticle syntheses investigated by *in-situ* X-ray powder diffraction.

Experiment	Run 1	Run 2	Run 3
Reaction type	isothermal	isothermal	isothermal
Temperature / °C	160	160	200
Concentration AgNO ₃ / mmol	0.18	0.54	0.54
Mass AgNO ₃ / mg	30	90	90
Concentration PVP / mmol	0.18	0.54	0.54
Mass PVP / mg	20	60	60
Volume diethylene glycol / mL	5	5	5

A baseline for the two altered reactions was established by performing a reaction with standard conditions (Run 1). Figure 97 shows the obtained 3D *in-situ* powder data obtained from all three runs. Overall six different diffraction peaks of the fcc-system can be observed. Background subtracted 3D plots of the different reactions are shown in Figure 98. The data obtained for Run 1 reveals an increase of the scattering intensity over time. The maximum is reached over a 14 minute period into the reaction (Fig. 97, A; Fig. 98, A). After this point, there is no further increase in scattering intensity. This observation is in good agreement with the reported 20 minutes for a completed reaction by Helmlinger et al.^[186] The powder data obtained for Run 2 with the tripled concentration of AgNO₃ and PVP shows a decreased growth rate developing slowly over time. The point, where a stable scattering intensity is reached occurs after 20 minutes. In contrast to the other two reactions, the scattering intensity in Run 3 maximizes in only two minutes indicating a huge influence of the reaction kinetics and reduction potential of diethylene glycol (DEG) by temperature.^[187]

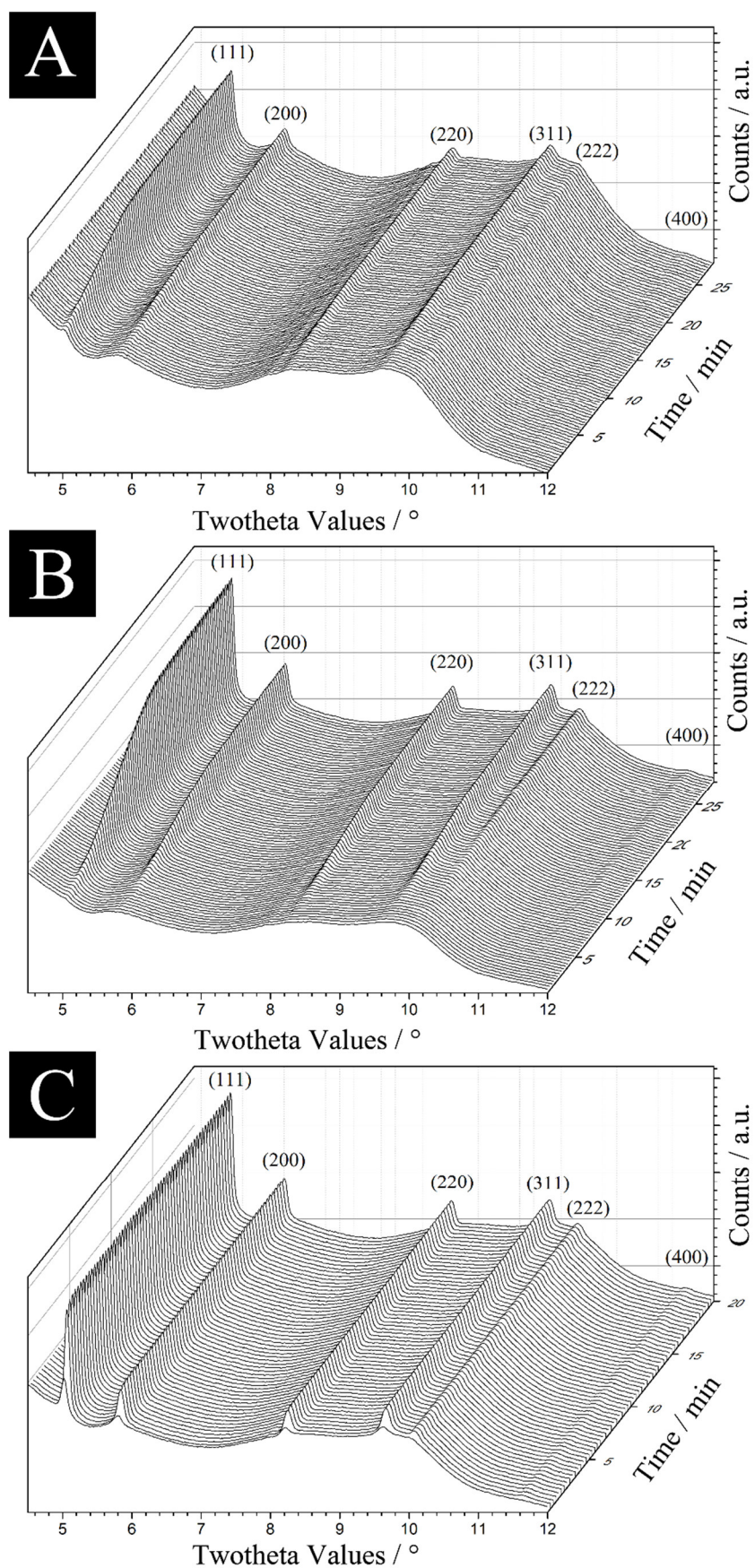


Fig. 97: Untreated 3D powder data over time (min) for all 3 performed runs, Run 1 (A), Run 2 (B) and Run 3 (C).

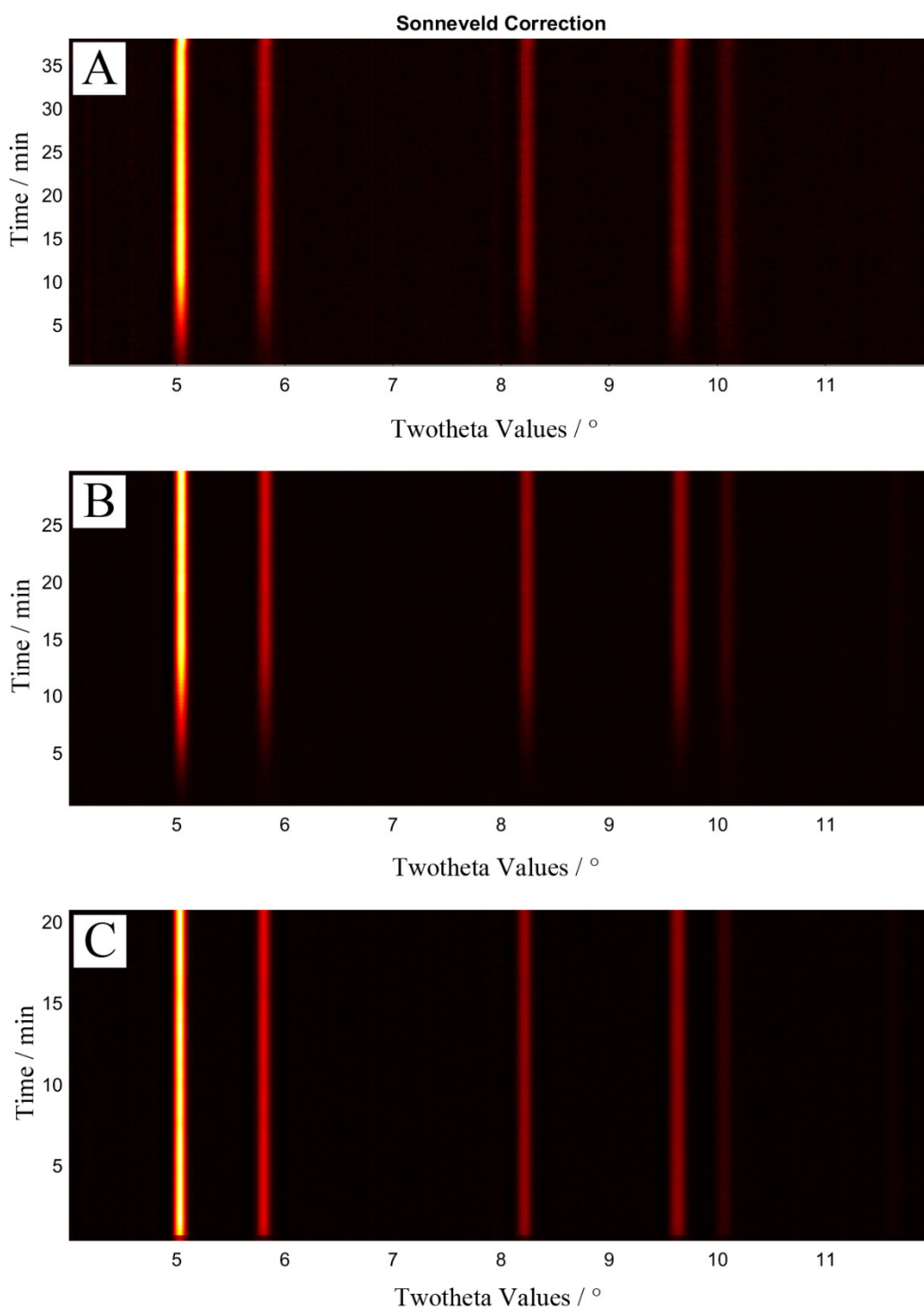


Fig. 98: Background subtracted 3D plots of the different *in-situ* reactions, Run 1 = A, Run 2 = B and Run 3 = C. Reaction time (min) is plotted as function of the scattering angle (°).

The data was further investigated with an auto sequential Rietveld refinement (ASR). From this analysis, different parameters, such as lattice parameter, crystallite size as well as peak areas could be obtained.

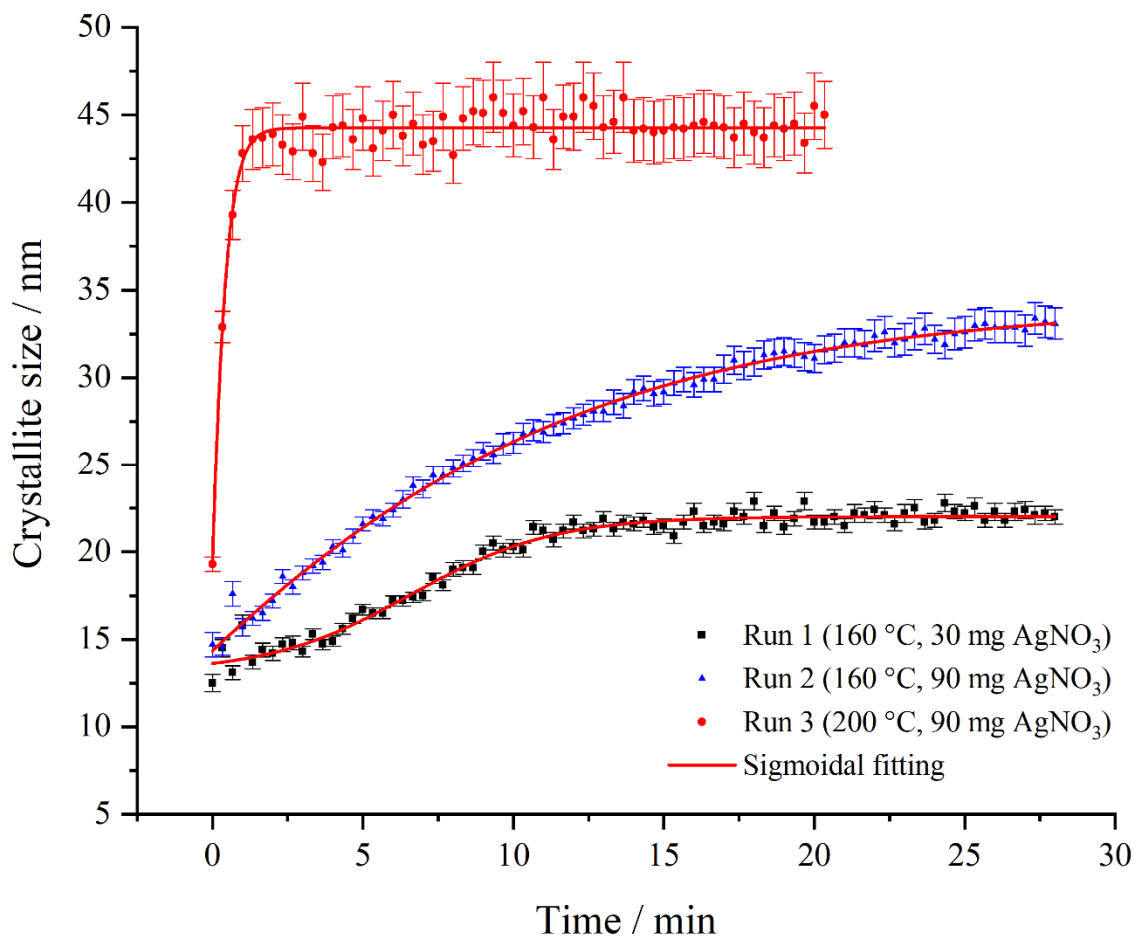


Fig. 99: Comparison of the crystallite size (nm) over time (min) and the corresponding sigmoidal fits (red curves) for all performed runs.

The regularly performed synthesis of Run 1 shows a crystallite growth rate of 0.72 nm min^{-1} in the beginning. This rate is decreasing strongly after 11 minutes indicating a nearly completed reaction (Fig. 99). The growth rate between 11 minutes and the end of the measurement ($t = 28 \text{ min}$) drops to 0.05 nm min^{-1} . The lowest crystallite size derived by ASR is 13 nm leading to a maximum of 23 nm at the end of the reaction. The increase of metal precursor in Run 2 leads to a different growth behavior. At the beginning of the reaction, a fast crystallite growth with a rate of 1.28 nm min^{-1} is observed. This rate decreases in comparison to Run 1 after a time of six minutes to 0.78 nm min^{-1} (Fig. 99). The growth rate decreases even further after 13 minutes down to 0.36 nm min^{-1} leading to a final crystallite size of 33 nm. Run 3, where both parameters, concentration and reaction temperature (90 mg, $200 \text{ }^\circ\text{C}$), were altered, reveals a rapid growth of the crystallites at the beginning of the reaction. The crystallite size changes from 19 nm in the beginning to 42 nm over a period of one minute developing a growth rate of $23.07 \text{ nm min}^{-1}$. A dramatic growth decrease occurs directly after one minute (1.02 nm min^{-1}).

Any growth of the crystallites is *de facto* discontinued after two minutes into the reaction (0.04 nm min^{-1}). This behavior presents a huge influence of the temperature towards nucleation and growth times indicating a faster growth and a reduced seed formation compared to Run 2 with the same concentration. To investigate a possible anisotropic growth behavior of the developing crystallographic lattice planes during the reaction, the peak areas of the planes were obtained from Rietveld refinement. The individual evaluation of the peak area can be used to identify an inhomogeneous growth. Since the reflexes of the single lattice planes have different intensities, the peak area values need to be normalized to see possible anisotropic growth behavior.

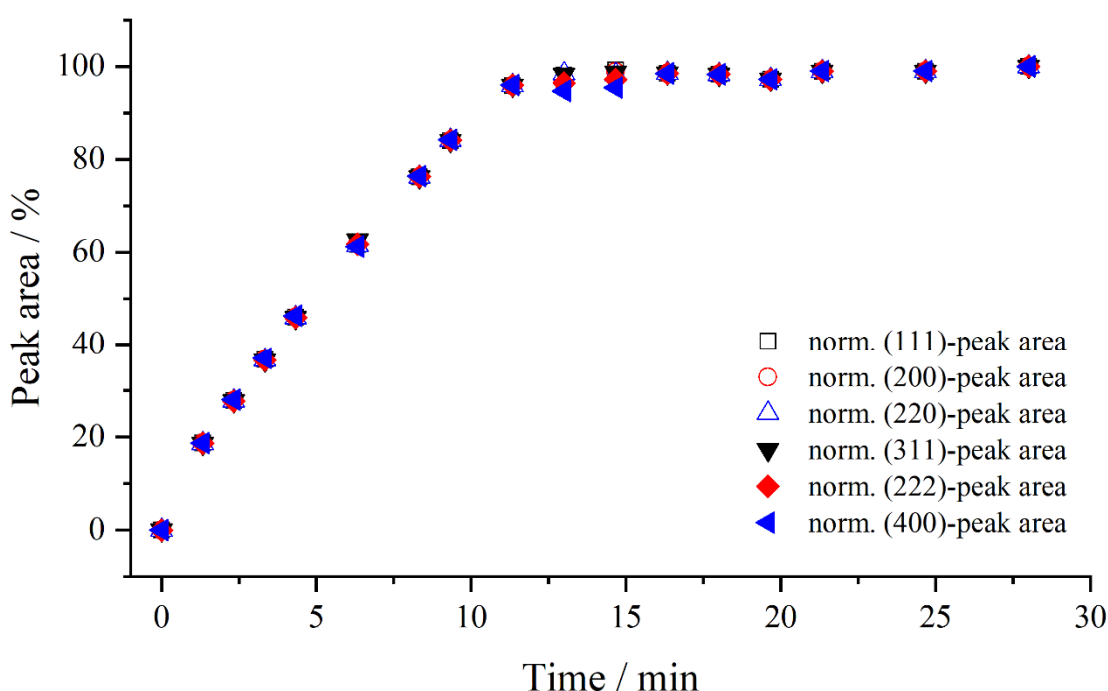


Fig. 100: Representative data of the normalized peak areas for all six observed crystallographic lattice planes of Run 1. The peak area (%) is shown as a function of time (min).

The investigation of the peak areas of Run 1 shows a homogenous growth of all lattice planes. Regarding the data, no delays or slowed growth processes of single planes are observed (Fig. 100). All areas show an identical growth of $0.12 \text{ \% per second}$ in the first 11 minutes of the reaction. The data of Run 2 and 3 reveal the exact same trend. Even the harsh conditions of $200 \text{ }^\circ\text{C}$ and a tripled precursor concentration in Run 3 have no influence on the homogenous, isotropic growth behavior of the lattice planes. However, the difference of the growth rate in Run 3 is enormous. In the first minute of the reaction a peak area increases of $1.74 \text{ \% per second}$ is observed. This data is in good agreement with the development of the crystallite size

(Fig. 99). Since the crystallite size and peak area show the same curve shape it leads to the conclusion that in Run 1 and Run 3 the increase of scattering intensity is almost completely contributed by the growth of the particles and not caused by nucleation of new seeds. Run 2 reveals also an isotropic growth of all lattice planes. But in contrast to Run 1 and 3 the development of the peak areas and the crystallite size are different (compare Fig. 101).

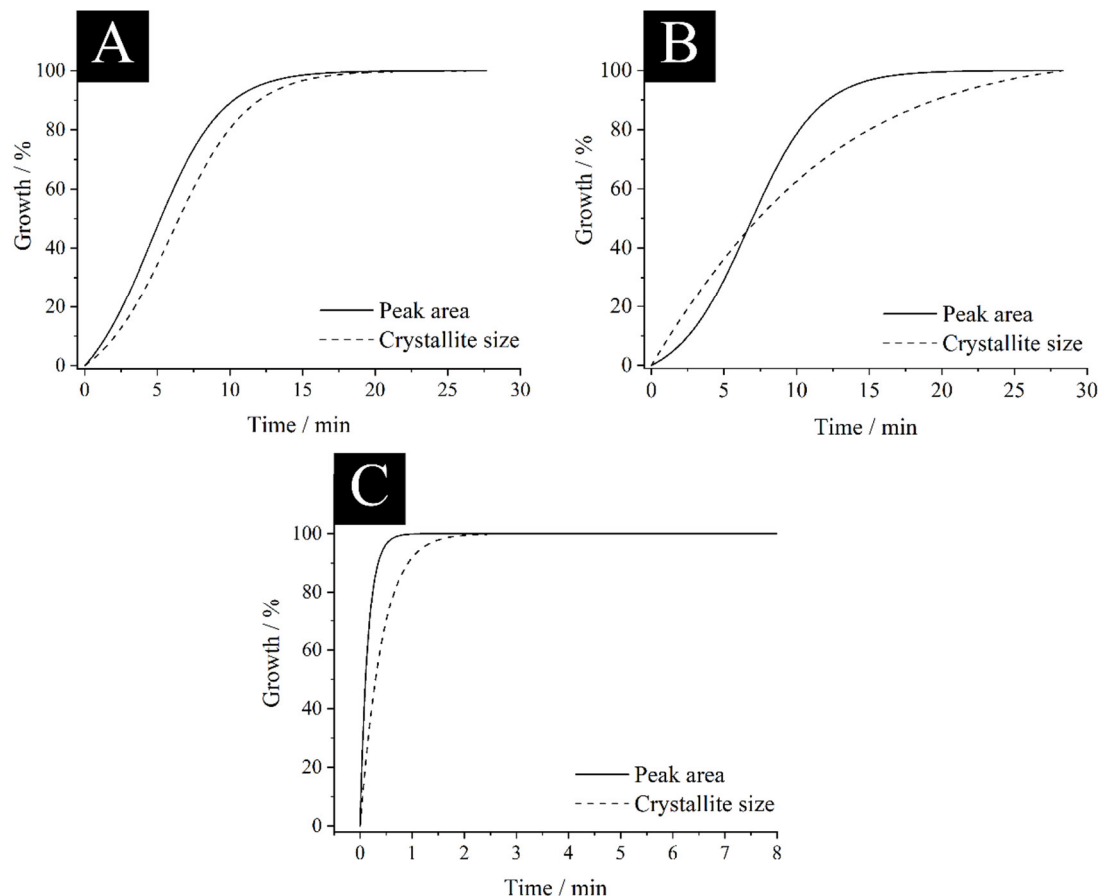
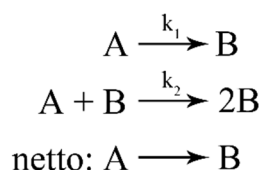


Fig. 101: Representative fitting for the growth of peak areas (%) and the crystallite sizes (%) obtained from Run 1 (A), Run 2 (B) and Run 3 (C) as a function of time (min). The graphic shows a good agreement between CS and PA growth for Run 1 and Run 3 indicating that the scattering intensity increase is mostly contributed by crystallite growth.

Investigations regarding the formation of nanoparticle seeds and the particle growth by Finke et al. have shown that nanoparticle growth is a two-step mechanism.^[79] The model consequently expands the theory of LaMer which was already proposed in 1948. LaMer's theory describes a state of supersaturation where seeds are formed. When the atom concentration leaves this state the nucleation stops immediately and the nuclei grow to particles.^[188] However, not only Finke et al. but also different other groups could show that a formation underlies a two-step mechanism.^[77-78] This mechanism consists of a slow, continuously nucleation with a rate

constant k_1 and an autocatalytic surface growth with a rate constant k_2 showing that both reactions occur over the whole reaction but with different rates. This mechanism leads to the following equation after Finke et al.:



In the equations A stands for the Ag^+ ion and B for a silver nanoparticle. In general, the rate constant k_1 is much smaller than k_2 . This is also the case in the performed Run 1. Therefore, the scatter intensity is mostly contributed by the particle growth (compare Fig. 101). The increase of silver precursor without an altering of the temperature (Run 2) creates a situation where the rate constant k_1 , and consequently the seed formation is increased. The raise of temperature in Run 3 increases the rate constant k_2 . This leads again to a strong autocatalytic surface growth of the particles.

Consequently, the observations for Run 2 can be separated in three different phases which can be explained as follows:

- I
 - ♦ The first seeds (A) are already formed by the addition of silver nitrate into DEG (compare chapter 4.6.3).
 - ♦ A second fraction of seeds (B) arises in the heating progress, due to the two-step mechanism, while the first fraction already is growing.
 - ♦ Supported by the observations that small silver nuclei (B) have fluctuating crystalline structures at elevated temperatures, they do not contribute scatter intensity to the observed powder pattern^[144].
 - ♦ Consequently, in the first time interval ($t = 0-7$ min) only seeds from the initial nucleation are grown enough to build up a well-defined XRPD pattern which leads to the same percentage growth of peak area and crystallite size (see Table 30).
- II
 - ♦ More seeds (B) reach the size were well defined crystallite structures are formed ($t = 7-14$ min).
 - ♦ Since those seeds add intensity to the pattern (increase in peak area) but do not increase the mean crystallite size, the peak area growth is faster than the crystallite size growth (compare Fig. 102 and Table 30)
 - ♦ This leads to a significantly reduction in crystallite growth (37.7 %) and an overall increase of peak area growth (24.4 %).
- III
 - ♦ In the last phase of the reaction ($t = 14-28$ min) the peak area of the powder diffraction data exhibits a plateau while the crystallite size is still increasing. This observation is associated to an Ostwald ripening process (Fig. 102).^[80, 189]

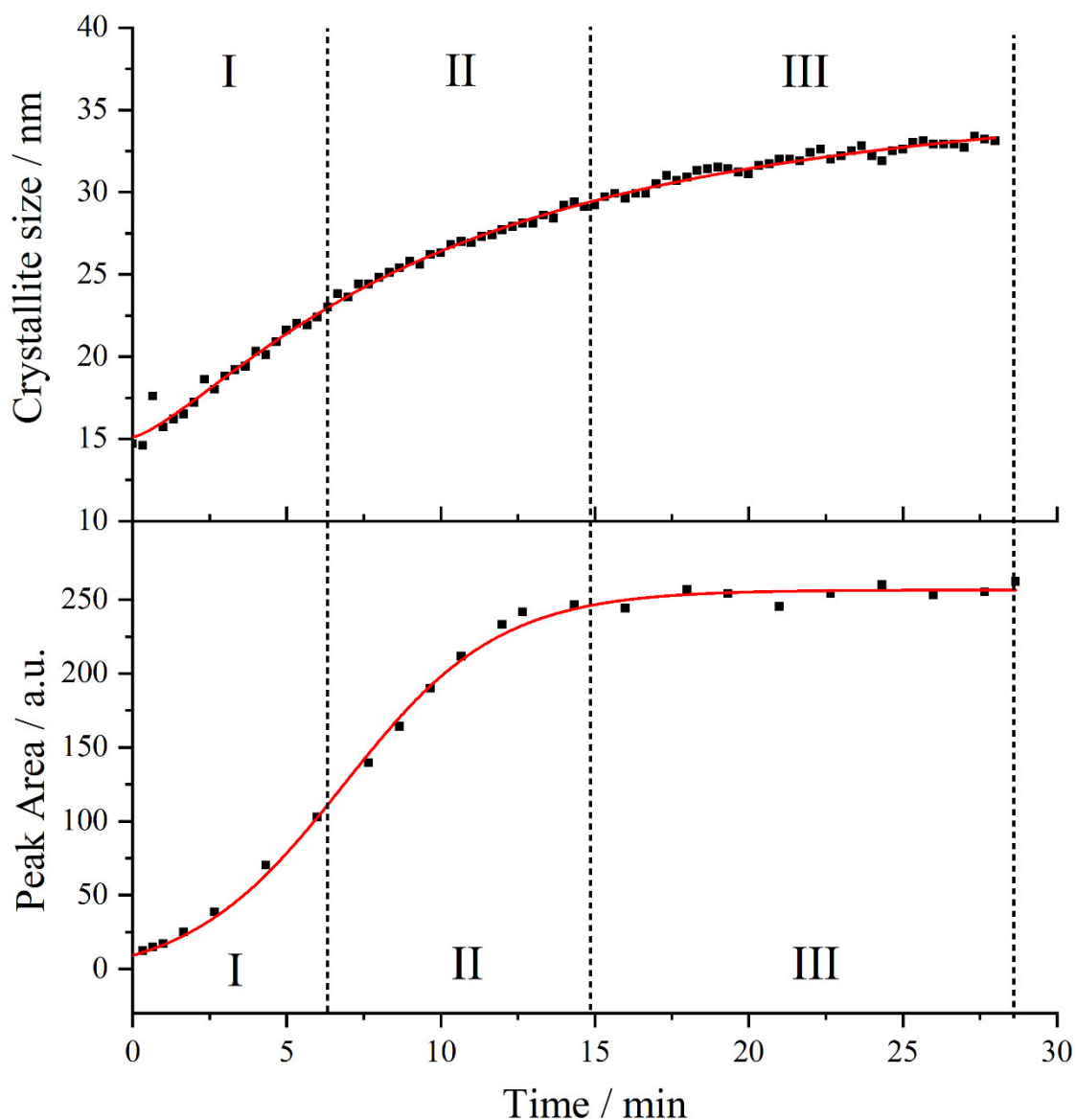


Fig. 102: Peak area evolution of the (111)-silver lattice planes as a function of time (min) and the corresponding sigmoidal fits (red lines), (bottom) and a comparison of the crystallite size as function of time (min) (top) of Run 2. The whole reaction can be separated in three different zones (marked by dotted lines and roman numbers).

Since the reaction time was limited to 28 minutes, the Ostwald ripening process was not finished. This leads to a broad, bimodal size distribution of particles. The proposed growth scheme for Run 2 is displayed in Figure 103. Conditioned by the inferior concentrations of silver precursor in Run 1 and the elevated temperature in Run 3 the rate constant k_1 is significantly decreased which leads to a scatter intensity increase only contributed by the autocatalytic surface growth.

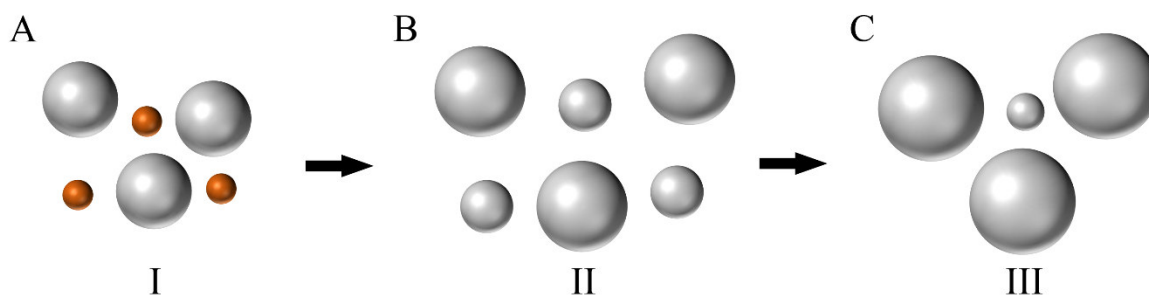


Fig. 103: Purposed reaction scheme of Run 2. The brownish spheres (I) represent nuclei which do not add scatter intensity. Silverish spheres represent particles which contribute scatter intensity. The roman numbers correspond to the zones from Figure 102. Number III shows Ostwald ripening.

Table 30: Growth rates of the crystallite size (CS) and the peak area (PA) and the associated time intervals. The growth rates were calculated assuming a linear behavior in the specified intervals.

Experiment → Parameter ↓	Run 1	Run 2	Run 3
Time interval / min	0-11	0-7	0-1
CS-Growth rate / nm min ⁻¹	0.72	1.28	23.07
CS-Growth rate / % s ⁻¹	0.11	0.11	1.87
PA-Growth rate / % s ⁻¹	0.12	0.10	2.33
Time interval / min	11-14	7-14	1-2
CS-Growth rate / nm min ⁻¹	0.15	0.78	1.02
CS-Growth rate / % s ⁻¹	0.03	0.07	0.06
PA-Growth rate / % s ⁻¹	0.02	0.12	0.05
Time interval / min	14-28	14-28	2-20
CS-Growth rate / nm min ⁻¹	0.05	0.36	0.04
CS-Growth rate / % s ⁻¹	0.01	0.03	0.00
PA-Growth rate / % s ⁻¹	0.00	0.01	0.00

The investigation of the mean lattice parameters over time gives a presumption of size distribution of colloidal systems. Several studies have demonstrated that a lattice parameter contraction occurs and even increases with the decrease of particle size.^[162-164, 190-191] Taken into consideration that the crystallite size increases stronger in the beginning of Run 2, a steep slope of the lattice parameter is observed (Fig. 104). The formation of new seeds over the whole reaction in Run 2 (Fig. 103) shows a direct effect on the calculated lattice parameters obtained from the ASR in period II (Fig. 104). A high fraction of growing particles over this period leads to a slower increase of the mean lattice parameter compared to both other runs.

In comparison, Run 1 and Run 2 reach the same mean lattice parameter in the end of both measurements (Fig. 104) which assumes comparable particle sizes.

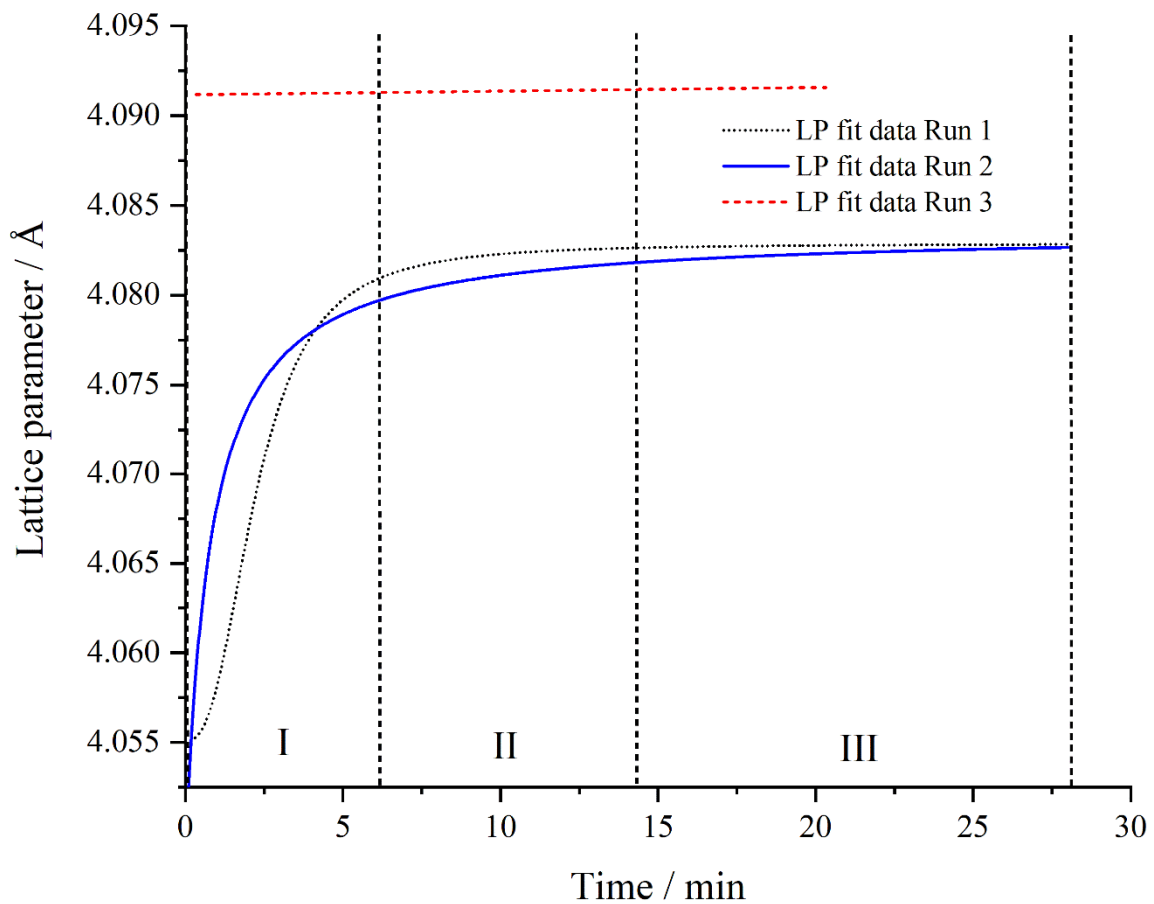


Fig. 104: Comparison of the fit data obtained for the lattice parameters (\AA) over time (min) from all three performed runs. The dotted lines and roman numbers indicate the growth steps which were identified for Run 2. The reaction of Run 3 was already ended after 20 minutes since no further changes in scatter intensity occurred.

When the reaction enters period III, no more small particles which alter the lattice parameter are formed. Therefore, the lattice parameter expands to a maximum for this measurement temperature ($160\text{ }^{\circ}\text{C}$). The temperature increase in Run 3 leads to a fast formation of big particles. This is indicated by a linear behavior of the lattice parameter over time. The formation of new seeds is small. The higher lattice parameters for the experiments can be explained by the thermal expansion of the unit cell using different temperatures (see Fig. 104).^[113, 192-194]

To compliment the characterization of the particles, all performed runs were further investigated using colloidal methods. DCS, DLS and SEM were used to determine the final size and shape as well as the dispersity of the particles after purification. Furthermore, the yield of the reactions was determined by AAS. The comparison of the DCS data is shown in Figure 105. All size distributions and standard deviations were derived from log normal fits.

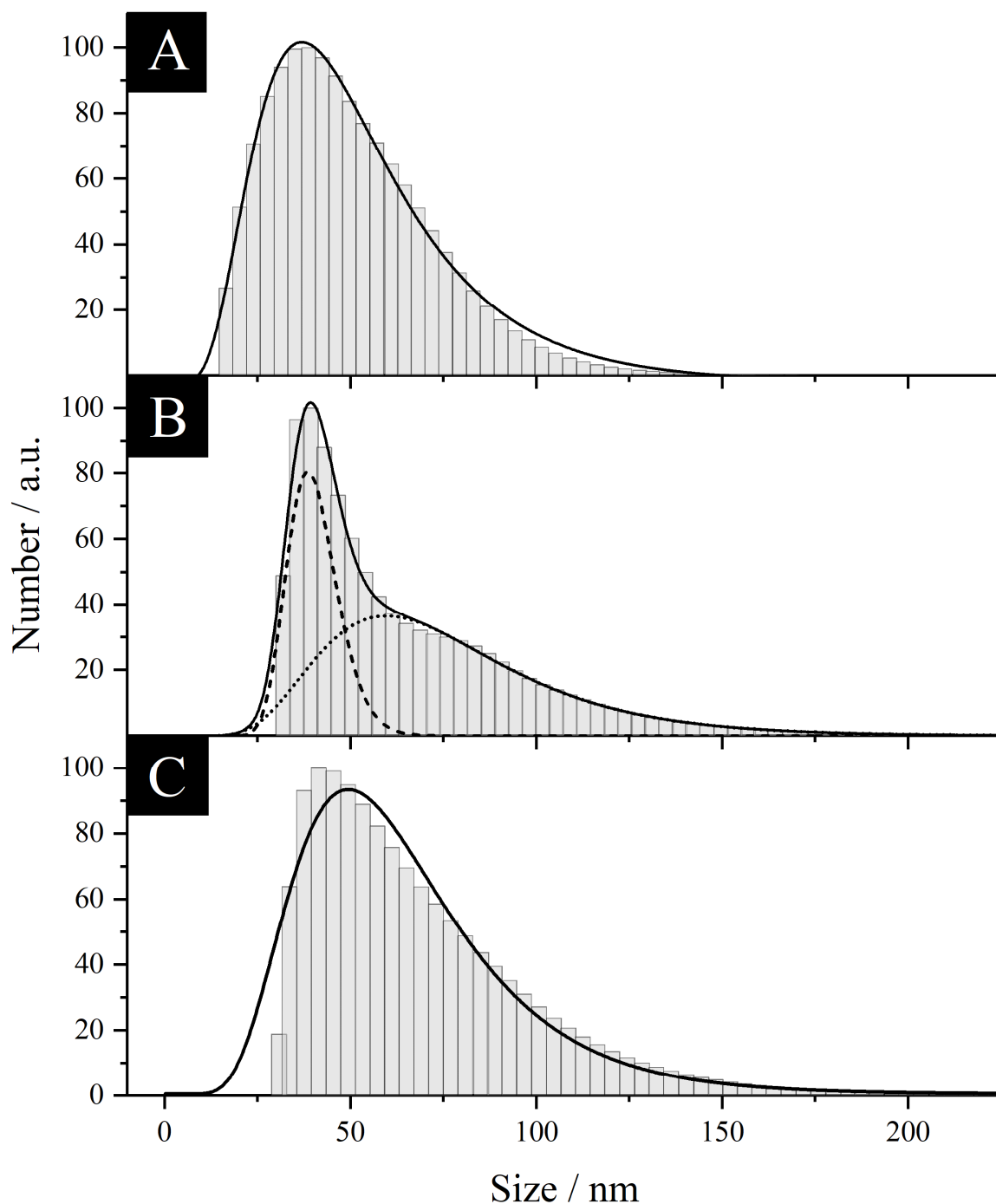


Fig. 105: Particle size distribution derived from differential centrifugal sedimentation (DCS) for the performed microwave syntheses (Run 1 (A), Run 2 (B), Run 3 (C)). The graphs show the number (a.u.) as a function of size (nm).

The particles obtained from Run 1 show a unimodal size distribution with a maximum size of $48 \text{ nm} \pm 29 \text{ nm}$ (Fig. 105, A and Table 31). In contrast to Run 1, the particles synthesized in Run 2 show a bimodal size distribution which can be described using two independent log normal fits with size maxima at 40 nm and 69 nm (Fig. 105, B and Table 31). The DCS therefore testifies the statement of polydisperse nucleation in Run 2. An increase of the reaction temperature using otherwise the same conditions leads to faster autocatalytic growth, decreasing the available concentration of Ag^+ -ions. The resulting particles of Run 3 increase in size and show a narrower size distribution. The altered reaction parameters lead to a higher number of bigger particles and a decreasing fraction of small particles. Besides that, the overall mean size of the particles increases (Fig. 105, C and Table 31). To further investigate the particle size and shape, SEM and TEM images were prepared (Fig. 106).

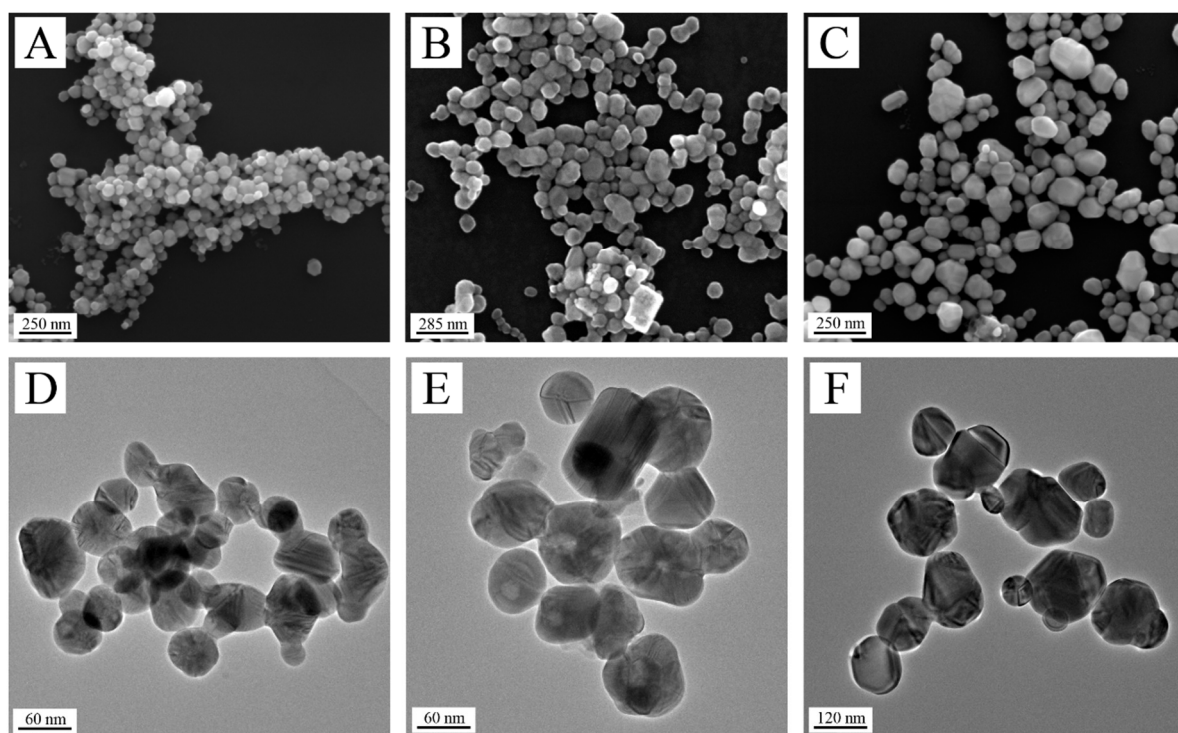


Fig. 106: SEM and TEM images of the *in-situ* experiments Run 1 (A+D), Run 2 (B+E) and Run 3 (C+F). Particles show a size increase analogous to the crystallite size increase derived from ASR.

Particles obtained from Run 1 show a homogenous size distribution between 30-70 nm. This result differs from the description by Helmlinger et al., in their work, particles between 80-120 nm were observed applying the same reaction conditions.^[186] A possible explanation for this could be the use of a different microwave reactor. The SEM images of Run 2 and Run 3 indicate broader size distributions. The SEM and TEM images also confirm the mean size

increase of the particles after increasing the concentration in Run 2 (30-130 nm) as well as the temperature in Run 3 (40-150 nm). For an in-depth analysis, 110 particles of every reaction were measured. Extrapolated from this data, histograms were created showing a unimodal size distribution for Run 1 and 3 and bimodal size distributions for the Run 2 underlining the previously described results. To compliment the investigations regarding the colloidal characterization, the size and the polydispersity index of all particle dispersions were collected using dynamic light scattering. The entire data regarding the size and dispersity obtained from all performed methods is shown in Table 31. Note that DLS overestimates the particle size due to the hydrodynamic diameter. Furthermore, this method is oblivious to bimodal size distributions. DCS slightly underestimates the particle size due to density deviation from the polymeric shell (PVP) of the particles.^[135]

Table 31: Overview of the data obtained by DLS, DCS and SEM. Shown are the sizes (diameter), size distribution and the polydispersity index (PDI, obtained from the DLS measurements). Additionally, the yields were determined by AAS.

Synthesis → Method ↓	Run 1	Run 2	Run 3
DCS size / nm	48 ± 29	40 ± 7, 71 ± 33	60 ± 29
SEM size / nm	54 ± 9	56 ± 10, 84 ± 11	101 ± 46
DLS size / nm	86 ± 17	107 ± 26	117 ± 20
PDI	0.22	0.27	0.21
Size distribution	unimodal	bimodal	unimodal
AAS yield / %	66.9	28.5	70.9

With all limitations of each method taken into consideration, the obtained sizes from the applied methods are in good agreement and confirm the observations from the XRPD measurements. To finalize the investigations, the yield of each synthesis was determined by AAS. A threefold increase of the concentration leads to a drastic impact on the reaction yield. The yield is lowered by 38.4 %. However, raising the concentration as well as the temperature shows a positive effect resulting in a total yield of 70.9 % and therefore 4 % higher than obtained from the standard reaction conditions.

In summary, the combination of *in-situ* powder diffraction and characterization methods for colloidal systems revealed a significant influence of the concentration and temperature on the performed polyol process. Run 1 showed a normal growth behavior like it is proposed in the literature, including a first step of nucleation followed by growth of the crystallites. However, the increase of concentration in Run 2 resulted in a competition between nucleation and growth. In the beginning of the reaction the intensity increase in the XRPD measurements is mainly conditioned to the growth of the former generated seeds. At a certain point into the reaction, in our case seven minutes, the slow, continuous formation of new seeds with the rate constant k_1 becomes a factor. The altered reaction parameter increases the rate constant k_1 of the two-step mechanism. This can be verified by the data obtained for the crystallite growth, the peak area growth as well as the delayed growth of the lattice parameter over time. Consequently, the reaction of Run 2 can be divided into three different zones (I. Growth of nuclei arose at different times, II. Growth of separate nuclei fractions, III. Ostwald ripening).

This behavior leads to broad bimodal size distribution for Run 2 which could be validated by colloidal characterization methods. The increase in reaction temperature in Run 3 leads to an increase in the reduction potential of DEG strongly reducing the rate constant of k_1 . The formation of new seeds is consequently strongly reduced. A unimodal size distribution is the result.

The investigations gave an insight into the growth of silver nanoparticles of a polyol process using a microwave reactor. The increase in concentration leads to a reduced yield and furthermore to a polydisperse system. However, an increase in the temperature mostly compensates these negative effects. This insight might help to further optimize the synthesis. The experiments could show that a two-step mechanism, like described in the literature, with two different rate constants is a plausible explanation for the received data. Further experiments based on these findings might be used to optimize the efficiency of metal nanoparticle syntheses based on a polyol process.

5.6 Synthesis of iridium nanoparticles with the polyol process

Iridium nanoparticles can be synthesized using different reaction pathways. If the synthesis is performed in water a relatively strong reducing agent is needed, because most commonly hexachloridoiridate is used as a precursor. This complex undergoes a ligand exchange with water molecules which causes a rise of the standard potential. To reduce the newly formed $[\text{IrCl}_3(\text{H}_2\text{O})_3]^+$ aqua complex even to $[\text{IrCl}_3(\text{H}_2\text{O})_3]$, the standard potential of the half reaction is +1.3 V and is therefore alone much higher than the reduction potential of the half reaction from the $[\text{IrCl}_6]^{3-}$ complex to elemental iridium (+0.835 V).^[167] Hence, there are different dedicated approaches in the literature using superhydride (lithium triethylborohydride)^[195] or imidazolium based ionic liquids to reduce iridium ions.^[196]

Iridium nanoparticles can also be synthesized using a polyol process.^[197] Like previously described, solvents like ethylene glycol can be oxidized generating two electrons which become usable to reduce complexed metal ions. Since ethylene glycol also serves as solvent, a major advantage is that no stabilizing aqua complex of the iridium ion is formed, and the reduction can be performed with the fainter reducing agent. The forming nanoparticles will be complexed in the presence of PVP and become colloidal stable. The process can either be performed traditionally in an oil bath or using a more efficient heating method like microwave radiation. The homogenous distribution of thermal energy by microwave radiation is based on the energy transfer mechanism, where the polar solvent molecules start to rotate and move in the electrical field of the generated electromagnetic radiation. This movement is converted to thermal energy which leads to a homogeneous heating. The resulting temperature profile shows no gradient inside the reaction mixture.^[198]

In the frame of this work, a polyol based one-pot microwave synthesis was developed using PVP as capping agent and sodium hexachloridoiridate as metal precursor. A set requirement to the particles was the mean size which should be around 5-10 nm. Particles in this size range can be compared to the former with sodium borohydride synthesized and described silver nanoparticles. The formed nanoparticles were purified by ultra-centrifugation and stored in ultra-pure water. The dispersions were characterized using HRTEM, XRPD and DCS.

5.6.1 Characterization of iridium nanoparticles synthesized with the polyol process

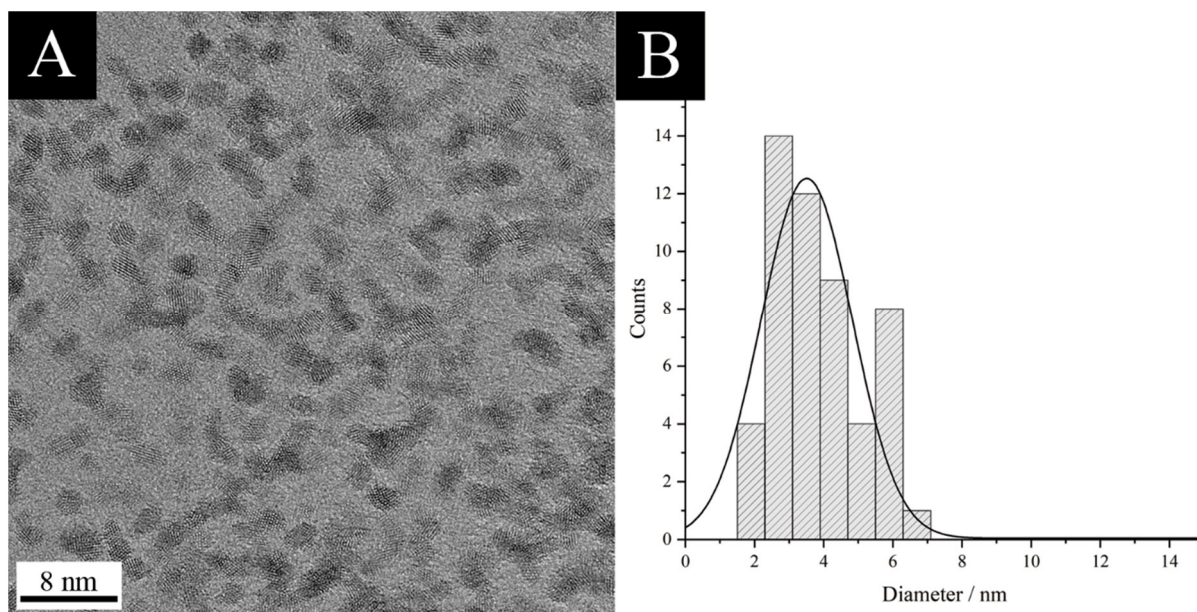


Fig. 107: HRTEM image of the obtained iridium nanoparticles from the polyol process (A) and the corresponding histogram (B). The counts are shown as a function of the particle diameter (nm).

The HRTEM image shows that iridium particles with different morphologies have been formed. The sample basically contains two different types. On the one hand, small spherical particles with a size of 2-3 nm can be observed. On the other hand, anisotropic branched structures with varying sizes between 3-10 nm are present. The formation of well faceted nanostructures of iridium is unlikely and hence not described by accessible literature. This phenomenon can be ascribed to the relatively low energy barrier for a homogenous nucleation compared with that for a heterogeneous nucleation. Newly formed iridium atoms will consequently self-nucleate which results in small particles rather than well-defined faceted structures.^[57] Consequently, only small spherical particles and branched irregular structures are observed (Fig. 107, A). The obtained histogram shows a mean particle size of 3.5 nm and a standard deviation of ± 1.3 nm. The calculated PDI obtained from the graphical evaluation is 0.78 and hence indicates a high polydisperse system. The high resolution of the HRTEM images reveal crystallites with sizes around 1-2 nm which are constructed of few atomic layers.

To investigate the crystallite size and the phase purity of the sample, an XRPD pattern was generated. The pattern was measured in Bragg-Brentano geometry with copper radiation. Since the HRTEM images only showed small crystallites, the particles were previously freeze-dried to enhance the scattering capability by the amount of used material.

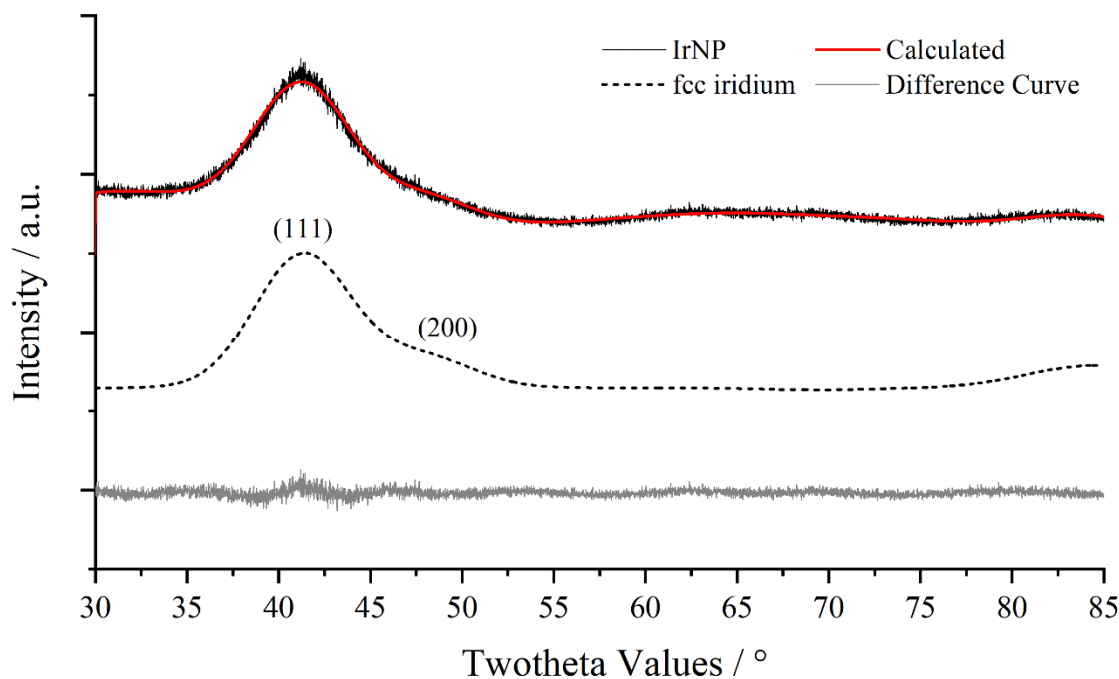


Fig. 108: Rietveld refined XRPD pattern of iridium nanoparticles synthesized with ethylene glycol. The intensity (a.u.) is shown as a function of twotheta values (°).

The obtained pattern shows two broad reflexes which correspond to the scattering of the (111) and (200) crystallographic lattice planes of iridium. Further reflexes, indicating higher indexed planes, which can normally be observed are not present. Those reflexes are highly influenced by the anisotropic broadening caused by the small crystallite size. However, the sample could be identified as a phase pure fcc-phase of iridium. Furthermore, the lattice parameter as well as the crystallite size could be obtained from the refinement.

Table 32: Calculated lattice parameter (LP), cell volume and crystallite size from the Rietveld refinement. The data is compared to the literature values obtained from a single crystal.^[178]

Phase	Space group	LP (a / Å)	Cell Volume / Å ³	Crystallite size / nm
fcc-iridium	$Fm-3m$	3.7795 (8)	54.014 (35)	1.5 (1)
fcc-iridium lit.	$Fm-3m$	3.8394	56.497	-

The sample shows a decrease in lattice parameter compared to the bulk material which directly corresponds to the small number of crystallographic planes in the sample. Consequently, the

cell volume is reduced. The small crystallites have a mean lateral dimension of 1.5 nm which lead to a massive reflex broadening. Furthermore, the particles must have a huge micro-strain based on the strong phase distortion. Both, micro-strain and crystallite size, will lead to a massive anisotropic reflex broadening with the utmost influence on the higher index crystallographic planes. Consequently, the reflexes of the (220), (311) and (222) crystallographic planes cannot be observed or identified. The calculation of the micro-strain by Rietveld refinement is not practical due to the missing of the diffraction peaks of the high indexed planes.

To characterize the size of the particles in dispersion, a DCS measurement was done. Since the particles do not possess a spherical morphology, the measurement is only partially helpful to determine the real particle size.

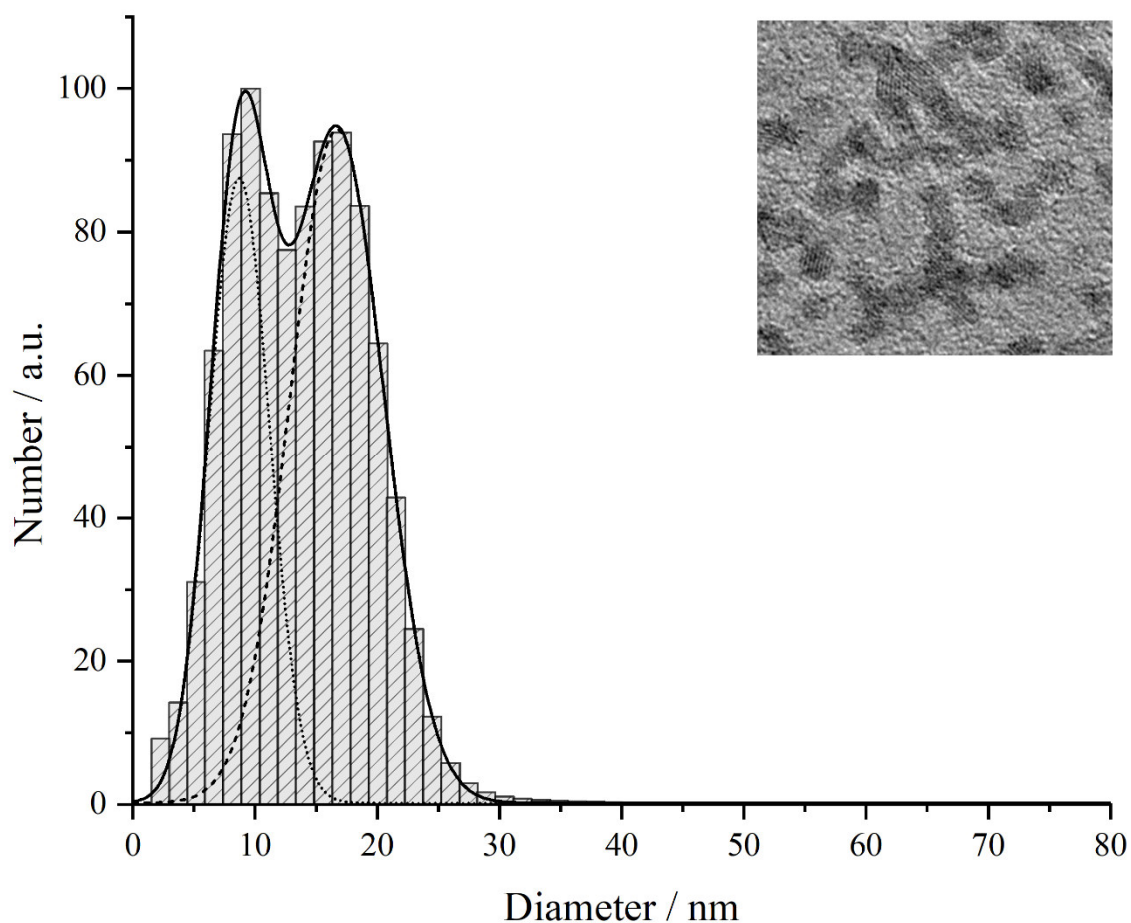


Fig. 109: DCS measurement of the iridium nanoparticles synthesized with ethylene glycol. The graph displays the number (a.u.) as a function of the particles diameter (nm). The depicted TEM image shows strongly branched nanoparticles with the highest observed lateral dimension of ~ 10 nm.

The DCS graph reveals a bimodal size distribution with two maxima. The first maximum appears at a mean diameter of $8.7 \text{ nm} \pm 2.5 \text{ nm}$ and the second at a mean size of $16.7 \text{ nm} \pm 3.8 \text{ nm}$. Consequently, the determined size strongly differs from the graphic evaluation by HRTEM. The strong anisotropic character of the particles (compare Fig. 109) leads to different sedimentation rates which might be an explanation for the bimodal size distribution. Furthermore, based on the high concentration which is used for the DCS measurement it is possible that some of the branched structures form agglomerates. This might lead to the second peak at 17 nm. The evaluation of the peak broadness in comparison to the mean size resulted in a PDI of 0.36 and hence still indicates a polydisperse system. However, compared to the data obtained from HRTEM, the PDI is decreased.

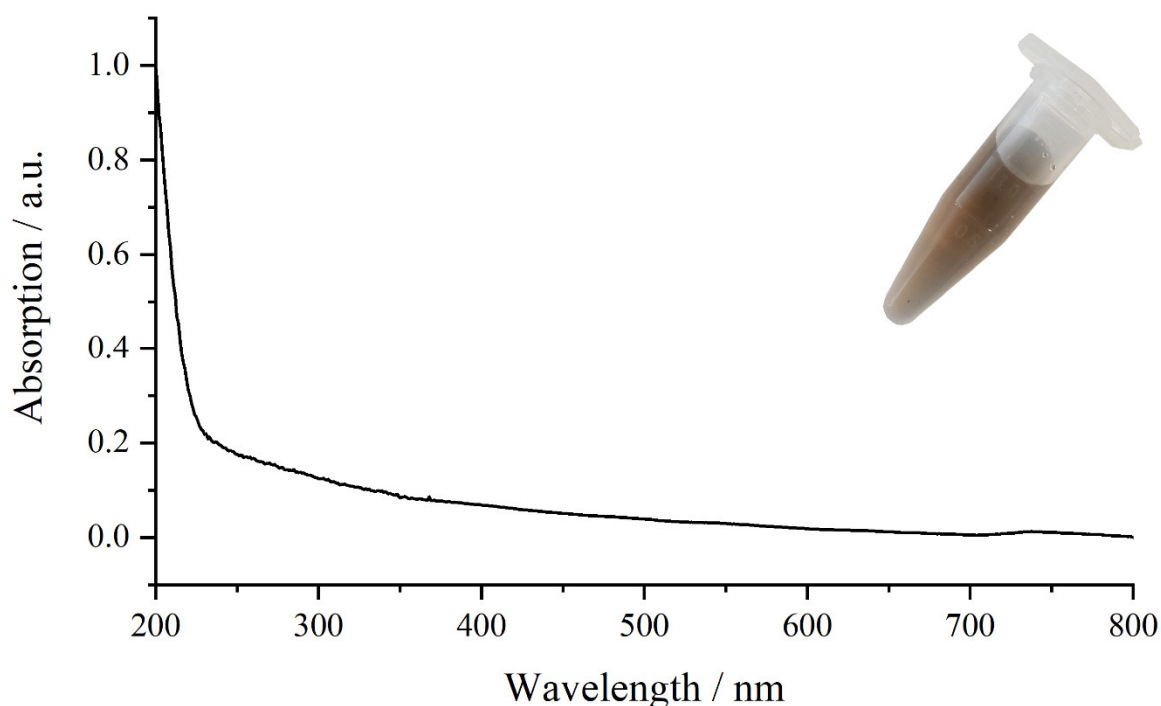


Fig. 110: UV/Vis spectrum of iridium nanoparticles and an additional image of the actual sample. The graph depicts the absorption (a.u.) as a function of the wavelength (nm).

An obtained UV/Vis spectrum shows a low absorption over the whole visible range (350-800 nm) which leads to a brownish dispersion color (see Fig. 110). Furthermore, there is a strong increase of absorption in the UV-region which is contributed to iridium and the capping agent PVP. This absorption characteristics are typical for iridium nanoparticles and are in good agreement with the literature.^[11, 199] The data shows that a mixture of branched and spherical iridium nanoparticles with a size range of 5-10 nm can be synthesized with a polyol process. The particles develop a polydisperse system with a high PDI of 0.36.

5.7 Synthesis of iridium nanoparticles using sodium borohydride

To improve the results regarding monodispersity and morphology, the synthesis for spherical silver nanoparticles with sodium borohydride was adapted to be used for iridium nanoparticles. To compensate the building of the stable iridium aqua complex ($[\text{IrCl}_3(\text{H}_2\text{O})_3]^+$), the amount of reducing agent was hugely increased. The particles obtained from this synthesis will be described in detail in chapter 5.7.1.

5.7.1 Characterization of iridium nanoparticles using sodium borohydride

The obtained particles from the reduction with sodium borohydride were characterized using HRTEM imaging. The images were taken with an acceleration voltage of 300 kV.

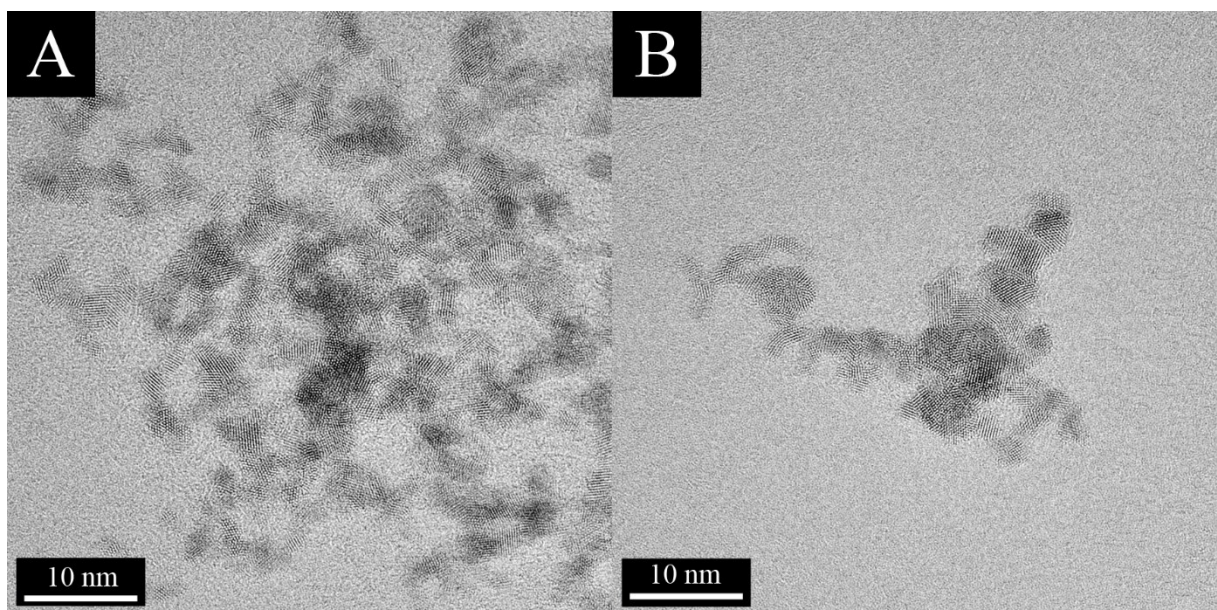


Fig. 111: HRTEM images of the obtained iridium nanoparticles from the synthesis with sodium borohydride (A+B).

The particles generated by the reduction with sodium borohydride also result in branched structures. Additionally, no spherical structures are formed. To identify single crystallites, high resolution TEM images were generated. The formed particles show smaller crystallites compared to the samples that are synthesized with ethylene glycol. Only few of the observed crystallites are bigger than 0.5 nm. Since the synthesis is performed at a pH of 12 to destabilize

the iridium precursor (compare chapter 5.2.3), it will be easier to reduce the complex. The resulting nucleation process leads to an increased number of seeds which result in smaller crystallites compared to the synthesis with ethylene glycol. A histogram for the sample could not be generated because of the strong anisotropic particle shape. To gain a deeper insight in to the crystallographic properties and identify the phase purity of the system XRPD measurements were performed. Unfortunately, the generated pattern showed no reflexes and could hence not be used to perform a Rietveld refinement. The absence of reflexes is caused by the small crystallites. The investigation of particles obtained from the synthesis with ethylene glycol (chapter 5.5) already showed a massive reflex broadening. Since the particles from sodium borohydride have even smaller crystallites, the resolution of the method cannot visualize the broad peaks of the sample.

The colloidal stability, the nanoparticle size and their optical properties in dispersion were investigated by DCS and UV/Vis spectroscopy.

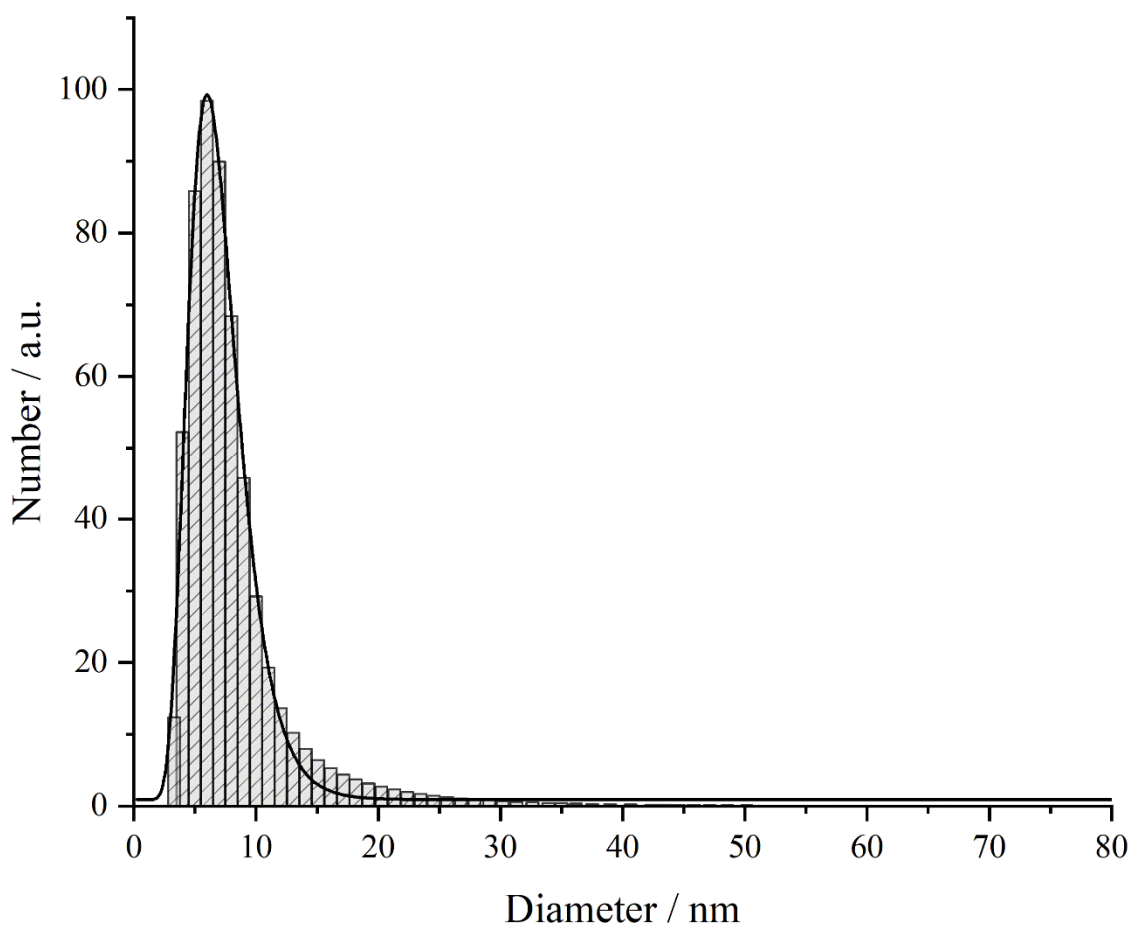


Fig. 112: DCS measurement of the iridium nanoparticles synthesized with ethylene glycol. The graph displays the number (a.u.) as a function of the particles diameter (nm). The graph was plotted with a log normal fit function.

The dataset obtained from the DCS reveals that the particles possess a mean size of 6.7 nm with a standard deviation of ± 2.4 nm. Additionally, the size distribution shows a high FWHM resulting in a PDI of 0.57 which leads to a classification as a polydisperse system. This result was expected since the sample showed branched structures with varying sizes. However, the particle size obtained from DSC must be evaluated with care because the anisotropic nature has a strong influence on the sedimentation of the particles.

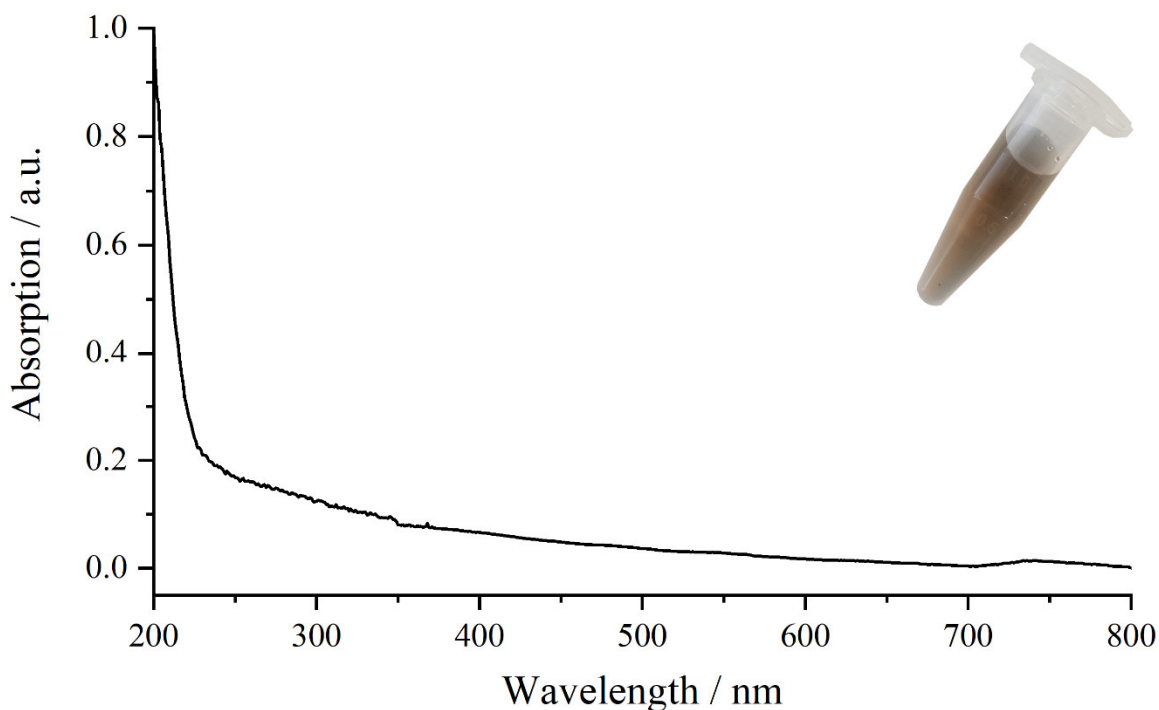


Fig. 113: UV/Vis spectrum of iridium nanoparticles obtained from reduction with sodium borohydride and an additional image of the actual sample. The graph depicts the absorption (a.u.) as a function of the wavelength (nm).

Since the particles show comparable structures and sizes to the particles obtained with the polyol process, the absorption spectrum collected with UV/Vis spectroscopy is identical. The particle dispersion possesses the same brown color which is a consequence of the absorption of every wavelength in the visible spectrum (compare chapter 5.6.1).

The synthesis with sodium borohydride using water as solvent did not lead to spherical nanoparticles. Thus, optimizations and modifications like precursor concentration, reducing agent concentration or the earlier addition of capping agent in the process were tried to generate spherical particles

5.8 Synthesis of porous nanospheres of Ir/IrO₂ with sodium borohydride

During optimizations to generate “spherical” monometallic iridium nanoparticles, observations were made regarding the color of the obtained dispersion. Due to the early addition of PVP and a longer stirring time, the solution developed a blue color and therefore a different plasmonic resonance to the previously reported branched structures in this work. This altered plasmonic resonance could indicate a formation of iridium dioxide or a different morphology. The formation of iridium oxide is likely due to the high amount of sodium borohydride forming boric acid which transforms to the tetrahydroxyborate anion in aqueous solution.^[200] The reaction therefore results in a pH value of 10.5.^[165] The basic conditions combined with a high stirring time can result in the formation of iridium dioxide. Comparable reaction parameters are often used to generate iridium dioxide particles in the literature.^[199, 201] Consequently, a formation is likely. The initial addition of sodium borohydride also generates small iridium nanoparticles with small crystallites of around 1-2 nm which can be incorporated in to the forming nanoparticles. This will result in a mixed phase system.

Mixed phased systems of iridium and iridium oxide show a high potential for catalytical applications. Former investigations of iridium/iridium oxide composites by Xu et al. have shown that these systems possess a higher electrocatalytic activity compared to the pure phased materials.^[199] Furthermore, the materials have several fields of catalytic applications like stimulating nitrides^[202], enhancing and performing water splitting^[51, 53] or they are incorporated in catalytic sensor systems.^[55] Therefore, the newly formed particles might show potential to be used in similar applications.

5.8.1 Characterization of porous Ir/IrO₂ nanostructures

The particles were investigated using high resolution transmission electron microscopy (HRTEM) to determine the nature of the systems and to examine the changes in plasmonics which might correspond to morphologic changes.

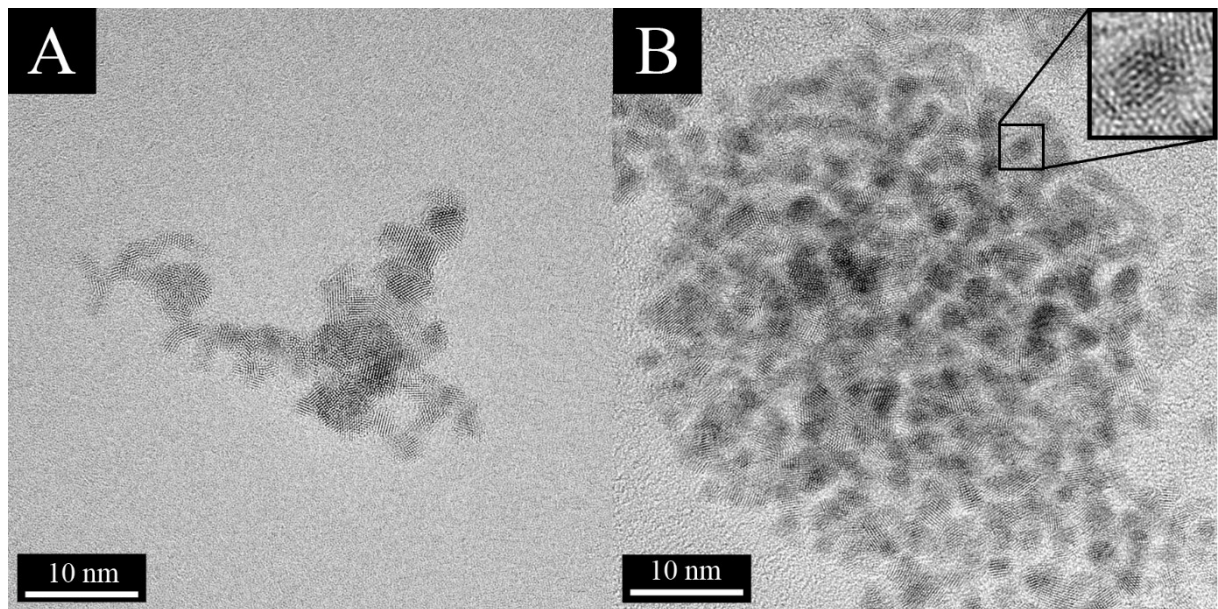


Fig. 114: HRTEM images of branched iridium nanoparticles obtained from the synthesis with sodium borohydride (A) in comparison to porous iridium-based nanostructures obtained from the modified synthesis (B).

A comparison between former described particles with sodium borohydride (Fig. 114, A) and the newly formed particles (Fig. 114, B) reveals that a spherical porous structure with a diameter of 43 nm results from the modified synthesis. Images with a lower magnification show an overview of the sample indicating a polydisperse size distribution of porous structures. Overall, the particles are spherical with a small quantity of elongated oval structures (Fig. 115, A). To determine the size distribution from HRTEM images, 42 porous structures were measured. The evaluation resulted in a histogram with a bimodal size distribution (compare Fig. 115, B). To calculate the mean sizes and the corresponding standard deviations of the observed peaks, two independent Gaussian functions were used to fit the dataset. Furthermore, the PDI of the system could be calculated from the obtained full width at half maximum (FWHM) of each peak.

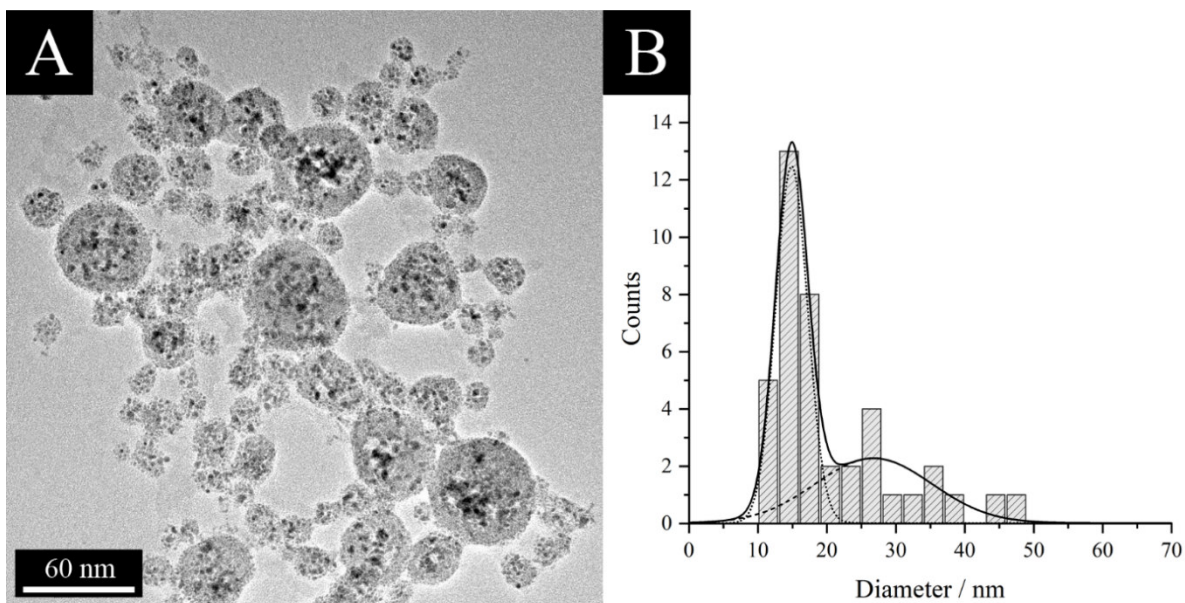


Fig. 115: Overview HRTEM image of porous iridium-based nanospheres (A) and the corresponding histogram (B) showing the particles counted as a function of particle size (nm).

The fits reveal a first maximum size of the particles around $26.8 \text{ nm} \pm 8.4 \text{ nm}$ and a second maximum at $14.9 \text{ nm} \pm 2.3 \text{ nm}$. The calculated weighted PDI of both peaks is 0.20 and therefore in the size range of a monodisperse system. Due to the high resolution of the HRTEM images the crystallinity and the grain sizes could be further investigated. The particles consist of 0.8 - 1.4 nm small crystallites that build the porous spherical structures with a low degree of crystallinity.

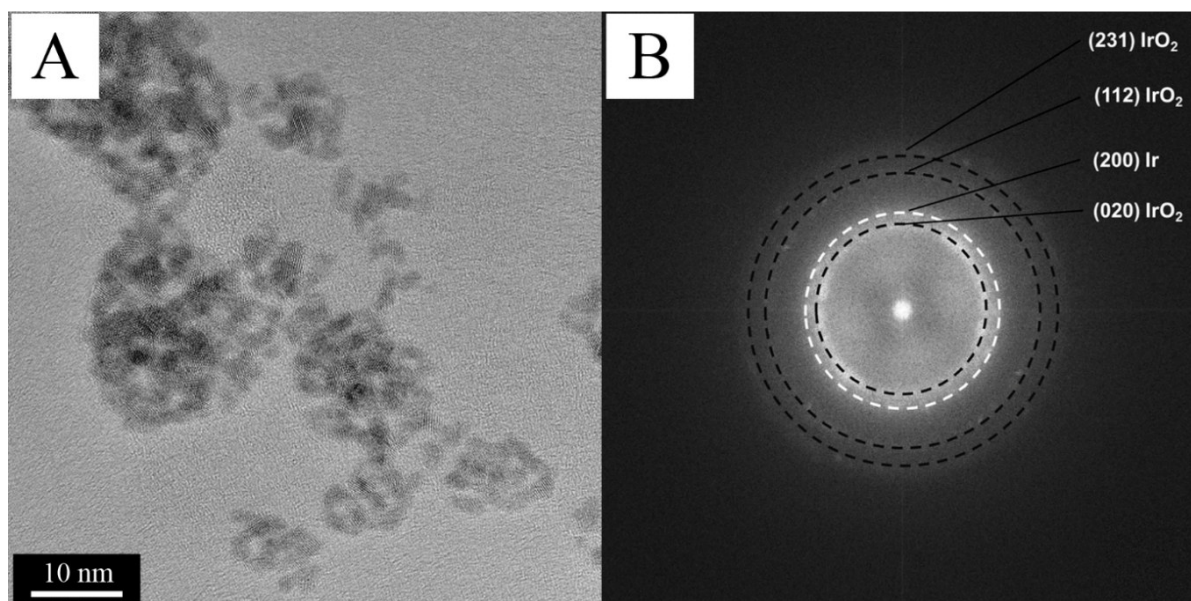


Fig. 116: HRTEM image (A) and corresponding diffraction pattern (B) of porous iridium-based nanostructures. The pattern shows four diffraction rings which can be assigned to iridium and iridium oxide.

Because of the high resolution of the HRTEM images, a diffraction pattern of single particles could be obtained. This pattern reveals (020), (112) and (231) diffraction rings of iridium oxide. The ring intensities of the higher indexed (112) and (231) lattice planes are rather low but still in a detectable range. Additionally, the (200) diffraction ring corresponding to iridium could be identified. Consequently, the sample accommodates two oxidation states of iridium resulting in a mixture of iridium and iridium dioxide.

Regarding the porosity of the particles, the complexation of certain crystallographic facets of the seeds by PVP might be an explanation. Former studies of silver morphologies have shown that PVP complexes the {100}-facets of silver nanocrystals. Since iridium and silver have the same crystal system and space group, the differentiation by surface energy of the crystallographic lattice planes stays the same ($\gamma_{\{111\}} < \gamma_{\{100\}} < \gamma_{\{110\}}$). Hence, a complexation by PVP of the (100) plane of iridium is likely. Accordingly, the preformed seeds of iridium will be complexed by PVP (Fig. 117, A). Since the formation of iridium oxide is a slow process, the molecules will not form new seeds but will attach to the iridium seeds instead. It is likely that certain crystallographic planes of iridium oxide will also be complexed by PVP. This will subsequently lead to a directional growth of iridium oxide (Fig. 117, B). Unfortunately, there is no literature regarding the influence of PVP on iridium or iridium oxide nanostructures to confirm this supposition. Finally a porous structure of iridium and iridium oxide will develop (Fig. 117, C). The spherical nature of the systems will minimize the surface energy and is hence a logical consequence.

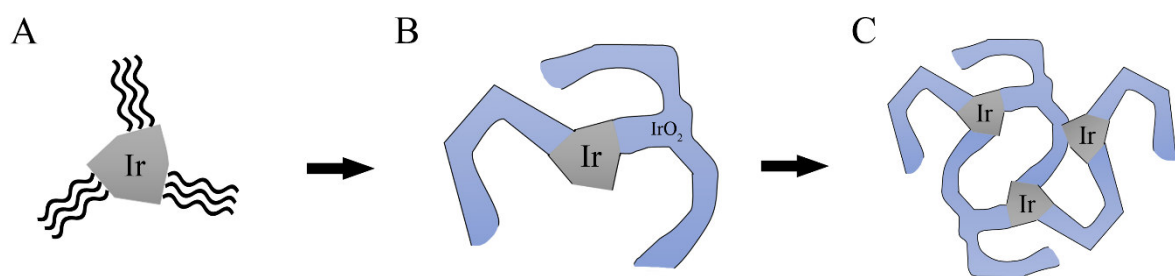


Fig. 117: Schematic process of the formation of porous iridium/iridium oxide nanostructures. At first, the iridium seeds are capped by PVP at the {111}-crystallographic facets (A). After formation of iridium oxide molecules a network of iridium oxide will grow at not complexed facets (B). In the end, a porous spherical particle stabilized by PVP will be formed (C). The black outer lines indicate PVP complexed facets. The branched IrO₂ structures contain a lot of small crystallites.

To further investigate the crystallographic properties of the particles as well as to support the finding of the TEM diffraction pattern, an XRPD pattern was measured. For the preparation of the measurements, a fraction of the dispersion was lyophilized producing 4.5 mg of powder. The obtained pattern was evaluated using Rietveld refinement (Fig. 118).

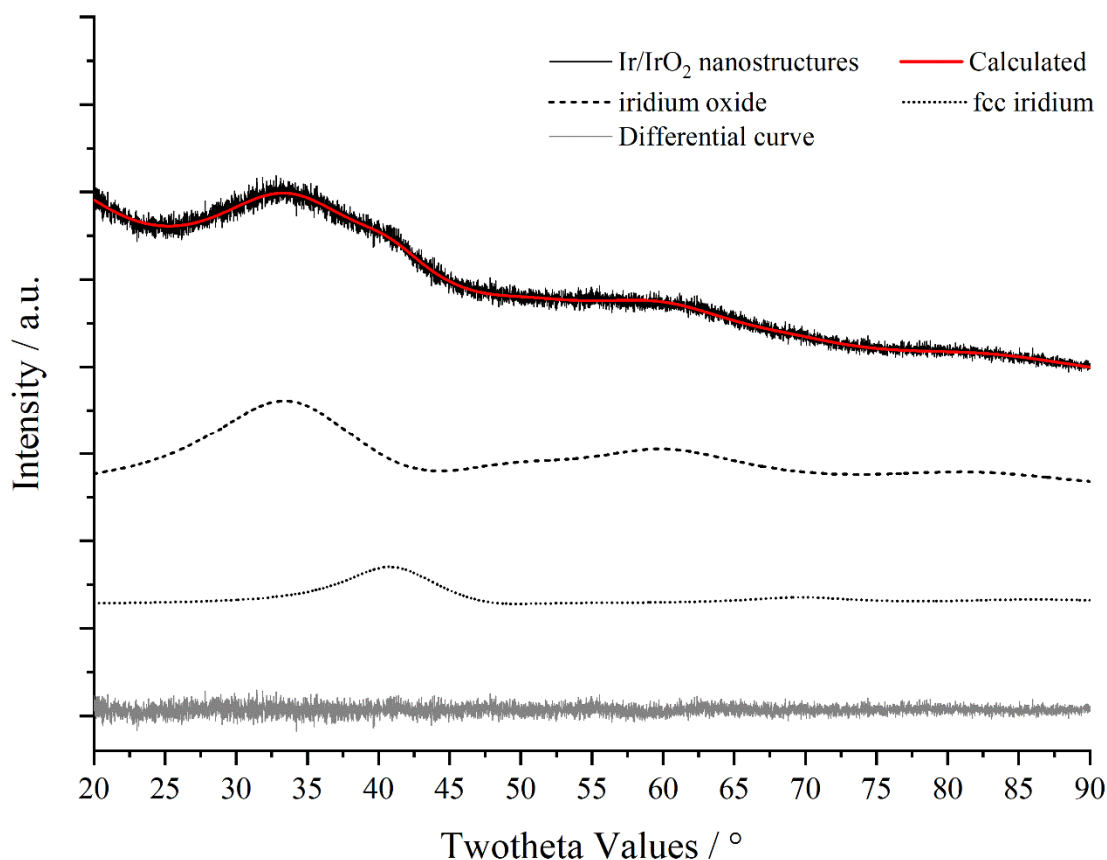


Fig. 118: Rietveld refinement of the powder pattern of the porous iridium structures. The refinement indicates a composition of the two different phases (iridium and iridium oxide). An indexation of single reflexes was not rational because of the high peak broadening.

The sample shows a rather strong peak broadening which could be expected from the HRTEM images indicating small crystallites between 0.8 – 1.4 nm. The refinement also reveals two different phases in the particle system. Namely iridium oxide which crystallizes in the rutile (tetragonal) system and iridium which crystallizes in the face-centered cubic (fcc) system. The crystallographic data from literature of both phases is shown in Table 33.

Table 33: Space groups, lattice parameters (LP) and cell volume of iridium and iridium oxide.

Phase	Space group	$LP (a / \text{Å})$	$LP (c / \text{Å})$	Cell volume / Å^3
Ir ^[116]	$Fm-3m$	3.839	-	56.597
IrO ₂ ^[117]	$P4_2/mnm$	4.505	3.159	64.107

The mean crystallite sizes, the lattice parameters as well as the percental composition were obtained from Rietveld analysis. The data from the refinement is shown in Table 34.

Table 34: Lattice parameter (LP), cell volumes, crystallite sizes (CS) and composition of the phases derived from Rietveld refinement.

Phase	LP ($a / \text{\AA}$)	LP ($c / \text{\AA}$)	Cell volume / \AA^3	CS / nm	Amount / at %
Ir	3.820 (7)		55.750 (32)	1.0 (0)	28.2
IrO ₂	4.255 (2)	3.703 (4)	58.362 (30)	0.7 (1)	71.8

The mean crystallite sizes were calculated using a Lorentzian peak profile. The lack of high angle refraction peaks is caused by anisotropic peak broadening corresponding to the small crystallites. Both phases show crystallites between 0.7 – 1.0 nm and are therefore in good agreement with the observations from HRTEM images. Furthermore, the c-axis lattice parameter of iridium oxide strongly differs from the lattice parameters of the bulk material (compare Table 33 and Table 34). The strong deviation of the c-axis parameter might be an indication that the iridium oxide crystallites have grown on not complexed facets of iridium seeds. This leads to a strong unit cell distortion of iridium dioxide to adapt the lattice parameter of iridium. The amount of both phases could also be obtained from Rietveld refinement. The evaluation resulted in a ratio of 28.2 at% iridium to 71.8 at% iridium dioxide. The peak broadening of the sample reduces the information obtainable from the pattern and the results hence need to be treated with caution. However, calculations only using one of the two phases led to much inferior Rwp-values and therefore worse refinement results. The analysis consequently reveals a mixture of elemental iridium and iridium dioxide confirming two different oxidation states of iridium in the system. To gain more information about the oxidation states and the chemical composition, XPS measurements were carried out to corroborate the data obtained from XRPD and HRTEM.

The XPS measurements and data evaluation was carried out by Dr. Ulrich Hagemann in the Center for Nano Integration at the University of Duisburg-Essen. For the measurement, 4 mg of freeze-dried particles were prepared and placed on a sample holder. The measurement was then carried out in ultra-high vacuum using copper radiation with an energy of 1486.8 eV.

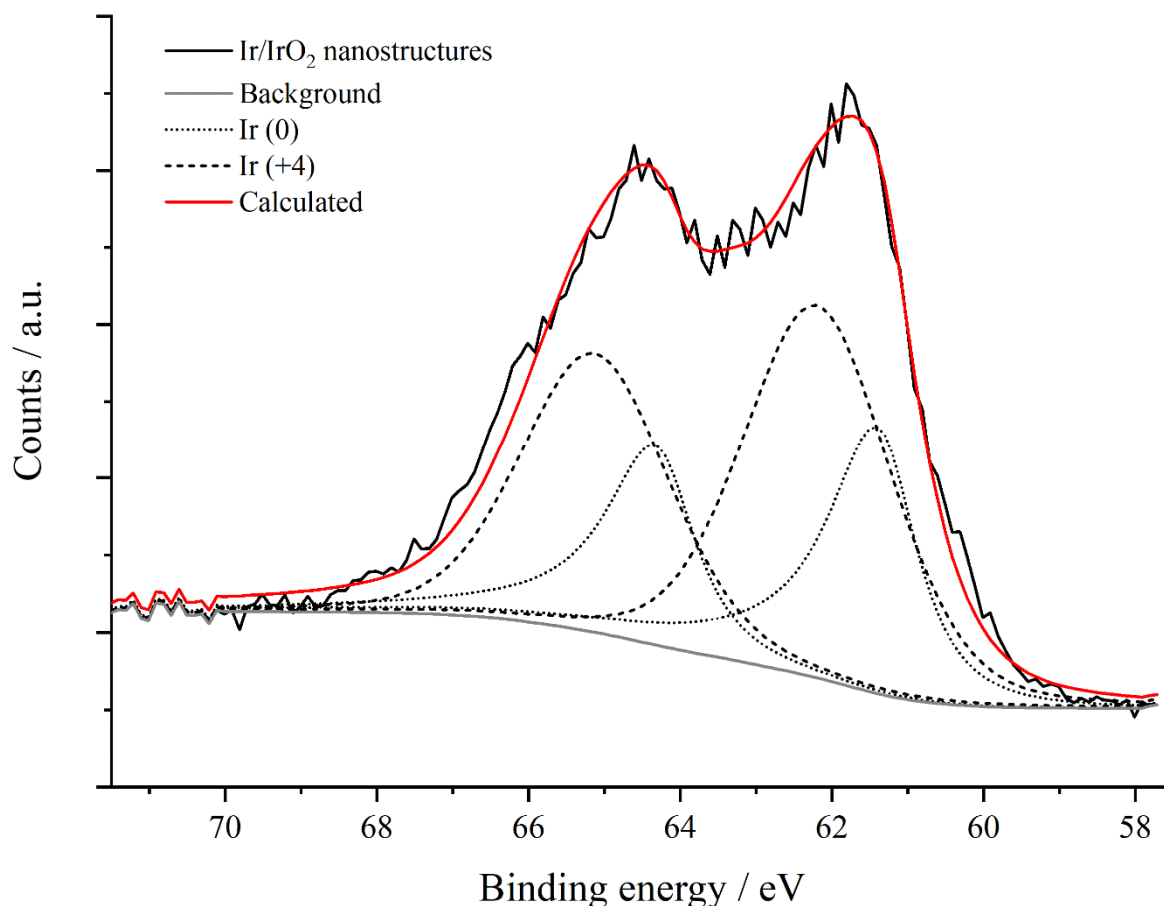


Fig. 119: XPS measurement of the porous iridium structures obtained from the synthesis with sodium borohydride. The graph shows the intensity (a.u.) as a function of the binding energy (eV). The obtained peak corresponds to the binding energies of the 4f orbitals of iridium and iridium oxide.

Due to the amount of stabilizing PVP, the iridium signal in an XPS measurement is strongly reduced. However, an identification of the signal was possible. The peak shows two maxima at 61.7 eV and 64.5 eV. The energies observed cannot be directly associated to Ir(0) or Ir(+4) only and consequently confirm a mixture of both oxidation states. The binding energies of electrons corresponding to the 4f orbitals and the oxidation states can be identified by the peak position and shape. The data from the literature is needed to distinguish between oxidation states. In the case of iridium the binding energies of the 4f_{5/2} and 4f_{7/2} for both oxidation states are examined.

Table 35: Derived XPS binding energies from the cumulative peaks and the corresponding peaks of iridium (0) and iridium (+4) in comparison to literature values.^[203]

Sample	Peak	Binding energy / eV
Ir/IrO ₂ NP	1	61.7
	2	64.5
Ir	4f _{7/2}	61.4
	4f _{5/2}	64.4
IrO ₂	4f _{7/2}	62.2
	4f _{5/2}	65.2
Ir (anhydrous, lit.)	4f _{7/2}	60.8
	4f _{5/2}	63.8
IrO ₂ (anhydrous, lit.)	4f _{7/2}	61.9
	4f _{5/2}	64.9
IrO ₂ (hydrated, lit.)	4f _{7/2}	62.5
	4f _{5/2}	65.5

The cumulative peaks can be constructed of separated weighted peaks of iridium and iridium dioxide with different energies (compare Fig. 119 and Table 35). The obtained binding energies for the 4f_{5/2} and 4f_{7/2} electrons of iridium and iridium dioxide are slightly shifted compared to the literature. This might be due to the functionalization of the particles with PVP. The nanostructures only consist of small crystallites which consequently have a huge surface area. A functionalization consequently has a strong influence of the binding energy. This is also shown in the literature where the binding energies of iridium dioxide and hydrated iridium dioxide have been measured. The absorbance of water molecules shifts the binding energy of the 4f_{5/2} and 4f_{7/2} to 0.6 eV higher values (compare Table 35). Consequently, an addition of PVP can also alter the binding energy and shift it 0.3 eV higher values. The binding energies of elemental iridium experience an even stronger shift of 0.6 eV.

The XPS measurement can be used to determine the ratio of Ir(0) to Ir(+4) in the sample. The fitted data was used to calculate the at% of both species. This evaluation resulted in a ratio of 44:56 at% (Ir:IrO₂). The amount of iridium is much higher compared to what is found in XRPD (28:72 at% (Ir:IrO₂)). This deviation is related to the low quality of the XRPD data where the quantification is strongly depended on the background of the measurement. The low-quality leads to difficult evaluable data and hence to strongly divergent results compared to XPS. The XPS measurement also led to the at% of each element contained in the sample. The composition determined by XPS is shown in Table 36.

5.8 Synthesis of porous nanospheres of Ir/IrO₂ with sodium borohydride

Table 36: Composition by atom percentage (at%) of the elements contained in the Ir/IrO₂ sample determined by XPS. The values in blue are theoretical and assumed from the measured data.

Element	Symbol	Mass / at%
Nitrogen	N	4.2
Nitrogen in PVP	N	4.2
Carbon	C	27.8
Carbon in PVP (based on N)	C	25.2
Oxygen	O	39.3
Oxygen in PVP (based on N)	O	4.2
Oxygen in IrO ₂	O	6.2
Oxygen in trisodium citrate (based on C)	O	3.0
Oxygen in SiO ₂ (glass corrosion)	O	13.6
Oxygen in B ₂ O ₃ (glass corrosion)	O	4.8
Oxygen in Na ₂ O (glass corrosion)	O	3.7
Boron	B	3.2
Sodium	Na	7.4
Sodium in TSC (based on C)	Na	1.3
Silicon	Si	6.8
Iridium (+4)	Ir	3.2
Iridium (0)	Ir	1.8

The XPS measurement reveals that besides iridium and the elements of PVP and trisodium citrate (C, N, Na and O) also other elements are present. The sample contains boron and silicon. The presence of the elements sodium and boron can be explained since the used reducing agent is sodium borohydride and trisodium citrate is used to stabilize the seeds. However, the presence of silicon cannot be explained that easily. A reasonable explanation for the occurrence of silicon is the corrosion of the used glass flask under alkaline conditions. As former described, the synthesis develops a pH value of ~11. The basic conditions and the long stirring time can lead to glass corrosion where oxides leached from the glass vessel.^[204] The laboratory glass contains a high amount of SiO₂ and also smaller quantities of B₂O₃ and Na₂O. This might be an explanation for the occurrence of silicon. Since the detected elements are present in several compounds, a quantification of every possible byproduct is not possible. Nevertheless, the XPS measurement confirms that the system is a mixture of iridium and iridium dioxide and consequently shows high potential for possible electrochemical applications.

To determine the size distribution and the colloidal stability of the Ir/IrO₂ nanostructures in ultra-pure water, additional methods like disc centrifugation sedimentation (DCS) were used. The DCS confirms the observations from HRTEM (Fig. 115, A) revealing a bimodal size distribution.

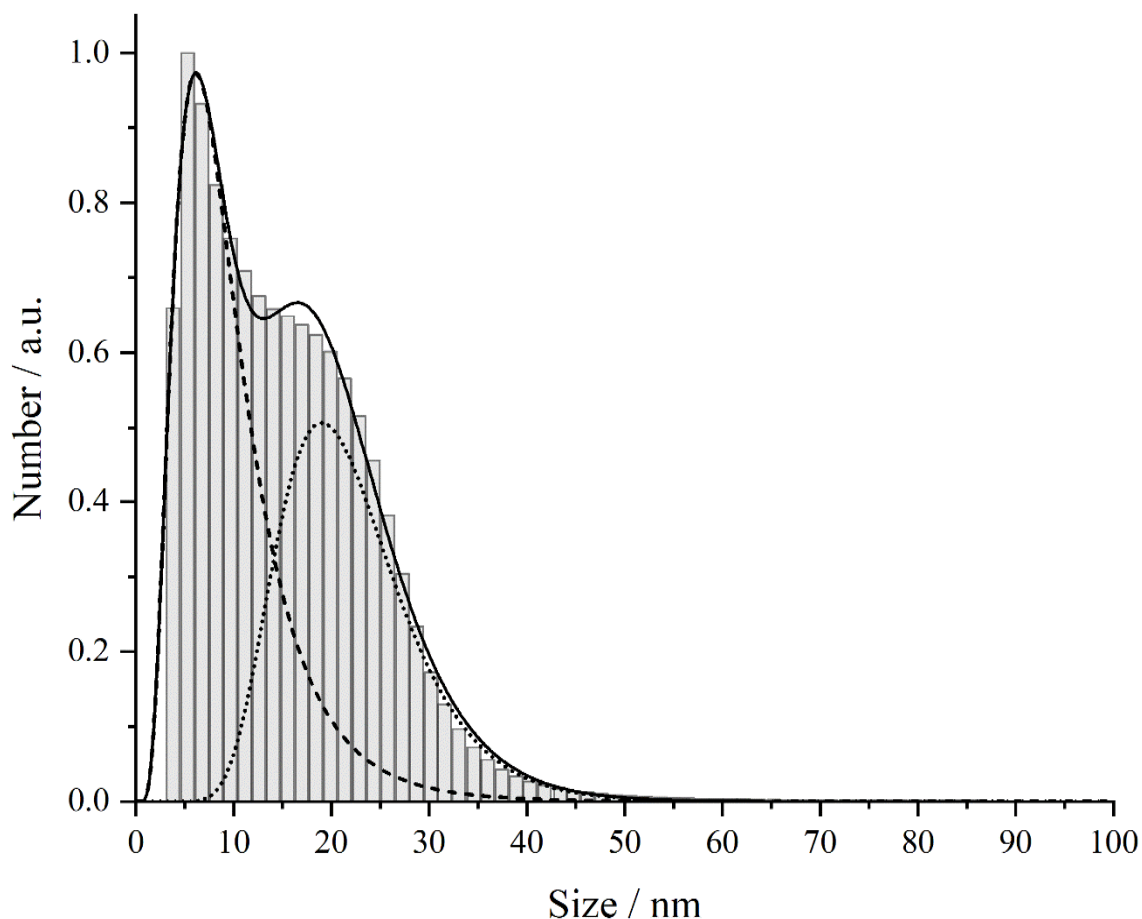


Fig. 120: DCS measurement of the synthesized porous Ir/IrO₂ nanostructures. The number (a.u.) is shown as a function of size (nm). The data was fitted using two independent Gaussian fits.

The data was analyzed using two independent Gaussian fits to calculate the mean particle sizes and the standard deviations from the data set. The results derived from the modelled fits are shown in Table 37.

Table 37: Mean size, standard deviation and the coefficient of determination (COD) for the applied Gaussian fits for the DCS measurements. The PDI was calculated using a Gaussian fit function.

Peak	Size / nm	Standard deviation / nm	PDI from Gaussian fit	COD (R ²)
Maximum 1	7.7	± 3.9	1.71	0.9459
Maximum 2	20.4	± 6.1	0.50	0.9792

5.8 Synthesis of porous nanospheres of Ir/IrO₂ with sodium borohydride

The mean size at the peak maximum is smaller compared to the data obtained from the generated histogram from HRTEM (Fig. 115, A). This observation can be explained by the functionality of the method. The DCS uses the relative density of the particles to calculate the size. Therefore, variations in density which may be caused by the porous nature of the particles have a direct impact on the calculated size distribution, underestimating the real particle size. Also, the polymeric shell of PVP, which is build up around the particles to stabilize them, causes a change in the real density of the system.

The optical properties of metallic nanoparticles in dispersion can be investigated using UV/Vis spectroscopy. These absorption-based measurements can be used to obtain information about the size, degree of aggregation and the morphology of the investigated colloid. UV/Vis spectroscopy was done to determine the exact excitation energy of the plasmons and therefore the maximum wavelength of the absorption band in the visible region of the porous structures.

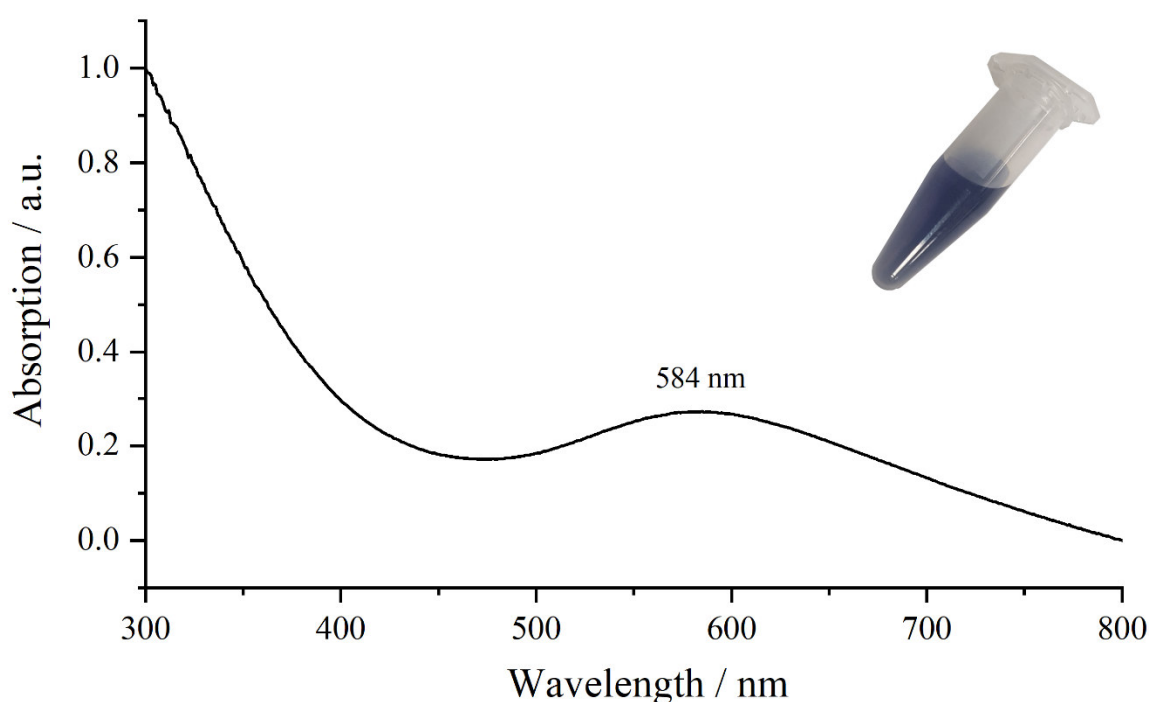


Fig. 121: UV/Vis spectrum of the porous iridium particles and an additional image of the actual sample. The graph shows the absorption (a.u.) as a function of the wavelength (nm).

The UV/Vis spectrum shows a broad absorption band with a low maximum intensity at 584 nm (2.12 eV). Furthermore, a steep and broad increase in absorption between 300 – 400 nm can be observed. This absorption is typically for IrO₂ nanoparticles in dispersion and therefore reaffirms the formation of iridium dioxide in the dispersion.^[201]

5.8.2 Temperature-dependent investigations of porous Ir/IrO₂ nanostructures

Iridium and iridium dioxide films and particles generate a huge interest due to a lot of possible applications. There are various fields including sensing and detecting, catalysis and applications in fuel cells. Some of those fields require a thermal stability of the catalyst. To confirm that the porous structures not only exist in short-term and that the porosity is maintained after energy application, the particles were investigated by thermogravimetric analysis in different atmospheres (O₂ and Argon). Furthermore, the thermal behavior was characterized by *in-situ* TEM heating in different atmospheres (vacuum, O₂, N₂, and Argon + H₂). All measurements were performed up to a temperature of 1000 °C with heating rates of 5 K min⁻¹.

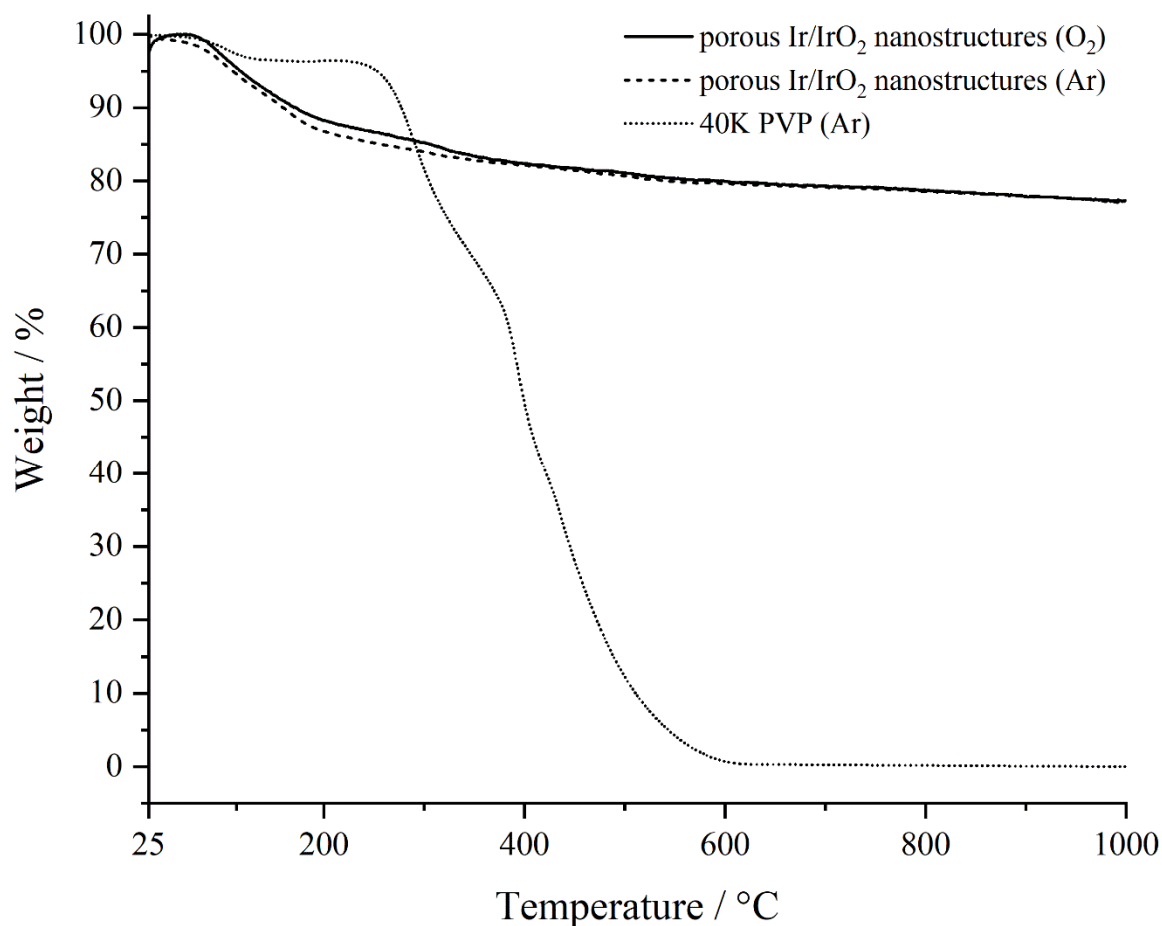


Fig. 122: Comparison of thermogravimetric measurements of porous iridium nanostructures carried out in argon and oxygen with pure PVP (40K) in argon. The mass loss (%) is shown as a function of the temperature (°C). The heating rate for all samples was 5 K min⁻¹.

5.8 Synthesis of porous nanospheres of Ir/IrO₂ with sodium borohydride

The flow rate for both accomplished thermogravimetric experiments was set to 50 mL min⁻¹ and hence consisted of either 50 mL min⁻¹ argon or a mixture of argon and oxygen with 25 mL min⁻¹ each. The TG analysis leads to nearly matching thermograms for both used atmospheres. There is no notable difference which indicates that no mass increase by oxidation of the sample occurs. Furthermore, the total mass loss for both samples with 23 % and 22.7 % comparable. In the early stage between 25-215 °C both samples experience a significant mass loss. This loss might be contributed from remaining solvent molecules. A comparison of the TG measurements of porous iridium structures and a TG analysis of PVP shows that the mass loss is partially resulting from the complete decomposition of PVP which occurs in a temperature range between 215-625 °C (compare Fig. 122 and Table 38).

Table 38: Mass loss determined by TG in different temperature intervals for the synthesized Ir/IrO₂ nanostructures measured in an argon or oxygen atmosphere in comparison to 40K PVP measured in argon.

Sample	Mass loss / % (25-215 °C)	Mass loss / % (215-625 °C)	Mass loss / % (625-1000 °C)	Remaining mass / %
Ir/IrO ₂ (O ₂)	12.4	7.9	2.5	77.3
Ir/IrO ₂ (Ar)	13.8	6.7	2.5	77.0
PVP 40K (Ar)	3.8	94.2	0.0	2.0

Since PVP completely decomposes, the amount after purification of the iridium nanostructures, and consequently the amount needed for a colloidal stabilization, can be estimated. It equals approximately the mass loss between 215-625 °C for both samples (compare Table 38). The amount for a functionalization of the porous iridium nanostructure surface lies in a range between 6.7-7.9 % of the overall mass. Furthermore, the mass loss in the region between 625-1000 °C might be explained by a formation of volatile IrO₃ which decomposes at 1050 °C.^[4] To confirm this assumption, an XPS measurement of a sample heat treated in oxygen was performed. A freeze-dried sample was divided into two fractions. One fraction was measured without a heat treatment (compare Fig. 119) and the second one was annealed in an oven under atmospheric conditions. The used temperature program of the oven was chosen to match the TG experiment. Consequently, the heating rate was set to 5 K min⁻¹ which resulted in a heating ramp over a time span of 3:15 h.

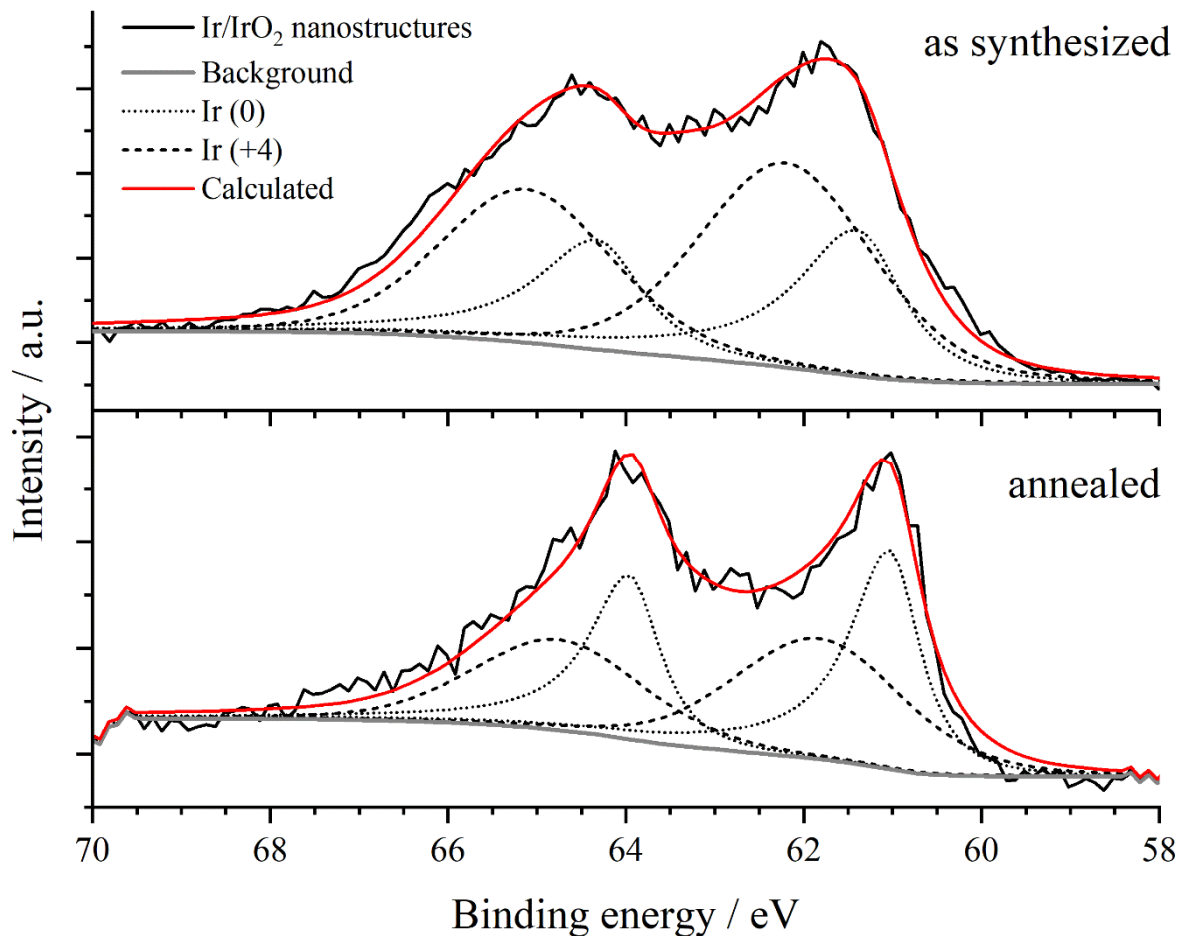


Fig. 123: XPS measurement of the porous iridium structures obtained from the synthesis with sodium borohydride (as synthesized) compared to the same sample after a heat treatment up to 1000 °C in atmospheric conditions (annealed). The graphs show the intensity (a.u.) as a function of the binding energy (eV). The obtained peak corresponds to the electron binding energies of the 4f orbitals of iridium in elemental iridium and iridium oxide.

The maxima of the cumulative peak profile obtained after the heat treatment are strongly shifted to lower energy values compared to the sample as synthesized. The data evaluation reveals a decrease in the overall intensity implying that after the thermal treatment less iridium remains in the sample. The peak profile can still be described by a fit of 4f_{5/2} and 4f_{7/2} electron binding energies of both oxidation states but compared to the untreated sample, the amount of iridium oxide has decreased significantly. This leads to the conclusion that the former expected reaction from IrO₂ to volatile IrO₃ has decreased the amount of iridium dioxide in the annealed sample. Hence, the observation from the TG and XPS are in good agreement. Since the TG measurement under argon shows the same results as the one under oxygen, the only possible explanation is that the used argon contains too much oxygen which allows the reaction to happen (see Fig. 122).

5.8 Synthesis of porous nanospheres of Ir/IrO₂ with sodium borohydride

A further investigation of the crystallographic properties and the behavior of the porous structure towards thermal energy can be realized by *in-situ* heating TEM experiments. Therefore, several atmospheres like ultra-high vacuum, oxygen, nitrogen as well as a reducing atmosphere containing argon and 4% hydrogen were used. All experiments were performed and evaluated by Dr Kateryna Loza.

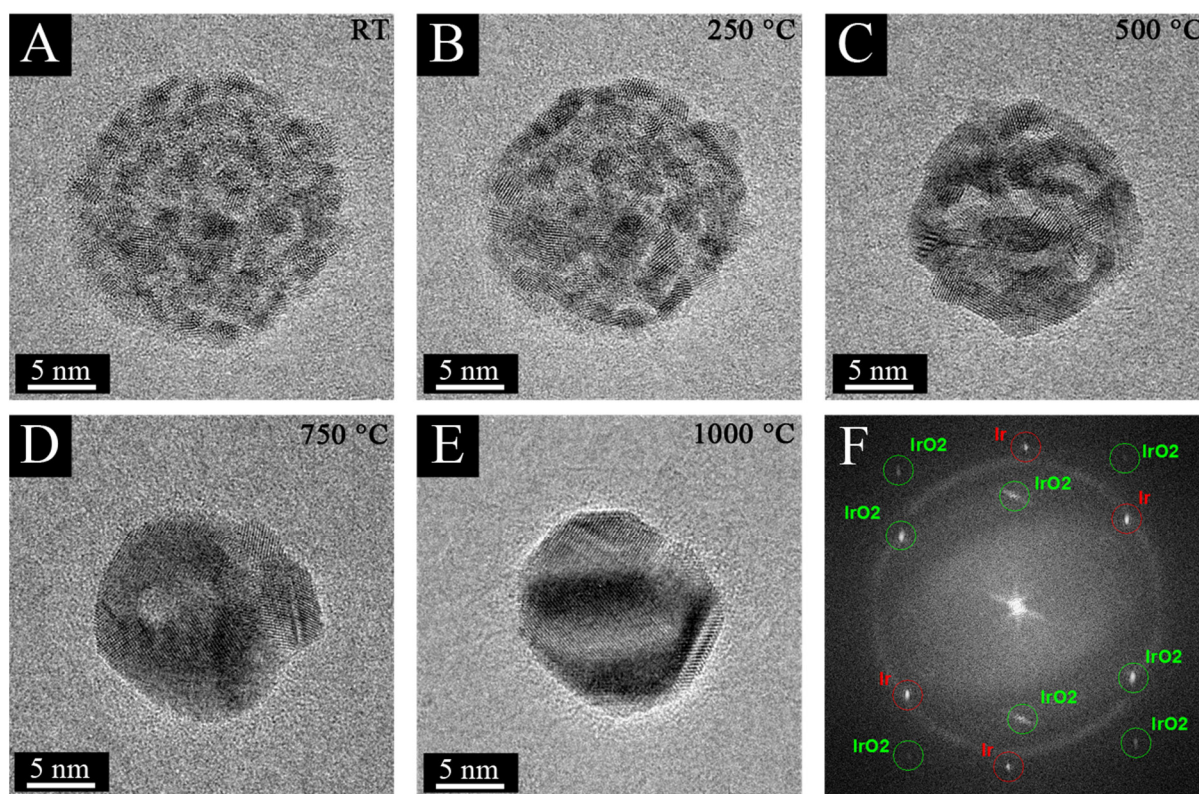


Fig. 124: HRTEM images of porous Ir/IrO₂ nanostructures at different temperatures (A-E) and an electron diffraction pattern of the particle at 1000 °C (F). The results shown were performed under ultra-high vacuum.

The images obtained from *in-situ* heating TEM show that the porous particles remain in their porous structure up to a temperature of 250 °C (Fig. 124, B). This observation can still be made up to a temperature of 400 °C (image not shown). If a temperature around 500 °C is reached, the particles start to recrystallize forming bigger, well-ordered grains. The porous structure also starts to be sacrificed for the higher degree of crystallinity. After a temperature of 750 °C is reached the small crystallites have fused to minimize the lattice energy of the system which results in a few bigger grains (Fig. 124, D). At a temperature of 1000 °C, the particle seems to be a faceted single crystal which has undergone a complete recrystallization (Fig. 124, E). The melting point of IrO₂ is at 1100 °C. Consequently, the observed transition is due to a recrystallization process and not caused by the melting of the sample.

Since the porous structure is lost in the formation of the highly packed, ordered structure, the particle diameter has decreased notably. The former diameter of 21.0 nm has decreased to 15.7 nm which corresponds to a shrinkage of 25.2 %. The Particle at 1000 °C was used to generate an electron diffraction pattern (Fig. 124, F). Caused by the higher crystallinity, the intensity of the diffraction pattern has increased compared to the former investigation (compare Fig. 116, B): The pattern still shows a mixture of iridium and iridium dioxide. The investigation in ultra-high vacuum have shown that the particles retain their porous nature up to temperatures of 400-500 °C. The wildfire system which is used for the experiments can be combined with a gas flow system to control the atmosphere during the experiment. To investigate the thermal induced changes in an oxygen atmosphere, the experiment was again performed with 1 atm of oxygen.

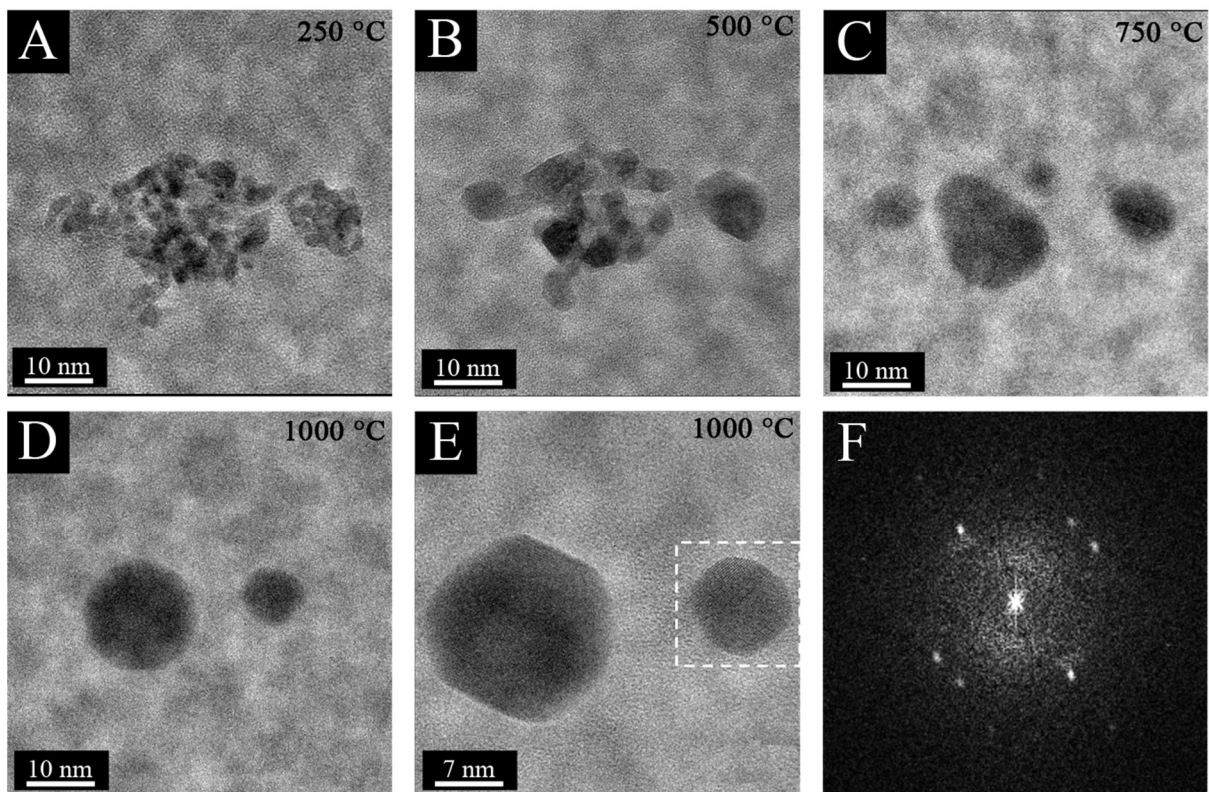


Fig. 125: HRTEM images of porous Ir/IrO₂ nanostructures at different temperatures (A-D) and an electron diffraction pattern (F) of the particle at 1000 °C (E, white dashed box). The results shown are from the experiment under oxygen atmosphere with 1 atm.

The images obtained have a decreased resolution because of the used oxygen atmosphere. The electron beam is deflected by oxygen molecules which leads to an overall intensity decrease. However, the particles could still be visualized at different temperatures. Comparable to the result of the experiments in vacuum, the particles retain the porous structure up to a temperature

of 250 °C. No morphologic changes or recrystallization processes can be observed (Fig. 125, A). The particles recrystallize slowly with an increase in temperature. The resolution is still high enough to distinguish between different grains which start to grow. Pores inside the structure are still observable up to a temperature of 400 °C. Single grains start to fuse at a temperature of 500 °C (Fig. 125, B). Exactly like the sample obtained from vacuum, the particle is completely recrystallized at a temperature of 750 °C (Fig. 125, C). At this temperature, the sample in vacuum had already started to build facets at some particle edges. The morphology of the particle has changed to a nearly perfect sphere and starts to build clearly visible facets at 1000 °C (Fig. 125, D). The electron diffraction pattern of the particle at 1000 °C only shows diffraction points of iridium dioxide. This might be related to the lower intensity caused by the oxygen atmosphere compared to the measurements in high vacuum. The experiment with the same conditions was again performed in nitrogen.

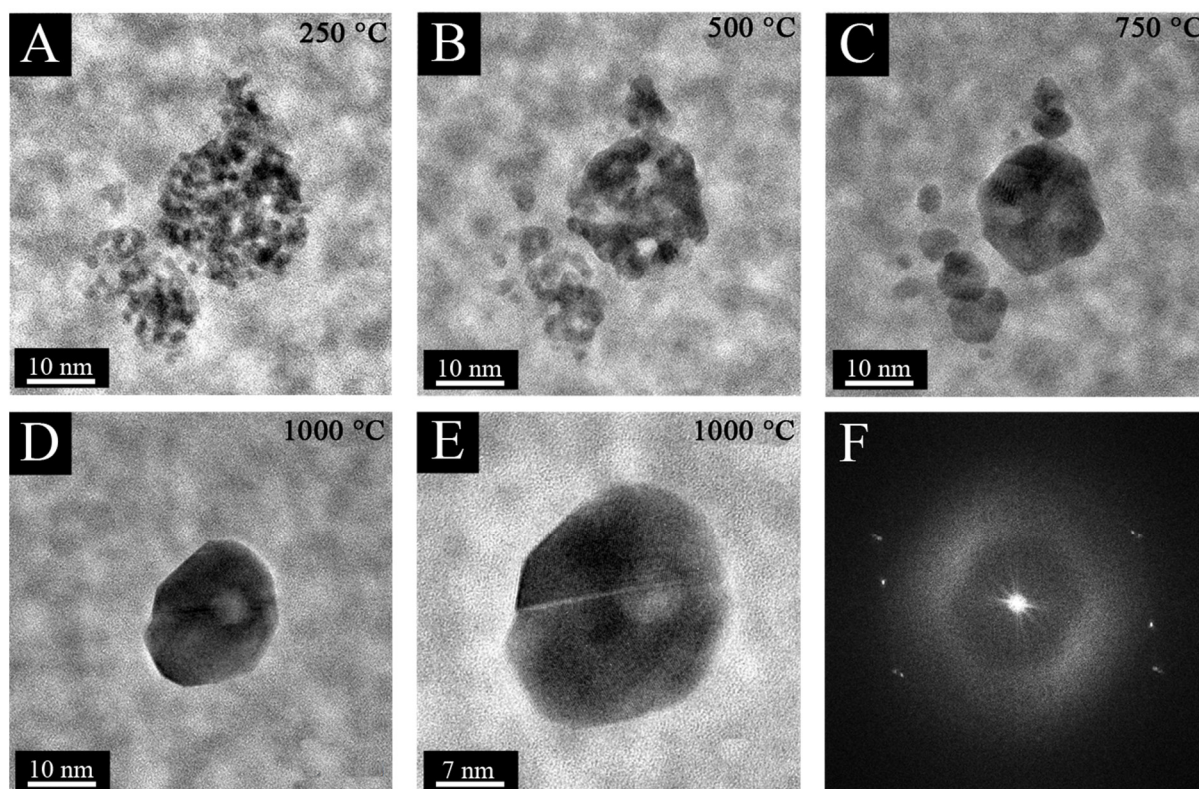


Fig. 126: HRTEM images of porous Ir/IrO₂ nanostructures at different temperatures (A-D) and an electron diffraction pattern (F) of the particle at 1000 °C (E). The results shown are from the experiment under nitrogen atmosphere with 1 atm.

The images obtained from a nitrogen atmosphere show the same trend. The porous structure is maintained up to 400-500 °C (Fig. 126, A+B). After a temperature of 750 °C is reached, the particles have lost their porosity completely (Fig. 126, C). However, the resulting particles at

1000 °C show well-formed facets which is comparable to the particles obtained from high vacuum (compare Fig. 126, D and Fig. 124, D). The electron diffraction pattern only shows iridium oxide (Fig. 126, F). This observation might correspond to the lower intensity of the measurement caused by the nitrogen atmosphere with 1 atm. To complement the investigation of the temperature dependence of the Ir/IrO₂ nanostructures, an atmosphere with reducing properties was tested. This atmosphere contained 4% hydrogen in pure argon.

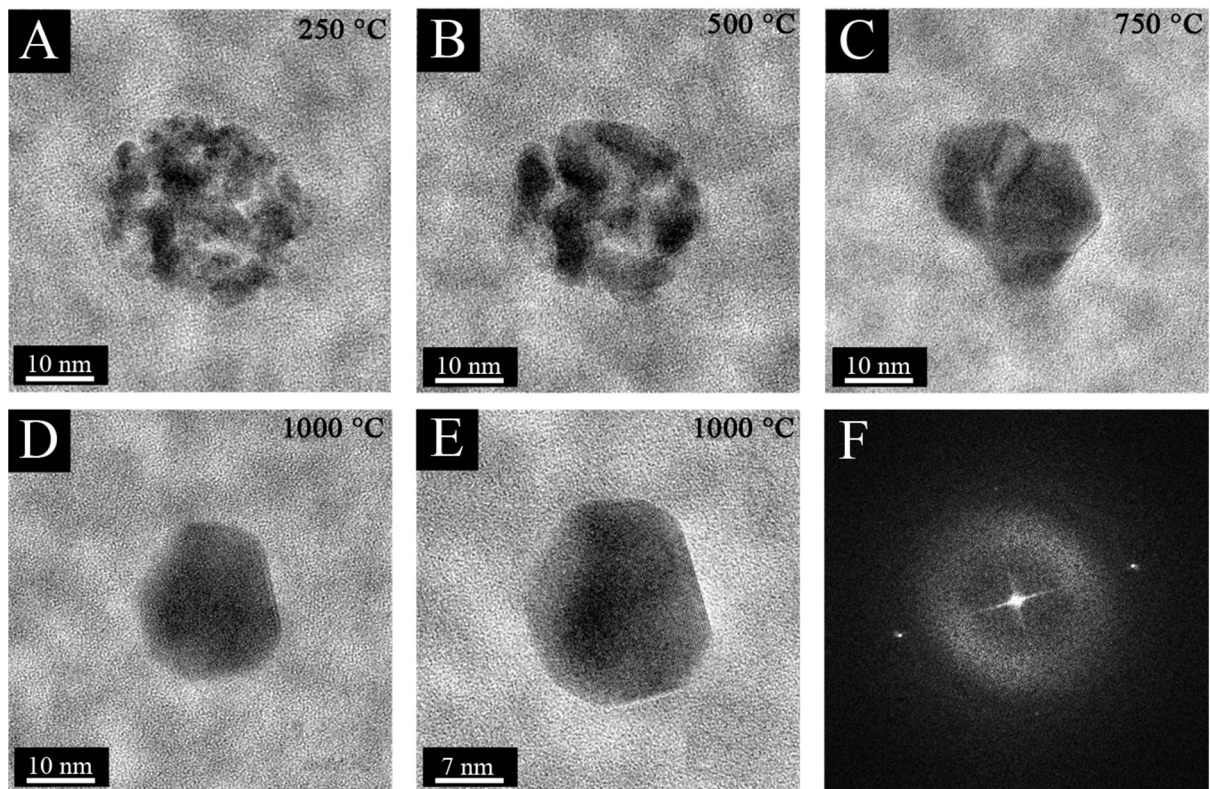


Fig. 127: HRTEM images of porous Ir/IrO₂ nanostructures at different temperatures (A-D) and an electron diffraction pattern (F) of the particle at 1000 °C (E). The results shown are from the experiment under argon/hydrogen (4%) atmosphere with 1 atm.

The trend of recrystallization for the system stays the same compared to the three different tested atmospheres. However, the reducing atmosphere leads to strongly faceted crystals compared to the former experiments. Already at 750 °C, clear facets of the grain are visible. One of the grains even develops a hexagonal habitus (Fig. 127, C). After a further temperature increase, the grains completely recrystallize to a single crystal. This crystal has well defined facets (compare Fig. 127, E). The electron diffraction reveals only iridium dioxide which is comparable to the results from the experiments with oxygen and nitrogen atmospheres. In all experiments, the porous structure of the particles is maintained up to 400 °C which shows that

the particles can be used in processes up to this temperature. A HAADF measurement of a particle in vacuum at a temperature of 400 °C is shown in Figure 128.

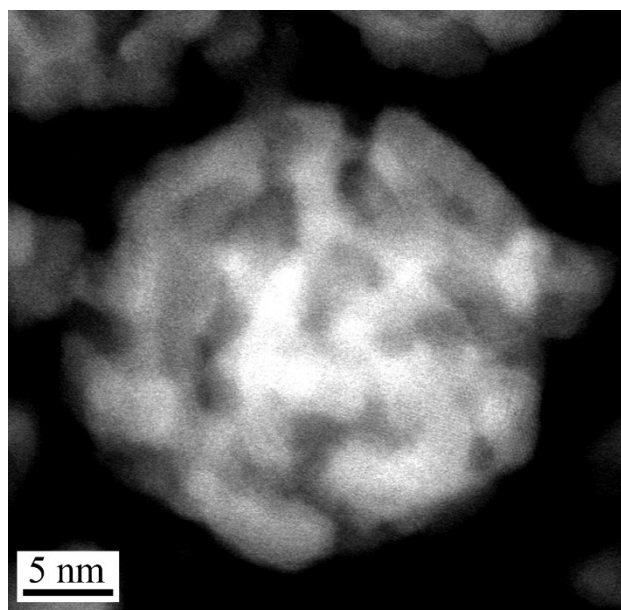


Fig. 128: HAADF image of a porous Ir/IrO₂ nanostructure after applying 400 °C. The morphology and hence the porous structure is maintained.

The different thermally treated particles were further investigated by linear sweep voltammetry. The catalytic potential of the systems was tested against commercially available iridium and iridium oxide powder. The electrochemical characterization of porous Ir/IrO₂ nano-catalysts was performed in a rotation disc electrode (RDE) half-cell containing 0.1 M sulfuric acid equipped with a polished polycrystalline gold working electrode, a platinum counter electrode, and a reversible hydrogen electrode (RHE) connected to the electrochemical cell. The working electrode rotation was controlled with a modulated speed rotator (Pine Instruments). All electrochemical measurements were taken with a bio-logic potentiostat. Overall four different systems based on the same synthesis were evaluated. The experiments were carried out and evaluated by Dr. Meital Shviro from the institute of Elektrochemische Verfahrenstechnik (IEK-3) under the supervision of Prof. Dr. Detlef Stolten in the Forschungszentrum Jülich.

Table 39: Overview of the used samples for electrochemical analysis. The used atmosphere and temperature are shown.

Sample	Preparation
Ir/IrO ₂	As synthesized
Ir/IrO ₂ after 400 °C (O ₂)	Heated in an oven (normal atmosphere)
Ir/IrO ₂ after 1000 °C (O ₂)	Heated in an oven (normal atmosphere)
Ir/IrO ₂ after 1000 °C (Ar)	Heated in TGA (argon atmosphere)

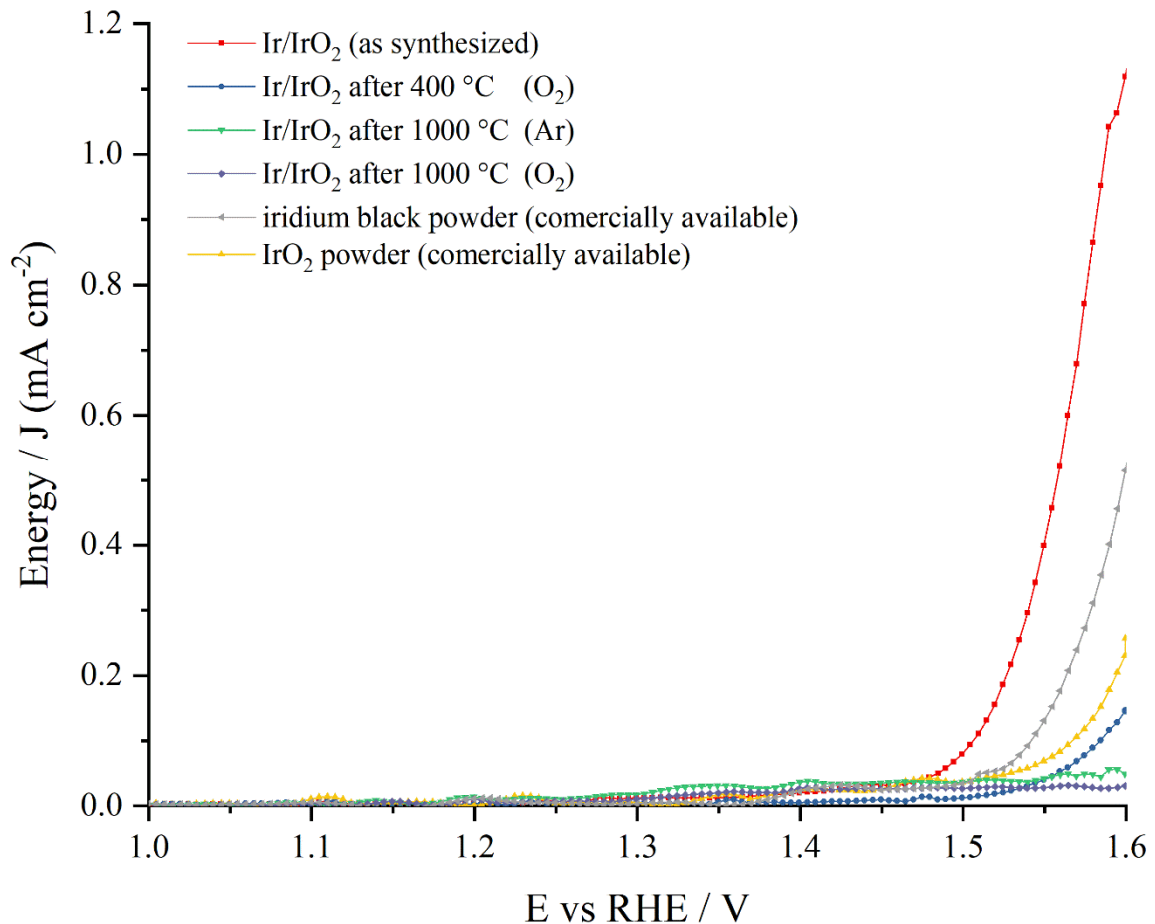


Fig. 129: Electrochemical measurements of differently treated porous Ir/IrO₂ structures compared to commercially available iridium and iridium dioxide powder. The Energy (J) is shown as a function of the potential (E) versus the reference reversible hydrogen electrode (V).

The voltammograms reveal that the synthesized porous nanostructures without any treatment show the highest efficiency compared to all other systems. The treatment of the particles at different temperatures leads to a drastic increase of applied potential. However, the sample without any treatment performs even better than the commercially available powders of iridium and iridium dioxide. The decreased performance for the heat-treated samples might be explained by a closer look on the preparation. The lyophilized particles were transferred to porcelain crucibles. The investigation by *in-situ* heating HRTEM had already shown that particles within a certain distance will fuse together. Since the particles in the crucibles are stacked upon each other, a thermal treatment will consequently have a huge effect on the particle size. Furthermore, the particle surface compared to the volume will shrink drastically. To confirm this approximation a fraction of the particles treated under argon atmosphere which were heated up to a temperature of 1000 °C were investigated by XRPD. LaB₆ as a high

crystalline standard was added to the sample to get a higher accuracy for the calculated crystallite size.

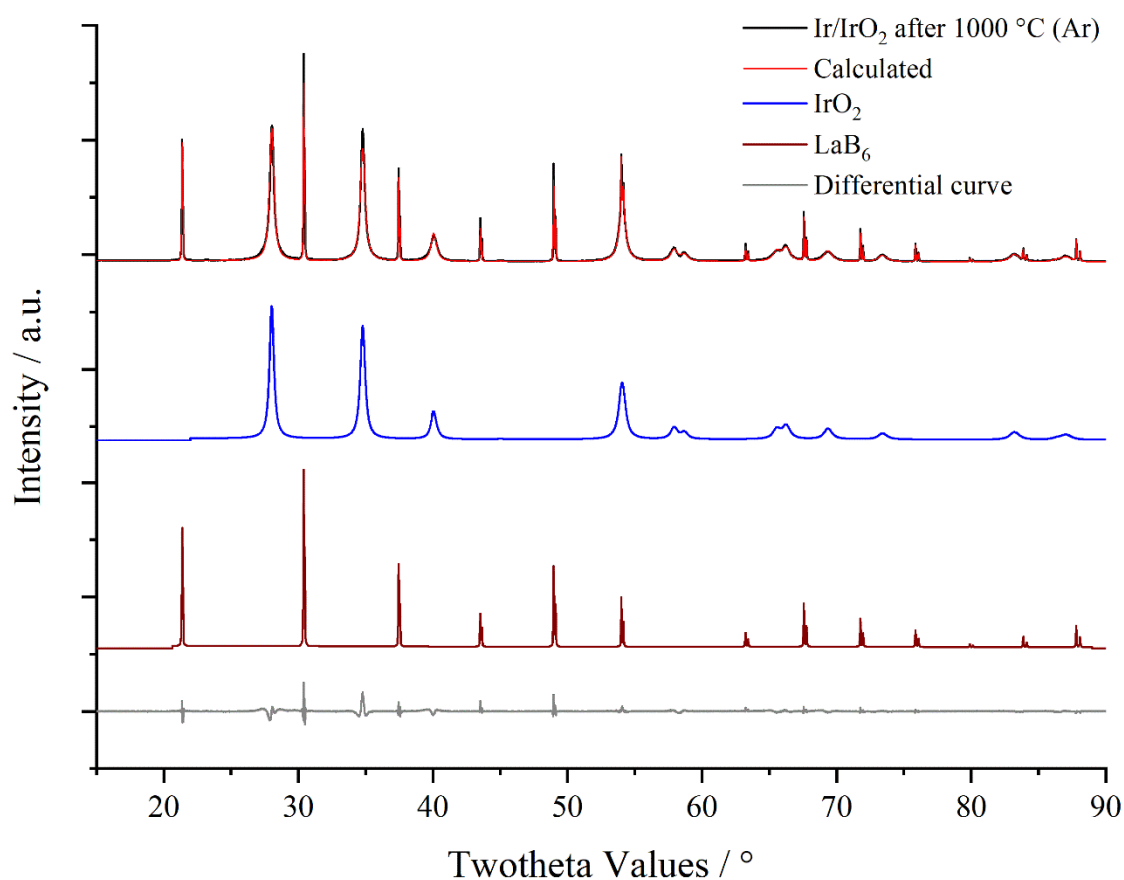


Fig. 130: Rietveld refinement of porous Ir/IrO₂ nanostructures after annealing to 1000 °C in an argon atmosphere. The sample was mixed with LaB₆ for better results regarding the crystallite size. The diffractogram was taken at room temperature. The Intensity (a.u.) is shown as a function of the twotheta values (°) (Not $k_{\alpha 2}$ stripped).

The calculated crystallite size by the refinement is 45.1 nm and consequently indicates a sintering process. Furthermore, the HRTEM images have shown that the porous structures is completely lost after applying more than 500 °C. Both results lead to a decrease in surface area compared to the volume. Since catalytic effects directly correspond to the active surface an increase in required potential in the linear sweep voltammograms is observed. The sintering effect at 400 °C is not that strong, and therefore this sample performs better than the samples treated at 1000 °C in different atmospheres. Phase pure iridium cannot be identified in the sample. This is explained by the still small crystallites. A recrystallization of iridium only occurs at much higher temperatures since the melting point of iridium is at 2466 °C. Consequently, the small crystallites fade into the background when the crystallinity of iridium dioxide is increased.

A second explanation for the decreased performance of the particles might be a layer of carbon which is forming on the surface after the heat treatment. The TGA has shown that not all mass of PVP is lost after the heat treatment. The carbon rest mass could also be quantified by the former shown XPS measurement of the annealed particles (compare Fig. 123).

Table 40: Comparison of the composition by atom percentage of porous Ir/IrO₂ nanostructures before and after the thermal treatment at 1000 °C.

Element	Symbol	Mass / at% (as synthesized)	Mass / at% (annealed)
Nitrogen	N	4.2	0.7
Carbon	C	27.8	6.9
Oxygen	O	39.3	57.0
Boron	B	3.2	6.0
Sodium	Na	7.4	8.4
Silicon	Si	6.8	16.5
Iridium (+4)	Ir	3.2	1.0
Iridium (0)	Ir	1.8	0.9

The carbon mass after the heat treatment is strongly decreased. However, the measurement shows that still 6.9 at % of carbon are present in the sample. A layer of carbon produced after the decomposition of the former bound PVP is hence likely. The occurrence of boron, sodium and silicon was already explained in chapter 5.7.1. The high amount of silicon can be explained by glass corrosion caused by the experimental conditions. The increase of these species is caused by the decrease of iridium dioxide by oxidation to volatile iridium trioxide as well as the decomposition of PVP. This leads to an enrichment of boron, sodium and silicon which represent as oxides in the sample. These compounds do not decompose at 1000 °C and therefore remain in the measured sample.

5.8.3 Reproducibility and size control of porous Ir/IrO₂ nanostructures

To confirm the reproducibility of the synthesis, the reaction was repeated several times using the same reaction conditions. This was done to verify that the formation of porous particles was not due to an incident but rather induced by certain reaction pathways. An efficient way to confirm the renewed formation of the system is to investigate the colloids with UV/Vis spectroscopy and therefore their optical properties. Figure 131 illustrates the UV/Vis spectra of the original synthesis and two reproductions (repro1 and repro2) using the exact same parameters.

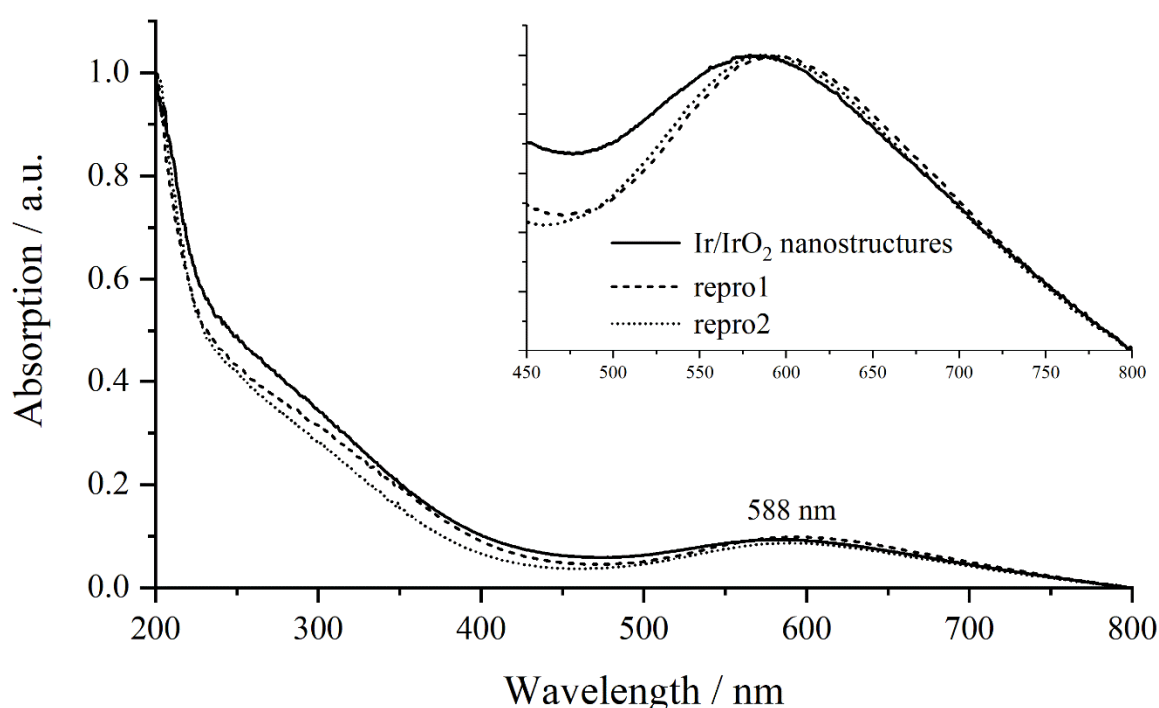


Fig. 131: UV/Vis spectra of the first synthesis and of the two colloids obtained under the same reaction conditions. The graph shows the absorption (a.u.) as a function of the wavelength (nm).

The UV/Vis spectra of the reproduction experiments generate identical absorption spectra as the original sample. Nevertheless, the absorption maximum of resonance is slightly red shifted to 591 nm indicating a small size difference of the particles. To confirm the formation of the spherical porous particles, HRTEM images were repeatedly taken revealing the same particle morphology. The HRTEM images of the repro 1 are shown in Figure 132.

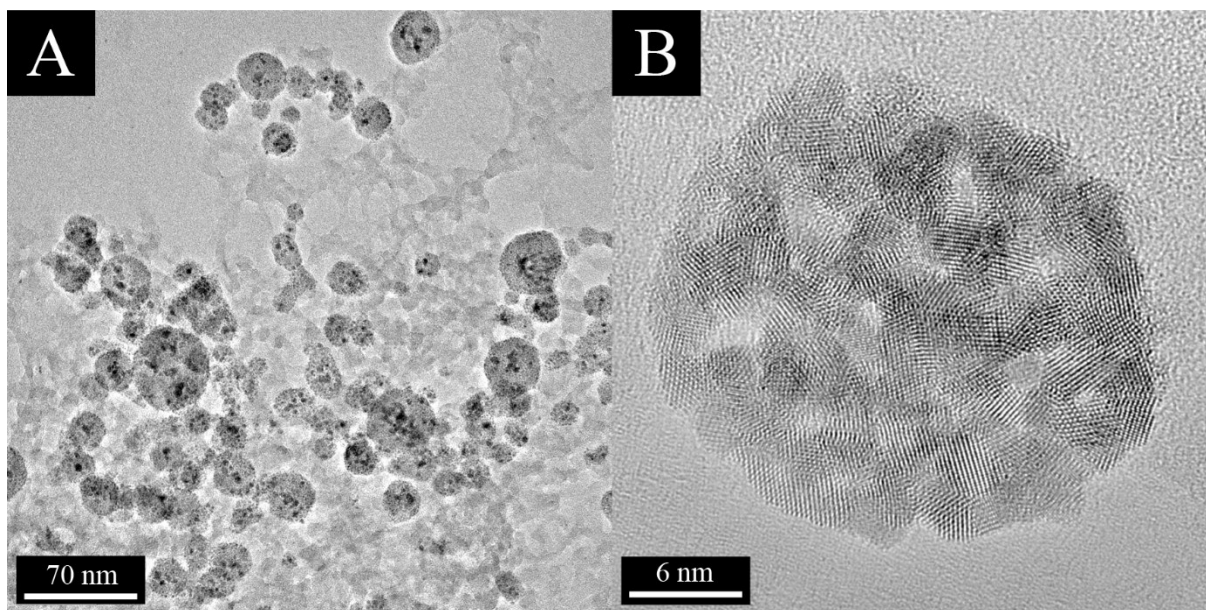


Fig. 132: Overview of the repro 1 (A) and a single particle of the same sample (B). Both images show the same particle morphology and porous structures as the original synthesis.

From the displayed image (Fig. 132, A) 56 particles were counted and measured to determine the size distribution of the sample. In comparison to the original synthesis, the particles show a smaller and more unimodal size distribution with a maximum particle size of 19.2 nm and a size distribution of ± 6.5 nm. The data was derived using Gaussian functions to fit the corresponding histogram. Repro 2 also shows a more unimodal size distribution with a maximum particle size of 24.9 nm and a standard deviation of ± 10.0 nm. Additionally, DCS measurements were performed to confirm the colloidal stability of the particles. The performed experiments show a complete reproducibility of the synthesis using the same parameters. The results of all performed characterization methods are listed in Table 41.

Table 41: Comparison of the mean size, standard deviation and the absorption maxima of the particles obtained from the reproduction experiments and the original sample (Ir/IrO₂ nanostructure (NS)).

Sample	DCS Size / nm	TEM size / nm	UV/Vis absorption maxima / nm
Repro1	10.7 ± 3.8	19.2 ± 6.5	591
Repro2	12.5 ± 6.1	24.9 ± 10.0	591
Ir/IrO ₂ NS	11.7 ± 13.5	14.9 ± 2.3	588
	19.9 ± 7.2	26.8 ± 8.4	

The obtained data from DCS is in good agreement with the HRTEM data. It can therefore be concluded that the synthesis and the corresponding colloidal stability of porous structures is completely reproducible.

5.8 Synthesis of porous nanospheres of Ir/IrO₂ with sodium borohydride

Additional investigations regarding the size control of the particles were carried out. Therefore, all used reactant amounts were taken by the factor of five whereas the amount of the used solvent stayed the same. The higher amount and concentration of metal should lead to bigger particles. An up-scaled synthesis was investigated by HRTEM. The obtained images are shown in Figure 133.

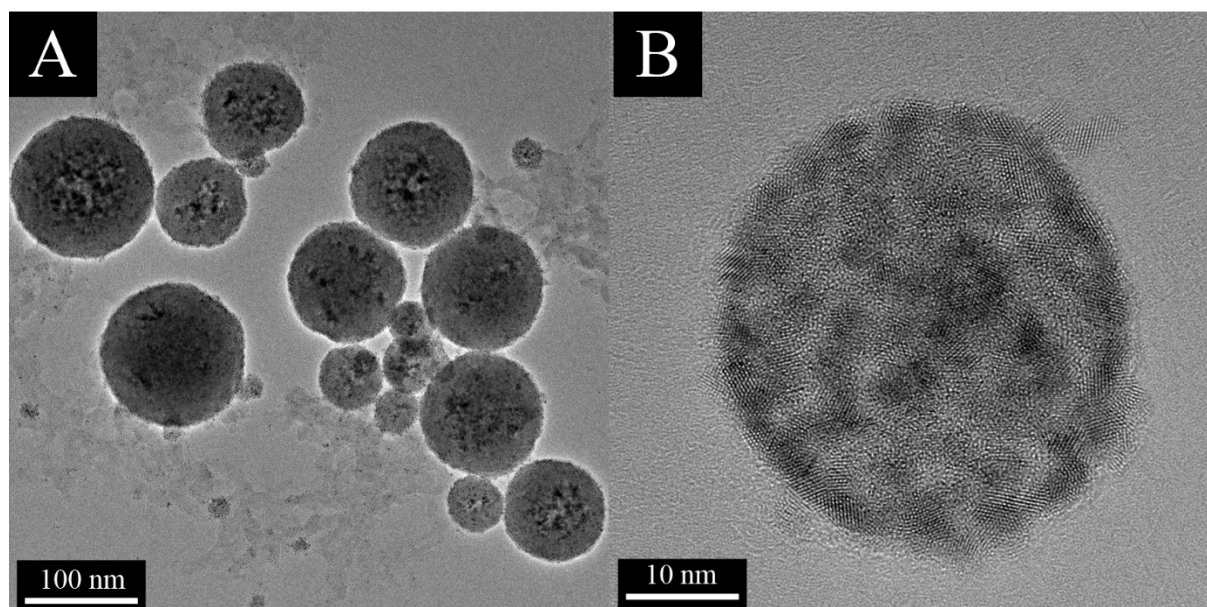


Fig. 133: HRTEM images of the up-scaled synthesis. Overview of several particles (A) and a single particle with a size of 30 nm (B).

The particles obtained from the up-scaled synthesis as expected are bigger. The overall morphology and porosity does not change, but the particles are building nearly geometrically perfect spheres and elongated structures cannot be observed any more. To complement the data of the upscaled particles, DCS and UV/Vis measurements were also performed. The obtained data is summarized in Table 42.

Table 42: Obtained sizes from TEM and DCS and the observed absorption maximum in UV/Vis.

Sample	DCS size / nm	TEM size / nm	UV/Vis absorption maxima / nm
Up-scaled	53.8 ± 10.1	66.0 ± 27.2	594

The study shows that it is possible to control the size of the particles using higher concentrations of reactants. A size control of the porous structures is therefore possible.

In summary, porous nanostructures containing iridium and iridium dioxide were obtained from a modified wet chemical synthesis with sodium borohydride. The porous structures are constructed of small crystallites around 0.7-1.2 nm. Three different methods confirm that not only elemental iridium but also iridium dioxide is present in these particles. XPS measurements could identify that the system's ratio of iridium (0): iridium (+4) is 44:56 at%. Thermogravimetric analysis could show that the particles are stabilized by 6.7-7.9 wt% of PVP. Further investigation by *in-situ* heating TEM could reveal that the porous structure of the system is maintained up to a temperature of 500 °C. After this point, the crystallites start to reorganize building up a system with a higher degree of crystallinity. This observation was not only confirmed in vacuum but could also be seen in different other atmospheres like oxygen, nitrogen and even a reducing atmosphere of argon containing 4% hydrogen. The resulting TEM images at 1000 °C in these atmospheres result in differently faceted particles which indicates an atmospheric influence on the crystallization process.

To examine the catalytical properties of the newly formed system, different batches of the particles were investigated by linear sweep voltammetry. The batches contained particles as synthesized as well as particles treated at 400 °C and 1000 °C in different atmospheres. These systems were further compared to commercially available iridium and iridium dioxide powder. All heat-treated samples performed worse than the commercially available powder, however the sample without any treatment performed noticeably better. Consequently, these particles might be further investigated for the use in catalytical applications.

The particles can be easily reproduced and the size of the spherical porous structures can be tuned by the amount of used reactants using a fixed reaction volume. The particles are consequently an interesting topic for additional investigations

6. Conclusion

The results in this work show that silver nanoparticles in different shapes and sizes can be synthesized through variation of the used reducing agent and reaction conditions. The established method for the synthesis of silver nanoparticles by glucose mostly yields penta-twinned crystalline structures which develop a decahedral assembly. This geometric order leads to disc like structures. This observation could be affirmed by the performed DLS measurements where particles from the glucose synthesis reveal a bimodal size distribution caused by the anisotropic form. This was further confirmed by the DCS measurement where a second fraction could not be detected. The synthesized particles are monodisperse, colloidal stable, and show an absorption in the visible range with a maximum at 440 nm. All these data are comparable to the literature and the particles were consequently suitable for the synthesis of core-shell nanoparticles and dissolution experiments.

The newly developed synthesis for 9 nm spherical silver particles by sodium borohydride yields highly monodisperse and colloidal stable particle dispersions. The brisk crystallization of silver leads to high amounts of stacking faults. Investigations by XRPD as well as HRTEM could show that these stacking faults are a hexagonal phase of the silver lattice. The quantification by Rietveld refinement yielded a phase composition of 67:33 at% for the fcc- and hcp-phase. Further investigation by DSC showed that these stacking faults can be recrystallized by a thermal treatment. A strong endothermic peak is observed at a temperature of 257.4 °C. The recrystallization can only be observed in an oxygen containing atmosphere. Comparable experiments in vacuum showed that the processes are significantly decreased in the absence of oxygen. This could impressively be visualized by *in-situ* heating HRTEM imaging where the recrystallization was visible in altering frames at different temperatures. Studies depending on the reproducibility as well as the stability of the particles showed that the synthesis fulfills both requirements. The particles are at least stable for one month if the dispersion has a concentration of 50 µg/mL. Consequently, the obtained particles were suitable for further biological as well as dissolution kinetic experiments.

The oxidative etching of twinned seeds in a polyol process led to silver nanocubes with a size of ~200 nm and with a good colloidal stability and similar values for plasmonic resonance absorption when compared to the literature. A small number of anisotropic particles like tetrahedra, cuboids and spheres could also be observed. The presence however makes the DLS size distribution by number not usable. The polyol process with silver chloride seeds yielded

silver nanowires with a length of 10-20 μm and a cross-section around 90-110 nm. The stacking faults and twinned defects caused by the penta-twinned seeds are constructed of an ambient stable silver bct-phase. This observation, firstly reported by Sun et al. could be confirmed by crystallographic measurements and corresponding Rietveld refinement in this work. Due to the high anisotropic structure the bct-phase is strongly pronounced along the (110)-axis of the silver nanowires. The particles are monodisperse, colloidal stable and show absorption maxima at 348 nm and 377 nm which are caused by the longitudinal and transversal surfaces and the induced *out-of-plane* dipole and quadrupole moments. Based on the received data, the synthesized morphologies were further used for the synthesis of core-shell particles as well as dissolution experiments.

The successful synthesis of core-shell systems is dependent on several reaction parameters. Synthesis with ascorbic acid of silver nanoparticles showed that a galvanic replacement reaction occurs when a nobler metal is applied as shell material. As a result, the particles completely recrystallize and form hollow structures of an alloyed-core and a shell of one of the used materials. The nature of the outer shell is hereby determined by the standard potential as well as the oxidation state. Hollow spheres of silver-gold develop a gold shell around the silver enriched alloyed-core due to the formation of silver chloride and the +3-oxidation state of the nobler gold. In contrast, a second mechanism is observed if the standard potential and the oxidation states of both mated metals are more similar. In this reaction both metals form a homogenous alloyed-core with a silver enriched shell. Those observations could be confirmed by Rietveld refinement as well as HAADF images and corresponding EDX maps. Due to the recrystallization process, the particles are highly monodisperse. Furthermore, they are colloidal stable. Investigations in literature and comparison with own results showed that the absorptions of the particles are not comparable to neither alloyed nor core-shell particles. This observation is most likely caused by the inhomogeneous rough surface of the particles.

The results regarding core-shell particles in this work show that a synthesis could be developed which is universal by usable for all tested morphologies. The same parameters can be applied to different particle sizes, forms as well as shell materials. The core-shell particles are monodisperse and colloidal stable. The application of a second material leads in all cases to a directional growth of the shell. This result is explained by the functionalization with PVP which inhibits the growth of the (100)-facet. The directional growth of the shell material can directly be seen in the UV/Vis spectra of anisotropic samples, where the accretion directly leads to the attenuation or complete vanishing of certain absorption maxima. The success of the shell

application is strongly dependent on the addition rate of the precursor, the control of the pH value and the concentration of the seeds.

All synthesized monometallic particles and core-shell systems based on silver were investigated by dissolution kinetic experiments. The adapted setup from Dr. Viktoria Grasmik was tested and examined. This investigation showed that the diffusion of the silver ions does not influence the data of the dissolution for nanoparticles, since the rate constant of the diffusion is much higher than the rate constant of the nanoparticle dissolution. Of the 17 tested nanoparticle systems only five showed silver dissolution in a detectable range. Neither morphologies like wires or cubes nor their core-shell systems showed any dissolution. Only spherical silver particles of the synthesis with sodium borohydride (~ 4.3 %) and the glucose synthesis (~ 2.9 %) showed dissolution over the monitored 70 days. The only core-shell particles which released silver ions were small silver nanoparticles with a size around 9 nm. In the end, the dissolution of small silver nanoparticles is significantly higher than the dissolution of the core-shell systems based on the same particles. The adopted sacrificial anode effect could not be confirmed for nanoparticulate systems. Furthermore, core-shell particles with gold or palladium as shell material showed no dissolution in the detectable range. However, the systems containing iridium showed a time-shifted dissolution compared to pure silver nanoparticles. This dissolution was significantly lower but showed that the trend, where bimetallic systems of silver-iridium are more toxic than silver-gold or silver-palladium systems, found by Köller et al. is in accordance with the determined ion release rates in this work.

The performed *in-situ* powder diffraction experiments which were combined with colloidal characterization methods could show that the growth of nanoparticles is strongly dependent on the concentrations as well as the temperature of the carried-out polyol process. A tripling of the precursor concentrations led to a higher increase in scattering intensity which was not only attributed to the nanoparticle growth. This confirms the two-step model proposed by Finke et al. where the reaction of the nanoparticle formation has two different rate constants. One for the seed formation and one for the autocatalytic surface growth. Because of the tripled precursor concentration, the rate constant of the seed formation increase. That could be concluded from the peak area growth which is not completely attributable to the crystallite growth. Furthermore, the investigations of the particle size show a bimodal size distribution which can only be explained by separate growing particle fractions and consequently differently arising seeds over the reaction time. A rise in temperature from 160 °C to 200 °C increases again the rate constant k_2 of the autocatalytic surface growth due to the increase of reduction potential of

the used reducing agent DEG. This leads to a particle dispersion with a narrower size distribution.

Monometallic iridium nanoparticles could be synthesized in aqueous solution as well as ethylene glycol using a microwave reactor. The particles show branched structures which can be ascribed to the relatively low energy barrier for a homogenous nucleation compared with that for a heterogeneous nucleation. Consequently, iridium favours to form new crystallites instead of growing on already existing ones ($k_1 \gg k_2$). The obtained particles are in a size range between 4-10 nm and are colloidal stable. In the scope of this work, porous spherical structures based on iridium and iridium dioxide were synthesized. The composition was determined by Rietveld refinement as well as XPS. The particles contain iridium (0) and iridium (+4) (iridium dioxide) in a ratio of 44:56 at%. Thermal investigations (*in-situ* heating TEM imaging) regarding the stability of the product showed that the porous structure is obtained up to a temperature of 400 °C. Investigation showed that the recrystallization which occurs above this temperature is strongly influenced by the atmosphere of the experiment (O₂, Ar, Ar + H₂). The recrystallization in a reducing atmosphere for example resulted in multifaceted crystals. First studies using linear sweep voltammetry showed high potential of the untreated porous nanostructures, which performed even better than commercially available products. The particles are reproducible, and the size can be easily modified by the amount of precursor used.

7. Zusammenfassung

Die Ergebnisse dieser Arbeit zeigen, dass verschiedene Größen sowie Morphologien von Silbernanopartikeln durch die Variation verschiedener Reaktionsparameter realisiert werden können. Hierbei erzeugt die Reduktion von Silbersalzen mit Glucose hauptsächlich fünffach verzwilligte pentagonale Kristalle, welche Dodekaeder ausbilden. Die anisotrope Struktur der Partikel konnte hierbei durch DLS gezeigt werden, wobei eine bimodale Größenverteilung entsteht. Die synthetisierten Partikel sind monodispers, kolloidal stabil und zeigen Oberflächenplasmonenresonanz mit einem Absorptionsmaximum bei 440 nm. Durch die erhaltenen Ergebnisse und deren Übereinstimmung mit Literaturdaten waren die erzeugten Partikel zur Synthese von Kern-Schale Systemen sowie zur Bestimmung der Silberionenfreisetzung (Auflösungskinetik) geeignet.

Die neu etablierte Synthese zur Generierung von 9 nm großen Silbernanopartikeln, die im Rahmen dieser Arbeit entwickelt wurde, liefert kolloidal stabile und gut reproduzierbare Partikel. Die schnelle Kristallisation führt zur Ausbildung einer stabilen hexagonalen Silberphase (hcp) was sowohl anhand von Röntgenpulverdiffraktometrie, als auch hochauflösenden Transmissionselektronenmikroskop-Aufnahmen gezeigt werden konnte. Die Phasenquantifizierung zeigte, dass ca. 33 % der vorhandenen Silbernanopartikel eine hcp-Struktur aufweisen. Untersuchungen erwiesen, dass die hcp-Phase eine Phasenumwandlung bei thermischer Energiezufuhr durchläuft. Dieser Vorgang ist jedoch signifikant vermindert sobald Sauerstoff bei der Reaktion abwesend ist. Dies konnte durch *in-situ* HRTEM Heizexperimente gezeigt werden. Weitere Experimente bestätigten die Langzeitstabilität sowie die Reproduzierbarkeit der Synthese.

Im weiteren Verlauf wurden Silber-Nanowürfel durch den Prozess des oxidativen Ätzens realisiert. Hierbei wurden verzwilligte Keime durch Salzsäure entfernt. Die verbliebenen einkristallinen Keime durchliefen im Anschluss durch penibel durchgeführte Reaktionsbedingungen sowie die Zugabe von PVP ein gerichtetes Wachstum. Im Verlauf der Reaktion kommt es ebenfalls zur Ausbildung von weiteren anisotropen Strukturen wie Tetraedern, Quadern und Sphären, welche die Größenverteilung in Abhängigkeit der Anzahl bei der DLS Messung unbrauchbar machen. Des Weiteren konnten durch die Nutzung von Natriumchloridkeimen Silber-Nanodrähte erzeugt werden, welche Längen zwischen 10-20 μm und Breiten zwischen 90-110 nm aufwiesen. Durch die fünffach verzwilligte Struktur der

Keime kommt es bei der Ausbildung von Nanodrähten besonders stark zur Ausbildung von Stapelfehlern und Zwillingsdefekten. Diese bilden auch unter Normalbedingungen eine stabile tetragonale Phase (bct) aus, welche bereits durch Sun et al. nachgewiesen wurde. Vergleichbare Beobachtungen konnten anhand einer Rietveldverfeinerung in dieser Arbeit bestätigt werden. Durch eine starke Vorzugsorientierung entlang der (110)-Achse ist die Silber bct-Phase sehr stark ausgeprägt. Die erhaltenen Partikel sind kolloidal stabil und zeigen Absorption im sichtbaren Wellenlängenbereich mit Absorptionsmaxima bei 348 nm und 377 nm. Diese Banden werden durch *out-of-plane* Dipol- und Quadrupolmomente hervorgerufen. Die gute Vergleichbarkeit mit den Literaturwerten sowie die Monodispersität der Systeme führte zur weiteren Nutzung und Umsetzung zu Kern-Schale Nanopartikeln.

Die erfolgreiche Synthese von Kern-Schale Systemen beruht auf einer Vielzahl von Reaktionsparametern. Synthesen mit Ascorbinsäure in Kombination mit Silberpartikeln als Keime zeigten galvanische Austauschreaktionen sobald ein edleres Metall als Schale aufgebracht werden sollte. Hieraus resultierten nach Rekristallisation hohle legierte Sphären, welche als äußere Schicht eines der beiden verwendeten Materialien aufwiesen. Das endgültige Schalenmaterial ist hierbei sowohl abhängig vom Standardpotential als auch der Oxidationsstufe des verwendeten Elements. Bei der Reaktion von Silbernanopartikeln mit einem Gold-Precursor entstehen stark silberhaltige, legierte Kerne mit einer äußeren Goldschicht. Begründet wird dies durch eine Nebenreaktion von Silber-Ionen mit Chloridionen des Gold-Precursors zu Silberchlorid sowie der Oxidationsstufe (+3) des Goldes. Verwendet man anstatt Gold Palladium, so bilden sich homogene legierte Kerne mit gering erhöhtem Silberanteil in der Schale aus. Diese Schlüsse konnten mit Hilfe von Rietveldverfeinerung sowie HAADF Aufnahmen und dazugehörigen EDX maps getätigt werden. Durch den in der Reaktion auftretenden Rekristallisationsprozess sind die erhaltenen Nanopartikel monodispers. Darüber hinaus zeigt ein Vergleich mit der Literatur, dass die optischen Eigenschaften der Systeme weder mit monometallischen, noch mit bimetallic Systemen gleicher Größe übereinstimmen. Dies ist mit hoher Wahrscheinlichkeit auf die anisotrope Oberflächenbeschaffenheit der Partikel zurückzuführen.

Die Ergebnisse der Kern-Schale Systeme in dieser Arbeit zeigen, dass eine Syntheseroute entwickelt werden konnte, welche gleichermaßen für alle hergestellten Morphologien genutzt werden kann. Alle erhaltenen Kern-Schale Systeme sind nach der Synthese kolloidal stabil und monodispers. Unabhängig von der Morphologie führt die Zugabe eines zweiten Metalls zu einem directionalen Wachstum, welches über die Komplexierung der kristallografischen (100)-Fläche durch das verwendete Polymer PVP erklärt werden kann. Dieses gerichtete Wachstum

kann mit Hilfe der UV/Vis-Spektroskopie und dem dortigen Verschwinden bestimmter Absorptionsbanden Nachgewiesen werden.

Im weiteren Verlauf wurden alle hergestellten monometallischen sowie bimetallicen Nanopartikel auf ihr Auflösungsverhalten hin untersucht. Hierbei orientierten sich der Aufbau sowie die Auswertung der Ergebnisse an vorangegangene Arbeiten von Dr. Viktoria Grasmik. Ergänzende Experimente zeigten, dass die Auflösung der Nanopartikel wesentlich langsamer als die Diffusion der Silber-Ionen stattfindet. Bedingt hierdurch konnten auswertbare Ergebnisse geliefert werden. Von den 17 getesteten Systemen zeigten nur fünf eine Auflösung von Silber über den getesteten Zeitraum von 70 Tagen. Vor allem monometallische Silbernanopartikel mit einer großen Oberflächen (9 nm) sowie Silbernanopartikel aus der Glucose Synthese (35 nm) zeigten Auflösung in dem überwachten Zeitintervall. Des Weiteren zeigten nur Kern-Schale Systeme mit einer Iridium Schale Auflösung von Silber. Die Daten zeigen eine signifikant höhere Auflösung von monometallischen Silberpartikeln im Vergleich zu bimetallicen Systemen gleicher Größen. Daraus ergibt sich, dass der angestrebte Opfer-Anoden Effekt in nanopartikulären Systemen nicht eintritt. Der Trend nach Köller et al., in dem Iridium haltige bimetalliche Systeme mehr Silber freisetzen als vergleichbare gold- oder palladiumhaltige Systeme konnte dagegen bestätigt werden.

Die am Synchrotron durchgeführten *in-situ* Röntgenpulverdiffraktometrie Messungen konnten darlegen, dass das Wachstum und die Dispersität eines nanopartikulären Systems hergestellt in einem Polyol-Prozess (Diethylenglycol) sowohl stark abhängig von der Konzentration als auch der Reaktionstemperatur sind. Eine Verdreifachung der Precursormenge bei gleichbleibender Temperatur (160 °C) führt zu einem Anstieg der Streuintensität, welche nicht mit dem Zuwachs der Kristallitgröße korreliert. Diese Beobachtung kann durch das von Finke et al. aufgestellte two-step Wachstumsmodell für Nanopartikel erklärt werden, in dem die Keimbildung und das autokatalytische Oberflächenwachstum zwei unterschiedliche Reaktionsgeschwindigkeitskonstanten besitzen. Durch das Erhöhen der Konzentration steigt die Geschwindigkeitskonstante k_1 der Keimneubildung, was eine polydisperse Größenverteilung des Systems zur Folge hat. Dies konnte auch Anhand von kolloidchemischen Methoden wie DLS, DCS sowie mikroskopischen Methoden wie REM und HRTEM gezeigt werden. Die Erhöhung der Reaktionstemperatur (200 °C) hat einen Anstieg des Reduktionspotenzials von DEG zufolge, welches in einem Zuwachs der Geschwindigkeitskonstante des autokatalytischen Wachstums resultiert. Infolge dessen ist das Wachstum schneller als die erneute Keimbildung was ein monodisperses System zur Folge hat.

Monometallische Iridium Nanopartikel konnten im Rahmen dieser Arbeit sowohl durch wässrige Synthese als auch durch Synthese in Ethylenglycol unter Nutzung eines Mikrowellen Reaktors dargestellt werden. Beide Systeme weisen undefinierte verzweigte kristallografische Strukturen auf. Diese werden durch eine niedrige Energiebarriere, welche zur erneuten Keimbildung führt, hervorgerufen. Diese Keimbildung ist gegenüber dem autokatalytischen Wachstum energetisch bevorzugt ($k_1 \gg k_2$). Die resultierenden Partikel besitzen Größen zwischen 4-10 nm und sind kolloidal stabil in Wasser. Darüber hinaus wurden poröse Nanostrukturen aus einer Mischung von Iridium und Iridiumoxid aus wässriger Synthese erhalten. Die Zusammensetzung sowie die Phasenidentifikation wurden mit Hilfe des PXRD, der FFT von hochauflösenden TEM Aufnahmen sowie XPS Messungen durchgeführt. Die Partikel bestehen aus Iridium (0) und Iridium (+4) (Iridiumoxid) in einem Verhältnis von 44:56 at%. Thermische Elektronenmikroskopie (*in-situ* Heiz TEM) konnte zeigen, dass die porösen Strukturen bis zu einer Temperatur von 400 °C in verschiedenen Atmosphären (O₂, Ar, Ar + H₂) keine Rekristallisationsprozesse durchlaufen. Die Rekristallisation, die nach dieser Temperatur auftritt, führt vor allem in einer reduzierenden Atmosphäre (Ar + H₂) zu hochgradig facettierten Kristallen. Erste Studien mit Linear Sweep Voltammetry konnten darlegen, dass das benötigte Potential zur Wasserspaltung mit den Nanopartikeln deutlich gesenkt werden kann. Dabei erzielten die genutzten Nanopartikel sogar bessere Ergebnisse als kommerziell erwerbliche Produkte (Iridium- und Iridiumoxid-Pulver). Die Synthese der Partikel ist reproduzierbar und die Größe kann mit der eingesetzten Precursorkonzentration moduliert werden.

8. References

- [1] B. R. Chalamala, Y. Wei, R. H. Reuss, S. Aggarwal, S. R. Perusse, B. E. Gnade, R. Ramesh, *J. Vac. Sci. Technol., B* **2000**, *18*, 1919-1922.
- [2] P. Buffat, J. P. Borel, *Phys. Rev., A* **1976**, *13*, 2287-2298.
- [3] W. H. Qi, M. P. Wang, *Mater. Chem. Phys.* **2004**, *88*, 280-284.
- [4] A. F. Holleman, N. Wiberg, E. Wiberg, *Lehrbuch der Anorganischen Chemie*, **2007**.
- [5] E. Riedel, C. Janiak, *Anorganische Chemie*, **2011**.
- [6] V. K.-Y. Lo, A. O.-Y. Chan, C.-M. Che, *Org. Biomol. Chem.* **2015**, *13*, 6667-6680.
- [7] C. Wen, A. Yin, W.-L. Dai, *Appl. Catal., B* **2014**, *160-161*, 730-741.
- [8] Y. Jiang, S. Pillai, M. A. Green, *Sci. Rep.* **2016**, *6*, 30605.
- [9] D. Pile, *Nat. Photonics* **2016**, *10*, 565.
- [10] G. Mattei, L. G. Quagliano, M. Pagannone, *EPL (Europhysics Letters)* **1990**, *11*, 373.
- [11] J. A. Creighton, D. G. Eadon, *J. Chem. Soc., Faraday Trans.* **1991**, *87*, 3881-3891.
- [12] R. M. Gnanamuthu, N. Wilson, R. Bhagat, *Mater. Chem. Phys.* **2018**, *205*, 147-153.
- [13] T. Rai, A. Sharma, D. Panda, *New J. Chem.* **2017**, *41*, 2029-2036.
- [14] J. W. Alexander, *Surg. Infect.* **2009**, *10*, 289-292.
- [15] S. Chernousova, M. Epple, *Angew. Chem., Int. Ed.* **2013**, *52*, 1636-1653.
- [16] J. R. Fitzgerald, D. E. Sturdevant, S. M. Mackie, S. R. Gill, J. M. Musser, *Proc. Natl. Acad. Sci. U.S.A.* **2001**, *98*, 8821-8826.
- [17] M. C. Enright, D. A. Robinson, G. Randle, E. J. Feil, H. Grundmann, B. G. Spratt, *Proc. Natl. Acad. Sci. U.S.A.* **2002**, *99*, 7687-7692.
- [18] C. Marambio-Jones, E. M. V. Hoek, *J. Nanopart. Res.* **2010**, *12*, 1531-1551.
- [19] D. Zhan, X. Li, A. B. Nepomnyashchii, M. A. Alpuche-Aviles, F.-R. F. Fan, A. J. Bard, *J. Electroanal. Chem.* **2013**, *688*, 61-68.
- [20] U. Hansen, A. F. Thuenemann, *Toxicol. In Vitro* **2016**, *34*, 120-122.
- [21] S. Kittler, C. Greulich, J. Diendorf, M. Koeller, M. Epple, *Chem. Mater.* **2010**, *22*, 4548-4554.
- [22] K. Loza, J. Diendorf, C. Sengstock, L. Ruiz-Gonzalez, J. M. Gonzalez-Calbet, M. Vallet-Regi, M. Koeller, M. Epple, *J. Mater. Chem. B* **2014**, *2*, 1634-1643.
- [23] J. Helmlinger, C. Sengstock, C. Groß-Heitfeld, C. Mayer, T. A. Schildhauer, M. Köller, M. Epple, *RSC Adv.* **2016**, *6*, 18490-18501.
- [24] V. Grasmik, University of Duisburg-Essen (Bibliothek), **2018**.

- [25] M. Köller, C. Sengstock, Y. Motemani, C. Khare, P. J. S. Buenconsejo, J. Geukes, T. A. Schildhauer, A. Ludwig, *Mater. Sci. Eng., C* **2015**, *46*, 276-280.
- [26] M. Köller, P. Bellova, S. M. Javid, Y. Motemani, C. Khare, C. Sengstock, K. Tschulik, T. A. Schildhauer, A. Ludwig, *Mater. Sci. Eng., C* **2017**, *74*, 536-541.
- [27] S. Ristig, O. Prymak, K. Loza, M. Gocyla, W. Meyer-Zaika, M. Heggen, D. Raabe, M. Epple, *J. Mater. Chem. B* **2015**, *3*, 4654-4662.
- [28] V. Grasmik, C. Rurainsky, K. Loza, V. Evers Mathies, O. Prymak, M. Heggen, K. Tschulik, M. Epple, *Chem. Eur. J.* **2018**, *24*, 9051-9060.
- [29] H. M. Chen, R.-S. Liu, M.-Y. Lo, S.-C. Chang, L.-D. Tsai, Y.-M. Peng, J.-F. Lee, *J. Phys. Chem. C* **2008**, *112*, 7522-7526.
- [30] S. J. Kim, C. S. Ah, D. J. Jang, *Adv. Mater.* **2007**, *19*, 1064-1068.
- [31] Z. Peng, J. Wu, H. Yang, *Chem. Mater.* **2010**, *22*, 1098-1106.
- [32] C. M. Copley, D. J. Campbell, Y. Xia, *Adv. Mater.* **2008**, *20*, 748-752.
- [33] M. Kamundi, L. Bromberg, E. Fey, C. Mitchell, M. Fayette, N. Dimitrov, *J. Phys. Chem. C* **2012**, *116*, 14123-14133.
- [34] Y. Sun, Y. Xia, *J. Am. Chem. Soc.* **2004**, *126*, 3892-3901.
- [35] Y. Yin, C. Erdonmez, S. Aloni, A. P. Alivisatos, *J. Am. Chem. Soc.* **2006**, *128*, 12671-12673.
- [36] D. Cheng, H. Xia, X. Zhou, H. S. O. Chan, *Chem. Mater.* **2005**, *17*, 3578-3581.
- [37] S. H. Im, Y. T. Lee, B. Wiley, Y. Xia, *Angew. Chem. Int. Ed.* **2005**, *44*, 2154-2157.
- [38] S. Kumar-Krishnan, M. Estevez-González, R. Pérez, R. Esparza, M. Meyyappan, *RSC Adv.* **2017**, *7*, 27170-27176.
- [39] Y. Yang, J. Liu, Z. W. Fu, D. Qin, *J. Am. Chem. Soc.* **2014**, *136*, 8153-8156.
- [40] N. Murshid, I. Gourevich, N. Coombs, V. Kitaev, *Chem. Comm.* **2013**, *49*, 11355-11357.
- [41] S. Cheong, J. D. Watt, R. D. Tilley, *Nanoscale* **2010**, *2*, 2045-2053.
- [42] K. Zhou, Y. Li, *Angew. Chem. Int. Ed.* **2011**, *51*, 602-613.
- [43] Q. Zhang, H. Wang, *ACS Catal.* **2014**, *4*, 4027-4033.
- [44] K. L. Kelly, E. Coronado, L. L. Zhao, G. C. Schatz, *J. Phys. Chem. B* **2003**, *107*, 668-677.
- [45] E. Hao, G. C. Schatz, J. T. Hupp, *J. Fluoresc.* **2004**, *14*, 331-341.
- [46] D. J. Tobler, S. Shaw, L. G. Benning, *Geochim. Cosmochim. Acta* **2009**, *73*, 5377-5393.
- [47] J. Polte, T. T. Ahner, F. Delissen, S. Sokolov, F. Emmerling, A. F. Thunemann, R. Kraehnert, *J. Am. Chem. Soc.* **2010**, *132*, 1296-1301.

- [48] C. Tyrsted, N. Lock, K. M. O. Jensen, M. Christensen, E. D. Bojesen, H. Emerich, G. Vaughan, S. J. L. Billinge, B. B. Iversen, *IUCrJ* **2014**, *1*, 165-171.
- [49] Q. Liu, M.-R. Gao, Y. Liu, J. S. Okasinski, Y. Ren, Y. Sun, *Nano Lett.* **2016**, *16*, 715-720.
- [50] D. R. Lyde, *Handbook of Chemistry and Physics, Vol. 82*, 82 ed., CRC Press LLC, **2001**.
- [51] S. D. Tilley, M. Cornuz, K. Sivula, M. Grätzel, *Angew. Chem. Int. Ed.* **2010**, *49*, 6405-6408.
- [52] E. Slavcheva, I. Radev, S. Bliznakov, G. Topalov, P. Andreev, E. Budevski, *Electrochim. Acta* **2007**, *52*, 3889-3894.
- [53] C. H. Chang, T. S. Yuen, Y. Nagao, H. Yugami, *J. Power Sources* **2010**, *195*, 5938-5941.
- [54] E. Antolini, *ACS Catal.* **2014**, *4*, 1426-1440.
- [55] C. Terashima, T. N. Rao, B. V. Sarada, N. Spataru, A. Fujishima, *J. Electroanal. Chem.* **2003**, *544*, 65-74.
- [56] W.-D. Huang, H. Cao, S. Deb, M. Chiao, J. C. Chiao, *Sens. Actuators A. Phys.* **2011**, *169*, 1-11.
- [57] X. Xia, L. Figueroa-Cosme, J. Tao, H. C. Peng, G. Niu, Y. Zhu, Y. Xia, *J. Am. Chem. Soc.* **2014**, *136*, 10878-10881.
- [58] *Concise English Dictionary* 7ed., Harper Collins Publ. UK, United Kingdom, **2008**.
- [59] K. K. Nanda, *Pramana* **2009**, *72*, 617-628.
- [60] V. I. Levitas, K. Samani, *Nat. Commun.* **2011**, *2*, 284.
- [61] S. K. Ghosh, T. Pal, *Chem. Rev.* **2007**, *107*, 4797-4862.
- [62] R. A. Ganeev, G. S. Boltaev, R. I. Tugushev, T. Usmanov, *Appl. Phys. B* **2010**, *100*, 571-576.
- [63] G. Schmid, *Nanoparticles: From Theorie to Application*, 2 ed., Wiley-VCH, **2010**.
- [64] S. Becht, S. Ernst, R. Bappert, C. Feldmann, *Chem. unserer Zeit* **2010**, *44*, 14-23.
- [65] T. Knuschke, O. Rotan, W. Bayer, S. Kollenda, J. Dickow, K. Sutter, W. Hansen, U. Dittmer, K. S. Lang, M. Epple, J. Buer, A. M. Westendorf, *Front. Immunol.* **2018**, *9*, 614.
- [66] S. Weske, M. Vaidya, A. Reese, K. von Wnuck Lipinski, P. Keul, J. K. Bayer, J. W. Fischer, U. Flögel, J. Nelsen, M. Epple, M. Scatena, E. Schwedhelm, M. Dörr, H. Völzke, E. Moritz, A. Hannemann, B. H. Rauch, M. H. Gräler, G. Heusch, B. Levkau, *Nat. Med.* **2018**, *24*, 667-678.
- [67] Z. P. Xu, Q. H. Zeng, G. Q. Lu, A. B. Yu, *Chem. Eng. Sci.* **2006**, *61*, 1027-1040.

- [68] V. Sokolova, M. Epple, *Angew. Chem. Int. Ed.* **2008**, *47*, 1382-1395.
- [69] A. Auvinen, J. Bridges, K. Dawson, W. D. Jong, P. Hartemann, P. Hoet, T. Jung, M.-O. Mattsson, H. Norppa, J.-M. Pagés, A. Proykova, E. Rodríguez-Farré, K. Schulze-Ostoff, J. Schüz, M. Thomsen, T. Vermeire, *European Commission, Scientific Basis for the Definition of the Term "Nanomaterial"* **2010**.
- [70] W. G. Kreyling, M. Semmler-Behnke, Q. Chaudhry, *Nano Today* **2010**, *5*, 165-168.
- [71] S. Horikoshi, N. Serpone, *Microwaves in Nanoparticle Synthesis - Fundamentals and Applications*, Wiley-VCH, **2013**.
- [72] T. Cosgrove, *Colloid Science: Principles, Methods and Applications*, 2 ed., Wiley, School of Chemistry, University of Bristol, Bristol, UK, **2010**.
- [73] H.-D. Dörfler, *Grenzflächen und kolloid-disperse Systeme*, Springer **2002**.
- [74] R. Gupta, Kompella, U., Swarbrick, J., Muller, R., Haskell, R., Sahoo, S., Borm, P., Oyewumi, M., Bhardwaj, V., Gelperina, S., Amrite, A., Rainbow, B., *Nanoparticle Technology for Drug Delivery*, 1 ed., CRC Press, **2006**.
- [75] M. Kim, S. Osone, T. Kim, H. Higashi, T. Seto, *KONA Powder Part. J.* **2017**, *advpub*.
- [76] V. K. La Mer, R. H. Dinegar, *J. Am. Chem. Soc.* **1950**, *72*, 4847-4854.
- [77] D. Erdemir, A. Y. Lee, A. S. Myerson, *Acc. Chem. Res.* **2009**, *42*, 621-629.
- [78] S. Özkar, R. G. Finke, *J. Phys. Chem. C* **2017**, *121*, 27643-27654.
- [79] M. A. Watzky, R. G. Finke, *J. Am. Chem. Soc.* **1997**, *119*, 10382-10400.
- [80] W. O. Ostwald, *An Introduction to Theoretical and Applied Colloid Chemistry*, John Wiley & Sons, Ltd, New York, **1917**.
- [81] N. G. Bastús, J. Comenge, V. Puentes, *Langmuir* **2011**, *27*, 11098-11105.
- [82] Y. Xia, Y. Xiong, B. Lim, E. Skrabalak Sara *Angew. Chem. Int. Ed.* **2008**, *48*, 60-103.
- [83] A. R. Siekkinen, J. M. McLellan, J. Chen, Y. Xia, *Chem. Phys. Lett.* **2006**, *432*, 491-496.
- [84] Q. Zhang, W. Li, C. Moran, J. Zeng, J. Chen, L.-P. Wen, Y. Xia, *J. Am. Chem. Soc.* **2010**, *132*, 11372-11378.
- [85] N. R. Jana, L. Gearheart, C. J. Murphy, *Chem. Comm.* **2001**, 617-618.
- [86] Y. Sun, Y. Xia, *Adv. Mater.* **2002**, *14*, 833-837.
- [87] Y. Sun, Y. Yin, B. T. Mayers, T. Herricks, Y. Xia, *Chem. Mater.* **2002**, *14*, 4736-4745.
- [88] Y. Gao, L. Song, P. Jiang, L. F. Liu, X. Q. Yan, Z. P. Zhou, D. F. Liu, J. X. Wang, H. J. Yuan, Z. X. Zhang, X. W. Zhao, X. Y. Dou, W. Y. Zhou, G. Wang, S. S. Xie, H. Y. Chen, J. Q. Li, *J. Cryst. Growth* **2005**, *276*, 606-612.
- [89] W. M. Schuette, W. E. Buhro, *ACS Nano* **2013**, *7*, 3844-3853.

- [90] M. F. Meléndrez, C. Medina, F. Solis-Pomar, P. Flores, M. Paulraj, E. Pérez-Tijerina, *Nanoscale Res. Lett.* **2015**, *10*, 48.
- [91] J. Helmlinger, University of Duisburg-Essen **2015**.
- [92] S. Chen, D. L. Carroll, *Nano Lett.* **2002**, *2*, 1003-1007.
- [93] D. Aherne, D. M. Ledwith, M. Gara, J. M. Kelly, *Adv. Funct. Mater.* **2008**, *18*, 2005-2016.
- [94] K. Kamata, Y. Lu, Y. Xia, *J. Am. Chem. Soc.* **2003**, *125*, 2384-2385.
- [95] S. I. Sanchez, M. W. Small, J.-m. Zuo, R. G. Nuzzo, *J. Am. Chem. Soc.* **2009**, *131*, 8683-8689.
- [96] P. Hou, H. Liu, J. Li, J. Yang, *CrystEngComm* **2015**, *17*, 1826-1832.
- [97] C. K. Narula, X. Yang, C. Li, A. R. Lupini, S. J. Pennycook, *J. Phys. Chem. C* **2015**, *119*, 25114-25121.
- [98] X. Xia, J. Zhang, N. Lu, M. J. Kim, K. Ghale, Y. Xu, E. McKenzie, J. Liu, H. Ye, *ACS Nano* **2015**, *9*, 9994-10004.
- [99] Y. Wang, Y. Zeng, W. Fu, P. Zhang, L. Li, C. Ye, L. Yu, X. Zhu, S. Zhao, *Anal. Chim. Acta.* **2018**, *1002*, 97-104.
- [100] S. Link, Z. L. Wang, M. A. El-Sayed, *J. Phys. Chem. B* **1999**, *103*, 3529-3533.
- [101] L. Kang, H. Chen, Z.-J. Yang, Y. Yuan, H. Huang, B. Yang, Y. Gao, C. Zhou, *J. Appl. Phys.* **2018**, *123*, 205110.
- [102] A. Jakab, C. Rosman, Y. Khalavka, J. Becker, A. Trugler, U. Hohenester, C. Sonnichsen, *ACS Nano* **2011**, *5*, 6880-6885.
- [103] U. Nobbmann, in *Polydispersity – what does it mean for DLS and chromatography?* (Ed.: U. Nobbmann), Malvern Panalytical, <http://www.materials-talks.com/blog/2014/10/23/polydispersity-what-does-it-mean-for-dls-and-chromatography/>, **2018**.
- [104] Handbook, *Introduction to Differential Sedimentation*, CPD Instruments Europe, **2018**.
- [105] D. A. Scoog, F. J. Holler, S. R. Crouch, *Principle of Instrumental Analysis*, 6 ed., **2007**.
- [106] A. R. Stokes, A. J. C. Wilson, *Proc. Phys. Soc.* **1944**, *56*, 174.
- [107] P. Scherrer, *Nachrichten von der Gesellschaft der Wissenschaften zu Göttingen, Mathematisch-Physikalische Klasse* **1918**.
- [108] J. I. Langford, A. J. C. Wilson, *J. Appl. Crystallogr.* **1978**, *11*, 102-113.
- [109] S. Mobilio, F. Boscherini, C. Meneghini, *Synchrotron Radiation - Basics, Methods and Applications*, Springer, **2015**.

- [110] T. Shibata, H. Tostmann, B. Bunker, A. Henglein, D. Meisel, S. Cheong, M. Boyanov, *J. Synchrotron Radiat.* **2001**, *8*, 545-547.
- [111] P. Santiago, L. Rendon Vazquez, C. Reza, U. Pal, *HAADF imaging: an effective technique for the study of nonhomogeneous nanostructures*, Vol. 5, **2005**.
- [112] M. I. Novgorodova, A. I. Gorshkov, A. V. Mokhov, *Zap. Vses. Mineral. O-va.* **1979**, *108*, 552-563.
- [113] I.-K. Suh, H. Ohta, Y. Waseda, *J. Mater. Sci.* **1988**, *23*, 757-760.
- [114] V. S. Urusov, V. V. Blinov, *Bull. Acad. Sci. USSR, Div. Chem. Sci.* **1970**, *19*, 231-234.
- [115] J. W. C. J. Spreadborough, *Journal of Scientific Instruments* **1959**.
- [116] J. Zemann, *Acta Crystallogr.* **1965**, *18*, 139-139.
- [117] A. A. Bolzan, C. Fong, B. J. Kennedy, C. J. Howard, *Acta Crystallogr. B* **1997**, *53*, 373-380.
- [118] M. M. Korsukova, V. N. Gurin, T. Lundström, L. E. Tergenius, *J. Less Common Met.* **1986**, *117*, 73-81.
- [119] A. Thust, J. Barthel, K. Tillmann, *Journal of large-scale research facilities* **2016**, *A41*.
- [120] A. Kovács, R. Schierholz, K. Tillmann, *Journal of large-scale research facilities* **2016**, *A43*.
- [121] P. C. M. Heinrich, M. ; Greave, L. , *Biochemie und Pathobiochemie*, Vol. 9, Springer-Verlag Berlin Heidelberg, **2014**.
- [122] H. Wang, X. Qiao, J. Chen, X. Wang, S. Ding, *Mater. Chem. Phys.* **2005**, *94*, 449-453.
- [123] S. Banerjee, K. Loza, W. Meyer-Zaika, O. Prymak, M. Epple, *Chem. Mater.* **2014**, *26*, 951-957.
- [124] S. Ahlberg, A. Antonopoulos, J. Diendorf, R. Dringen, M. Epple, R. Flock, W. Goedecke, C. Graf, N. Haberl, J. Helmlinger, F. Herzog, F. Heuer, S. Hirn, C. Johannes, S. Kittler, M. Koller, K. Korn, W. Kreyling, F. Krombach, R. Zellner, *Beilstein J Nanotechnol.* **2014**, *5*, 1944-1965.
- [125] D. Brogioli, D. Salerno, V. Cassina, S. Sacanna, A. P. Philipse, F. Crocchio, F. Mantegazza, *Opt. Express* **2009**, *17*, 1222-1233.
- [126] P. Diaz-Leyva, E. Perez, J. L. Arauz-Lara, *Rev. Mex. Fis.* **2004**, *50*, 633-638.
- [127] A. Ghoorchian, K. Vandemark, K. Freeman, S. Kambow, N. B. Holland, K. A. Streletsky, *J. Phys. Chem. B* **2013**, *117*, 8865-8874.
- [128] T. Watanabe, Y. Ikeda, M. Hibino, T. Kudo, M. Hosoda, M. Miyayama, K. Sakai, *Jpn. J. Appl. Phys., Part 1* **2002**, *41*, 3157-3158.

- [129] A. Hughes, Z. Liu, M. E. Reeves, *PAME: Plasmonic Assay Modeling Environment Vol. 1*, **2015**.
- [130] J. Helmlinger, O. Prymak, K. Loza, M. Gocyla, M. Heggen, M. Epple, *Cryst. Growth Des.* **2016**, *16*, 3677-3687.
- [131] J. Goldstein, D. E. Newbury, J. R. Michael, N. W. M. Ritchie, J. H. J. Scott, D. C. Joy, *Scanning electron microscopy and x-ray microanalysis*, Fourth edition H1 - D33 UPK1163(4)+1_d ed., Springer, New York, NY, **2018**.
- [132] J. C. Ghosh, T. L. R. Char, *Z. physiol. Chem.* **1937**, *246*, 115-123.
- [133] L. Vegard, *Z. Phys.* **1921**, *5*, 17-26.
- [134] W. B. Pearson, *A Handbook of Lattice Spacings and Structures of Metals and Alloys*, Pergamon Press LTD., **1958**.
- [135] D. Mahl, J. Diendorf, W. Meyer-Zaika, M. Epple, *Colloids Surf. A* **2011**, *377*, 386-392.
- [136] V. Amendola, M. Meneghetti, *J. Phys. Chem. C* **2009**, *113*, 4277-4285.
- [137] J. R. G. Navarro, F. Lerouge, *Nanophotonics* **2017**, *6*, 71-92.
- [138] A. Brioude, X. C. Jiang, M. P. Pileni, *J. Phys. Chem. B* **2005**, *109*, 13138-13142.
- [139] L. Tong, Q. Wei, A. Wei, J.-X. Cheng, *Photochem. Photobiol.* **2009**, *85*, 21-32.
- [140] A. Callegari, D. Tonti, M. Chergui, *Nano Lett.* **2003**, *3*, 1565-1568.
- [141] G. Park, D. Seo, J. Jung, S. Ryu, H. Song, *J. Phys. Chem. C* **2011**, *115*, 9417-9423.
- [142] Y. Sun, Y. Xia, *Science* **2002**, *298*, 2176-2179.
- [143] B. Wiley, Y. Sun, B. Mayers, Y. Xia, *Chemistry* **2005**, *11*, 454-463.
- [144] Y. Sun, *Chem. Soc. Rev.* **2013**, *42*, 2497-2511.
- [145] T. C. Deivaraj, N. L. Lala, J. Y. Lee, *J. Colloid. Interface. Sci.* **2005**, *289*, 402-409.
- [146] H. G. Liao, Y. X. Jiang, Z. Y. Zhou, S. P. Chen, S. G. Sun, *Angew. Chem. Int. Ed.* **2008**, *47*, 9100-9103.
- [147] W.-W. Wang, Y.-J. Zhu, *Inorg. Chem. Commun.* **2004**, *7*, 1003-1005.
- [148] A. J. Frank, N. Cathcart, K. E. Maly, V. Kitaev, *J. Chem. Educ.* **2010**, *87*, 1098-1101.
- [149] H. J. Lee, M. A. Do, E. J. Kim, J. H. Yeum, H. D. Ghim, J. H. Choi, *Adv. Mater. Res.* **2008**, *47-50*, 1080-1083.
- [150] P. E. J. Saloga, C. Kästner, A. F. Thünemann, *Langmuir* **2018**, *34*, 147-153.
- [151] S. W. Chaikin, W. G. Brown, *J. Am. Chem. Soc.* **1949**, *71*, 122-125.
- [152] R. L. Pecsok, *Polarographic Studies on the Oxidation and Hydrolysis of Sodium Borohydride I, Vol. 75*, **1953**.
- [153] H. I. Schlesinger, *J. Am. Chem. Soc.* **1953**, *75*.
- [154] M. M. Cook, J. A. Lander, *J. Appl. Photogr. Eng.* **1979**, 144-147.

- [155] G. Mettela, M. Bhogra, U. V. Waghmare, G. U. Kulkarni, *J. Am. Chem. Soc.* **2015**, *137*, 3024-3030.
- [156] V. Bansal, V. Li, A. P. O'Mullane, S. K. Bhargava, *CrystEngComm* **2010**, *12*, 4280-4286.
- [157] W.-Z. Li, Y. Zhou, F. Liu, Y. Li, M.-J. Xia, E.-H. Han, T. Wang, X. Zhang, Y. Fu, *Nanomaterials* **2017**, *7*, 237.
- [158] B. Wang, G. T. Fei, Y. Zhou, B. Wu, X. Zhu, L. Zhang, *Cryst. Growth Des.* **2008**, *8*, 3073-3076.
- [159] D. V. Zhelev, T. S. Zheleva, *J. Appl. Phys.* **2014**, *115*, 044309.
- [160] W. H. Qi, M. P. Wang, *J. Nanopart. Res.* **2005**, *7*, 51-57.
- [161] Y. Zhao, J. Zhang, *J. Appl. Crystallogr.* **2008**, *41*, 1095-1108.
- [162] C. Solliard, M. Flueli, *Surf. Sci.* **1985**, *156*, 487-494.
- [163] B. K. Pandey, *J. Chem. Pharm. Res.* **2017**, *9*, 204-209.
- [164] C. Song, O. Sakata, L. S. R. Kumara, S. Kohara, A. Yang, K. Kusada, H. Kobayashi, H. Kitagawa, *Sci. Rep.* **2016**, *6*, 31400.
- [165] J. Yamamoto, *The Sodium Borohydride Digest*, Rohm and Haas Company, **2003**.
- [166] I. McGraw, *Dean's Analytical Chemistry Handbook*, The McGraw-Hill Companies, **2004**.
- [167] A. J. Bard, F. Scholz, M. Stratmann, C. J. Packett, *Inorganic Electrochemistry, Vol. 7a*, Wiley-VCH, **2006**.
- [168] U. Nobbmann, in *PDI from an individual peak in DLS* (Ed.: U. Nobbmann), Malvern Panalytical, <http://www.materials-talks.com/blog/2015/03/31/pdi-from-an-individual-peak-in-dls/>, **2018**.
- [169] R. Das, S. Sarkar, *Opt. Mater.* **2015**, *48*, 203-208.
- [170] F. Zhou, Z.-Y. Li, Y. Liu, Y. Xia, *J. Phys. Chem. C* **2008**, *112*, 20233-20240.
- [171] B. Wang, L. Zhang, X. Zhou, *Spectrochim. Acta A* **2014**, *121*, 63-69.
- [172] S. H. Im, Y. T. Lee, B. Wiley, Y. Xia, *Angew. Chem. Int. Ed.* **2005**, *44*, 2154-2157.
- [173] J.-H. Oh, Y. J. Sa, S. H. Joo, J.-S. Lee, *Bull. Korean Chem. Soc.* **2012**, *33*.
- [174] M. Thiele, J. Z. E. Soh, A. Knauer, D. Malsch, O. Stranik, R. Müller, A. Csáki, T. Henkel, J. M. Köhler, W. Fritzsche, *Chem. Eng. J.* **2016**, *288*, 432-440.
- [175] Y. Sun, B. Gates, B. Mayers, Y. Xia, *Nano Letters* **2002**, *2*, 165-168.
- [176] Y. Sun, Y. Ren, Y. Liu, J. Wen, J. S. Okasinski, D. J. Miller, *Nat. Commun.* **2012**, *3*, 971.
- [177] Q. Guo, Y. Zhao, W. L. Mao, Z. Wang, Y. Xiong, Y. Xia, *Nano Lett.* **2008**, *8*, 972-975.

- [178] R. W. G. Wyckoff, *The Structure of Crystals*, Reinhold Publishing Corporation, 330 West Forthly-Second Street, New York, U.S.A., **1935**.
- [179] M. Ratti, J. J. Naddeo, Y. Tan, J. C. Griepenburg, J. Tomko, C. Trout, S. M. O'Malley, D. M. Bubb, E. A. Klein, *Appl. Phys. A: Mater. Sci. Process.* **2016**, *122*, 1-7.
- [180] P. J. Riggle, C. A. Kumamoto, *J. Bacteriol* **2000**, *182*, 4899-4905.
- [181] P. Costa, J. M. Sousa Lobo, *Eur. J. Pharm. Sci.* **2001**, *13*, 123-133.
- [182] B. Nowack, H. F. Krug, M. Height, *Environ. Sci. Technol.* **2011**, *45*, 1177-1183.
- [183] E. I. Maurer, M. Sharma, J. J. Schlager, S. M. Hussain, *Nanotoxicology* **2014**, *8*, 718-727.
- [184] J. A. Gerbec, D. Magana, A. Washington, G. F. Strouse, *J. Am. Chem. Soc.* **2005**, *127*, 15791-15800.
- [185] M. J. Gronnow, R. J. White, J. H. Clark, D. J. Macquarrie, *Org. Process Res. Dev.* **2005**, *9*, 516-518.
- [186] J. Helmlinger, M. Heise, M. Heggen, M. Ruck, M. Epple, *RSC Adv.* **2015**, *5*, 92144-92150.
- [187] F. Bonet, C. Guéry, D. Guyomard, R. Herrera Urbina, K. Tekaia-Elhsissen, J. M. Tarascon, *Int. J. Inorg. Mater.* **1999**, *1*, 47-51.
- [188] E. M. Zaiser, V. K. La Mer, *J. Colloid Sci.* **1948**, *3*, 571-598.
- [189] C. Wagner, *Z. Elektrochem.* **1961**, *65*, 581-591.
- [190] B. G. Kelly, A. B. Loether, A. D. Di Chiara, R. W. Henning, M. F. De Camp, K. M. Unruh, *J. Phys. Chem. Solids* **2017**, *108*, 104-108.
- [191] M. Y. Gamarnik, Y. Y. Sidorin, *physica status solidi (b)* **1989**, *156*, K1-K4.
- [192] V. V. Bardushkin, D. A. Kirillov, Y. I. Shilyaeva, S. A. Gavrillov, V. B. Yakovlev, M. V. Silibin, *Russ. J. Phys. Chem. A* **2017**, *91*, 1099-1104.
- [193] S. I. Sadovnikov, A. I. Gusev, *Phys. Solid State* **2017**, *59*, 1887-1894.
- [194] M. E. Straumanis, *Monatshefte für Chemie / Chemical Monthly* **1971**, *102*, 1377-1386.
- [195] C. K. Yee, R. Jordan, A. Ulman, H. White, A. King, M. Rafailovich, J. Sokolov, *Langmuir* **1999**, *15*, 3486-3491.
- [196] G. S. Fonseca, G. Machado, S. R. Teixeira, G. H. Fecher, J. Morais, M. C. Alves, J. Dupont, *J. Colloid. Interface. Sci.* **2006**, *301*, 193-204.
- [197] F. Bonet, V. Delmas, S. Grugeon, R. H. Urbina, P. Y. Silvert, K. Tekaia-Elhsissen, *Nanostruct. Mater.* **2000**, *11*, 1277-1284.
- [198] J.-S. Schanche, *Mol. Divers.* **2003**, *7*, 291-298.

- [199] D. Xu, P. Diao, T. Jin, Q. Wu, X. Liu, X. Guo, H. Gong, F. Li, M. Xiang, Y. Ronghai, *ACS Appl. Mater. Interfaces*. **2015**, *7*, 16738-16749.
- [200] N. Ingri, *Acta Chem. Scand.* **1962**, *16*, 439-448.
- [201] Y. Zhao, E. A. Hernandez-Pagan, N. M. Vargas-Barbosa, J. L. Dysart, T. E. Mallouk, *J. Phys. Chem. Lett.* **2011**, *2*, 402-406.
- [202] J. D. Weiland, D. J. Anderson, M. S. Humayun, *IEEE Trans. Biomed. Eng.* **2002**, *49*, 1574-1579.
- [203] S. J. Freakley, J. Ruiz-Esquiús, D. J. Morgan, *Surf. Interface Anal.* **2017**, *49*, 794-799.
- [204] S. Gin, P. Jollivet, M. Fournier, C. Berthon, Z. Wang, A. Mitroshkov, Z. Zhu, J. V. Ryan, *Geochim. Cosmochim. Acta* **2015**, *151*, 68-85.

9. Appendix

9.1 List of publications

D. Proudfoot, Y. Dautova, A. N. Kapustin, K. Pappert, M Epple, H. Okkenhaug, S. J. Cook, C. M. Shanahan, M. D. Bootman, “Calcium phosphate particles stimulate interleukin-1 β release from human vascular smooth muscle cells: A role for spleen tyrosine kinase and exosome release”, *J. Mol. Cell. Cardiol.* **2018**, 115, 82-93.

A. Rostek, M. Breisch, K. Pappert, K. Loza, M. Heggen, M. Köller, C. Sengstock M. Epple, „Comparative biological effects of spherical noble metal nanoparticles (Rh, Pd, Ag, Pt, Au) with 4–8 nm diameter“, *Beilstein J. Nanotechnol.* **2018**, 9, 2763–2774.

P. R. A. F. Garcia, K. Loza, S. Daumann, V. Grasmik, K. Pappert, A. Rostek, J. Helmlinger, O. Prymak, M. Epple, C. L. P. Oliveira, “Combining Small-Angle X-Ray Scattering and X-Ray Powder Diffraction to Investigate Size, Shape, and Crystallinity of Silver, Gold, and Alloyed Silver-Gold Nanoparticles“, **2018** (submitted).

9.2 Posters and presentations

23rd Annual Conference of the German Crystallographic Society, Göttingen, Germany, March 2015, K. Pappert, K. Merz, C. Schauerte “ Crystallography of protected amino acids in presence of amines ” (**poster contribution**).

Nanoparticles with Morphological and Functional Anisotropy: Faraday Discussion, Glasgow, Scotland, July 2016, K. Pappert, J. Helmlinger, C. Sengstock, C. Groß-Heitfeld, C. Mayer, T. A. Schildhauer, M. Köller, O. Prymak, K. Loza, M. Gocyla, M. Heggen, M. Epple, “Cytotoxicity, antibacterial effects, and crystallographic properties of different morphologies of silver nanoparticles” (**poster contribution**).

DAAD exchange with the University of Sao Paulo, Sao Paulo, Brazil, October 2016, K. Pappert, K. Loza, M. Etter, L. S. Germann, M. Epple, R. E. Dinnebier, “Synthesis and Characterization of Different Silvernanoparticle Morphologies” (**oral presentation**).

DAAD exchange with the University of Notre Dame, South Bend, USA, December 2017, K. Pappert, K. Loza, M. Epple, R. E. Dinnebier, L. S. Germann, “Synthesis and Characterization of Silver Morphology based Core-Shell Systems and Characterization of Monometallic Iridium Particles” (**oral presentation**).

26th Annual Conference of the German Crystallographic Society, Essen, Germany, March 2018, K. Pappert, K. Loza, M. Etter, L. S. Germann, M. Epple, R. E. Dinnebier, “In Situ X-Ray Powder Diffraction Measurements of a High-Yield Microwave Synthesis of Silver Nanoparticles using Synchrotron Radiation” (**oral presentation + poster contribution**).

9.3 Curriculum Vitae

„The Curriculum Vitae is due to reasons of data protection not included in the online version”.

"Der Lebenslauf ist in der Online-Version aus Gründen des Datenschutzes nicht enthalten".

9.4 Danksagung

An erster Stelle möchte ich Herrn Prof. Epple danken, der es mir durch die wissenschaftliche Unterstützung sowie das interessante zur Verfügung gestellte Thema ermöglicht hat mich wissenschaftlich weiterzubilden und zu reifen. Im Rahmen dieser Arbeit forderten mich vor allem die Vertiefung meiner festkörperchemischen Analysekenntnisse sowie das Erlernen anspruchsvollerer Methoden wie der Rietveldverfeinerung oder der Auswertung von Synchrotrondaten.

Tiefe Hochachtung möchte ich auch für das mir zu Seite stehende Kollegium aussprechen. Wo nicht nur technische Mitarbeiter wie Carola, Sabine K., Sabine B., Dietrich, Ursula, Robin oder Kerstin mich stehst unterstützten, sondern auch menschlich stets beispielhaft agierten. Auch allen Doktoranden und Doktorandinnen gilt mein Dank, mit denen man nicht nur fachliche Gespräche führen konnte, sondern auch private Unternehmungen immer viel Spaß brachten. In den drei Jahren an der Universität in Essen konnte ich somit nicht nur Kollegen sondern auch Freunde finden. Diese erstklassige Arbeitsatmosphäre hat mir die erfolgreiche Abgabe dieser Arbeit erst ermöglicht.

Auch allen Kooperationspartnern aus Jülich (Mark Heggen), Bochum (Christina Sengstock, Marina Breisch, Manfred Köller), Stuttgart (Luzia Germann, Robert Dinnebier), Hamburg (Martin Etter) sowie Brasilien (Paulo Ricardo de Abreu Furtado Garcia, Cristiano Luís Pinto de Oliveira) möchte ich herzlichst danken. Die Zusammenarbeit war stehst produktiv und die unterschiedlichen Fachgebiete konnten mein Wissen erweitern und ein tieferes Verständnis jeweiliger Fachbereiche generieren. Des Weiteren habe ich die Unterhaltungen auch abseits der Arbeit stets genossen.

Besonders danken möchte ich auch Kateryna Loza mit der meine fachlichen Diskussionen stets zu neuen Denkanstößen und Experimenten führten. Ich habe unsere wissenschaftliche Zusammenarbeit in meiner Zeit hier sehr genossen.

Mein größter Dank gilt jedoch Viktoria, die mich immer begleitet hat und mir nicht nur privat sondern auch fachlich immer zur Seite stand. Leider endete somit oftmals die Arbeit nicht an der Haustür da unsere Fachsimpelei auch Zuhause weitergeführt wurde. Jedoch möchte ich keine Sekunde dieser Zeit missen.

Als letztes möchte ich meiner Familie (Familie Grasmik natürlich eingeschlossen) danken, die aus mir den Menschen gemacht hat, welcher ich heute bin.

9.5 Eidesstaatliche Erklärungen

Hiermit versichere ich, die vorliegende Arbeit mit dem Titel

„Synthesis and in-depth characterization of mono- and bimetallic nanoparticles“

selbst verfasst und keine außer den angegebenen Hilfsmitteln und Quellen verwendet zu haben.

Zudem erkläre ich, dass ich die Arbeit in dieser oder einer ähnlichen Form bei keiner anderen Fakultät eingereicht habe.

Essen, den

Kevin Pappert